

Diss. ETH No. 16050

**DYNAMIC RECRYSTALLISATION AND MICROFABRIC DEVELOPMENT  
IN SINGLE CRYSTALS OF QUARTZ DURING EXPERIMENTAL DEFORMATION**

A dissertation submitted to the  
SWISS FEDERAL INSTITUTE OF TECHNOLOGY

For the degree of  
DOCTOR OF NATURAL SCIENCES

Presented by

**Martine G.C. Vernooij**  
drs. Geologie, Universiteit Utrecht

Born on November 19, 1977  
Citizen of the Netherlands

Recommended by:

Prof. Dr. Jean-Pierre Burg	ETH Zürich	examiner
Dr. Bas den Brok	ETH Zürich	co-examiner
Dr. Karsten Kunze	ETH Zürich	co-examiner
Prof. Dr. Dave J. Prior	University of Liverpool	co-examiner

Zürich, 2005





*“D'Wält isch so perfid, dass sy sech sälte oder nie,  
nach Bilder, wo'mer vore gmacht hei richtet”*

*Mani Matter*

**Aan mijn ouders**

**THANK YOU!**

Philip Allen, Marina Armann, Ronald Bakker, Auke Barnhoorn, Michel Bestmann, Hans de Bresser, Bas den Brok, Geoffrey Bromiley, Jean Pierre Burg, Misha Bystricky, Mirjam van Daalen, Miriam Dühnfort, Ulli Exner, Diego Gatta, Urs Gerber, Silvio Giger, Claudia Hegglin, Florian Heidelberg, René Heilbronner, Stefan Heuberger, Robert Hofmann, Stefan Keyssner, Lydia Kison-Herzing, Karsten Kunze, Falko Langenhorst, Neil Mancktelow, Michael Maxelon, Nele Meckler, Marcel Mettler, Andi Mueller, Frowin Pirovino, Ruth Prelicz, Dave Prior, Almar de Ronde, Dave Ruby, Regula Schaelchli, Rolf Schmid, Martin Schmocker, Hubert Schulze, Fritz Seifert, Diane Seward, Helmuth Sölva, Chris Spiers, Petra Ständner, Holger Stünitz, Peter Ulmer and Peter Wägli.

---

**TABLE OF CONTENTS**

<b>Abstract</b>	V
<b>Kurzfassung</b>	VII
<b>Chapter 1:</b>	1
<b>Introduction</b>	
1.1 General Background	1
1.2 Aim	2
1.3 Structure of the thesis	2
<b>Chapter 2:</b>	5
<b>CPO development in quartz: state of the art</b>	
2.1 Dislocation glide and CPO development	5
2.2 Temperature and CPO development	7
2.3 Flow type and CPO development	9
2.4 Strain and CPO development	10
2.5 Dynamic recrystallisation and CPO development	11
2.5.1 Models on the effect of dynamic recrystallisation on CPO development	12
2.5.2 Experimental data on the effect of dynamic recrystallisation on CPO development	13
2.5.3 CPOs in dynamically recrystallised rocks from nature	14
2.6 Influence of water on CPO development	16
2.7 Summary and conclusion	17
<b>Chapter 3:</b>	19
<b>Techniques and methods used in this study</b>	
3.1 Griggs solid medium deformation apparatus	19
3.2 Starting material and sample preparation for the deformation tests	21
3.3 Experimental procedure	22
3.4 Analysis of mechanical data	23
3.5 Microstructural analysis	26
3.5.1 Optical microscopy	26
3.5.2 Scanning electron microscopy	26
3.5.3 Transmission electron microscopy	27
3.5.4 Cathodoluminescence	27
3.6 Texture measurements	28

<b>Chapter 4:</b>	33
<b>Overview of mechanical data and deformation microstructures in quartz single crystals</b>	
4.1 Introduction	33
4.2 Mechanical data	33
4.2.1 The effect of the starting orientation	33
4.2.2 The effect of deformation conditions	35
4.3 Microstructural observations	36
4.3.1 Hydrostatically loaded samples	36
4.3.2 Sample deformed without water	37
4.3.3 Samples deformed with 1 vol% water	37
4.3.3.1 $\sigma_1$ at $45^\circ$ to $\langle c \rangle$	37
4.3.3.2 $\sigma_1$ parallel to $\langle c \rangle$	39
4.3.3.3 $\sigma_1$ $90^\circ$ to $\langle c \rangle$	40
4.3.4 Samples deformed with 1 vol% water and 20 mg $\text{Mn}_2\text{O}_3$ -powder	42
4.3.5 Sample deformed with 3 vol% water	43
4.3.6 Sample deformed at $10^{-7} \text{ s}^{-1}$	43
4.4 Summary	44
<b>Chapter 5:</b>	45
<b>Undulatory extinction, deformation lamellae and subgrains: lattice rotations in quartz single crystals</b>	
5.1 Introduction	45
5.2 Samples	45
5.3 Undulatory extinction	47
5.4 Subgrains	47
5.5 Deformation lamellae	49
5.6 Cathodoluminescence	52
5.7 Lattice rotation	54
5.8 Discussion	55
5.8.1 Deformation lamellae	55
5.8.2 Undulatory extinction	57
5.8.3 Subgrains	59
5.8.4 Water	59
5.9 Conclusions	59
<b>Chapter 6:</b>	61
<b>Development of crystallographic preferred orientations by nucleation and growth of new grains in experimentally deformed quartz single crystals</b>	
Abstract	61
Keywords	61
6.1 Introduction	61
6.2 Methods	62
6.2.1 Sample description	62
6.2.2 Deformation tests	62
6.2.3 Sample preparation for microstructural analysis	64
6.2.4 Electron backscatter diffraction	64

6.3	Results	65
6.3.1	Mechanical data	65
6.3.2	Deformation microstructures	65
6.3.2.1	<i>Domains with undulatory extinction and deformation lamellae</i>	67
6.3.2.2	<i>Domains with new grains</i>	67
6.3.3	Crystallographic orientation analysis	70
6.3.3.1	<i>Lattice rotations in low strain host domains</i>	70
6.3.3.2	<i>Transition from lattice rotation to new grain development</i>	72
6.3.3.3	<i>CPOs in the new grain aggregates</i>	74
6.4	Discussion	76
6.4.1	Deformation mechanisms	76
6.4.2	Crystal lattice rotations in the host domains	77
6.4.3	CPO development in the new grain aggregates	78
6.4.4	Comparison with previous data	79
6.5	Conclusions	80
 <b>Chapter 7:</b>		<b>81</b>
<b>'Brittle' shear zones in experimentally deformed quartz single crystals</b>		
	Abstract	81
	Keywords	81
7.1	Introduction	81
7.2	Methods	82
7.2.1	Sample description	82
7.2.2	Deformation test	82
7.2.3	Sample preparation for analysis	83
7.2.4	EBSD data acquisition and analysis	83
7.3	Results	84
7.3.1	Mechanical data	84
7.3.2	Microstructures	84
7.3.3	Crystallographic orientations	88
7.3.3.1	<i>Orientation maps</i>	88
7.3.3.2	<i>Zone A: Initial shear zones</i>	90
7.3.3.3	<i>Zone B: Dextral mature shear zones</i>	90
7.3.3.4	<i>Zone C: Sinistral mature shear zone and sinistral transitional shear zone</i>	91
7.3.3.5	<i>Zone D: Isolated pockets of new grains</i>	93
7.3.3.6	<i>Misorientation axes</i>	95
7.4	Discussion	95
7.4.1	Models for shear zone development	96
7.4.2	Shear zone development in the studied sample	98
7.4.3	CPO development in the shear zones	98
7.4.4	Isolated pockets of new grains	99
7.5	Summary and conclusions	100
 <b>Chapter 8:</b>		<b>101</b>
<b>General conclusions and suggestions for further research</b>		
8.1	Deformation behaviour of quartz single crystals in the present experiments	101
8.2	Comparison with CPO data and microstructures from other studies	102
8.3	Unanswered questions	104

<b>Appendix A:</b> <b>Raw load-displacement data</b>	107
<b>Appendix B:</b> <b>Fluid inclusions</b>	113
<b>Appendix C:</b> <b>Experimental reproduction of tectonic deformation lamellae in quartz and comparison to shock-induced planar deformation features</b>	117
<b>Appendix D:</b> <b>Conference contributions</b>	119
<b>References</b>	121
<b>Curriculum vitae</b>	127

**ABSTRACT**

Crystallographic preferred orientations (CPOs) are common in deformed rocks, and especially in deformed *quartz-rich* rocks. They provide important information on tectono-metamorphic processes. The best-developed CPOs are found in dynamically recrystallised quartz aggregates. Yet, it is only partly understood how dynamic recrystallisation affects the development of these CPOs.

To investigate the effect of dynamic recrystallisation on CPO development, natural quartz single crystals were experimentally deformed under conditions where dynamic recrystallisation and CPO development are known to occur (temperature 800°C, confining pressure ~1.2 GPa, strain rate  $10^{-6}$ - $10^{-7}$  s<sup>-1</sup>, bulk finite strain 5-50%, 1 vol% added water). Samples were uniaxially deformed in different crystallographic starting orientations. The highly heterogeneous microstructures and textures of the deformed samples were analysed by light microscopy, electron backscatter diffraction (EBSD) analysis, transmission electron microscopy (TEM), secondary electron imaging and cathodoluminescence.

It could be shown that the experimentally produced microstructures and CPOs, reported in this thesis, result from three different reorientation processes:

1. *Crystal reorientation by glide controlled lattice rotation.*

Within domains with *no* dynamic recrystallisation, characterised by undulatory extinction and deformation lamellae, gradual rotations of the crystal lattice are observed. The rotation axes are always about perpendicular to the compression direction and approximately parallel to low-index crystallographic directions. These axes are mostly compatible with rotation axes of basal and prism glide systems. Deformation is therefore interpreted to be crystal-plastic.

2. *Crystal reorientation by precipitation and growth of new grains.*

Within domains of dynamic recrystallisation characterised by aggregates of new grains, the *c*-axes show strong CPOs consisting of maxima at ~45° to the compression direction. This is the case in *all* experiments, irrespective of initial crystallographic orientation and irrespective of the amount of strain. The crystals are not continuously rotated out of the initial orientation towards these maxima. The CPO in the domains with new grains is unrelated to the gradual lattice rotations within the domains with undulatory extinction. New grains have a subeuhedral shape and numerous microcavities, voids, fluid channels and fluid inclusions at their grain boundaries. This suggests that the new grains developed by precipitation from a solution. Subsequently, the CPO must have developed by selective fluid assisted growth of new grains that were best suited for intracrystalline deformation at the imposed experimental conditions, i.e. *c*-axis at 45° to the compression direction.

3. *Crystal reorientation by rotation of fracture fragments.*

Within domains of dynamic recrystallisation characterised by intracrystalline shear zones, the grains show a strong CPO with *c*-axes perpendicular to the shear zone. EBSD and TEM data show evidence for shear zone development along planar microcracks oriented parallel to rhomb planes. It is suggested that further microcracking results in cataclastic shear zone development. Consequently, new grains developed by rotation of fracture fragments, facilitated by the high water pressure and the relatively high porosity within the shear zones. Subsequent selective growth of the new grains with *c*-axes oriented approximately perpendicular to the shear zone finally lead to the development of a CPO.

In the literature it is generally assumed that dynamic recrystallisation takes place as a consequence of dislocation creep. New grains are considered to develop by progressive subgrain rotation and further evolve by grain boundary migration. The experiments show, however, that new recrystallised grains can also be created by precipitation from solution as well as by rotation of fracture fragments along crystallographically oriented microfractures. The recrystallised grains do not inherit the CPO from their host grains, but assume orientations most suitable for glide during progressive grain boundary migration.





## KURZFASSUNG

Kristallographische Vorzugsorientierungen, sogenannte *crystallographic preferred orientations (CPO's)*, sind verbreitet in deformierten Gesteinen, insbesondere in quarzreichen Gesteinen. Sie sind von entscheidender Bedeutung, da sie Aufschluss über tektono-metamorphe Prozesse geben. Die am besten ausgebildeten CPO's treten hauptsächlich in dynamisch rekristallisierten Quarz-Aggregaten auf. Es ist jedoch nur teilweise bekannt, wie die dynamische Rekristallisation die Bildung von CPO's beeinflusst.

Natürliche Quarz-Einkristalle wurden experimentell deformiert um den Einfluss der dynamischen Rekristallisation auf die CPO-Bildung zu untersuchen. Es wurden dazu Bedingungen gewählt, von denen man weiss, dass dabei dynamische Rekristallisation und CPO-Entwicklung stattfinden (Temperatur: 800°C, Umgebungsdruck: ~1.2 GPa, Verformungsrate:  $10^{-6}$ - $10^{-7}$  s<sup>-1</sup>, durchschnittliche finite Verformung: 5-50%; 1 vol% beigefügtes Wasser). Die Proben wurden in verschiedenen kristallographischen Ausgangsorientierungen uniaxial deformiert. Die stark heterogenen Mikrostrukturen und Texturen der deformierten Proben wurden mittels Polarisationsmikroskopie, Elektronenrückstreubeugung (EBSD), Transmissionselektronenmikroskopie (TEM), Sekundärelektronen-Abbildung und Kathodenlumineszenz untersucht.

Es konnte gezeigt werden, dass die in dieser Arbeit beschriebenen, experimentell erzeugten Mikrostrukturen, aus drei verschiedenen Umorientierungsprozessen entstehen.

### 1. *Kristall-Umorientierung durch Gitterrotation mittels Gleiten.*

Innerhalb von Bereichen *ohne* dynamische Rekristallisation, charakterisiert durch undulöse Auslöschung und Deformationslamellen, werden graduelle Kristallgitterrotationen beobachtet. Die Rotationsachsen sind immer ungefähr senkrecht zur Kompressionsachse und ungefähr parallel zu niedrig indizierten kristallographischen Richtungen. Die Achsen sind meist kompatibel mit Rotationsachsen von basalen und prismatischen Gleitsystemen. Die Deformation wird als kristall-plastisch interpretiert.

### 2. *Kristall-Umorientierung durch Keimbildung und Wachstum von neuen Körnern.*

Innerhalb von Bereichen *mit* dynamischer Rekristallisation, charakterisiert durch Aggregate aus neuen Körnern, zeigen c-Achsen starke CPO's mit Maxima ~45° geneigt zur Kompressionsrichtung. Dies trifft auf *alle* Experimente zu, unabhängig von der ursprünglichen kristallographischen Orientierung und unabhängig vom Betrag der Verformung. Die Umorientierung der Kristalle fand nicht statt durch kontinuierliche Rotation aus der ursprüngliche Lage in die neuen Maxima. Die CPO in den Bereichen mit neuen Körnern hängt nicht mit den graduellen Gitterrotationen innerhalb der Bereiche mit undulöser Auslöschung zusammen. Die neuen Körner sind hypidiomorph und zeigen optisch keine Verformung. An ihren Korngrenzen treten zahlreiche Mikrohohlräume, Poren, Fluidkanäle und Fluideinschlüsse auf. Dies deutet darauf hin, dass diese neuen Körner das Produkt einer Ausfällung sind. Die CPO hat sich anschliessend durch bevorzugtes Wachstum derjenigen neuen Körner gebildet, welche am besten für kristall-plastische Deformation unter den experimentellen Bedingungen orientiert sind.

### 3. *Kristall-Umorientierung durch Rotation von Bruchfragmenten.*

Innerhalb von Bereichen *mit* dynamischer Rekristallisation, charakterisiert durch intrakristalline Scherzonen, zeigen die Körner eine starke CPO mit c-Achsen senkrecht zur Scherzone. EBSD- und TEM-Daten weisen auf eine Entstehung der Scherzonen entlang von Mikrobrüchen hin, die parallel zu den kristallographischen Rhomboederflächen sind. Es kann angenommen werden, dass anhaltende Mikrorissbildung zur Entstehung der kataklastischen

Scherzonen führt. Innerhalb dieser Scherzonen entstanden demzufolge neue Körner durch Rotation von Bruchfragmenten, wobei diese Rotation durch den hohen Wasserdruck und die relativ hohe Porosität begünstigt wurde. Darauf folgendes selektives Wachstum der neuen Körner, mit c-Achsen ungefähr senkrecht zur Scherzone, führte schliesslich zur Bildung der starken CPO.

In der Literatur wird allgemein angenommen, dass dynamische Rekristallisation als Folge von Versetzungskriechen stattfindet. Neue Körner sollen durch progressive Subkornrotation entstehen und sich durch Korngrenzenmigration weiterentwickeln. CPO's von dynamisch rekristallisierten Gesteinen werden üblicherweise als das Resultat von Gitterrotation mittels Gleitung interpretiert. Die Experimente zeigen jedoch, dass neue, rekristallisierte Körner auch durch Ausfällung und durch Rotation von Bruchfragmenten entlang von kristallographisch orientierten Mikrobrüchen entstehen können. Diese neuen, rekristallisierten Körner übernehmen nicht die Orientierungen der ursprünglichen Körner, sondern nehmen die für Gleitung am besten geeigneten Orientierungen während des weiteren Wachstums an.

## **CHAPTER 1: INTRODUCTION**

### **1.1 GENERAL BACKGROUND**

Studies of structural geology and tectonics mainly focus on deformation processes in the Earth's continental crust. Quartz is the most common mineral in the continental crust. Understanding the deformation behaviour of quartz is thus inevitable for a better understanding of the rheological behaviour of the crust. Quartz is generally regarded as one of the best-known minerals in terms of its deformation behaviour. Nevertheless, we are a long way from being able to unambiguously interpret quartz deformation microstructures in terms of deformation mechanisms, pressure, temperature and stress levels. One major problem is the incomplete knowledge of mechanisms by which crystallographic preferred orientations (CPOs) are formed in quartz. Several theoretical models have been proposed, but observations and predictions are often in disagreement and experimental verification of the models is poor or even lacking (e.g. Lister et al. 1978; Jessell 1988; Wenk and Christie, 1991, Bons and den Brok 2000).

CPOs are very common in the rock-forming minerals of ductilely deformed rocks, especially in deformed *quartz* rocks. They are a useful tool in structural geology, for example, to determine (i) the sense of shear (sinistral or dextral), (ii) the type of strain (e.g. simple or pure shear), (iii) the amount of strain, (iv) the temperature during deformation, or (v) the deformation mechanism active during its formation (e.g. Law 1990, Passchier & Trouw 1996). The best-developed CPOs are mostly found in dynamically recrystallised rocks (Schmid and Casey 1986). Nevertheless, the most important problem in understanding CPOs is that the effect of dynamic recrystallisation on CPO development is still ambiguous (e.g. Jessell 1988, Passchier and Trouw 1996, Wenk 1998). To be able to better understand CPO development in quartz, this problem must be solved. There are several possible effects of dynamic recrystallisation on CPO development. It could either (i) erase pre-existing CPOs, (ii) have no effect on CPO development and mimic pre-existing CPOs, or (iii) lead to the development of a CPO on its own (e.g. Burg et al. 1986, Karato and Masuda 1989, Gleason et al. 1993, Stallard and Shelley 1995, den Brok et al. 1999).

Dynamic recrystallisation is widely regarded as a process that accompanies dislocation creep. Two different processes are held responsible:

- i) *Subgrain rotation recrystallisation* (e.g. White 1977 and 1976, Urai et al. 1986). Small new recrystallised grains are formed by progressive misorientation of subgrains to form new grains. The misorientation between subgrains and host grains increases with proceeding deformation because of the addition of new dislocations into the subgrain boundaries. By definition, subgrains become new grains once the misorientation exceeds  $10^\circ$  (White 1977).
- ii) *Grain boundary migration recrystallisation* (e.g. Gordon and Vandermeer 1966, Urai et al. 1986). Grains recrystallise by local migration of grain boundaries. Grains with low defect density grow at the cost of their neighbour grains with higher defect content. Grain boundary migration recrystallisation is assumed to be driven by differences in crystal-plastic strain energy (density of dislocations, point defects).

Recent studies using electron backscatter diffraction (EBSD) analyses seriously questioned whether or not recrystallisation is exclusively caused by either of these two processes. It appeared that the misorientation relationship observed between parent and recrystallised

grains cannot be explained by subgrain rotation and/or grain boundary migration recrystallisation alone (Leiss and Barber 1999, van Daalen et al. 1999, Bestmann and Prior 2003). Hence, other processes must play an important role in dynamic recrystallisation (e.g. nucleation, grain boundary sliding, microcracking). Hobbs (1968), Shelley (1971), den Brok et al. (1999) and others showed that dynamic recrystallisation by grain boundary migration can also be driven by differences in *elastic* strain energy (i.e. differences in stress). Shelley (1971) proposed that such recrystallised grains may develop as entirely new nuclei.

### 1.2 AIM

CPO patterns are strongly controlled by the deformation processes. Above is indicated that the processes that are involved in dynamic recrystallisation are ambiguous. It is the aim of this thesis to investigate these dynamic recrystallisation processes, in order to find out *how dynamic recrystallisation influences CPO development*.

In order to answer this question, I have repeated certain experiments of Hobbs (1968) on natural quartz single crystals (with added water) to obtain renewed microstructural evidence for the predominant deformation mechanisms. The crystals were uniaxially deformed in a Griggs solid medium deformation apparatus in different starting orientations under conditions where dynamic recrystallisation and CPO development occur. This study focuses on in-depth observation of the microstructures that develop during the experiments by means of powerful tools such as electron backscatter diffraction (EBSD) and transmission electron microscopy (TEM) analyses.

### 1.3 STRUCTURE OF THE THESIS

This thesis presents an experimental study into the effect of dynamic recrystallisation on CPO development in deformed quartz single crystals.

As introduction and background information to the experimental data, a literature overview of CPO development in quartz is given in **Chapter 2**. This chapter focuses on the mechanisms by which CPOs may develop and the extrinsic factors that influence them (i.e. factors such as temperature, pressure, strain-symmetry, and water content). The data presented in this chapter are based on observations made on naturally deformed quartz, on experimentally deformed quartz, and on computer modelling.

**Chapter 3** provides details on the techniques and analytical models used in this experimental study.

**Chapter 4** reports the mechanical data and optical microstructures from the deformation experiments. The emphasis of this chapter lies on the effect of starting orientation, impurity content (Mn-oxide), the amount of water, as well as the strain rate on microstructure development in the sample.

**Chapter 5** is about the mechanisms that cause undulatory extinction, subgrains and deformation lamellae, all well-developed in most of the deformed samples. These microstructures were analysed with TEM, EBSD and cathodoluminescence (CL).

**Chapter 6** is about the mechanisms that cause dynamic recrystallisation. New recrystallised grains in aggregates at the sample ends possess a strong CPO. In order to assess what deformation mechanisms are responsible for these strong CPOs, detailed EBSD and TEM analyses of the recrystallised grains and of the adjacent areas with undulatory extinction were performed.

Dynamic recrystallisation was also observed in intracrystalline shear zones that crosscut samples that were deformed parallel to the *c*-axis. **Chapter 7** focuses on the formation of these shear zones and their evolution with increasing strain. The shear zones were analysed using TEM and detailed orientation and misorientation analysis based on EBSD data.

The results of this thesis are summarised and discussed in **chapter 8**.



## CHAPTER 2: CPO DEVELOPMENT IN QUARTZ: STATE OF THE ART

In many deformed rocks, the lattice orientations of crystals are not randomly distributed, but arranged in a systematic way. Such rocks have a crystallographic preferred orientation (CPO) and also referred to as “texture”). CPOs are common in dynamically recrystallised quartz rocks. Their patterns (e.g. Schmid and Casey 1986) can be broadly subdivided into five groups (Fig. 2.1). Each group has had a different deformation history which strongly depends on the temperature, the flow type, the amount of strain and the presence of fluids. Therefore CPOs can be in principle used to infer (1) whether deformation was coaxial or non-coaxial, (2) the sense of local shear, (3) the amount of strain, (4) the temperature during deformation and (5) the dominant deformation mechanisms (e.g. Law 1990). In this chapter the mechanisms by which CPOs develop, the corresponding CPO patterns, and the extrinsic factors that influence the patterns will be assessed. It will be shown that different interpretations are possible for the mechanisms by which CPO patterns develop, especially in rocks that are dynamically recrystallised. Furthermore, this chapter will provide important background for the remainder of the thesis.

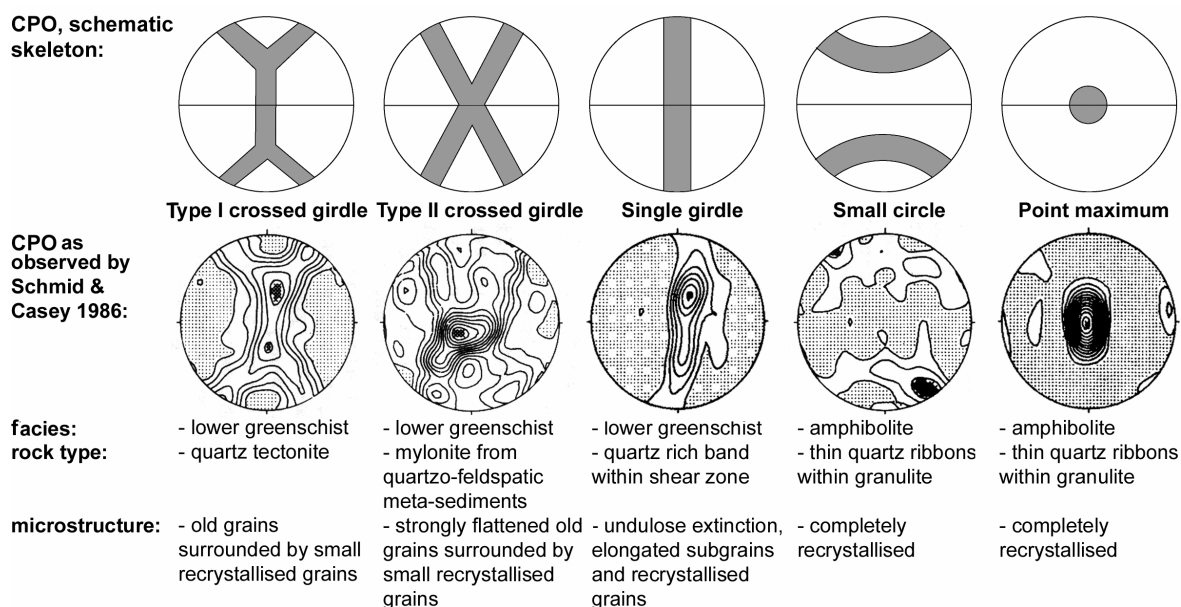


**Figure 2.1:** Most common *c*-axes preferred orientation patterns in quartz and corresponding natural examples, measured with a texture goniometer, from Schmid and Casey (1986).

### 2.1 DISLOCATION GLIDE AND CPO DEVELOPMENT

Models proposed for the development of CPOs during crystal-plastic deformation are mainly based on the activation of glide systems. A stressed crystal deforms by movement of dislocations on certain crystal planes. Dislocation movement changes the shape of the crystal. Additional interaction with neighbouring crystals, to accommodate an imposed deformation, may result in lattice rotations with respect to the stress field (Fig. 2.2). These lattice rotations lead to concentrations of grains in certain orientations, thus to preferred orientations. Tullis et al. (1973) suggested that this process is responsible for reorientation of the older quartz grains in experimentally deformed quartzites. A number of glide systems have been reported in

experimental studies on quartz on the basis of various types of observation (e.g. Morrison-Smith et al. 1976, Lister et al. 1978):

- 1) The observation of slip lines on surfaces polished prior to deformation.
- 2) TEM determination of Burgers vectors and of the planes in which dislocations propagate.
- 3) Energy arguments that the Burgers vectors should be the shortest translation vectors in the crystal lattice;  $1/3\langle 11\bar{2}0 \rangle$ , length 4.91Å;  $\langle 0001 \rangle$ , length 5.41Å;  $1/3\langle 2\bar{1}13 \rangle$ , length 7.30Å.
- 4) Observation of lattice rotations in domains with undulatory extinction or deformation bands.
- 5) The orientation of deformation lamellae, assuming them to represent slip systems.

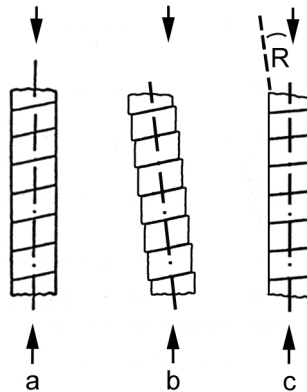


**Figure 2.2:** Reorientation of a crystal by uniaxial compression, modified after Kunze (1991). a) Starting orientation and compression direction. b) Simple shear along glide planes without a change in orientation of the crystal lattice. c) Orientation change (R) by rigid rotation of the crystal in order to fulfill the specified deformation.

The most commonly reported glide systems in quartz are the various combinations of an  $a$ -axis, a  $c$ -axis or the vector  $c+a$  as glide direction and the basal plane  $c(0001)$ , prism planes  $m\{10\bar{1}0\}$  or  $a\{11\bar{2}0\}$  and rhomb planes  $r\{10\bar{1}1\}$  or  $z\{01\bar{1}1\}$  acting as glide plane. The most frequently cited experimental studies that report these glide systems are listed in Table 2.1 with their experimental method, microstructures, observed slip systems and the identification method.

The basis for the assumption that deformation lamellae represent slip systems has been an observation of Christie et al. (1964); the orientation of optical lamellae coincided approximately with that of glide planes deduced from slip lines. However, subsequent TEM-studies revealed that submicroscopic structures identified as optical deformation lamellae had a diverse and complicated nature. The correspondence with the slip lines might thus have been the result of special circumstances and is not an invariable rule, especially since optical lamellae can also have irrational orientations (e.g. McLaren et al. 1970, McLaren and Hobbs 1972, White 1973 and 1975, Christie and Ardell 1974, Drury 1994).



Author	Material	Micro-structures	Conditions	Identified slip systems	Identification method
<b>Christie et al. 1964</b>	Quartz crystals $\perp \{r\}$ $// \langle o+ \rangle$	Slip bands on the surface Basal deformation lamellae	$T=500-750^{\circ}\text{C}$ $P_c=20$ kbar $t=23-38$ min $\varepsilon =1-10\%$	Basal $\langle a \rangle$	Optically (slip lines and def. lamellae)
<b>Baëta and Ashbee 1969a,b</b>	Synthetic quartz crystals $\perp \{r\}, \perp \{m\}$ . $// \langle a \rangle, // \langle c \rangle,$ $// \langle o+ \rangle$ and $70^{\circ}$ to $\langle c \rangle$ - $30^{\circ}$ to $\langle a \rangle$	Slip lines	$T=700-1000^{\circ}\text{C}$ $P_c=\text{atmospheric}$ $\dot{\varepsilon} =$ $10^{-3}-10^{-5} \text{ s}^{-1}$	Basal $\langle a \rangle$ Prism $\langle c \rangle$ Prism $\langle a \rangle$ $\{a\} \langle c \rangle$ Prism $\langle a+c \rangle$ Rhomb $\langle a \rangle$ Rhomb $\langle a+c \rangle$	Optically (slip lines)
<b>Ardell et al. 1974</b>	Natural and synthetic quartz crystals $\perp \{r\}$	-	Natural/synth $T=750/500^{\circ}\text{C}$ $P_c=5/2-5$ kbar $\dot{\varepsilon} =1-7 \cdot 10^{-6} \text{ s}^{-1}$	$\mathbf{b}=\langle a \rangle$ $\mathbf{b}=\langle c \rangle$	TEM (Burgers vectors)
<b>Twiss 1974</b>	Synthetic quartz crystal $\perp \{r\}$	Slip bands (dense tangles of dislocations)	$T=600-800^{\circ}\text{C}$ $P_c=1.3-7$ kbar $t=10-50$ min $\varepsilon = 3-6\%$	Prism $\langle c \rangle$ Prism $\langle a \rangle$	TEM (orientation of slip bands)
<b>Blacic 1975</b>	Natural and synthetic quartz crystals $\perp \{r\}$ $// \langle o+ \rangle$	Deformation bands Basal deformation lamellae Prism deformation lamellae	$T=300-900^{\circ}\text{C}$ $P_c=20$ kbar $\dot{\varepsilon} =8 \cdot 10^{-6} \text{ s}^{-1}$	Basal $\langle a \rangle$ Prism $\langle c \rangle$ $\{a\} \langle c \rangle$	Optically (def. lamellae and def. bands)
<b>Morrison-Smith et al. 1976</b>	Synthetic quartz crystals $\perp \{r\}$	Basal deformation bands Prism deformation bands Undulatory extinction Prism deformation lamellae Rhomb deformation lamellae Undeformed bands	$T=475-900^{\circ}\text{C}$ $P_c=3$ kbar $\dot{\varepsilon} =10^{-5} \text{ s}^{-1}$	Prism $\langle c \rangle$ Rhomb $\langle a \rangle$ Basal $\langle a \rangle$ Prism $\langle a+c \rangle$ Prism $\langle a \rangle$ $\{a\} \langle c \rangle$	TEM (Burgers vectors)

**Table 2.1:** Experimental studies that report glide systems.  $T$ , temperature;  $P_c$ , confining pressure;  $\dot{\varepsilon}$ , strain rate;  $t$ , deformation time;  $\mathbf{b}$ , Burgers vector. Synthetic crystals always have about 5 times higher intracrystalline water content than natural quartz, which occurs in tiny clusters that are evenly distributed through the synthetic crystals.

## 2.2 TEMPERATURE AND CPO DEVELOPMENT

The type of glide system that will be activated in a crystal depends on the orientation (Schmid factor) with respect to the stress field in a grain and on the critical resolved shear stress (CRSS) for that slip system. The CRSS must be exceeded by the resolved shear stress on a given slip system before dislocations move. The magnitude of the CRSS depends on the temperature (Hobbs 1985). In general the CRSS for slip decreases with temperature, but the rate of decrease is different for different slip systems (Fig. 2.3). Thus basal $\langle a \rangle$  slip is easier than prism $\langle a \rangle$  slip at low temperatures, whereas the situation is reversed at high temperatures (Blacic 1975, Wilson 1975). Models have indicated that such a switch in relative importance of glide systems can exert a remarkable effect on CPO development (Fig. 2.4).

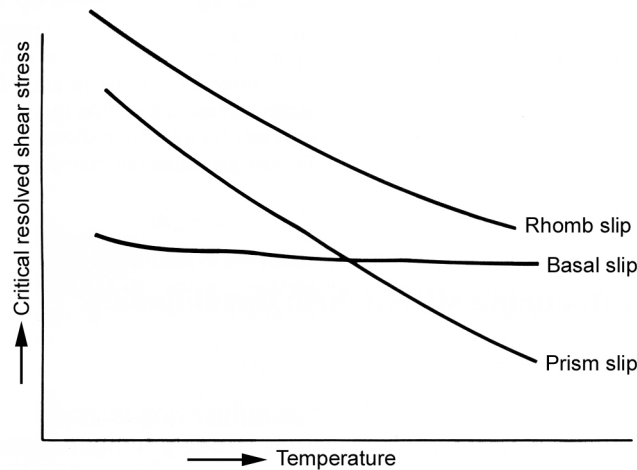


**Figure 2.3:** Schematic plot of critical resolved shear stress against temperature for various slip systems in quartz based on observations of Blacic (1975) and of Hobbs et al. (1972).

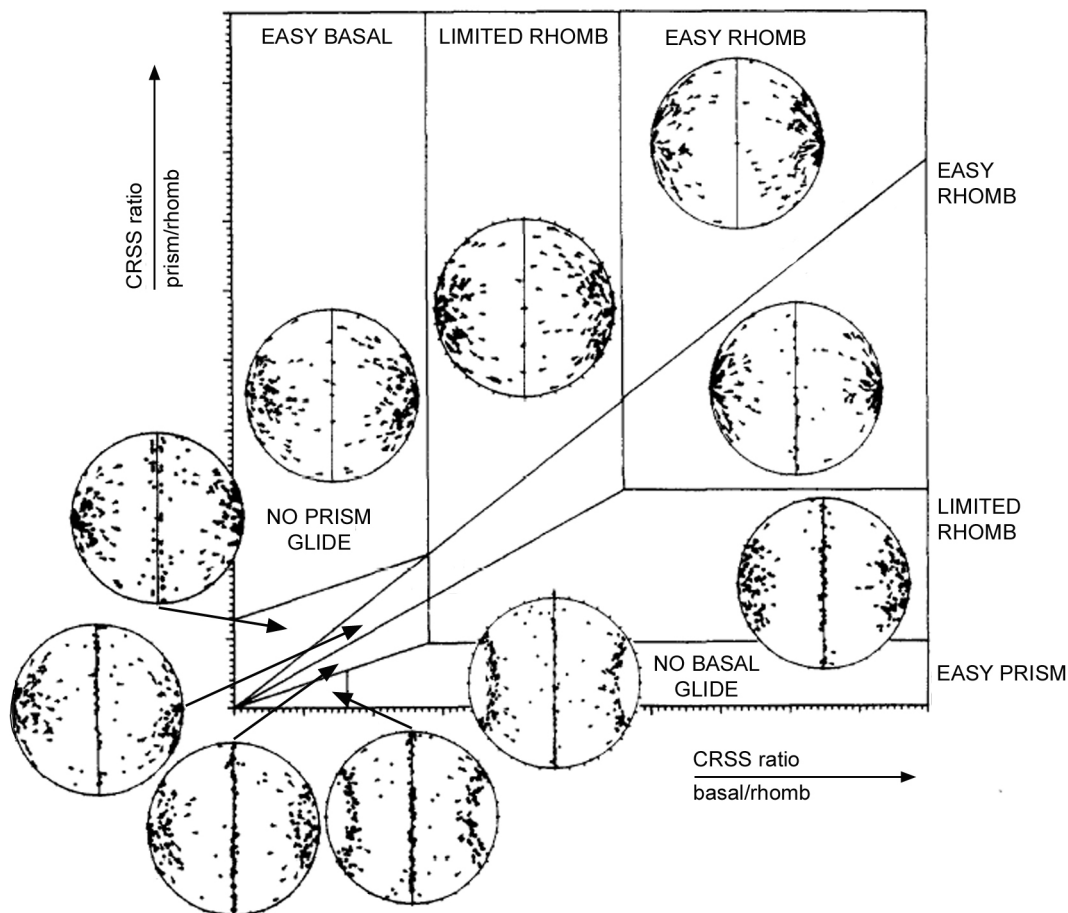


**Figure 2.4:** C-axis distributions in a transition diagram for three sets of slip systems; basal<a>, prism<a> and rhomb<a+c> in axial symmetric shortening, from Lister and Paterson (1979). Note that  $\sigma_1$  is horizontal.

Other factors, counteracting temperature, with a smaller influence on the CRSS are strain rate and differential stress. Very important is also the impurity content, especially of water (Passchier and Trouw 1998). Data on the absolute values of the CRSS in quartz are scarce (main publication by Baëta and Ashbee 1969b) and there are many uncertainties in using

these data to predict the relative strengths of the slip systems under geological conditions, because the experiments were done on synthetic quartz instead of natural quartz, under atmospheric pressure, and at extremely high strain rates ( $>10^{-5} \text{ s}^{-1}$ ). Therefore, in models for CPO development in quartz, relative CRSS values on selected slip systems were chosen to produce similar CPO patterns as found in nature and experiment (Lister et al. 1978, Lister and Hobbs 1980, Takeshita and Wenk 1988, Kunze 1991, Takeshita et al. 1999).

### 2.3 FLOW TYPE AND CPO DEVELOPMENT

Figure 2.5 illustrates the effect of the type of strain on the geometry of the *c*-axis patterns of coaxially deformed quartz at low to intermediate grade metamorphic conditions. The CPOs in this figure were predicted by a theoretical model for dislocation glide that is based on the Taylor-Bishop-Hill analysis (Lister et al. 1978, Lister and Hobbs 1980). These theoretical CPOs are supported by both experimental studies (Tullis et al. 1973, Tullis 1977) and analysis of naturally deformed quartzites (Price 1985, Schmid and Casey 1986). Small circle girdle distributions are expected for uniaxial extension or compression. In plane strain, small circle girdles are connected by a central girdle to produce type I crossed girdles. Type II crossed girdles develop in the constrictive field. Point maxima around the *y*-axis do not form in any simulation of dislocation glide alone, but are reproduced in models incorporating recrystallisation at higher temperatures (Jessell and Lister 1990). Increase in temperature also seems to cause an increase in the opening angle of small circle girdles (Schmid and Casey 1986). The predicted relationship between fabric pattern and the principal extension directions may be used to test whether an individual lineation is indicating a real or an apparent extension (Law 1990).

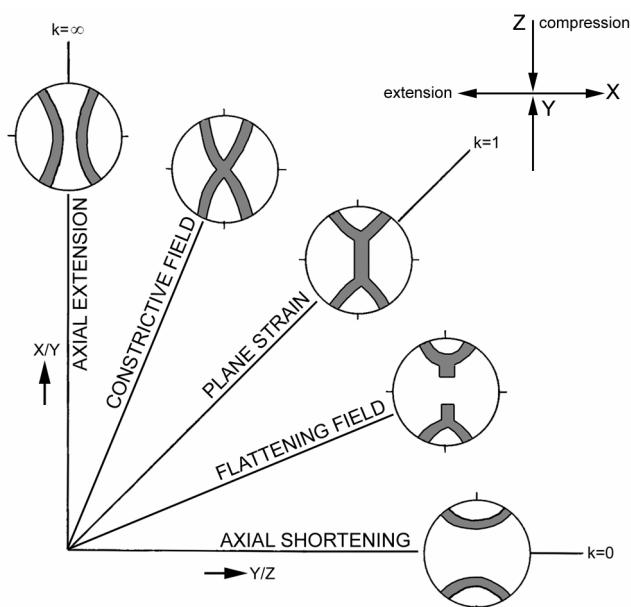


**Figure 2.5:** Flinn diagram showing the theoretical relationships (for coaxial deformation) between strain symmetry and quartz *c*-axis fabrics. After Lister and Hobbs (1980) and Schmid and Casey (1986).

## 2.4 STRAIN AND CPO DEVELOPMENT

Increasing strain at constant flow parameters and temperature will theoretically lead to strengthening of the CPO-pattern, but will not change its general type (Lister and Hobbs 1980). However, in many naturally deformed rocks, a spatial transition of symmetrical crossed girdles to asymmetrical single girdles occurs, related to an increasingly non-coaxial strain path (Fig. 2.6). Schmid and Casey (1986) suggested that this transition marks the bulk finite strain at which grains in unfavourable orientations for continued intracrystalline slip are partially substituted through grain boundary migration of more favourably oriented grains, and partially reoriented by selective recrystallisation. The transition from crossed girdle to single girdle *c*-axis preferred orientation is not predicted by the full constraints fabric simulation model of Lister and co-workers (e.g. Lister and Hobbs 1980) using a given set of active slip systems. Such simulations actually resulted in *c*-axis maxima tilted against the sense of shear, while the natural observations show the opposite. Fabric transitions similar to those in natural rocks are, however, predicted for increasing rotational strain in simple shear by the fabric transition model of Etchecopar and Vasseur (1987), Jessell (1988) and Jessell and Lister (1990) involving combined crystallographic slip and dynamic recrystallisation.

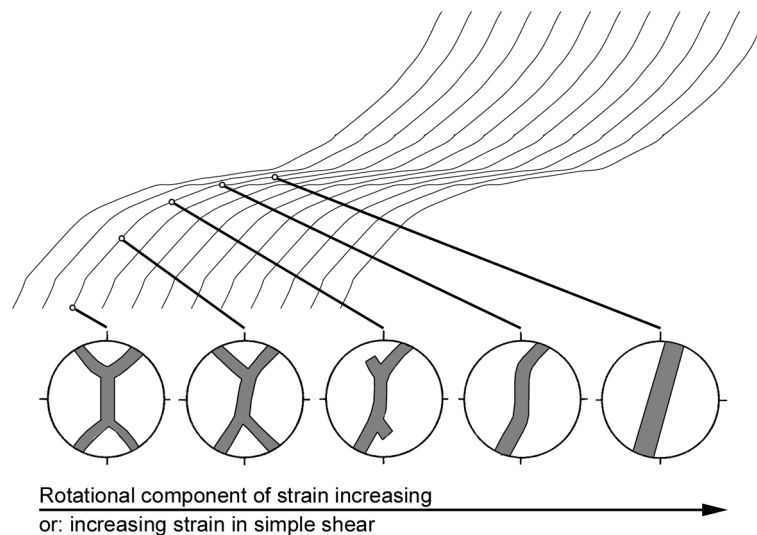


**Figure 2.6:** Interpretation of quartz *c*-axis fabric transitions produced in plane strain ( $k=1$ ) deformation with a dextral sense of movement. In all stereograms foliation is perpendicular to the projections. After Schmid and Casey (1986).

A transition in CPO-pattern with increasing strain is also observed in experimentally deformed rocks (Fig. 2.7). This transition, however, is slightly different than in naturally deformed rocks. The lowest strain sample of the experiments carried out by Dell'Angelo and Tullis (1989) exhibits a type I crossed girdle (Fig. 2.7a), strongly flattened grains with deformation lamellae and only minor recrystallisation. The pole figure has orthorhombic symmetry with respect to the foliation. At slightly higher strain, the CPO shows a similar rhombic symmetry (Fig. 2.7b), but the maxima are inclined opposite to the sense of shear, instead of symmetric to the foliation. At highest strain (Fig. 2.7c and d), a broad single maximum developed that is slightly inclined with the sense of shear. Such maxima are assumed to develop because the basal plane progressively rotates into (and slightly beyond) the shear plane and the slip direction into the shear direction (Burg and Laurent 1978, Wenk and Christie 1991). The sample exhibits elongated original grains with subgrains in their

interiors and recrystallised grains along their grain boundaries. Grains that are unfavourably oriented for slip remain as undeformed augen.

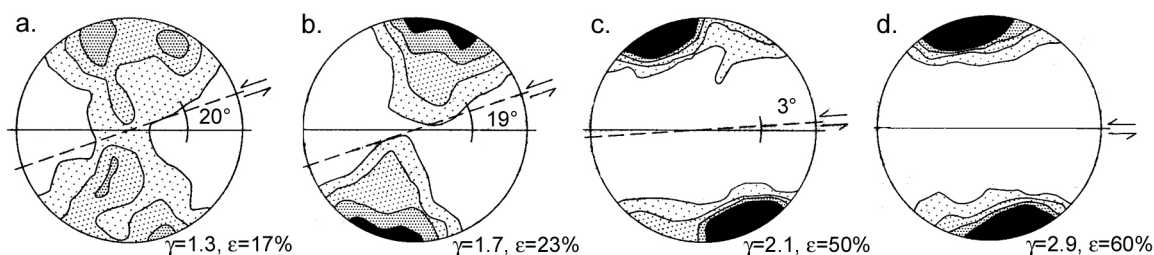


**Figure 2.7:** C-axis pole figures for experimentally deformed quartzite samples in combined shear and axial compression (Dell'Angelo and Tullis 1989) illustrate the effect of increasing strain. All samples deformed at 800°C,  $\sim 10^{-6} \text{ s}^{-1}$ , and 1500 MPa. The foliation is horizontal, the shear zone boundary is marked by a dashed line when not coincident with the foliation. C-axis preferred orientation measured with the universal stage in non-recrystallised old grains.

## 2.5 DYNAMIC RECRYSTALLISATION AND CPO DEVELOPMENT

Most of the best developed CPOs are measured in dynamically recrystallised quartzites. Dynamic recrystallisation involves the formation and/or migration of grain boundaries during deformation (Vernon 1981, Urai et al. 1986). Up to the middle of last century, geologists thought of dynamic recrystallisation as a cataclastic process (the origin of the name mylonite) and not being related to intracrystalline crystal plastic deformation. Subgrains, recrystallised grains and even CPOs were interpreted as due to water-assisted brittle processes (e.g. Lapworth 1885, Sander 1930). Other scientists started to see recrystallisation in rocks as a process involving long-range (fluid-assisted) diffusive transfer (e.g. Griggs 1940), a process referred to as 'solution transfer' by Durney (1972).

During the 1950's, the concepts of recrystallisation in rocks were profoundly influenced by existing metallurgical work on annealing recrystallisation (Fairbairn 1949, Turner and Weiss 1963). Later, Poirier and Nicolas (1975) explained the development of new grains by progressive subgrain rotation. Nowadays, dynamic recrystallisation is basically assumed to comprise two processes: progressive subgrain rotation (e.g. Poirier and Nicolas 1975, White 1977, Guillopé and Poirier 1979) and grain boundary migration (e.g. Poirier and Guillopé 1979, Means 1983, Poirier 1985, Drury and Humphreys 1986). Typical microstructures for these processes are shown in Figure 2.8a and b (subgrain rotation) and Figure 2.8c and d (grain boundary migration). A third type of dynamic recrystallisation is grain boundary bulging recrystallisation (Hirth and Tullis 1992, Stipp et al. 2002), which occurs mainly at low temperatures and affects only negligible volume proportions. The CPO that develops in rocks undergoing this deformation mechanism are dominated by the contribution of the old grains.

There has been some discussion as to whether the processes controlling the CPOs in dynamically recrystallised grain aggregates are the same as those in non-recrystallised rocks. Price (1985) compared fabrics from samples without significant recrystallisation (Tullis et al. 1973) with fabrics in completely recrystallised samples (Green et al. 1970) and observed that they are similar. White (1976) and Lister and Price (1978) have argued that in such circumstances the recrystallisation processes are not dramatically important and that dislocation glide remains the principal reorientation mechanism. Other authors have suggested that strain-induced grain boundary migration allows some crystal orientations to grow at the

expense of others, resulting in CPOs different than those produced by slip only (e.g. Schmid and Casey 1986).

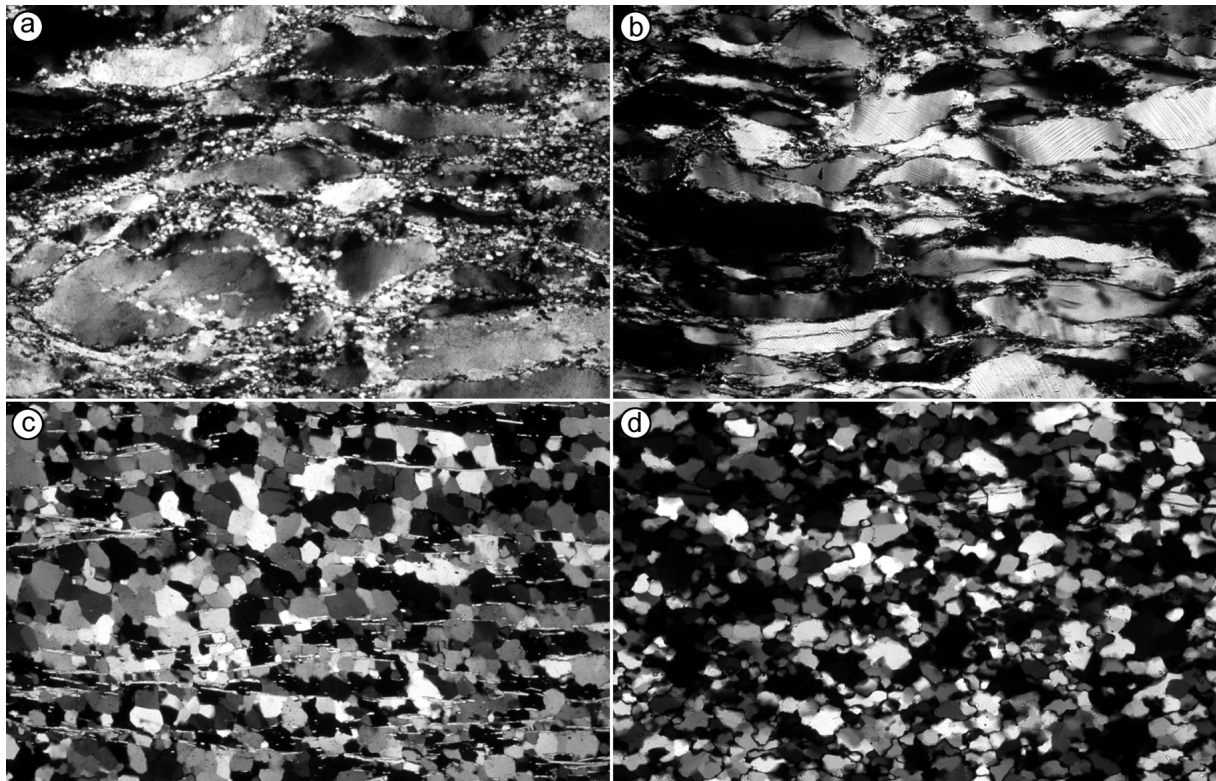


**Figure 2.8:** Optical micrographs of dynamically recrystallised microstructures. a) Subgrain rotation recrystallisation in naturally deformed quartzite (Ruby Gap Duplex, central Australia). Original detrital quartz grains are flattened and stretched and show severe undulatory extinction due to the internal development of subgrains by lattice rotation. The large grains are surrounded by a mantle of fine recrystallised quartz grains ~50 microns in size. Image width 3.2mm. b) Subgrain rotation recrystallisation in experimentally deformed Heavytree quartzite ( $\epsilon=42\%$ ;  $T=800^{\circ}\text{C}$ ; strain rate= $10^{-6} \text{ s}^{-1}$  and  $P_c=1200 \text{ MPa}$ ). Original grains have been fairly homogeneously flattened, and exhibit smooth and continuous undulatory extinction; sub-basal deformation lamellae are quite common. Recrystallised grains form at original grain boundaries as a result of progressive subgrain misorientation. Magnification: x10. c) Naturally deformed quartzite (Ruby Gap Duplex, central Australia), entirely recrystallised by rapid grain boundary migration. Mica foliae define strong macroscopic fabric (the foliation-lineation measured at the outcrop). Strain-free recrystallised quartz grains show little elongation or shape preferred orientation. Image width 3.2mm. d) Experimentally deformed Blackhills quartzite with strain-free recrystallised grains ( $\epsilon=50\%$ ;  $T=1200^{\circ}\text{C}$ ; strain rate= $10^{-6} \text{ s}^{-1}$  and  $P_c=1200 \text{ MPa}$ ), entirely recrystallised by rapid grain boundary migration. Magnification: x10. Source of pictures: <http://talc.geo.umn.edu/orgs/struct/microstructure>, by Jan Tullis, Christian Teysier, and Holger Stünitz, *sample descriptions are exactly copied from the source.*

### 2.5.1 Models on the effect of dynamic recrystallisation on CPO development

Jessell (1988a and b) and Jessell and Lister (1990) have modified the Taylor-Bishop-Hill model for dislocation glide by incorporating grain boundary migration and the nucleation of new grains (as a substitute for subgrain rotation). Their models indicate that fabrics evolve continuously with deformation and produce crossed girdles, single girdles and point maxima for a single deformation geometry and for constant deformation conditions. Their results suggest that the coupling of dynamic recrystallisation with dislocation slip can actually produce a larger variation in CPOs than is predicted by using a model that only considers glide as a cause for lattice rotations (Lister et al.1978). Point maxima develop even though a multiple slip model has been assumed (Fig. 2.9).

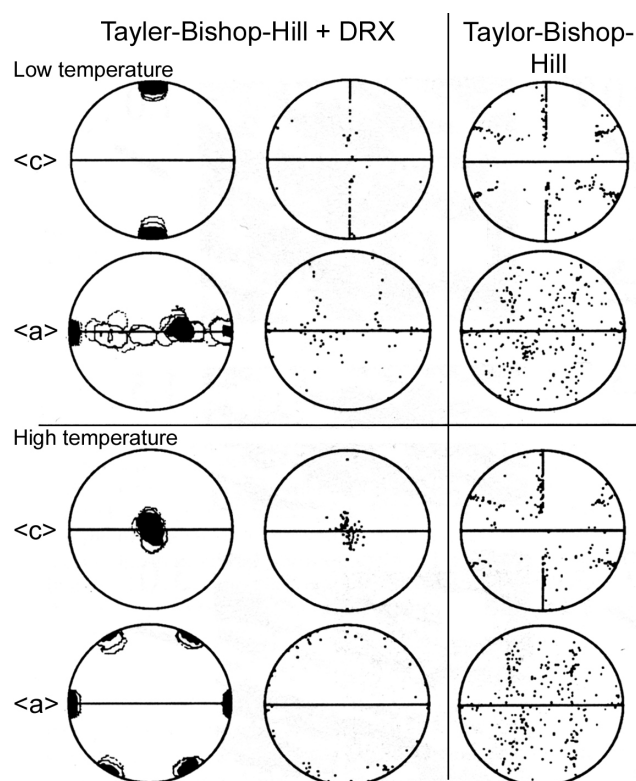


**Figure 2.9:** Crystallographic preferred orientations predicted by the model of Jessell and Lister (1990) for a shear strain of 5 to illustrate the difference in fabrics if dynamic recrystallisation is invoked in the model. The left column is contoured according to axis density and grain size; the middle and right column simply show the axes. Shear plane is horizontal.

### 2.5.2 Experimental data on the effect of dynamic recrystallisation on CPO development

The orientations Jessell and Lister (1990) assumed to be favoured by grain boundary migration were just based on observations in experimentally deformed ice, camphor and octochloropropane, because such observations were not yet systematically made in quartz. Therefore Gleason et al. (1993) assessed the effect of dynamic recrystallisation on the CPOs in experimentally deformed quartz aggregates. This study, performed on samples deformed in three different dislocation creep regimes (Hirth and Tullis 1992), indicated that at relatively low temperatures and fast strain rates grain boundary migration recrystallisation favours the growth of grains that are poorly oriented for slip on the basal and prism planes, resulting in a *c*-axis preferred orientation parallel to the compression direction. At intermediate temperatures and slower strain rates (microstructure in Fig. 2.8b), progressive subgrain rotation produces recrystallised grains which inherit the crystallographic orientation of their deformed host grains. At high temperatures and even slower strain rates (microstructure in Fig. 2.8d), subgrain rotation is superseded by rapid grain boundary migration, which does not favour grains of any particular orientation; thus the CPO is again similar to that of the non-recrystallised grains. It must, however, be noted that the dynamic recrystallisation-CPO relationships observed by Gleason et al. (1993) should be treated with care, because they did not strictly depend on the temperature and strain rate alone, but also on the starting material and water content. Starting material and water content were alternated in the experiments. Previously, Hobbs (1968) investigated the effect of dynamic recrystallisation on CPO development in experimentally deformed quartz single crystals. Single crystals are an excellent starting material for a study on CPO development, because the effect of both the original crystal orientation of the sample and of the compression direction can be controlled. Hobbs (1968) observed that at conditions similar to the intermediate temperature regime of

Gleason et al. (1993), new grains developed with their  $c$ -axes at  $30\text{--}50^\circ$  to that of the adjacent host (as also observed by Wheeler et al. 2004). Hobbs (1968) proposed that there might be a control exerted by the stress in that new  $c$ -axes also tend to lie at  $50^\circ$  to  $\sigma_1$ , irrespective of their starting orientation and of the amount of strain (Fig. 2.10). The recrystallised grains were sub-euhedral and strain-free.

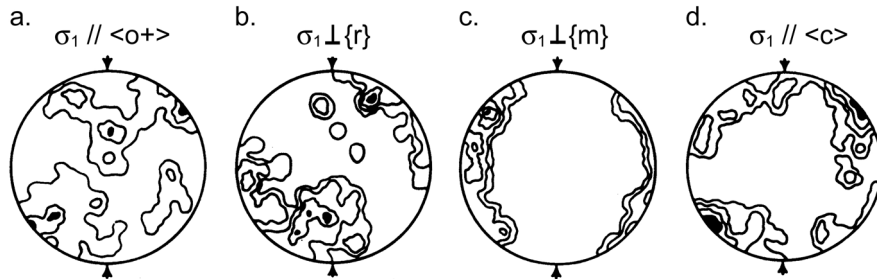


**Figure 2.10:**  $c$ -axes of newly recrystallised grains in experimentally deformed natural quartz single crystals (Hobbs 1968). The measurements were collected throughout the sample and not only in the central homogeneously strained area. The arrows represent the direction of shortening of the specimen. a) 200  $c$ -axis orientations, b) 96  $c$ -axis orientations, c) 112  $c$ -axis orientations and d) 155  $c$ -axis orientations.

### 2.5.3 CPOs in dynamically recrystallised rocks from nature

Stipp et al. (2002) studied natural quartz deformation fabrics over a range of metamorphic temperatures from approximately  $250^\circ\text{C}$  to  $700^\circ\text{C}$  across the eastern Tonale fault zone in the Italian Alps. In the fault zone, changes in the dominant type of dynamic recrystallisation correspond to the progressively increasing temperatures in a similar way as in the experimentally deformed samples of Hirth and Tullis (1992) and Gleason et al. (1993). The CPO in the low temperature regime is dominated by the contribution of the porphyroclasts, which form a  $c$ -axis maximum approximately perpendicular to the foliation. Significant amounts of recrystallised grains are first observed in the intermediate temperature regime. The  $c$ -axis pole figures of the recrystallised grains in the intermediate temperature regime (Fig. 2.11) exhibit asymmetric crossed girdles or single girdles. The differences between the low temperature fabrics (within porphyroclasts) and the intermediate temperature fabrics (within recrystallised domains) are explained by Stipp et al. (2002) as follows: (1) progressive subgrain rotation may have been effective in generating new orientations in the intermediate temperature regime, and/or (2) porphyroclasts, with  $c$ -axis orientations unsuitable for slip on the basal plane preferentially recrystallised, thereby enriching porphyroclast orientations favourable for basal slip. Within the pole figures of Figure 2.11, however,  $c$ -axis orientations favourable for slip on the basal plane are only observed at the lowest intermediate temperature ( $\sim 400^\circ\text{C}$ ) together with  $c$ -axis orientations favourable for slip on the prism plane. With increasing temperatures, grains with  $c$ -axis orientations favourable for slip on the basal plane are progressively removed. At high temperatures, where old grains are no more discernable, a single maximum near the intermediate principal strain axis is observed (Fig. 2.11). This maximum is interpreted to be formed by prism<a> slip. This slip system is assumed to be more easily activated than basal slip at higher temperatures (Schmid et al. 1981, Mainprice et al. 1986). The microstructure is completely recrystallised at these temperatures.

Stöckhert and Duyster (1999) investigated CPO development in a quartz sample with a bimodal grain size distribution. The sample consisted of small recrystallised matrix grains that deformed by dislocation creep and larger blast grains that grew during subsequent annealing. The microfabrics in the sample are interpreted as a frozen transient state developed during texture induced grain boundary migration. Only grains with misorientation larger than  $30^\circ$  had mobile grain boundaries. Consequently, the crystallographic orientations of these blast



grains (Fig. 2.12b) differ from the overall CPO (Fig. 2.12a). If the process of grain boundary migration would have gone to completion, the resulting CPO (Fig. 2.12c) would be different from that present before annealing.

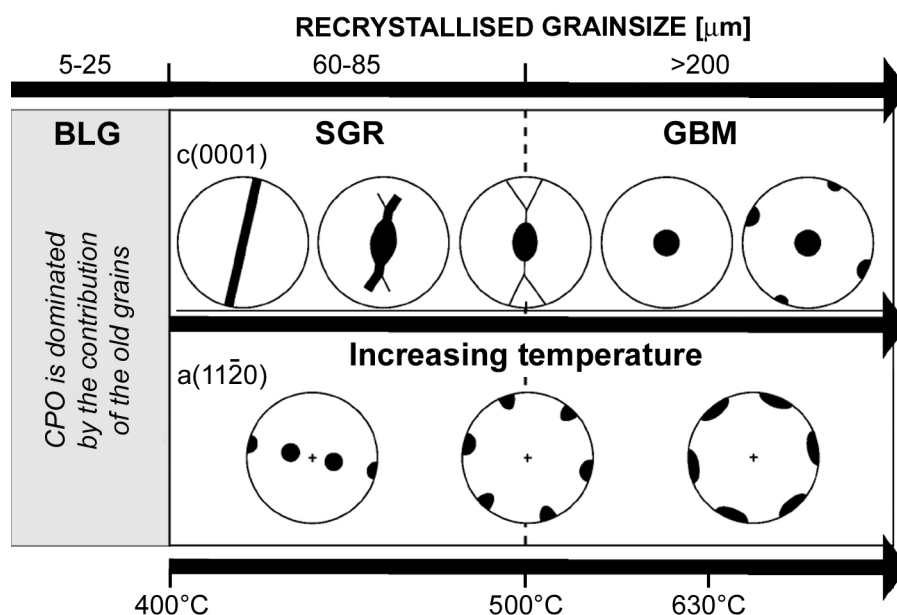


**Figure 2.11:** Schematic diagram modified after Stipp et al. (2002) by Mancktelow and Pennacchioni (2004) showing the correlation between recrystallised grain size, CPO and temperature for the new grains in dynamically recrystallised Tonale quartz mylonites (dextral shear). BLG, dominant bulging (low temperature regime); SGR, dominant subgrain rotation (intermediate temperature regime); GBM, dominant grain boundary migration (high temperature regime).

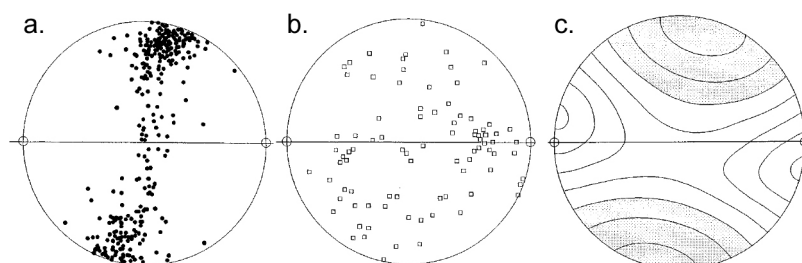


**Figure 2.12:** *c*-axis pole figures of Stöckhert and Duyster (1999) measured by universal stage from quartz grains in a quartz layer from the Sesia zone, Western Alps. a) Matrix grains, b) blast grains that grew by post deformation grain boundary migration and c) hypothetically complementary texture if grain boundary migration would have gone to completion at the cost of the matrix grains. Density in grey area is less than average.

Shelley (1971) studied flattened quartz phenocrysts from deformed quartz porphyry. Each crystal had been replaced by a mosaic of new grains. The *c*-axes of these new grains formed type II crossed-girdles with an opening angle of  $\sim 40^\circ$  (Fig. 2.13b). The individual grains of the quartz mosaics were optically strain-free (similar to those produced by Hobbs 1968) even under stress. The CPO patterns in all the phenocrysts were the same, although they were deformed to different strains. A stable orientation was thus produced during recrystallisation. Shelley (1971) suggested that such a stable orientation might be explained by the development of new grains as entirely new nuclei, a process also described by den Brok and Spiers (1991) in experimentally deformed quartzites.

During dynamic recrystallisation by subgrain rotation, new grains should exhibit the same rotation axis as their precursors in the parent grains. If single slip is assumed, the subgrain boundaries should be tilt boundaries and consist of edge dislocations (Nicolas and Poirier 1976). If this is the case, the rotation axis will be characteristic for the activated slip system (Neumann 2000). However, detailed EBSD analyses have shown that the misorientation axes between new grains and parent grains do not always coincide with predictions for common slip systems and are different from the misorientation axes within the parent grains. Thus, either crystallographic orientations easily “forget” the influence of the earlier increments of the deformation history (Lister and Price 1978), or processes different from subgrain rotation and grain boundary migration must be invoked (Leiss and Barber 1999, Bestmann and Prior 2003, van Daalen et al. 1999) : (1) nucleation, (2) diffusion accommodated grain boundary sliding or (3) microcracking and passive rigid rotation of grain fragments.

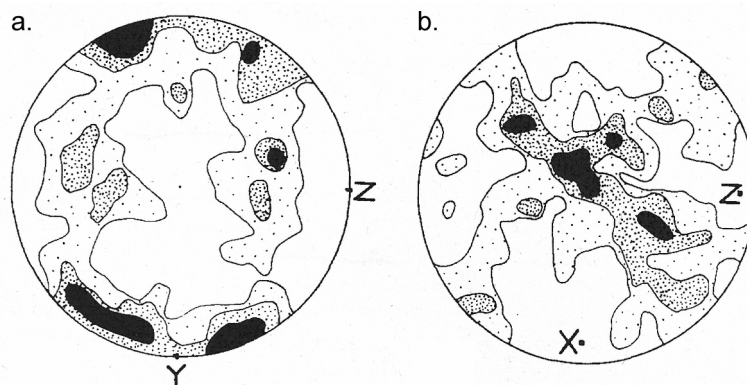


**Figure 2.13:** C-axes pole figures (equal area, 400 measurements) of newly recrystallised grains within flattened quartz porphyry (Shelley 1971). Z is the compression direction.

## 2.6 INFLUENCE OF WATER ON CPO DEVELOPMENT

It is well established that water (as any fluid) has a strong influence on the deformation behaviour of minerals. ‘Wet’ quartz is easier to deform than ‘dry’ quartz which only exhibits deformation lamellae and is extremely strong when deformed experimentally (den Brok 1992). Consequently, water must be present if experimental deformation should lead to large strain and produce a strong CPO.

Substantial grain growth was observed during experimental deformation of wet fine-grained natural quartz aggregates (Green et al. 1970, Masuda and Fujimura 1981, Karato and Masuda 1989, Schmocker et al. 2003). Two different fabric types are obtained in such aggregates (Green et al. 1970): (1) at low temperatures, high strain rates and high differential stresses, grains were strongly flattened and a maximum of *c*-axes formed parallel to the compression direction. (2) At high temperatures, low strain rates and low differential stresses, grains were optically strain-free and the *c*-axes tended to lie at 40-50° to  $\sigma_1$ . It was suggested that the CPO in the high temperature, low stress regime was caused by strain-induced recrystallisation, and in the low temperature, high stress regime by stress controlled grain growth (Green et al. 1970).

In nature, water can be responsible for localised deformation in the continental crust. Takeshita and Hara (1998) investigated the microstructures and *c*-axis fabrics of a recrystallised quartz vein that was deformed under fluid-rich greenschist conditions and suggested a pronounced effect of water. Dissolution microstructures are ubiquitous in the

sample. Grains with large host-grain misorientations (up to  $90^\circ$ ) were ascribed to be formed by solution precipitation creep. Rotation recrystallisation was only responsible for the creation of relatively small misorientation angles. Mancktelow and Penacchioni (2004) investigated CPO development in quartz for water deficient conditions. They argue that the presence or absence of abundant water-rich fluid on the grain boundaries (1) is critical for grain boundary mobility and therefore the transition from slow to fast grain boundary migration, but (2) has little influence on the mechanisms of intracrystalline dislocation glide. For water-deficient conditions, the restriction of grain boundary mobility limits the rate of recovery of strain-hardened microstructures.

## 2.7 SUMMARY AND CONCLUSION

Most of the crystallographic preferred orientations in quartz can be very well imitated by models based on dislocation glide. Experimentalists reported CPOs in old grains of deformed quartzites that did not exhibit significant recrystallisation. These CPOs were interpreted as developed by mechanical reorientations as a result of intracrystalline slip. CPOs observed in nature, however, are mostly measured in dynamically recrystallised rocks. Dynamic recrystallisation occurs by (1) progressive subgrain rotation and (2) grain boundary migration, and is considered to be a process accompanying crystal-plastic deformation.

*Subgrain rotation microstructures* are assumed to exhibit CPOs that are similar to CPOs in old host grains. However, recent EBSD measurements have shown that the rotation axes of recrystallised grains neither coincide with rotation axes in the old host grains nor with specified crystallographic orientations. This could mean that the deformation mechanisms were maybe not entirely crystal plastic. Diffusion accommodated grain boundary sliding was invoked in rocks that did not significantly change CPO in recrystallised domains. Microcracking and rotation of fracture fragments in recrystallised domains were assumed to be a dominant mechanisms in rocks, deformed at lower greenschist facies that displayed strong CPOs.

*Grain boundary migration* is usually leading to the development of CPO patterns different from CPOs that are measured in rocks that were deformed solely by dislocation glide. At low temperatures, experimental studies indicated that grains with  $c$ -axes parallel to  $\sigma_1$  grew; i.e. grains poorly oriented for glide on basal and prism systems. It was suggest that these grains grew by stress-induced grain boundary migration. At intermediate to high temperatures (greenschist facies) it was observed in experimentally and naturally deformed rocks that new grains with  $c$ -axes at  $40\text{-}50^\circ$  to the compression direction (i.e. grains that are well oriented for basal glide) and a large (much larger than  $15^\circ$ ) misorientation with the adjacent host  $c$ -axes grew. At even higher temperatures (amphibolite facies), new grains with  $c$ -axes at  $90^\circ$  to  $\sigma_1$  were observed to grow; i.e grains well oriented for prism glide. In polycrystals, such CPOs are interpreted to develop by preferred growth of grains, well oriented for intracrystalline slip, at the cost of less favourable oriented grains. It has, however, also been suggested that new grains with these orientations may develop as entirely new nuclei. Generally it has been observed that grains only grew if there was sufficient water present on the grain boundaries. Under fluid-rich conditions grains may grow by solution-precipitation creep.

We conclude that although various studies demonstrate that CPOs can develop by crystal-plastic mechanisms, other processes like rotation of fracture fragments, nucleation and solution precipitation creep can also initiate CPO development. In this thesis, we will try to gain further experimental and microstructural evidence on the processes leading to CPO development.



## CHAPTER 3

### TECHNIQUES AND METHODS USED IN THIS STUDY

#### 3.1 GRIGGS SOLID MEDIUM DEFORMATION APPARATUS

All deformation experiments described in this thesis were performed in a Griggs solid medium apparatus (Griggs rig), installed at the ETH Zürich. The apparatus was originally developed by Griggs (1967) and later modified by Griggs and Blacic (Green et al. 1970). The Griggs rig in Zürich is a Tullis modified version (Tullis and Tullis 1986) and is capable of reaching confining pressures of up to 1300 MPa and temperatures of up to 1000°C. Quartz can only be deformed in a ductile manner in a solid medium apparatus, because only these apparatuses are capable of reaching high enough pressures. A brief description of the Griggs rig is given in this section. For details see den Brok (1992).

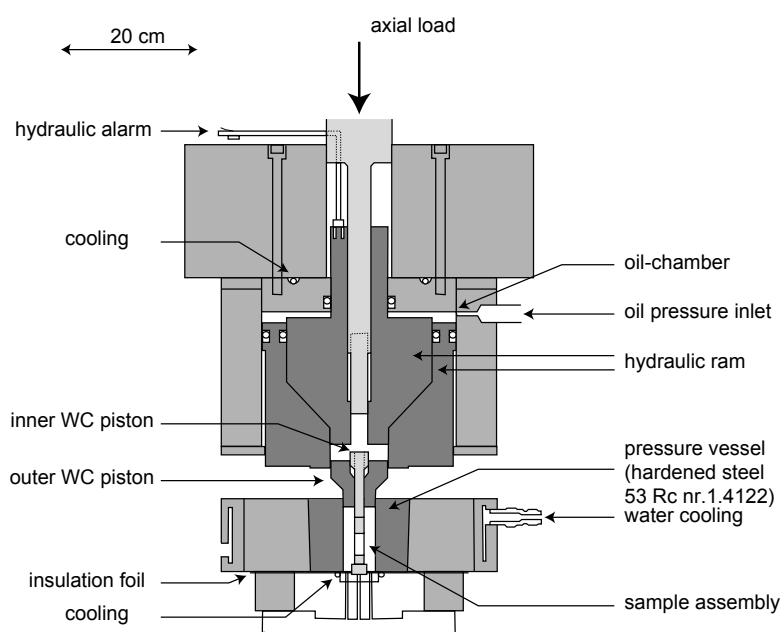


**Figure 3.1:** Sketched section showing the hydraulic ram, pressure vessel and sample loading system of the Griggs deformation apparatus.

The Griggs solid medium deformation apparatus is basically a piston-cylinder apparatus that uses NaCl as a solid medium. The sample assembly is embedded in NaCl. The sample assembly and NaCl are placed in a pressure vessel (Fig. 3.1). Pressure is applied to the NaCl-solid medium by an axial force (hydraulic ram). This force is distributed on the outer tungsten carbide (WC) piston (or pressure piston). The pressure is measured in the oil chamber using a pressure transducer. The confining pressure within the sample assembly is calculated from this value. A lead disk between the outer WC piston and the NaCl-solid confining medium ensures uniform transmission of the pressure (Fig. 3.2). The lead is prevented from extruding past the outer WC piston by two stainless steel sealing rings (Fig. 3.2).

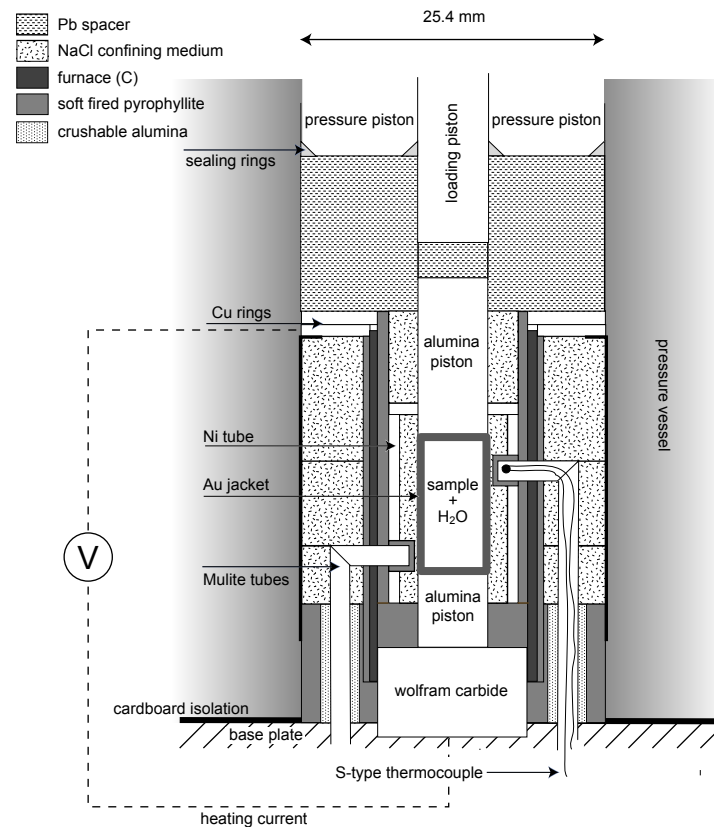


**Figure 3.2:** Sketch of the sample assembly.

The sample assembly (Fig. 3.2) is internally heated with a cylindrical graphite resistance furnace which surrounds the sample. The furnace is isolated from the salt on each side by sleeves of soft-fired pyrophyllite. The temperature within the sample assembly is measured and controlled by an upper and a lower Pt-Pt10%Rh thermocouple that are embedded in mulite tubes. These mulite tubes are surrounded by crushable alumina at the bottom of the sample assembly to prevent them from being pushed out during pressurising. A nickel tube between the furnace and the sample minimises the temperature gradients. The temperature differences between the two thermocouples were usually less than 10°C.

Deformation of the sample is achieved by axially loading the inner WC piston (Fig. 3.1). This piston moves through a hole in the outer WC piston. In the sample assembly, the temperature is 800°C. This is too high for the tungsten carbide to support the stresses needed to deform quartz. Therefore the axial load is passed from the inner WC piston to alumina pistons at the top and the bottom of the sample. A lead spacer is placed between the upper alumina piston and the inner WC piston so that the sample cannot be loaded during the initial pressurisation and heating stage. The lead is prevented from extruding past the inner WC piston by a stainless steel sealing ring. The axial load is measured outside the pressure vessel with an external load cell. The displacement is measured with a linear variable differential transformer (LVDT) that is mounted on a cross arm on the axial load cell and measures the displacement with respect to the steel base plate.

### 3.2 STARTING MATERIAL AND SAMPLE PREPARATION FOR THE DEFORMATION TESTS

Samples were cored from natural quartz single crystals from Arizona (Fig.3.3). The crystals were optically clear and had very well developed crystal faces. The intracrystalline water content of the crystals was very low;  $\sim 0.002$  wt% (measured by Fourier transform infrared spectroscopy (FTIR) and calculated using the calibration of Paterson, 1982). There was no OH-zonation and electron backscatter diffraction (EBSD) measurements have shown that the crystals were free of Dauphiné twins.

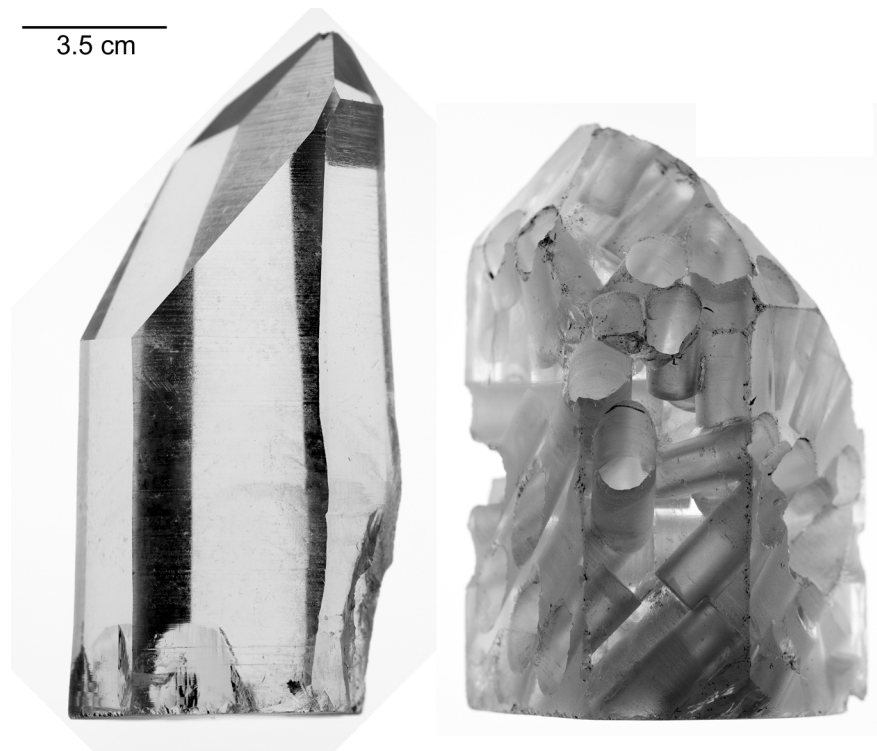


**Figure 3.3:** Starting crystals. The left crystal illustrates that the material was optically clear. The right crystal shows holes from the coring of the samples.

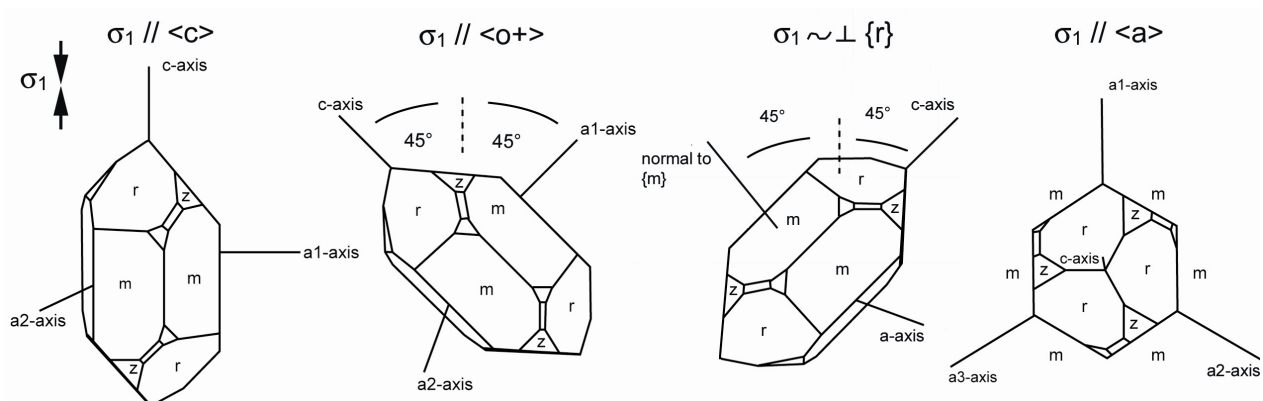


**Figure 3.4:** Starting orientations.

The samples were cored in four different orientations (Fig. 3.4): with the cylinder axis ( $\sigma_1$  direction) (1) parallel to  $\langle c \rangle$ , (2) parallel to  $\langle a \rangle$ , (3) parallel to  $\langle o+ \rangle$  ( $45^\circ$  to  $\langle c \rangle$  and  $45^\circ$  to  $\langle a \rangle$ ) and (4) roughly perpendicular to  $\{r\}$  (exactly  $45^\circ$  to  $\langle c \rangle$  and  $45^\circ$  to  $\{m\}$ ). The faces of

the crystals were used to position the crystal in a vice in one of these four orientations, before coring. The cylindrical samples measured 11.5-12.0 mm in length and 5.8 mm in diameter. The ends were manually ground flat and parallel to within 30  $\mu\text{m}$ . All samples were weld-sealed into gold jackets (400  $\mu\text{m}$  wall thickness) either without water, together with 1 or 3 vol% of distilled water or together with 1 vol% of distilled water and 20 mg  $\text{Mn}_2\text{O}_3$ -powder.  $\text{Mn}_2\text{O}_3$ -powder has been added intentionally to trigger the development of new grain, as observed by Ord and Hobbs (1986) and Fitz Gerald et al. (1991). The jacketing procedure is described by den Brok (1992).

### 3.3 EXPERIMENTAL PROCEDURE

At the beginning of each experiment, the pressure in the oil chamber was raised to  $\sim 5$  MPa (corresponding to  $\sim 100$  MPa within the sample assembly) over 0.4-1.5 hours (Fig. 3.5, phase A-B). The sample assembly was held at this pressure for 15-95 hours before the furnace was switched on (Fig 3.5, phase B-C). This was done for equilibration, to compact the sample assembly and to provide good electrical contacts to the furnace. Heating and further loading to  $800^\circ\text{C}$  and 1150 MPa was then accomplished in 5-10 hours (Fig. 3.5, phase C-D). In this phase, the temperature and pressure were simultaneously increased, closely following the 1  $\text{gcm}^3$  water isochore. After heating and pressurising, the apparatus was left for another equilibration period of 16-20 hours (Fig 3.5, phase D-E). Within this period, the axial load and the oil pressure reached equilibrium values, both increasing slowly because of warming up and thermal expansion of the loading frame.

After equilibrium was reached, the inner WC piston was pushed  $\sim 0.5$  mm into the lead at a relatively high speed (70 $\mu\text{m}/\text{min}$ ) and subsequently retracted again  $\sim 0.3$  mm at the same rate. This was done to determine the pressure in the solid medium independently from the value calculated from the pressure of the oil. In addition, the frictional force acting on the inner WC piston could be determined (see den Brok 1992). After that, the inner WC piston was pushed further into the lead until  $\sim 1$ mm before the ‘hit-point’, again at a 70 $\mu\text{m}/\text{min}$ . The deformation experiment was started with a ‘take-off’ run through the lead. Loading of the sample and subsequent deformation started once the lead was squeezed out and the inner WC piston touched the alumina piston. The displacement rate during the ‘take-off run’ and the deformation run were the same and kept constant. Strain rate thus increased slightly during the experiments. The displacement rate corresponded to a desired strain rate ( $\sim 10^{-7}$  or  $\sim 10^{-6}$   $\text{s}^{-1}$ ). After deformation of the sample, the piston was retracted at maximum speed (180  $\mu\text{m}/\text{min}$ ) and the pressure and temperature were lowered in  $\sim 1$  hour (Fig. 3.5, phase F-G), again closely following the 1  $\text{gcm}^3$  water isochore. The sample assembly was forced out of the vessel with a hydraulic press (force needed 20-30 kN) and manually disaggregated. The nickel-tube was dissolved in nitric acid, to be able to take out the gold capsule including the deformed sample. The sample was not mechanically removed to avoid damaging.



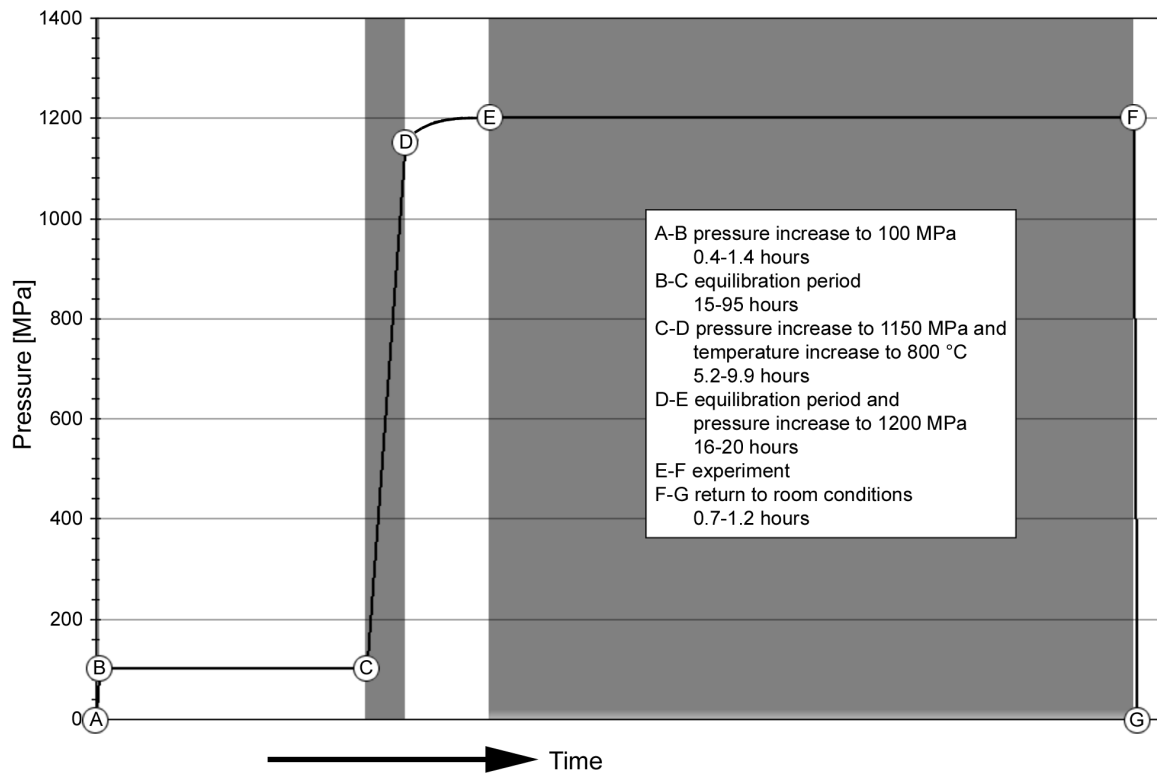


**Figure 3.5:** Sketch of the pressurisation history for experiments performed in the Griggs apparatus.

### 3.4 ANALYSIS OF MECHANICAL DATA

During the experiment, the temperature of both thermocouples, the load, the pressure in the oil chamber, the displacement of the axial load cell, the displacement of the hydraulic ram, the output of the furnace power unit and the temperature of the cooling water were monitored with a chart recorder. The raw axial load versus displacement data are displayed in Figure 3.6 and in Appendix A. First the piston is pushed through the lead disk. During this period, the axial load primarily increases linearly. The ‘take-off run’ is extrapolated from this linear part. Approaching the sample, the axial load starts to increase faster until a linear increase is achieved again once the lead and the gold of the jacket are completely squeezed out and the inner WC piston touches the alumina piston (which is in direct contact with the sample). The ‘yield-line’ is extrapolated from this linear part. The load increases until the sample begins to yield. The ‘hit-point’ is located at the crossing point of the extrapolated ‘take-off’ run and the extrapolated ‘yield-line’. The ‘hit-point’ is not sharp, because the lead and the gold had to be squeezed out between the two pistons.

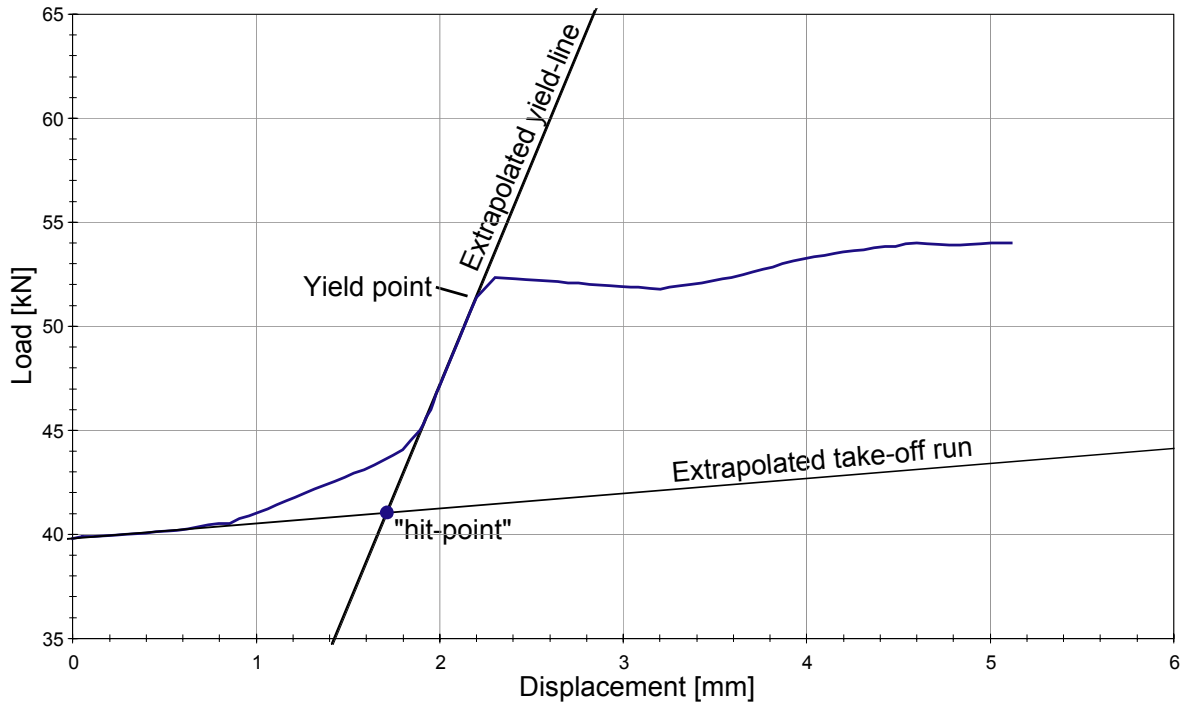


**Figure 3.6:** Raw axial load versus displacement data for experiment GRZ25 ( $\sigma_1 // <c>$ ). Diagram serves to illustrate the extrapolated ‘take-off run’, the extrapolated ‘yield-line’ and how the location of the ‘hit-point’ is established.

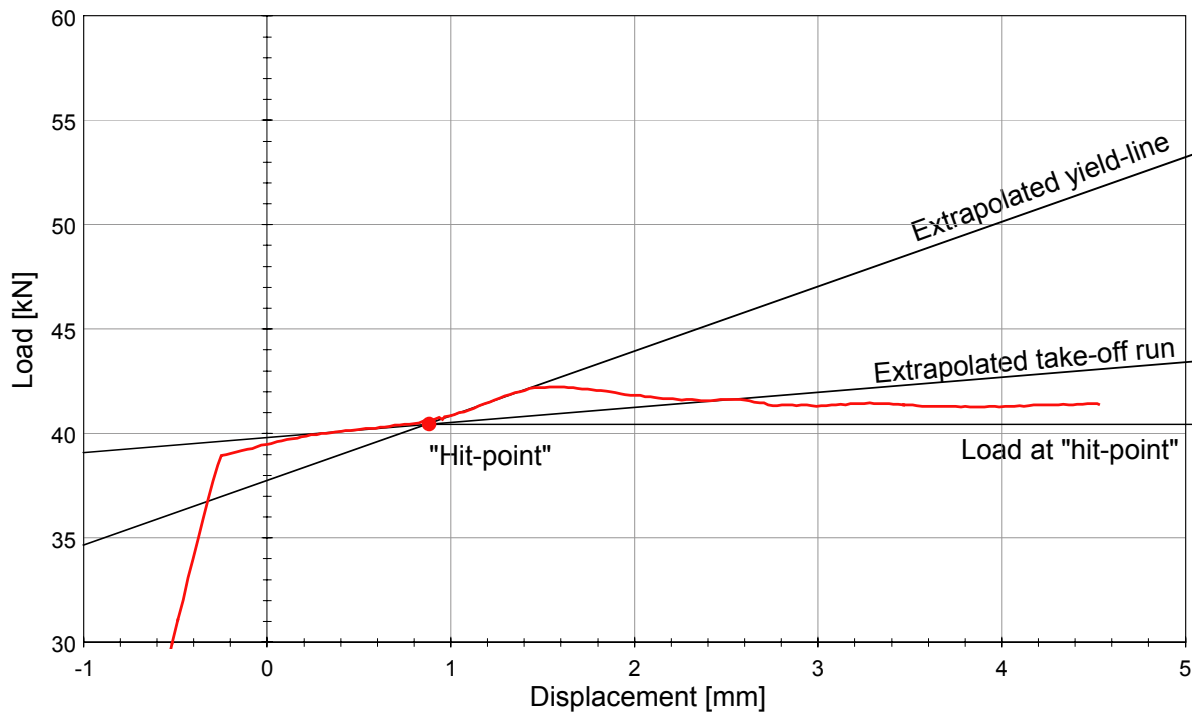


**Figure 3.7:** Raw axial load versus displacement data for experiment GRZ20 ( $\sigma_1 // <o+\>$ ). Diagram serves to illustrate that the ‘take-off run’ crosses the experimental data in some experiments. Therefore it was decided not to subtract the extrapolated ‘take-off run’ from the experimental data, but just the load at the ‘hit-point’ during data processing.

The externally measured load includes the sample strength, the confining pressure and the frictional stress for advancing the piston. The confining pressure and frictional stresses increase slightly ( $<100$  MPa) during experiments with Griggs-type machines (Gleason and Tullis 1995, Rybacki et al. 1998, Stipp and Tullis 2003). There are two methods to extract the confining pressure and frictional stresses from the axial load data: (1) assuming the friction during deformation is given by the ‘take-off run’ (den Brok 1992, Rybacki et al. 1998), (2) inferring friction from additional displacement cycles through the lead before and after the experiment, assuming the increase is linear (Gleason and Tullis 1995, Stipp and Tullis 2003). The second method would give most reliable results, but was not applied in this study because it would potentially damage the deformation microstructures. The first method could not be applied, because the deformation curves of the samples crossed the ‘take-off run’ in a few cases, especially if the load was small (Fig. 3.7). This is probably because the ‘take-off run’ does not only include the friction (den Brok 1992, Rybacki et al. 1998) but also the strength of the lead. Therefore it was not possible to define the change in frictional stress during the run and it was chosen to just extract the axial load at the ‘hit-point’ from the raw load data. Although this is not entirely correct, it is a valid approach for our data.

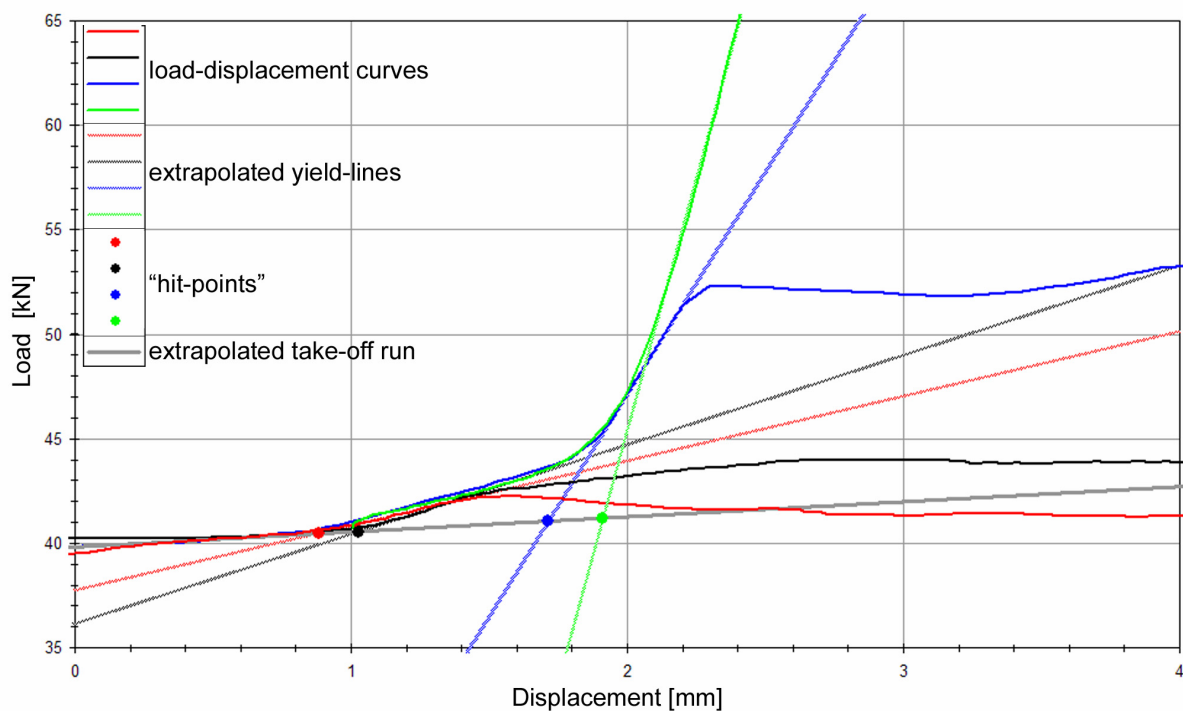


**Figure 3.8:** Raw axial load versus displacement data for experiments GRZ20, GRZ23, GRZ25 and GRZ15 (in order of increasing strength). This diagram serves to illustrate that the extrapolated ‘take-off run’ is more or less similar at all strengths, but that the slope of the ‘yield-line’ depends on the strength of the sample. The location of the ‘hit-point’ changes with the steepness of the ‘yield-line’. The strain taken from the processed diagrams for strong samples coincides best with the strain measured in the sample.

After applying the above mentioned correction, the differential stress supported by the samples was calculated by dividing the axial load by the original cross section of the samples. No corrections were made on the increase in cross-section during the experiment, since the true increase is not known. The displacement data were also corrected for apparatus stiffness (deformation). The apparatus deformation was determined to be  $20 \mu\text{m/kN}$  in a calibration run with a sample assembly with a through going alumina piston. The effect of subtracting the apparatus deformation from the displacement data is illustrated in Fig. A11 of den Brok (1992).

Measurement of the sample length after the experiments showed that the finite strains measured in the stress-strain curves were systematically too high by 1-14%. The largest errors are found in the samples with low strength. This error occurs because the strain in the stress-strain curve strongly depends on positioning the 'hit-point' in the raw axial load-displacement curves. The position of the 'hit-point' is determined by the crossing point of the extrapolated linear 'take-off run' and the extrapolated 'yield line'. At the beginning of the experiments, the load-displacement curves are similar (primary curve); a linear 'take off run' when the inner WC piston moves through the lead, followed by a rise in load when the piston approaches the sample and the lead is squeezed out (Fig. 3.8). Because of the similarity of the primary curves the extrapolation of the 'take-off run' is always more or less similar. The slope of the yield line depends on the point where the deformation curve leaves the exponential part of this primary curve. For a sample with a low strength, this occurs at an early stage and the slope of the yield line is flat (Fig. 3.8), for a sample with a high strength, this occurs at a later stage and the slope of the yield line is steep. If the slopes get steeper, the 'hit-point' moves to the right and the strain in the stress-strain curve will be more and more realistic.

### 3.5 MICROSTRUCTURAL ANALYSIS

During deformation, the originally cylindrical samples had obtained an elliptical cross section (Fig. 3.9). To prepare the sections for microscopical analysis, the samples were cut parallel to the compression direction ( $\sigma_1$ ) and parallel to the long axis of the finite ellipse in this plane. In this way,  $\langle c \rangle$  was about perpendicular to the thin section in the samples deformed parallel to  $\langle a \rangle$  and about parallel to the thin section in the samples deformed parallel to  $\langle c \rangle$ , parallel to  $\langle o \rangle$  and perpendicular to  $\{r\}$ . One half of the samples was impregnated with Epofix so that thin sections could be made without losing too much material during polishing. The thin sections were polished to a very fine polishing grade (0.05  $\mu\text{m}$  alumina suspension). The not-impregnated half of the samples was used to prepare thin sections for transmission electron microscope (TEM) analysis and to prepare 200  $\mu\text{m}$  thick sections used for electron backscatter diffraction (EBSD) analysis. In sample GRZ30, a 200  $\mu\text{m}$  thick slice was cut from the not-impregnated half of sample and manually broken to investigate the grain boundary microstructures by secondary electron (SE) imaging in the scanning electron microscope (SEM).

#### 3.5.1 Optical microscopy

Microstructures were studied in standard thin sections with a polarising microscope (Nikon Optiphot-pol) with a 12.5x ocular and different objective lenses (5x, 10x, 20x and 40x). The thin sections were polished to a very fine polishing grade (0.05  $\mu\text{m}$  alumina suspension). Most imaging was carried out with crossed polars or with crossed polars and with the gypsum plate inserted (530 nm).

#### 3.5.2 Scanning electron microscopy

To investigate the shape of the grain boundaries and individual pores, secondary electron (SE) images were made in a LEO field emission gun (FEG) scanning electron microscope (SEM) that was located at the University of Bayreuth. The specimen were prepared by cutting a 200  $\mu\text{m}$  slab from the not-impregnated halve of sample GRZ30. The slab was carefully fractured by hand more or less parallel to the compression direction. A thin slab ( $< 200 \mu\text{m}$ ) mostly breaks along the grain boundaries, thicker slabs and larger grains tend to break across the grains. Details of the method can be found in Mancktelow et al. (1998). The sample was

sputter-coated with gold. The SE images were acquired using an acceleration voltage of 20 kV.

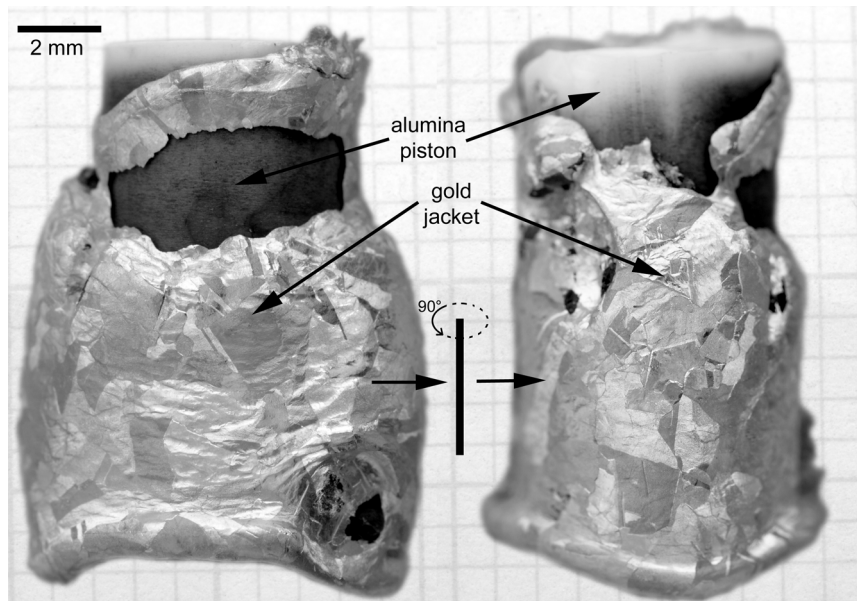


**Figure 3.9:** Gold jacket and upper alumina piston of sample GRZ23, total strain 49%. View direction perpendicular from left to right image. Images illustrate that the sample developed an elliptical shape during deformation. NaCl crystals of the solid confining medium left marks in the gold jacket.

### 3.5.3 Transmission electron microscopy

The transmission electron microscope allows the analysis of submicroscopic structures. The arrangement and densities of dislocations and the (sub-)grain structure were analysed on a Phillips field emission gun (FEG) CM20 TEM located at the University of Bayreuth. For TEM examination of the selected areas, small parts from the not-impregnated petrographic thin sections were thinned by ion milling in a GATAN DUOMILL until electron transparency was reached ( $\pm 0.1\text{-}0.2\ \mu\text{m}$ ). To avoid charging problems, the samples were carbon coated. The TEM images were acquired at an acceleration voltage of 200 kV. We employed conventional bright-field and dark-field imaging techniques. TEM images were taken with diffraction vectors  $g=10\bar{1}1$ ,  $g=0003$  and  $g=10\bar{1}0$  in order to determine the Burgers vector by applying the  $g\cdot b=0$  criterion (McLaren 1991).

### 3.5.4 Cathodoluminescence

Cathodoluminescence (CL) can reveal growth zones and healed cracks which are not optically visible (Marshall 1988). The CL signal can also be strongly influenced by defects in the crystal structure. In this study we used CL to verify the origin of deformation structures. A CL-detector installed in a Camscan CS44 SEM at the ETH electron microscopy centre (EMEZ) was used. Analyses were done on polished thin sections coated with carbon.

### 3.6 TEXTURE MEASUREMENTS

Electron backscatter diffraction (EBSD) techniques were used to analyse the texture of the samples, i.e. grain and subgrain structure and complete crystallographic orientation. The EBSD-system is installed in a Camscan CS44 SEM at the ETH. Measurements were done on mechanically polished, 200  $\mu\text{m}$  thick sections that were lapped with Syton to reduce the surface damage. Syton is an alkaline colloidal silica suspension with a particle size of 25 nm and polishes the sample surface both mechanically and chemically. After 6 hours of lapping, the surface damage was reduced enough to produce EBSD-patterns with a sufficient quality (confidence index  $>0.1$ ). The quality of the data was enhanced by longer lapping. A thin layer of carbon (2-4 nm) was then deposited on the sample surface to reduce the influence of surface charging. The EBSD patterns were obtained using a 15 kV acceleration voltage, 35 mm working distance,  $\sim 3$  nA beam current and  $70^\circ$  sample tilt.

EBSD patterns are generated by multiple scattering of incident electrons within the crystal structure of a bulk specimen. EBSD patterns are the backscattered equivalent of the Kikuchi patterns observed in the TEM (Kikuchi, 1928). The patterns consist of a series of bands, each of which corresponds to a specific lattice plane (hkil). The width of the bands is related to the Bragg angle that is approximately inversely proportional to the lattice plane spacing. Using the angles between the bands and their width the diffraction pattern can be indexed to determine the crystallographic orientation for a known crystal structure. Details on the technique can be found, in e.g. Adams et al. (1993), Prior et al. (1999), Mauler Steinmann (2000).

The EBSD patterns were automatically collected at a typical scan speed of 9 patterns per second with scanning step sizes of 1-10  $\mu\text{m}$  covering different areas. The patterns were collected and indexed with the commercial TSL software OIM DC 3.5<sup>TM</sup> and analysed with OIM Analysis 3.0<sup>TM</sup> and OIM Analysis 3.5<sup>TM</sup>. The analyses show a large number of data with a high reliability (confidence index  $>0.1$ ). The obtained data are presented in (1) orientation maps and pattern quality maps, (2) misorientation profiles and (3) pole figures.

In orientation maps, the colour of each pixel corresponds to an orientation defined by the crystal direction parallel (or perpendicular) to the compression axis ( $\sigma_1$ ) in the colour key (Fig. 3.10a). In pattern quality maps (Fig. 3.10b), grey shades relate to band sharpness of the EBSD-pattern. Since these pattern quality maps reproduce surface damage, fractures and (sub)grain boundaries they are an additional image of the microstructure and useful to verify the reliability of the orientation maps. The presentation of the data in the orientation map for trigonal quartz (Fig. 3.10a) is complicated by Dauphiné twin-orientations. It is not clear if the indexed Dauphiné twins are induced during cooling (the starting material has no Dauphiné twins) or induced by deformation, because the deformation experiments were performed close to the transition zone from trigonal ( $\alpha$ -) to hexagonal ( $\beta$ -)quartz (Haar et al. 1984). Further ambiguous results may come from misindexing in potential Dauphiné twin orientations. Therefore the quartz data in our samples are plotted as being hexagonal (Fig.3.10c). The raw orientation maps for hexagonal quartz still contain a number of erroneous data, especially along grain boundaries where the pattern quality is low. The OIM software provides a simple algorithm to clean these erroneous data by replacing them by the most common neighbouring orientations (Fig. 3.10d). Because the step-size is much smaller than the grain size, erroneous data can be identified as single pixels that are different from all surrounding points.

Misorientation profiles were drawn along lines in the cleaned orientation maps (Fig. 3.10d). The misorientation angle between adjacent points along these lines was calculated by selecting the minimum angle that enables the lattice of one point to be rotated into that of the other (Wheeler et al. 2001).

Pole figures were used (1) for crystallographic preferred orientation (CPO) analyses and (2) to infer rotation axes. CPOs are analysed in the areas with new grains. Only the recorded data with a confidence index above 0.1 were used (Fig. 3.10e and 3.11). Contouring of the discrete data was carried out with the OIM 3.0™ software using a smoothing of 6° Gaussian width (Fig. 3.11). Rotation axes were specified in the so called host areas. In these areas, only gradual rotations of the host lattice are observed and no new grains. Data were selected along linear segments. We developed a program to calculate the rotation axes based on the determination of second order moments of the orientation distributions. The corresponding errors to the rotation axes were calculated from the maximum misorientation angle along the profiles according to equation A10 of Kruse et al. (2002).

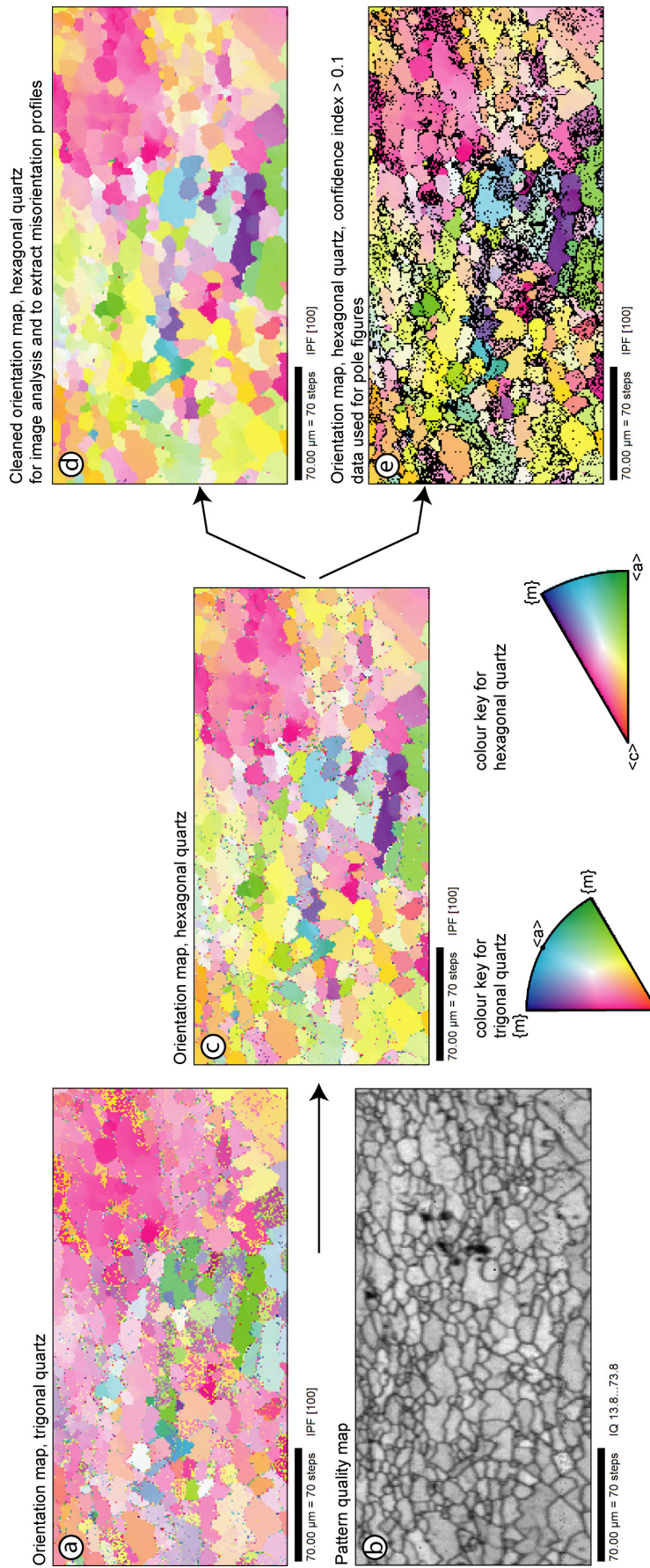


**Figure 3.10:** Orientation maps from EBSD scans of recrystallised domains in sample GRZ30: a) Raw orientation map that is coloured by the colour key for trigonal quartz for the  $\sigma_1$ -direction. Data are disrupted by Dauphiné twins and erroneous data on the grain boundaries. b) Pattern quality map that reproduces surface damage and (sub)grain boundaries. c) Raw orientation map that is coloured by the colour key for hexagonal quartz for the  $\sigma_1$ -direction. Erroneous data are still present on the grain boundaries. d) Orientation map for hexagonal quartz from which the erroneous data are corrected. e) Orientation map for hexagonal quartz containing only data with confidence index > 0.1.



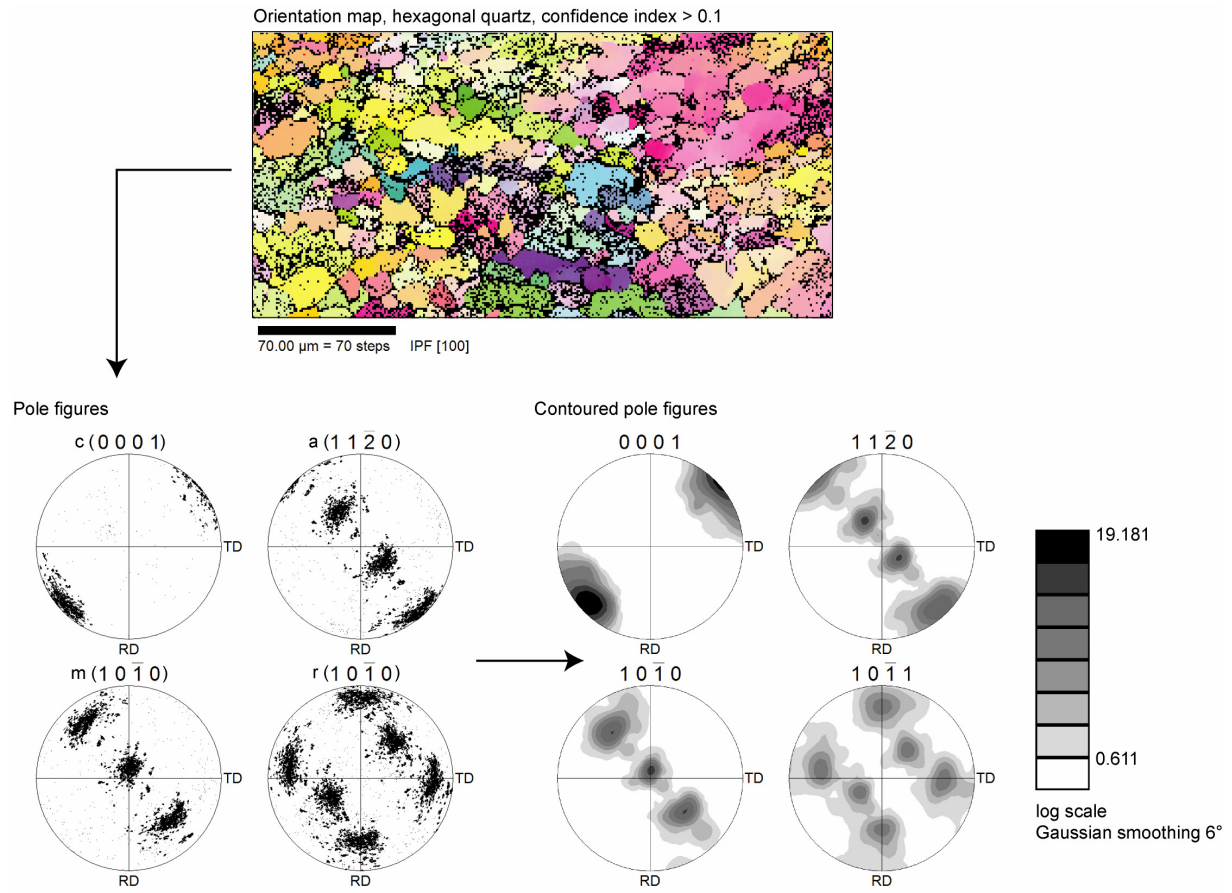


**Fig. 3.11:** Pole figures were constructed from data with confidence index > 0.1 (Fig. 3.10). Contouring of the data was carried out with OIM 3.0™ using a smoothing of  $6^\circ$  Gaussian width.



## CHAPTER 4

### OVERVIEW OF MECHANICAL DATA AND DEFORMATION MICROSTRUCTURES IN QUARTZ SINGLE CRYSTALS

#### 4.1 INTRODUCTION

This chapter presents an overview of the mechanical and microstructural results obtained from all experiments on single crystals of quartz that were performed in the course of this study (Table 4.1). The hydrostatical loading and deformation experiments were performed under a variety of experimental conditions. The aim of this chapter is to delineate the optical microstructures that are related to crystal reorientation mechanisms in single crystals of quartz in dependence of host orientation, finite strain and water content. Details and interpretations of the reorientation mechanisms are given in chapters 5, 6 and 7.

#### 4.2 MECHANICAL DATA

The mechanical data obtained from the deformation tests are presented in stress-strain curves, i.e. differential stress versus bulk finite strain curves. We investigated the effect of starting orientation and the effect of varying deformation conditions on the mechanical behaviour of quartz single crystals.

##### 4.2.1 The effect of the starting orientation

All samples deformed with 1 vol% of added water initially showed work hardening towards peak values (Fig. 4.1a). The strain at which the peak stress was achieved varied between 2 and 4%. Gentle weakening was observed in most runs immediately after the peak stress. In experiments GRZ25 ( $\sigma_1 // \langle c \rangle$ ) and GRZ27 ( $\sigma_1 \sim \perp \langle r \rangle$ ), the differential stress increased again after weakening. The flow stress values in the samples were related to their starting orientation, in the same order as reported by Blacic and Christie (1984). Sample GRZ25 ( $\sigma_1 // \langle c \rangle$ ) showed the highest peak stress (about 410 MPa). Sample GRZ20 ( $\sigma_1 // \langle o+ \rangle$ ) showed the lowest peak stress (about 60 MPa).

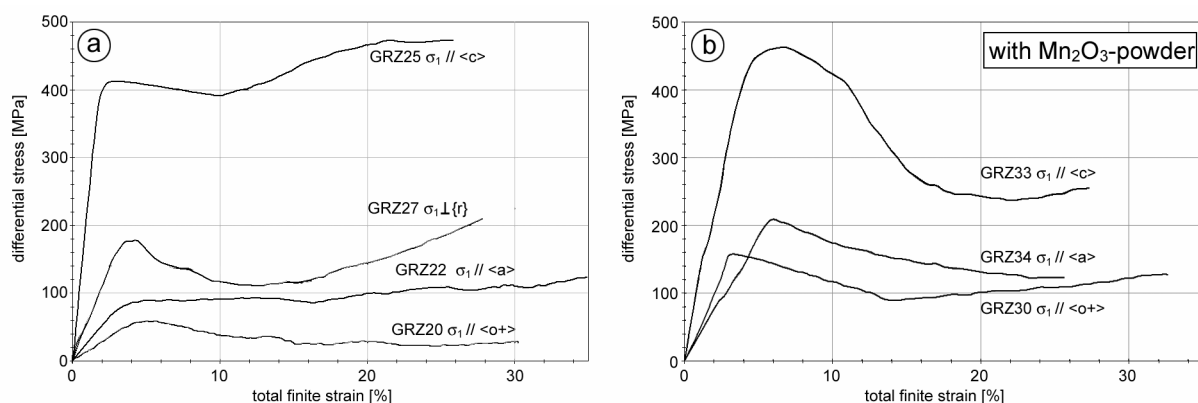


**Figure 4.1:** Stress-strain curves for samples deformed in different starting orientations at an approximately constant strain rate, temperature and confining pressure; a) together with 1 vol% added water and b) together with 1 vol% added water and 20 mg  $Mn_2O_3$ -powder.

Sample number	Starting orientation	Strain rate	$\epsilon$ from sample	$\epsilon$ from data	$P_c$	$UTC$	$LTC$	$t_1$	$t_2$	$t_3$	$t_4$	Peak stress
	$[\sigma_1 // ]$	$[s^{-1}]$	$[\%]$	$[\%]$	$[MPa]$	$[^{\circ}C]$	$[^{\circ}C]$	$[h]$	$[h:m]$	$[h:m]$	$[h:m]$	$[MPa]$
Hydrostatically loaded												
GRZ26	$\langle o+\rangle$	-	-	-	1180	805	798	95	06:55	221:03	00:44	-
GRZ29	$\langle o+\rangle$	-	-	-	1150	793	799	63	09:54	15:36	00:42	-
No water added												
GRZ19	$\langle a\rangle$	$1.1 \cdot 10^{-6}$	0.03	7	1220	802	783	16	07:26	17:21	00:56	-
1 vol% water added												
GRZ16	$\langle o+\rangle$	$0.7 \cdot 10^{-6}$	11	26	1200	786	800	18	07:54	16:21	01:09	130
GRZ17	$\langle o+\rangle$	$1.1 \cdot 10^{-6}$	21	28	1190	811	785	68	08:22	15:34	00:58	170
GRZ20	$\langle o+\rangle$	$1.0 \cdot 10^{-6}$	28	30	1120	808	801	46	05:14	19:12	00:58	60
GRZ21	$\langle o+\rangle$	$1.0 \cdot 10^{-6}$	50	50	1110	805	800	67	07:02	14:50	00:53	90
GRZ22	$\langle a\rangle$	$1.0 \cdot 10^{-6}$	32	36	1240	799	810	69	06:55	16:21	01:07	90
GRZ23	$\langle a\rangle$	$1.1 \cdot 10^{-6}$	43	54	1100	803	810	81	07:42	17:30	00:48	120
GRZ25	$\langle c\rangle$	$1.1 \cdot 10^{-6}$	26	26	1220	799	805	17	07:29	16:50	00:55	410
GRU27	$\perp\{r\}$	$1.0 \cdot 10^{-6}$	26	28	1190	800	800	67	08:02	17:15	00:49	175
GRZ28	$\perp\{r\}$	$1.0 \cdot 10^{-6}$	5	8	1200	802	798	22	08:07	19:57	00:47	340
GRZ32	$\langle o+\rangle$	$1.0 \cdot 10^{-7}$	12	-	1190	808	798	16	07:15	16:30	00:22	-
3 vol% water added												
GRZ31	$\langle o+\rangle$	$1.1 \cdot 10^{-6}$	30	33	1230	808	800	20	06:47	16:30	00:47	130
1 vol% water added + 20 mg $Mn_2O_3$ powder												
GRZ30	$\langle o+\rangle$	$1.0 \cdot 10^{-6}$	29	32	1220	794	806	22	07:12	16:00	00:42	150
GRZ33	$\langle c\rangle$	$1.0 \cdot 10^{-6}$	26	27	1210	804	796	16	07:18	17:36	00:48	440
GRZ34	$\langle a\rangle$	$1.1 \cdot 10^{-6}$	24	26	1210	800	800	16	07:12	19:24	00:42	210
GRU37	$\langle o+\rangle$	$1.1 \cdot 10^{-6}$	14	-	1200	820	795	-	23:50*	75:00	02:10	-

**Table 4.1:** Experimental data of all the samples deformed in this study.  $\epsilon$ , finite strain;  $P_c$ , confining pressure;  $UTC$ , temperature of upper thermocouple;  $LTC$ , temperature of lower thermocouple,  $t_1$ , time at 100 MPa  $t_2$ , elapsed time to reach  $PT$  conditions;  $t_3$ , time at  $PT$  conditions before deformation;  $t_4$ , elapsed time after deformation to reach room conditions; \*,  $t_1+t_2$ . Both the strain measured in the sample ex-situ at room PT ( $\epsilon$  from sample), and the strain measured from the processed mechanical data are displayed.

The mechanical behaviour of the samples deformed with  $Mn_2O_3$ -powder and added water (Fig. 4.1b) was similar to that of the samples deformed without the powder (Fig. 4.1a). All experiments showed initial work hardening until a peak stress was reached beyond which weakening took place. The strain at which the peak stress was reached varied between 3 and 6%. The weakening effect was much more pronounced in sample GRZ33 ( $\sigma_1 // \langle c\rangle$ ). In experiments GRZ30 ( $\sigma_1 // \langle o+\rangle$ ) and GRZ33 ( $\sigma_1 // \langle c\rangle$ ), the differential stress increased slightly after weakening. Sample GRZ33 ( $\sigma_1 // \langle c\rangle$ ) showed the highest peak stress ( $\sim 450$  MPa). Sample GRZ30 ( $\sigma_1 // \langle o+\rangle$ ) showed the lowest peak stress ( $\sim 150$  MPa). Marking

differences of the experiments performed with  $\text{Mn}_2\text{O}_3$  powder and those without powder are increased peak stresses and the drastic weakening in sample GRZ33 ( $\sigma_1 // \langle c \rangle$ ).

#### 4.2.2 The effect of deformation conditions

The effect of varying the deformation conditions is illustrated in Figure 4.2. Figure 4.2a shows the stress-strain curves of two similarly oriented samples ( $\sigma_1 // \langle o + \rangle$ ) deformed with different amounts of water; GRZ20 had 1 vol% of added water and GRZ31 had 3 vol% of added water. Both experiments showed an initial period of work hardening until a peak stress was reached at  $\sim 4\%$  finite strain. Weakening, immediately after the peak stress was more pronounced in sample GRZ31. The peak stress in the sample (GRZ31) with 3 vol% of water ( $\sim 140$  MPa) was higher than the peak stress in sample GRZ20 deformed with 1 vol% of water ( $\sim 60$  MPa).

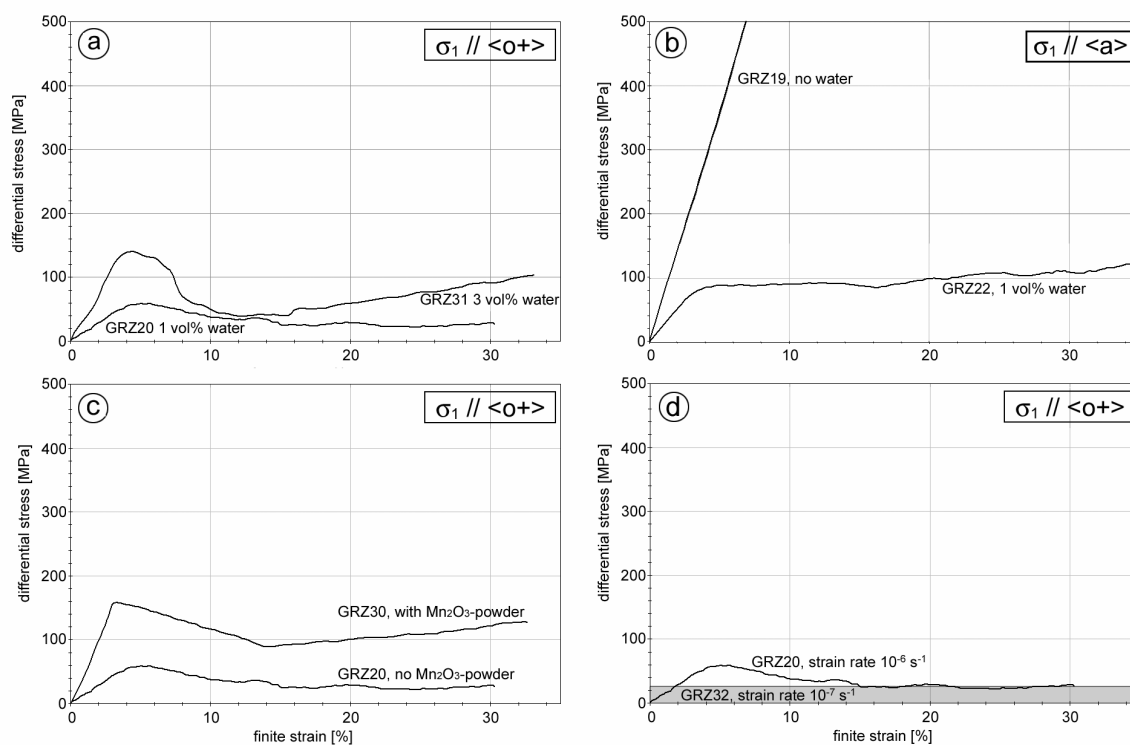


**Figure 4.2:** Stress-strain curves for samples deformed at a constant starting orientation, but with different experimental conditions; a) illustrates the effect of added extra water, b) illustrates the effect of not adding water, c) illustrates the effect of adding 20 mg  $\text{Mn}_2\text{O}_3$ -powder and d) illustrates the effect of strain rate.

Figure 4.2b shows the stress-strain curves of two similarly oriented samples ( $\sigma_1 // \langle a \rangle$ ) deformed with 1 vol% of water (GRZ22) and without water (GRZ19). Sample GRZ19 did not yield within this experiment. Experiment GRZ22 showed an initial period of work hardening until a peak stress of  $\sim 90$  MPa at  $\sim 4\%$  finite strain, followed by nearly constant flow stress.

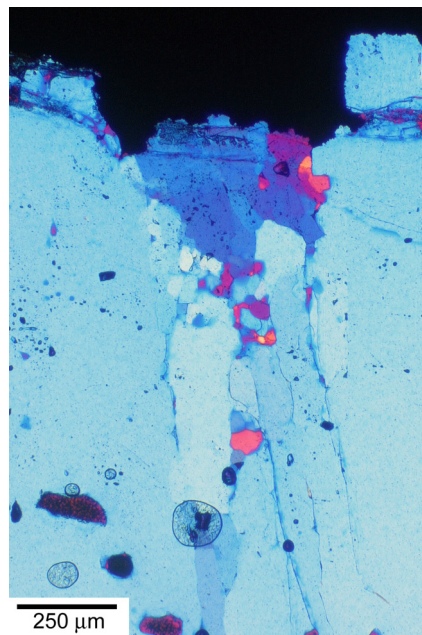
Figure 4.2c shows the stress-strain curves of two similarly oriented samples ( $\sigma_1 // \langle o + \rangle$ ) deformed with (GRZ30) and without  $\text{Mn}_2\text{O}_3$ -powder (GRZ20). Both experiments showed similar stress-strain curves. Initial work hardening occurred until a peak stress was reached between 3 and 4% strain followed by a period of weakening. The difference between the samples was that the peak stress of sample GRZ30 is  $\sim 160$  MPa whereas the peak stress of sample GRZ20 is only  $\sim 60$  MPa.

Figure 4.2d shows the stress-strain curve of sample GRZ20 again, which was deformed at  $10^{-6}$   $s^{-1}$ . The curve of sample GRZ32, deformed at  $10^{-7}$   $s^{-1}$ , is not visible because the differential stress was below the detectable limit of the Griggs Rig ( $\sim 25$  MPa).

### 4.3 MICROSTRUCTURAL OBSERVATIONS

#### 4.3.1 Hydrostatically loaded samples

Two hydrostatic loading experiments have been carried out for purposes of microstructural control (Table 4.1): (1) the sample of experiment GRZ29 has been at *PT* conditions for  $\sim 19$  hours, i.e. as long as the deformed samples were before deformation (until E in Fig. 3.5) and (2) the sample of experiment GRZ26 has been at *PT* conditions for  $\sim 221$  hours, i.e. as long as the duration of a complete deformation experiment (until F in Fig. 3.5).



**Figure 4.3:** Longitudinal cracks within a hydrostatically loaded sample (GRZ26,  $\sim 221$  hours at  $800^{\circ}\text{C}$  and  $1180$  MPa). The cracks generate offsets at the sample boundary, which was originally horizontal. Small new grains developed within the cracks. Black field in the upper part of the image is the gold jacket. Optical micrograph with crossed polarisers and the gypsum plate.

Both hydrostatic loading experiments produced substantial microstructural modifications in the samples. Longitudinal (healed) cracks are dominant microstructures in both samples. These cracks are marked with fluid inclusions. Through going longitudinal cracks generate small offsets at the sample ends (Fig. 4.3). The longitudinal cracks are typically interconnected by smaller slightly curved oblique cracks.

In sample GRZ29, the longitudinal cracks are partly healed and filled with a few very small ( $< 5$   $\mu\text{m}$ ) non euhedral grains near the sample ends. The small oblique cracks are completely healed. In sample GRZ26, all cracks are healed. Locally, these cracks separate areas of slightly different optical extinction, thus different crystal orientation. The longitudinal cracks in this sample are also decorated by a few new grains (size  $< 75$   $\mu\text{m}$ ) near the sample ends (Fig. 4.3).

### 4.3.2 Sample deformed without water

Experiment GRZ19 was performed with  $\sigma_1$  parallel to  $\langle a \rangle$  and without added water. This sample did not yield during the experiment. The deformation lamellae, which are observed close to the sample boundaries (Fig. 4.4) developed during loading along the linear slope. These deformation lamellae are very thin planar structures that locally induce a different refractive index and a change in birefringence in the crystal. They are present in two different orientations, which may be sub-parallel to prism  $\{a\}$  or  $\{m\}$  planes. There is no undulatory extinction observed in this sample. Cracking was of minor importance and only related to unloading.

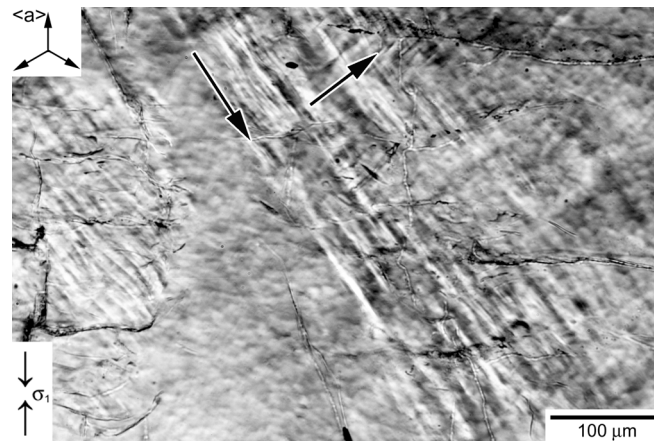


**Figure 4.4:** Optical micrograph with crossed polarisers showing deformation lamellae (black arrows are parallel to the lamellae) at the border of sample (GRZ19) deformed dry at  $T=800^\circ\text{C}$ ,  $P_c=1220\text{ MPa}$  and  $\dot{\epsilon}=1.1 \cdot 10^{-6}\text{ s}^{-1}$ , parallel to  $\langle a \rangle$ . The local change in birefringence from grey to white along the lamellae indicates a slight misorientation of the lattice. Fractures that are perpendicular to  $\sigma_1$  represent unloading fractures. Arrows in the upper left indicate the starting orientation of the sample.

### 4.3.3 Samples deformed with 1 vol% water

Samples that were deformed with added water display an inhomogeneous distribution of deformation microstructures. Most strain is accommodated in the lower half of the sample. Therefore, the samples bulge at this end with increasing strain. Several deformation microstructures are observed: continuous undulatory extinction, deformation lamellae, fractures, dissolution at the sample boundaries and recrystallised grains. Cracks and healed cracks are observed at all strains and in all samples, irrespective of initial crystal orientation. Unloading cracks are perpendicular to  $\sigma_1$  and most extensive at relatively high differential stresses. The appearance of the other microstructures depends on finite strain and on the starting orientation of the crystal. In the following sections the microstructures will be separately presented for  $\sigma_1$  at  $45^\circ$  to  $\langle c \rangle$ ,  $\sigma_1$  parallel to  $\langle c \rangle$  and  $\sigma_1$  at  $90^\circ$  to  $\langle c \rangle$ .

#### 4.3.3.1 $\sigma_1$ at $45^\circ$ to $\langle c \rangle$

Two different series of samples with  $c$ -axes at  $45^\circ$  to the compression direction (starting orientation  $\sigma_1 // \langle o+ \rangle$  and starting orientation  $\sigma_1 \sim \perp \{r\}$ ) evolve similar microstructures.

At (low) finite strains of  $<10\%$ , samples mainly show continuous undulatory extinction in elongated bands (Fig. 4.5a). These bands (also referred to as deformation bands, Passchier and Trouw 1998) are approximately parallel to  $\langle c \rangle$  and terminated by longitudinal fractures. Within these bands,  $\langle c \rangle$  has gradually changed its orientation towards  $\sigma_1$ . The elongated bands of undulatory extinction are often associated with deformation lamellae. Deformation lamellae are perpendicular to the undulatory bands and approximately parallel to the basal

plane. They represent a reorientation of the crystal lattice and they have a lower refractive index than the rest of the sample.

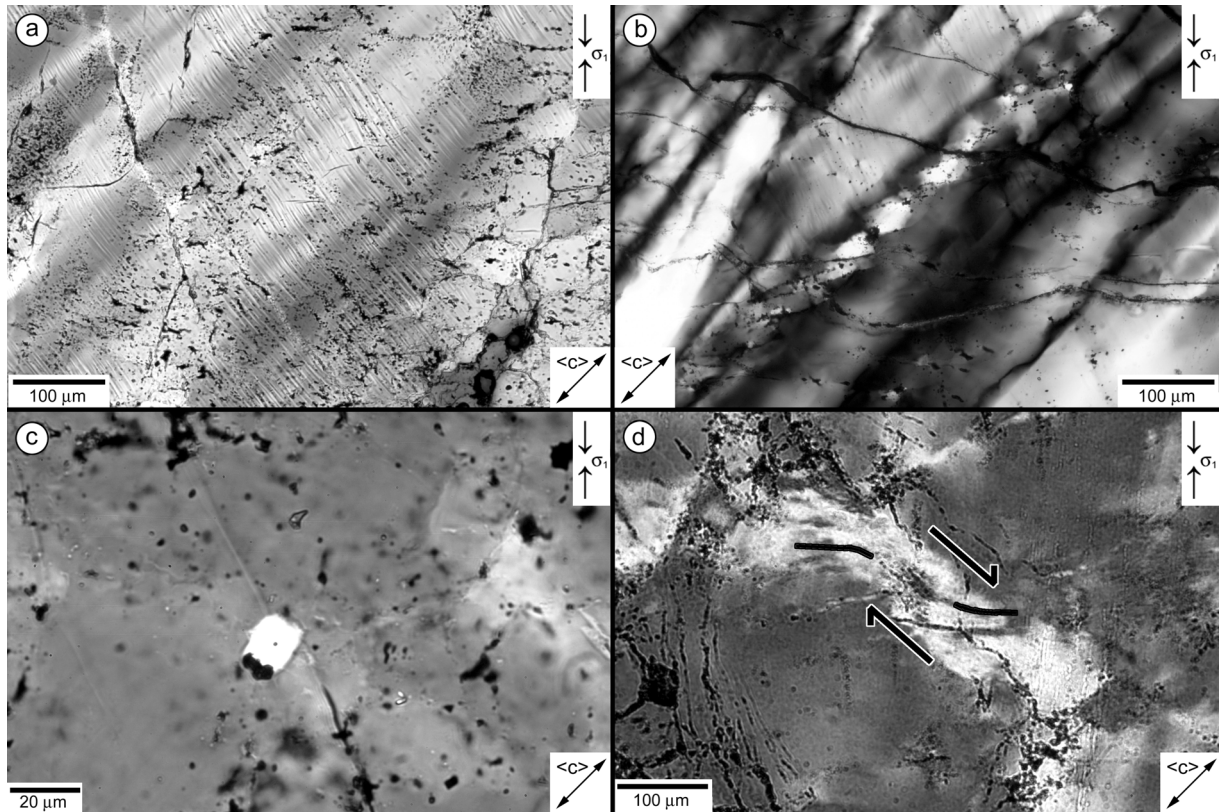


**Figure 4.5 :** Optical micrographs with crossed polars of microstructures in samples deformed with  $\langle c \rangle$  at  $45^\circ$  to  $\sigma_1$ , at  $T = 800^\circ\text{C}$ ,  $P_c \sim 1200 \text{ MPa}$  and  $\dot{\epsilon} \sim 10^{-6} \text{ s}^{-1}$ . Arrows in the lower part of the pictures indicate the starting orientation of the deformed samples. a) GRZ28,  $\epsilon \sim 5\%$ . Undulatory extinction and perpendicular through-going deformation lamellae. b) GRZ20,  $\epsilon \sim 28\%$ . Undulatory extinction and subgrains. Deformation lamellae are less extensive than in (a). c) GRZ17,  $\epsilon \sim 21\%$ . Small new subeuhedral grain with a large fluid inclusion on its grain boundary. d) GRZ21,  $\epsilon \sim 50\%$ . Microshear zone that is approximately parallel to the basal plane. Black lines and arrows indicate the amount and sense of shear.

At (intermediate) finite strains of 20-30%, undulatory extinction is still extensive, but much smaller amounts of deformation lamellae are observed. Domains with subgrains partly crosscut the elongated bands with undulatory extinction (Fig. 4.5b). The boundaries of the subgrains are decorated with abundant fluid inclusions, which are also present in the subgrain interiors. Subgrains have irregular shapes and sizes and the orientation difference with respect to the host sample is only a few degrees. In the samples deformed to intermediate finite strains few isolated strain-free grains recrystallised. These new grains generally occur along longitudinal fractures (Fig. 4.6). In contrast to the subgrains, new grains have a polygonal to euhedral shape (Figs. 4.5c and 4.7a), inclusion free interiors and their crystallographic orientation is often at a large angle (tens of degrees) to the surrounding host domains. New grains occur in areas with a relatively high density of fluid inclusions and apparent fluid channels associated with healed longitudinal fractures (Fig. 4.6). The grain boundaries of the new grains are also decorated with fluid inclusions. These are generally tinier than fluid inclusions on the subgrain boundaries.

At high finite strains ( $\sim 50\%$ , sample GRZ21), undulatory extinction is still observed, while deformation lamellae are absent. Even at this strain level, only a few new recrystallised grains are present in the sample. They are associated with longitudinal fractures and have indented



grain boundaries (Fig. 4.7b). Additionally, small shear zones have developed more or less parallel to the basal plane (Fig. 4.5d).

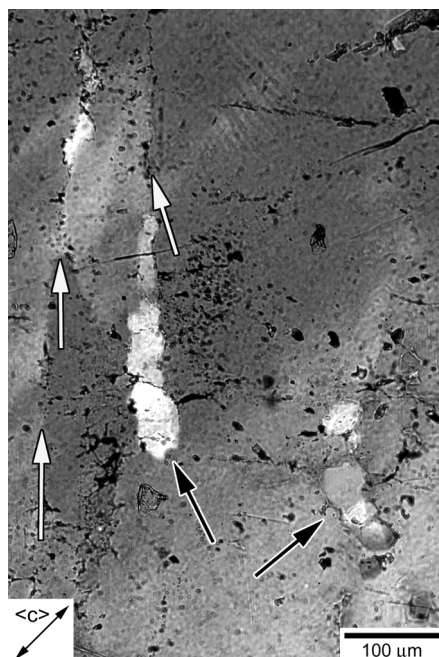


**Figure 4.6 :** Optical micrographs with crossed polars showing new grains (black arrows) on longitudinal healed cracks (white arrows and traced with fluid inclusions) in sample GRZ17 uniaxially compressed parallel to  $\langle o+ \rangle$ , at  $T=795^{\circ}\text{C}$ ,  $P_c=1190\text{ MPa}$ ,  $\dot{\epsilon}=1.1 \cdot 10^{-6}\text{ s}^{-1}$  to 21% finite strain. Arrow in the lower left indicates the starting orientation of the sample.

#### 4.3.3.2 $\sigma_1$ parallel to $\langle c \rangle$

One sample (GRZ25) was deformed with  $\langle c \rangle$  initially parallel to  $\sigma_1$  to a finite strain of 26%. The flow stress of this sample was very high with respect to the other samples (Fig. 4.1a). The microstructures in this sample look different from the microstructures in the samples deformed with  $\langle c \rangle$  at  $45^{\circ}$  to  $\sigma_1$ .

Undulatory extinction occurs in bands that are parallel to  $\langle c \rangle$ , i.e. in this sample more or less parallel to  $\sigma_1$ . Within these zones  $\langle c \rangle$  is slightly further away from  $\sigma_1$  than in the surrounding domains. Deformation lamellae are observed in three different orientations, two sets of orientations at  $\sim 45^{\circ}$  to  $\sigma_1$  and one set about perpendicular to  $\sigma_1$ . Subgrains have irregular shapes and abundant fluid inclusions on their boundaries. The domains with subgrains are not related to the undulatory bands. Microscale intracrystalline shear zones are locally present in the sample (Fig. 4.8a). The shear zone boundaries are at  $45^{\circ}$  to  $\sigma_1$ . Some shear zones generate an offset at the sample boundary (Fig. 4.8b). This offset can be used to determine the displacement direction along these shear zones. Within the thin section, left dipping shear zones show a sinistral sense of rotation of the crystal lattice and are yellow, right dipping shear zones show a dextral sense of rotation of the crystal lattice and are blue. On the offsets at the sample boundaries, few new recrystallised grains are present (Fig. 4.8b). They have a subeuhedral shape and sometimes indented grain boundaries.

Most strain is accommodated in the lower end of the sample, which shows a wedge-shaped network of conjugate shear zones (Fig. 4.8c). The shear zones encompass blocks of the host crystal with a rather homogeneous size (Fig. 4.8d). These blocks display continuous undulatory extinction and in some cases deformation lamellae.

4.3.3.3  $\sigma_1$  at  $90^\circ$  to  $\langle c \rangle$ 

Sample GRZ22 and sample GRZ23 were deformed with one of the  $a$ -axes parallel and the  $c$ -axis perpendicular to  $\sigma_1$  to a bulk finite strain of 32 and 43%, respectively. Both samples display comparable deformation microstructures despite the strain difference. The most important observation is that the  $c$ -axis orientation remains more or less constant within the host domains, which consist of subgrains (Fig. 4.9a). Subgrains have irregular shapes and their boundaries are occupied with fluid inclusions. New recrystallised grains have their  $\langle c \rangle$  at a high angle (generally much larger than  $15^\circ$ ) to the deformed host (Fig. 4.9b). Part of the new recrystallised grains have indented grain boundaries.

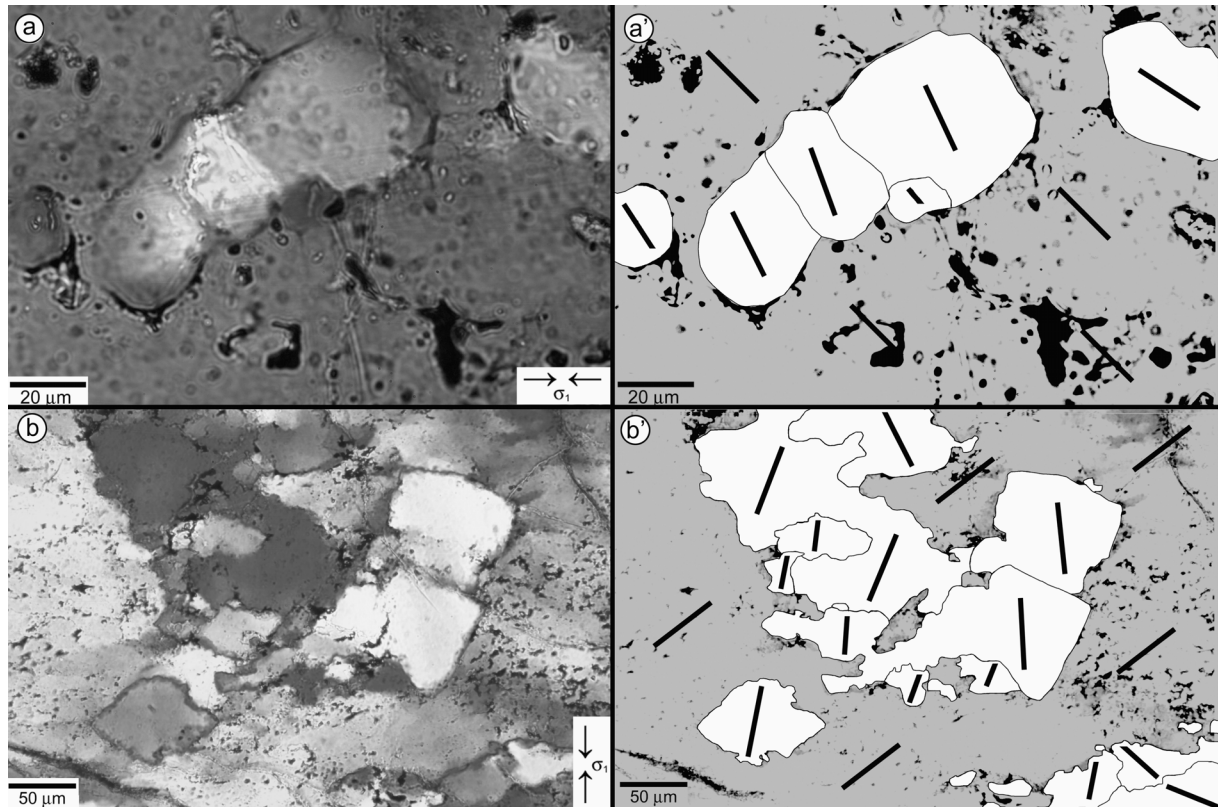


**Figure 4.7:** a) Small array of new grains in intermediate finite strain (21%) sample (GRZ17). b) Domain with larger new grains in large finite strain (50%) sample (GRZ21). Line drawings a' and b' serve to illustrate the nature of the grain boundaries: straight in a' and indented in b'. Black bars indicate the traces of the orientations of  $\langle c \rangle$ . Black spots coincide with fluid inclusions in Figs. a and b.

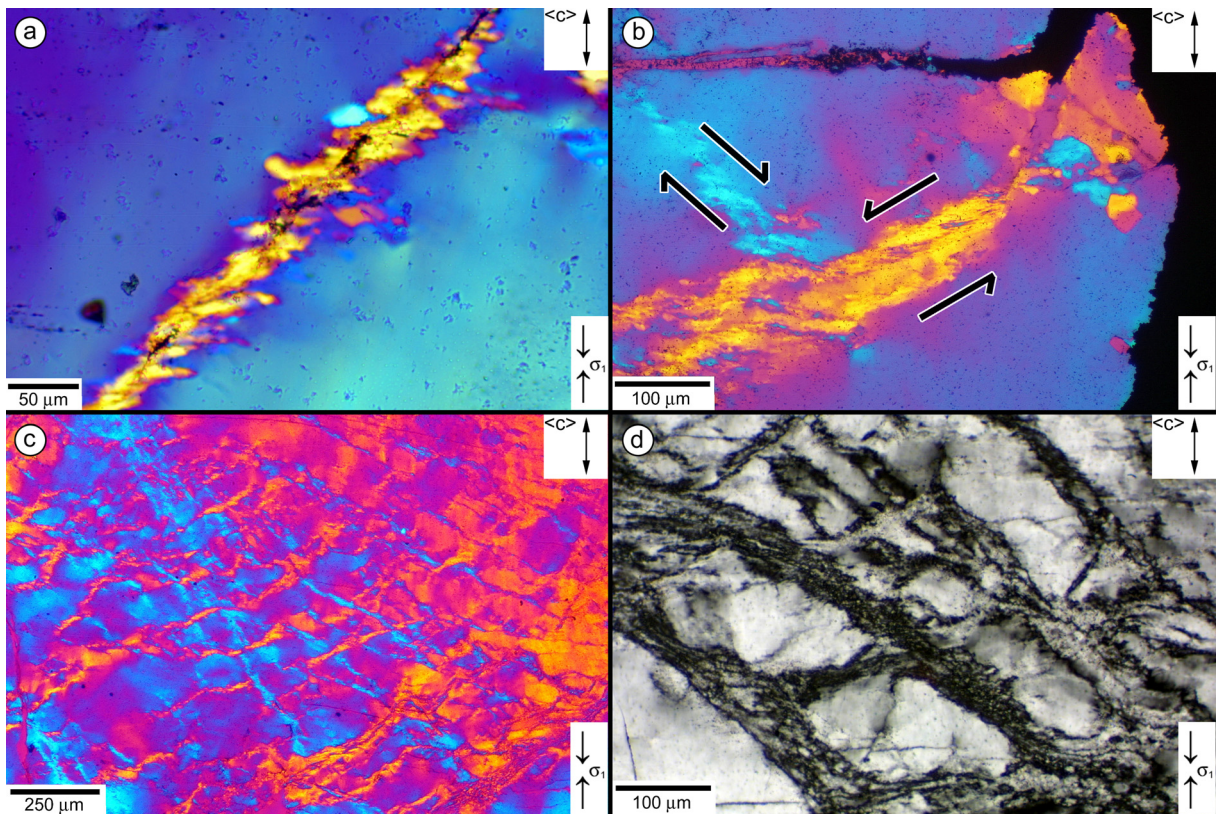


**Figure 4.8 :** Intracrystalline shear zones in sample (GRZ25) deformed with  $\langle c \rangle$  parallel to  $\sigma_1$ , at  $T=800^\circ\text{C}$ ,  $P_c=1220$  MPa,  $\dot{\epsilon}=1.1 \cdot 10^{-6} \text{s}^{-1}$  to 26% bulk finite strain. a) Left dipping shear zone that is traced by fluid inclusions. b) Conjugated set of shear zones in blue and yellow (see black arrows) close to the sample boundary. Yellow microshear zone generated an offset at the sample rim. New grains recrystallised on this offset. c) Network of conjugated shear zones in large strain domain. d) Conjugated sets of shear zones encompass rigid blocks of the host sample. Optical micrographs with crossed polarisers and the gypsum plate. Arrows in the upper right indicate the starting orientation of the sample.

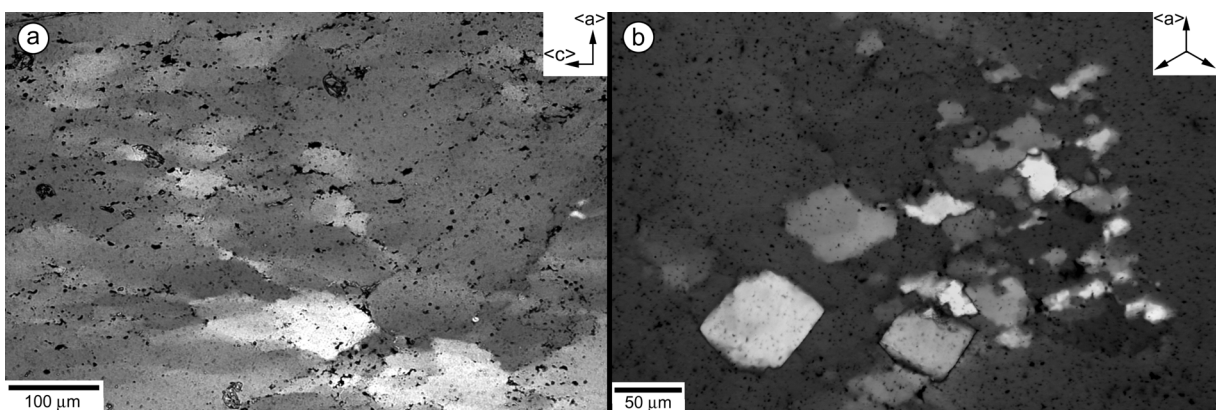


**Figure 4.9:** Subgrains and new grains in samples deformed with  $\sigma_1$  parallel to  $\langle a \rangle$ . a) Subgrains in sample GRZ22 ( $T=805^\circ\text{C}$ ,  $P_c=1240$  MPa,  $\dot{\epsilon}=1.0 \cdot 10^{-6} \text{s}^{-1}$  and  $\epsilon \sim 32\%$ ). b) New grains in sample GRZ23 ( $T=805^\circ\text{C}$ ,  $P_c=1100$  MPa,  $\dot{\epsilon}=1.1 \cdot 10^{-6} \text{s}^{-1}$  and  $\epsilon \sim 43\%$ ). The host domain is black, because  $\langle c \rangle$  is  $\sim$ constant and perpendicular to the direction of observation. Optical micrographs with crossed polarisers. The arrows in the upper right indicate the starting orientations of the samples.



#### 4.3.4 Samples deformed with 1 vol% water and Mn<sub>2</sub>O<sub>3</sub>-powder

Three samples were deformed together with 1 vol% water and 20 mg Mn<sub>2</sub>O<sub>3</sub>-powder in different orientations (GRZ30,  $\sigma_1 // \langle o+\rangle$ ; GRZ33,  $\sigma_1 // \langle c \rangle$ ; GRZ34,  $\sigma_1 // \langle a \rangle$ ). The Mn<sub>2</sub>O<sub>3</sub>-powder was added to trigger the development of new grains (Fitz Gerald et al. 1991). New grains occur in aggregates at the contact surfaces between the sample and the Mn<sub>2</sub>O<sub>3</sub>-powder. The aggregates are ~500  $\mu\text{m}$  thick and several millimetres in width, and cover almost the complete lower end of the sample. The new grains within the aggregates are optically strain-free and subeuhedral in shape. Grains in samples GRZ30 and GRZ34 have straight grain boundaries and round edges (Figs. 4.10b and c). The rounded corners are facing the compression direction. Grains in sample GRZ33 locally have grain boundaries that are indented parallel to  $\sigma_1$  (Fig. 4.10a). Tiny (~1  $\mu\text{m}$ ) fluid inclusions are located on the grain boundaries and not in the grain interiors. The three dimensional grain (boundary) microstructure (Fig. 4.10d) shows that new grains have an equidimensional shape and abundant voids and cavities at their contact surfaces. Circular depressions on the grain boundaries indicate the presence of fluid inclusions.

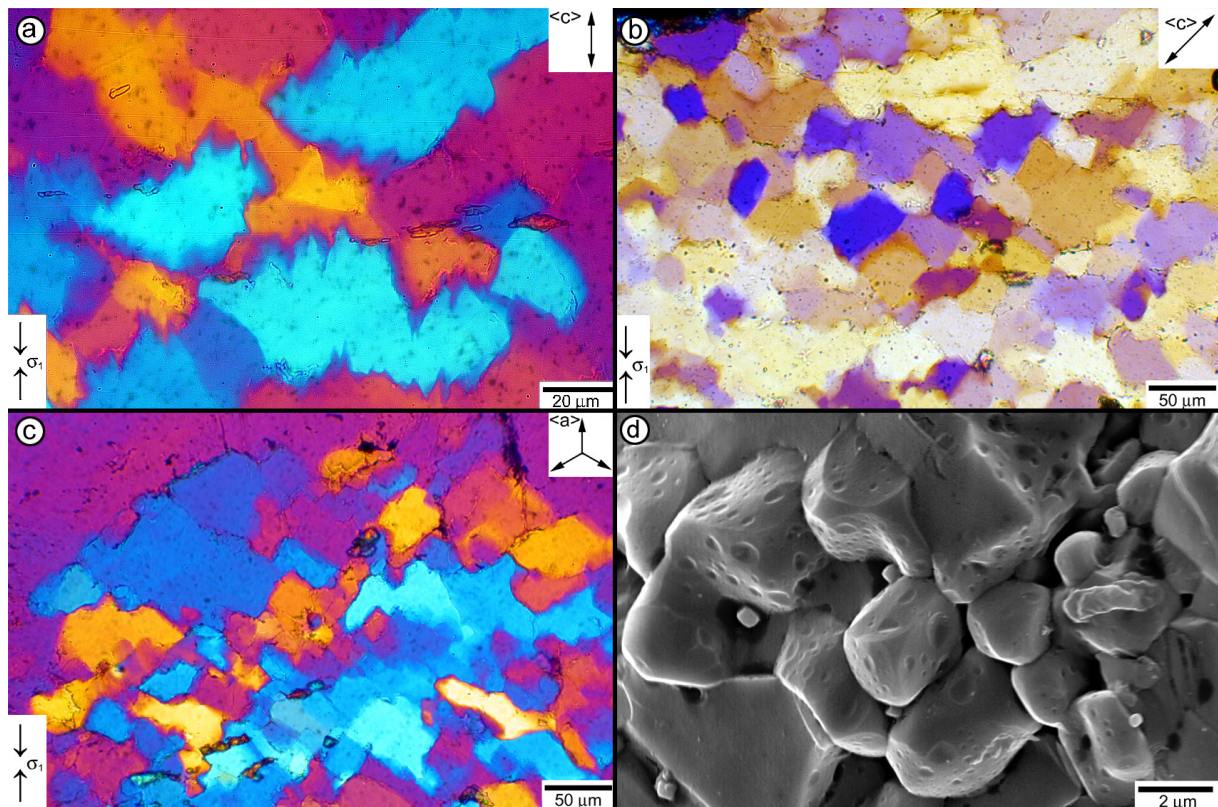


**Figure 4.10 :** New grains in samples deformed with Mn<sub>2</sub>O<sub>3</sub>-powder added to the water (particles that are elongated perpendicular to  $\sigma_1$  at the grain boundaries in pictures a, b and c). a) GRZ33 ( $T=800^\circ\text{C}$ ,  $P_c=1210\text{ MPa}$ ,  $\dot{\epsilon}=1.0\cdot 10^{-6}\text{ s}^{-1}$  and  $\epsilon\sim 26\%$ ), new recrystallised grains have indented grain boundaries. Edges are facing  $\sigma_1$ . b) GRZ30 ( $T=800^\circ\text{C}$ ,  $P_c=1220\text{ MPa}$ ,  $\dot{\epsilon}=1.0\cdot 10^{-6}\text{ s}^{-1}$  and  $\epsilon\sim 29\%$ ). Note the fluid inclusions along the grain boundaries, c) GRZ34 ( $T=800^\circ\text{C}$ ,  $P_c=1210\text{ MPa}$ ,  $\dot{\epsilon}=1.1\cdot 10^{-6}\text{ s}^{-1}$  and  $\epsilon\sim 24\%$ ). Note the transition from host to new grain aggregates in the uppermost part of the picture. d) 3D grain boundary microstructure of sample GRZ30. Secondary electron image of a broken surface. Optical micrographs (a, b, c) are made with crossed polarised light and the gypsum plate. Arrows in the upper right indicate the starting orientations of the samples.

The microstructures in the other parts of the samples are similar to those in the samples deformed with added water and without Mn<sub>2</sub>O<sub>3</sub>-powder: banded undulatory extinction, deformation lamellae, subgrains with irregular shapes and few patches of recrystallised grains

along longitudinal healed fractures. In sample GRZ33 ( $\sigma_1 // \langle c \rangle$ ) intracrystalline shear zones occur as well.

#### 4.3.5 Sample deformed with 3 vol% water

Sample GRZ31 was deformed with three times more water than the other samples, without addition of  $\text{Mn}_2\text{O}_3$ -powder. It also displays an inhomogeneous distribution of deformation microstructures. Most strain is again accommodated at one end of the sample. This end of the sample is characterised by a relatively large amount of subgrains with respect to the samples deformed with 1 vol% water (Fig. 4.11a). Fluid inclusions occur on subgrain boundaries. The upper end of the sample, where fluid inclusions occur strictly on healed cracks is characterised by deformation lamellae. Their spacing is large (up to  $30 \mu\text{m}$ ) and they are slightly curved (Fig. 4.11b). An abrupt change in birefringence can be observed across the deformation lamellae. New grains are scarce and only observed in the domains with subgrains.

#### 4.3.6 Sample deformed at $10^{-7} \text{s}^{-1}$

Sample GRZ32 was deformed ten times slower than the other samples. The strain is homogeneously distributed through this sample. Bands of faint undulatory extinction are observed approximately parallel to  $\langle c \rangle$ . Deformation lamellae are approximately orthogonal to the undulatory bands (Fig. 4.12a). They are straight and their orientation is not influenced by the undulatory bands. An axially oriented zone is observed in this sample. It consists of large axially elongated subgrains separated by healed longitudinal fractures (Fig. 4.12b). A few new recrystallised grains are observed along the fractures.

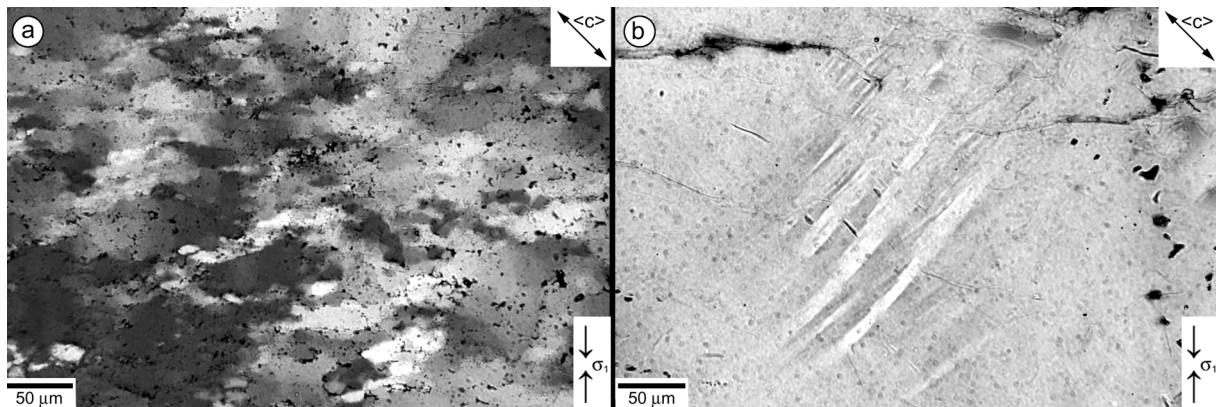


**Figure 4.11:** Subgrains (a) and deformation lamellae (b) in sample (GRZ31) deformed with 3 vol% of water,  $\sigma_1 // \langle o + \rangle$ ,  $T=800^\circ\text{C}$ ,  $P_c=1230 \text{ MPa}$ ,  $\dot{\epsilon}=1.1 \cdot 10^{-6} \text{ s}^{-1}$  and  $\epsilon \sim 30\%$ . Optical micrographs with cross polarised light. Arrows in the upper right indicate the starting orientation of the sample.

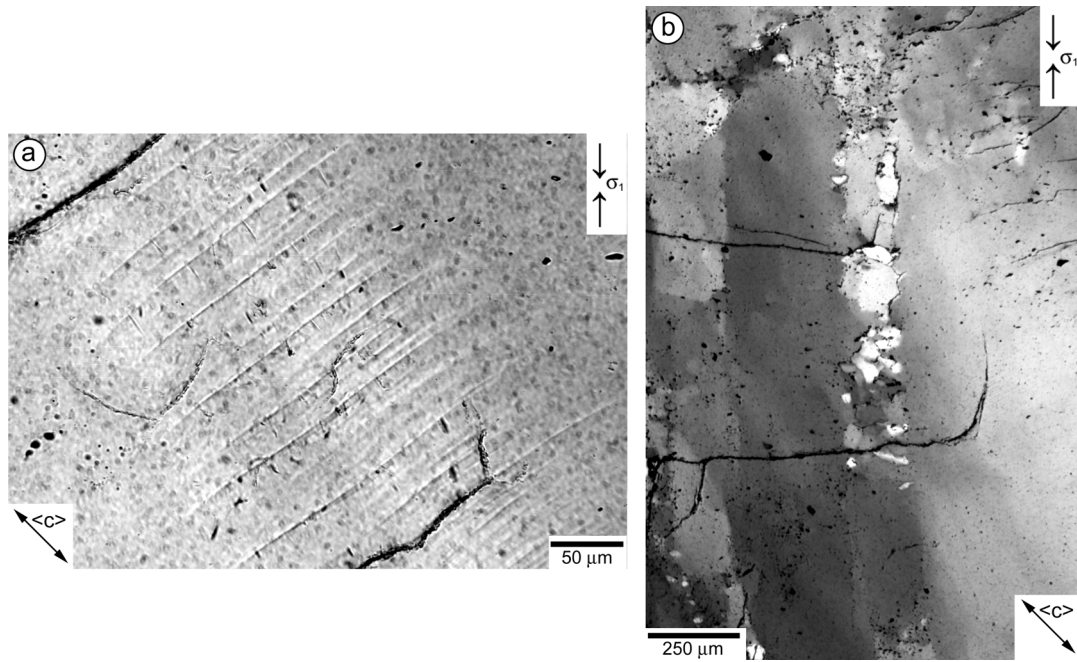


**Figure 4.12 :** Deformation lamellae (a), subgrains and new grains (b) in sample (GRZ32) deformed at a strain rate of  $10^{-7} \text{ s}^{-1}$ , with  $\sigma_1$  parallel to  $\langle o+\rangle$ ,  $T=800^\circ\text{C}$ ,  $P_c=1190 \text{ MPa}$  and  $\varepsilon \sim 12\%$ . Optical micrographs with cross polarised light. Arrows in the lower right indicate the starting orientation.

#### 4.4 SUMMARY

Experimentally deformed single crystals of quartz exhibit a variety of deformation microstructures. They can be broadly subdivided into four groups:

1) *Undulatory extinction and deformation lamellae*. Undulatory extinction was observed in all strained samples. Undulatory extinction occurs in diffuse ‘deformation’ bands that are approximately parallel to  $\langle c \rangle$ . The crystal lattice gradually changed its orientation across these bands. Deformation lamellae were associated with undulatory extinction. They typically occurred in areas deformed to low finite strains (usually  $<30\%$ ). Deformation lamellae were also observed in the sample deformed ‘dry’. This sample was only loaded and did not ‘yield’ during the experiment.

2) *Subgrains*. Subgrains were observed at intermediate to high strains ( $>20\%$ ), especially in densely cracked areas. They had irregular shapes and extensive fluid inclusions on their boundaries. Subgrains were most abundant in the sample deformed with most water (3 vol%).

3) *New recrystallised grains*. New recrystallised grains occurred in healed longitudinal cracks and in contact with the  $\text{Mn}_2\text{O}_3$ -powder at the sample boundary, but not in the domains with undulatory extinction and deformation lamellae. The  $c$ -axes of these new grains were mostly oriented at a high angle to the  $c$ -axis orientation of the surrounding domains. The amounts of new grains in healed cracks were relatively small. Extensive aggregates of new grains were only observed at the lower ends of samples deformed with  $\text{Mn}_2\text{O}_3$ -powder where the sample was in contact with the powder.

4) *Intracrystalline shear zones*. Shear zones were especially abundant in samples deformed parallel  $\langle c \rangle$ . The crystallographic orientation of the quartz within the shear zones was at a high angle (typically  $45^\circ$ ) to the host lattice. Few shear zones occurred in samples deformed parallel  $\langle o+\rangle$ , but only at 50% finite strain.

## CHAPTER 5

### UNDULATORY EXTINCTION, DEFORMATION LAMELLAE AND SUBGRAINS: LATTICE ROTATIONS IN QUARTZ SINGLE CRYSTALS<sup>1</sup>

#### 5.1 INTRODUCTION

The microstructure of all the samples deformed with water is dominated by undulatory extinction, irrespective of the amount of strain. Domains with undulatory extinction are characterised by gradual orientation changes of the crystal lattice. At low strains, domains with undulatory extinction are associated with deformation lamellae. New grains only developed extensively in samples that were deformed with water and Mn<sub>2</sub>O<sub>3</sub>-powder (see chapter 4) and not in samples deformed without the powder.

Undulatory extinction is used as an evidence for crystal-plastic deformation. It is observed in deformed samples if the crystal lattice is slightly bent, because it contains a high number of dislocations ('sweeping' undulatory extinction, Passchier and Trouw 1996). Undulatory extinction is, however, not an indisputable proof for crystal-plastic deformation, because it can also be associated with (microscopically invisible) small fractures and kinks besides dislocation tangles, because of cataclastic failure ('patchy' undulatory extinction, Tullis and Yund 1987, Hirth and Tullis, 1992). Deformation lamellae are also observed in samples that are assumed to deform by crystal-plastic deformation. A vast amount of work has been done on understanding the nature of deformation lamellae (e.g. McLaren et al. 1970, White 1973 and 1975, Christie and Ardell 1974). Still it is not well understood how deformation lamellae develop and how they should be interpreted.

In this chapter, we aim at better understanding the nature of the deformation processes that give rise to undulatory extinction and deformation lamellae in experimentally deformed quartz single crystals. To this end, the microstructures were further analysed by optical microscopy. Cathodoluminescence was used to verify the crystal-plastic origin of the undulatory extinction and deformation lamellae. The intracrystalline defects associated with these microstructures were visualised in the transmission electron microscope (TEM). The misorientation axes of rotations of the crystal lattice in the samples were deduced from electron backscatter diffraction (EBSD) orientation measurements.

#### 5.2 SAMPLES

The present work was performed on 11 samples that were deformed together with 1 vol% of *pure* (i.e. distilled) water and one further sample deformed with 0.02 g Mn<sub>2</sub>O<sub>3</sub>-powder added to the water (Table 5.1 and 5.2). The samples were subjected to the treatments as described in chapter 3.

The mechanical data of the experiments used in this chapter are displayed in differential stress versus bulk finite strain curves (Fig. 5.1). All experiments initially showed work hardening. The strain at which the peak stress was reached varied from 2-12%. The hardening continued until the end of the experiment in sample GRZ16. Gentle weakening was observed immediately after the peak stress in samples GRZ20, GRZ21, GRZ25, GRZ28 and GRZ29. The differential stress increased again after the period of weakening in samples GRZ21,

---

<sup>1</sup> Parts of this chapter are in press in *Meteoritics and Planetary Science: Experimental reproduction of tectonic deformation lamellae and comparison to shock-induced planar deformation features*. By M.G.C. Vernooij and F. Langenhorst.

GRZ25 and GRZ28. In samples GRZ17, GRZ22 and GRZ23 slow hardening occurred after the peak stress.

Sample Number	Starting orientation [ $\sigma_1$ ]	Strain rate [ $s^{-1}$ ]	Finite strain [%]	$P_c$ [MPa]	$UTC$ [ $^{\circ}C$ ]	$LTC$ [ $^{\circ}C$ ]	$t_1$ [h]	$t_2$ [h:m]	$t_3$ [h:m]	$t_4$ [h:m]	Peak stress [MPa]
Samples deformed with 1 vol% pure water											
GRZ16	// <o+>	$0.7 \cdot 10^{-6}$	11	1200	786	800	18	07:54	16:21	01:09	-
GRZ17	// <o+>	$1.1 \cdot 10^{-6}$	21	1190	811	785	68	08:22	15:34	00:58	170
GRZ19	// <a>	$1.1 \cdot 10^{-6}$	0.03	1220	802	783	16	07:26	17:21	00:56	-
GRZ20	// <o+>	$1.0 \cdot 10^{-6}$	28	1120	808	801	46	05:14	19:12	00:58	60
GRZ21	// <o+>	$1.0 \cdot 10^{-6}$	50	1110	805	800	67	07:02	14:50	00:53	90
GRZ22	// <a>	$1.0 \cdot 10^{-6}$	32	1240	799	810	69	06:55	16:21	01:07	90
GRZ23	// <a>	$1.0 \cdot 10^{-6}$	43	1100	803	810	81	07:42	17:30	00:48	120
GRZ25	// <c>	$1.1 \cdot 10^{-6}$	26	1220	799	805	17	07:29	16:50	00:55	410
GRZ27	$\sim \perp \{r\}$	$1.0 \cdot 10^{-6}$	26	1190	800	800	67	08:02	17:15	00:49	175
GRZ28	$\sim \perp \{r\}$	$1.0 \cdot 10^{-6}$	5	1200	802	798	22	08:07	19:57	00:47	340
Sample deformed with 1 vol% of water and 0.02 g $Mn_2O_3$ -powder											
GRZ30	// <o+>	$1.0 \cdot 10^{-6}$	29	1220	794	806	22	07:12	16:00	00:42	150

**Table 5.1:** Experimental details.  $P_c$ , confining pressure;  $UTC$ , temperature of upper thermocouple;  $LTC$ , temperature of lower thermocouple,  $t_1$ , time at 100 MPa,  $t_2$ , elapsed time to reach  $PT$  conditions;  $t_3$ , time at  $PT$  conditions before deformation;  $t_4$ , elapsed time after deformation to reach room  $PT$  conditions.

Overview of samples and microstructures analysed by TEM								
Sample Number	Starting orientation [ $\sigma_1$ ]	Strain [%]	Water content [vol%]	Deformation lamellae	Undulatory extinction	Recrys- tallised grains	Shear zones	Burgers vector
GRZ28	$\sim \perp \{r\}$	5	1	x	x	-	-	$1/3 \langle 11\bar{2}0 \rangle$
GRZ16	// <o+>	11	1	x	x	-	-	$1/3 \langle 11\bar{2}0 \rangle$
GRZ25	// <c>	26	1	x	x	-	x	$1/3 \langle 11\bar{2}0 \rangle$
GRZ22	// <a>	32	1	-	x	-	-	not determined
GRZ30	// <o+>	29	1+20mg $Mn_2O_3$	x	x	x	-	$1/3 \langle 11\bar{2}0 \rangle$

**Table 5.2:** Summary of samples used for TEM analyses and of the analysed microstructures.



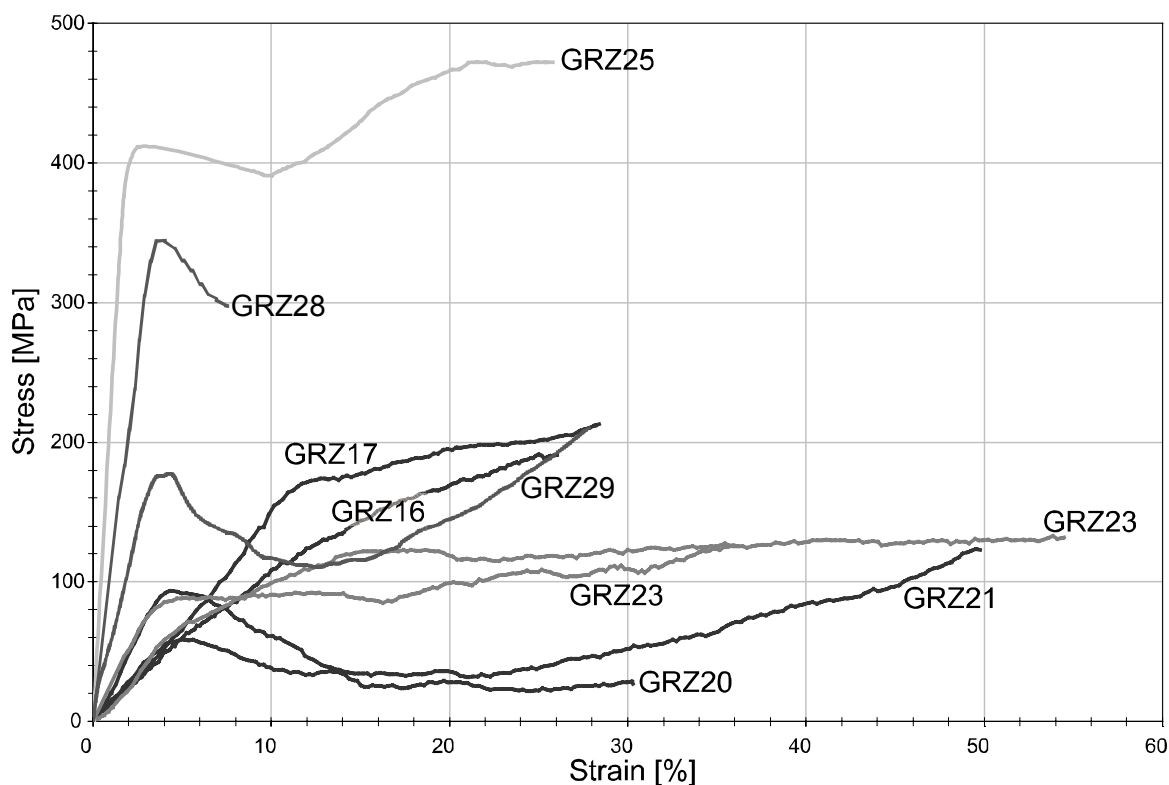


**Figure 5.1:** Mechanical data. Curves from experiments on samples with starting orientation  $\sigma_1 // \langle o+ \rangle$  are black,  $\sigma_1 \sim \perp \{r\}$  are dark grey,  $\sigma_1 // \langle a \rangle$  are middle grey and  $\sigma_1 // \langle c \rangle$  are light grey.

### 5.3 UNDULATORY EXTINCTION

Undulatory extinction is observed in samples that were deformed parallel to  $\langle o+ \rangle$ , parallel to  $\langle c \rangle$  and perpendicular to  $\{r\}$ , to various finite strains. Undulatory extinction was not observed in samples deformed parallel to  $\langle a \rangle$  because the quartz was in extinction. The domains with undulatory extinction are diffuse, i.e. sweeping undulatory extinction (Passchier and Trouw 1998), and elongated, approximately parallel to  $\langle c \rangle$  (Fig. 5.2). The domains are bounded by longitudinal fractures. At finite strains  $<30\%$ , domains with undulatory extinction are associated with deformation lamellae (Fig. 5.3).

In the TEM, the areas with undulatory extinction are associated with a high density of free dislocations ( $10^{10} \text{ cm}^{-2}$ ) (Fig. 5.4). TEM images were taken with diffraction vectors  $g=10\bar{1}1$ ,  $g=10\bar{1}0$  and  $g=0003$  in order to determine the Burgers vectors by applying the  $g \cdot b=0$  criterion. Most dislocations are out of contrast with  $g=0003$  and are well visible with  $g=10\bar{1}1$ . Therefore the most likely Burgers vector of the free dislocations is  $b=1/3\langle 11\bar{2}0 \rangle$ .

### 5.4 SUBGRAINS

Subgrains are found in the direct vicinity of longitudinal fractures (Fig. 5.5a). Their birefringence colour is only slightly different from that of the surroundings, indicating only a slight difference in crystallographic orientation. The interiors of subgrains display undulatory extinction. They have angular outlines and highly variable sizes (from  $\sim 10 \mu\text{m}$  up to  $\sim 250 \mu\text{m}$ ). Their boundaries are decorated with fluid inclusions (Fig. 5.5b). Domains with

subgrains crosscut domains with undulatory extinction. A few new grains, smaller in size than the subgrains, are observed within the longitudinal fractures. Their c-axes are mostly at a high angle to those in the surrounding domains (see chapter 6).

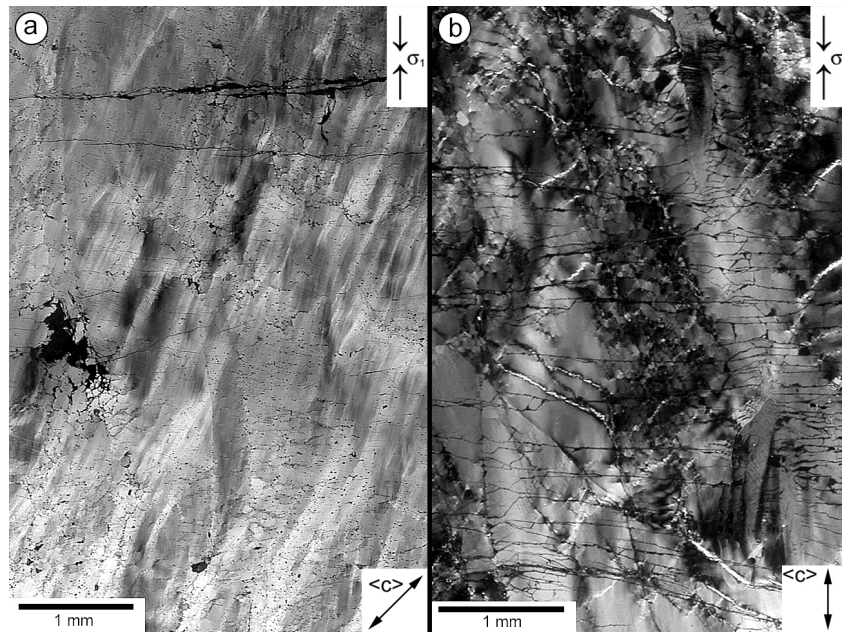


**Figure 5.2:** Domains with undulatory extinction a) in sample (GRZ30) deformed parallel to  $\langle c \rangle$  and b) in sample (GRZ25) deformed parallel to  $\langle c \rangle$ . In sample GRZ30 (a), deformation lamellae can be observed orthogonal to the domains with undulatory extinction, especially in the upper half of the figure. In sample GRZ25 (b), intracrystalline microshear zones crosscut the domains with undulatory extinction. Horizontal fractures are caused by unloading. Arrows in the lower right indicate the starting orientations of the samples. Optical micrographs with crossed polars.

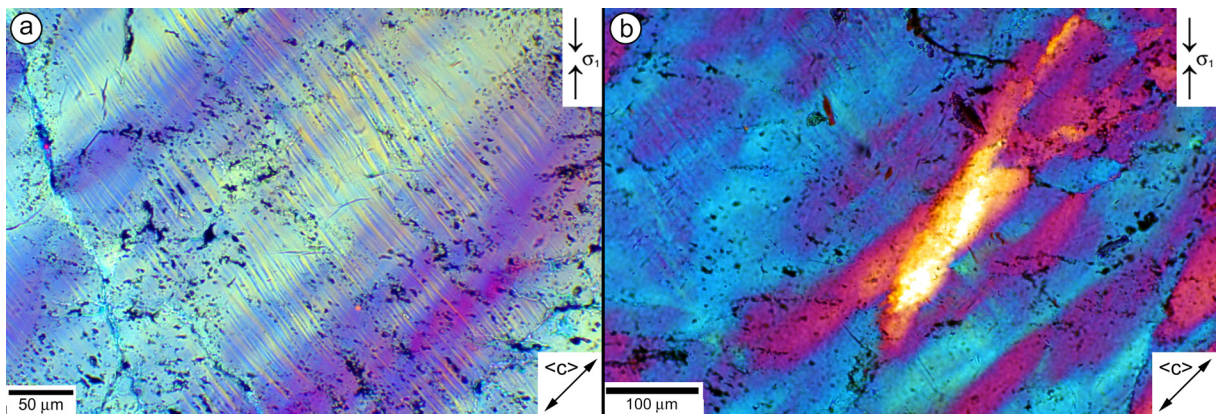


**Figure 5.3:** Domains with undulatory extinction and deformation lamellae a) in sample (GRZ28) deformed perpendicular to  $\{r\}$  to 5% finite strain and b) in sample (GRZ17) deformed parallel to  $\langle o \rangle$  to 21% finite strain. Arrows in the lower right indicate the starting orientations of the samples. Optical micrographs with gypsum plate.

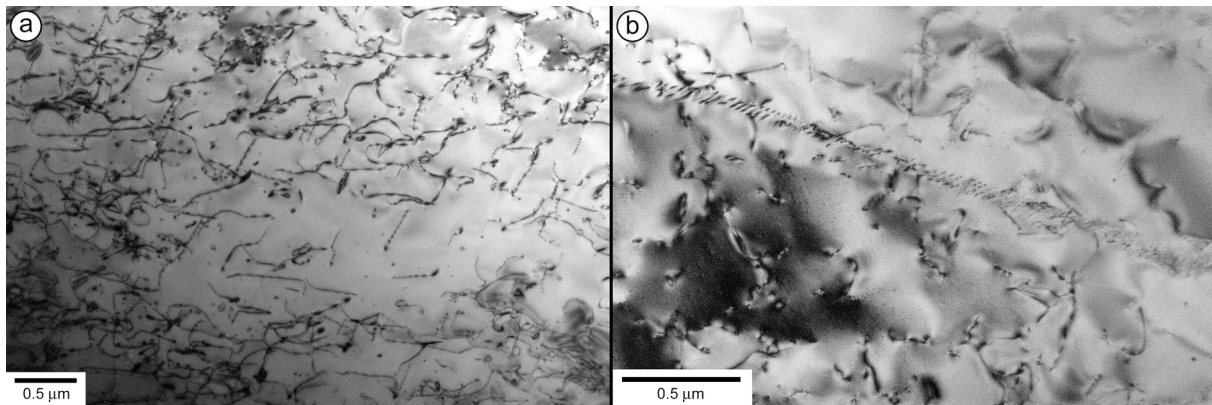


**Figure 5.4:** Free dislocations in a domain with continuous undulatory extinction (a) and subgrain walls (b) in a domain with deformation lamellae in sample (GRZ28) deformed about perpendicular to  $\{r\}$ . The density of free dislocations is  $10^{10} \text{ cm}^{-2}$ . Free dislocations are both straight and curved, dislocations in subgrain walls are straight. TEM bright field images.

## 5.5 DEFORMATION LAMELLAE

Deformation lamellae are slightly wavy planar features that sometimes branch into two lamellae (Fig. 5.6a). The boundaries of the lamellae are indicated by a sharp transition in birefringence, indicating a sharp transition in crystallographic orientation by only a few degrees. The deformation lamellae also have a different refractive index as the host crystal. Some deformation lamellae are of the Böhm type (Fig. 5.6c) as they are decorated with fluid inclusions (Christy and Raleigh 1959).

Deformation lamellae are directly associated with the domains of undulatory extinction (Fig. 5.3). But whereas domains with undulatory extinction can be observed in all the deformed samples, irrespective of the amount of finite strain, deformation lamellae only occur at strains  $<30\%$  (Table 5.3). Deformation lamellae are most pronounced and most abundant in sample GRZ28 deformed to the lowest finite strain (5%). In this sample, deformation lamellae are homogeneously distributed (Fig. 5.3a). In samples deformed to intermediate finite strain ( $\sim 5\text{--}30\%$ ), deformation lamellae are less pronounced and observed in patches (Fig. 5.3b). Deformation lamellae are not observed in samples deformed to finite strains larger than 30%. In the samples deformed parallel to  $\langle o \rangle$  and perpendicular to  $\{r\}$ , deformation lamellae are approximately parallel to the basal plane and perpendicular to the elongated bands of undulatory extinction (Fig. 5.3 and Table 5.3). In the sample deformed parallel to  $\langle c \rangle$ , deformation lamellae are either sub parallel to the basal plane (Fig. 5.6a and c) or at  $\sim 35^\circ$   $\langle c \rangle$ , probably sub parallel to the rhombohedral planes (Fig. 5.6b). The orientations of deformation lamellae with respect to the crystal lattice in deformed single crystals are very constant, like in one single grain of a deformed polycrystal. Therefore the orientation of the lamellae could not be measured in a statistically significant manner. Deformation lamellae in experimentally deformed polycrystals are generally sub basal, making on average an angle of  $12^\circ$  with the basal plane (den Brok 1992). Looking perpendicular to  $\sigma_1$ , they are generally steeper than the basal plane. Deformation lamellae are curved at the rims of the elongated bands of undulatory extinction (Fig. 5.6c).

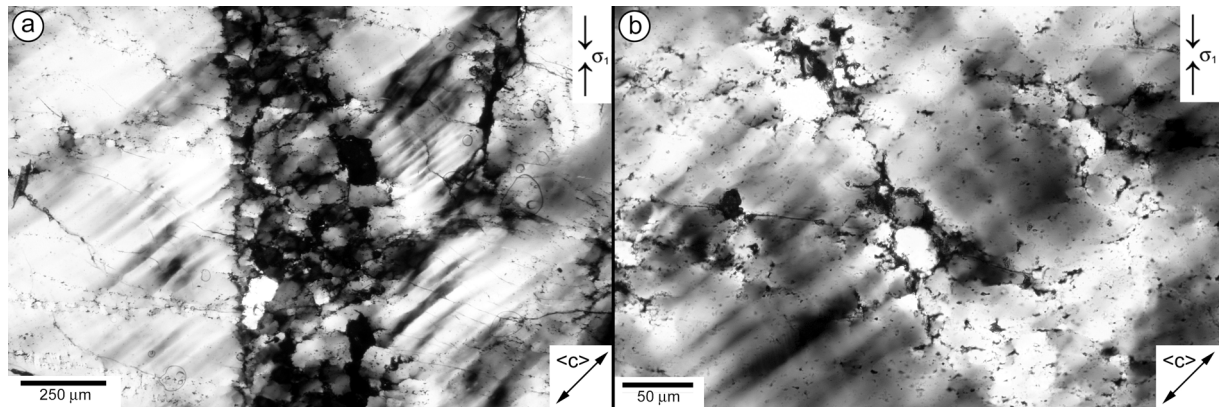


**Figure 5.5:** Domains with undulatory extinction and subgrains in sample (GRZ20) deformed parallel to  $\langle o \rangle$ . a) Subgrains within a longitudinal domain, bounded by healed longitudinal fractures. Domain with subgrains crosscuts the domains with undulatory extinction. b) Subgrains are decorated with fluid inclusions. Optical micrographs with crossed polars. Arrows in the lower right indicate the starting orientation of the sample.

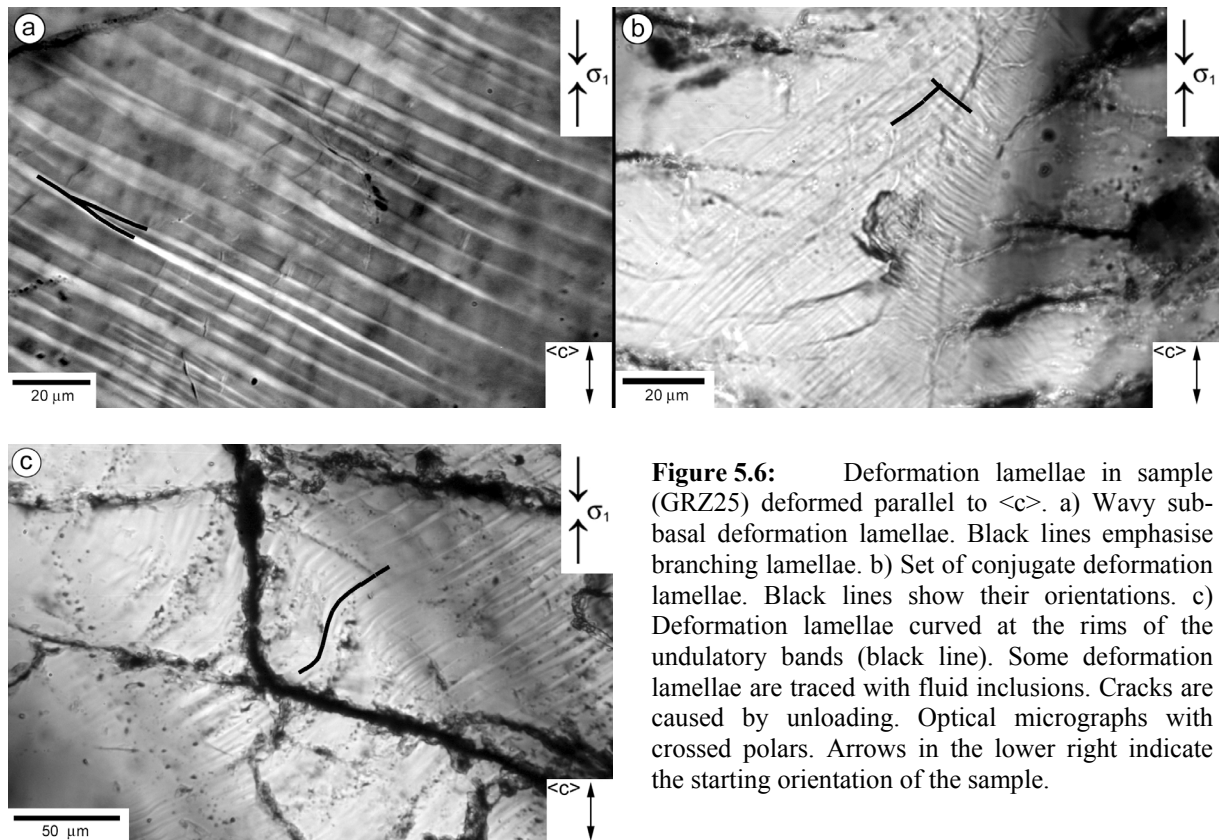


**Figure 5.6:** Deformation lamellae in sample (GRZ25) deformed parallel to  $\langle c \rangle$ . a) Wavy sub-basal deformation lamellae. Black lines emphasize branching lamellae. b) Set of conjugate deformation lamellae. Black lines show their orientations. c) Deformation lamellae curved at the rims of the undulatory bands (black line). Some deformation lamellae are traced with fluid inclusions. Cracks are caused by unloading. Optical micrographs with crossed polars. Arrows in the lower right indicate the starting orientation of the sample.

In the TEM, areas with deformation lamellae are associated with a similar high density of free dislocations as the domains with undulatory extinction ( $10^{10} \text{ cm}^{-2}$ ). Most dislocations are curved, entangled and sometimes connected to tiny water bubbles. Subgrain walls crosscut the domains with free dislocations (Fig. 5.4b). These subgrain walls are parallel to the deformation lamellae and define their boundaries (i.e. deformation lamellae are the areas between the subgrain walls). The subgrain walls themselves are only rarely decorated with fluid inclusions. In the domains with deformation lamellae large numbers of sub parallel



arranged subgrain walls occur (Fig. 5.7). At the TEM scale it is obvious that a unique crystallographic orientation of the subgrain walls cannot be identified because they are curved and do not define a low index crystallographic plane. Contrast changes across (Fig. 5.8a and b) and fringes at (Fig. 5.8b) subgrain walls indicate that the crystal is alternately tilted along the subgrain walls with a misorientation of about  $1-3^\circ$ . It is this alternating orientation that makes the deformation lamellae visible under the optical microscope. In principle, lamellae can thus be regarded as very elongated subgrains. Occasionally, tinier subgrains are observed between the aligned subgrain walls (Fig. 5.7).

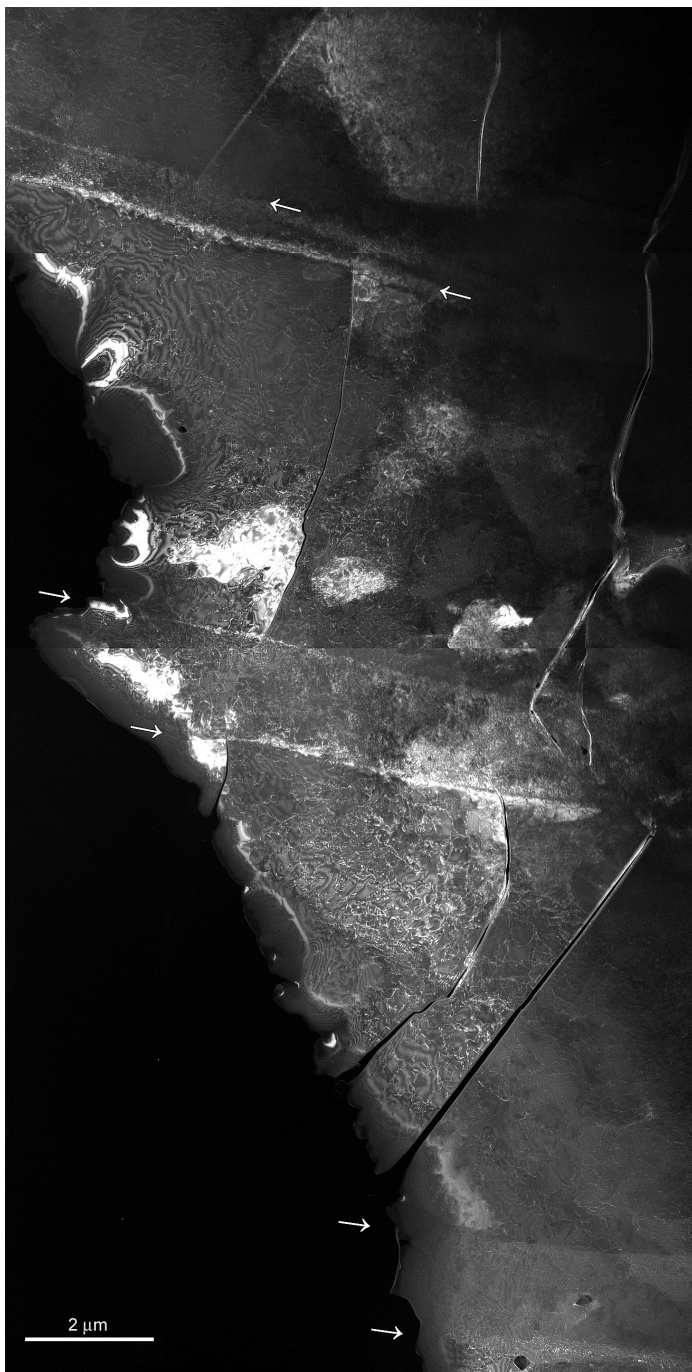


**Figure 5.7:** Aligned subgrain walls (white arrows) in sample (GRZ25) deformed parallel to  $\langle c \rangle$ . Deformation lamellae are the areas between the subgrain walls. Subgrain walls are not perfectly straight and parallel. TEM dark field weak beam image,  $g=10\bar{1}0$ . Black field in the lower left is empty. Cracks are caused by unloading of the sample after the deformation experiment or during preparation.

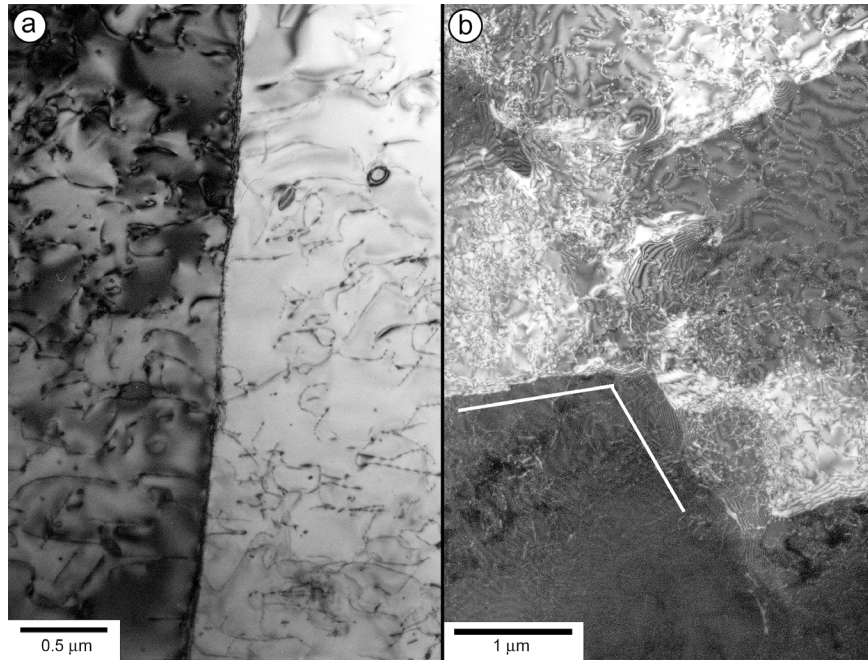


**Figure 5.8:** Orientation contrast along subgrain walls because of a change in crystallographic orientation of the crystal lattice. a) Sample (GRZ28) deformed perpendicular to  $\{r\}$ . TEM bright field image. b) Sample (GRZ25) deformed parallel to  $\langle c \rangle$  illustrates alternating misorientations along the subgrain walls. White lines indicate the orientations of the (sub)rhombohedral lamellae. This picture comes from the same area as Figure 5.5b (marker lines show identical directions). TEM dark field image,  $g=10\bar{1}0$ .

Sample number	Water [vol%]	Starting orientation [ $\sigma_1$ ]	Finite strain [%]	Deformation lamellae [orientation]	Appearance
GRZ16	1	// $\langle o+ \rangle$	11	~ basal	Isolated patches
GRZ17	1	// $\langle o+ \rangle$	21	~ basal	Isolated patches
GRZ19	0	// $\langle a \rangle$	0.003	~ prismatic	At the sample rims
GRZ20	1	// $\langle o+ \rangle$	28	-	-
GRZ21	1	// $\langle o+ \rangle$	50	-	-
GRZ22	1	// $\langle a \rangle$	32	-	-
GRZ25	1	// $\langle c \rangle$	26	~ rhombic ~ basal	Isolated patches
GRZ28	1	~ $\perp \{r\}$	3	~ basal	Continuous

**Table 5.3:** Summary of microstructural observations on deformation lamellae. Note that no deformation lamellae are observed at strains  $>30\%$ .

## 5.6 CATHODOLUMINESCENCE

Cathodoluminescence (CL) is a powerful tool to reveal growth zones and healed cracks which are not optically visible in quartz (Marshall 1988). The host domains of the deformed quartz single crystals emit a medium CL-signal intensity (Fig. 5.9). The longitudinal healed fractures (as in Fig. 5.5a) have a darker CL-signal. Therefore they are clearly visible in the CL-images.

The boundaries of the subgrains within the subgrain networks that are directly connected to these healed fractures have the same dark appearance. The interior of the subgrains emits a medium CL-signal, as the host crystal. The subgrain network extends about 200  $\mu\text{m}$  perpendicular to the healed crack into one side of the crystal. Deformation lamellae are observed in the host domains between the longitudinal fractures but not in the networks with subgrains. Deformation lamellae give a brighter CL-signal as the healed fractures and the subgrain boundaries (Fig. 5.10). The bands of undulatory extinction that occur perpendicular to the deformation lamellae also give a brighter CL-signal. The CL-signals are comparable for samples that are deformed with pure water and for samples that are deformed with  $\text{Mn}_2\text{O}_3$ -powder added to the water.

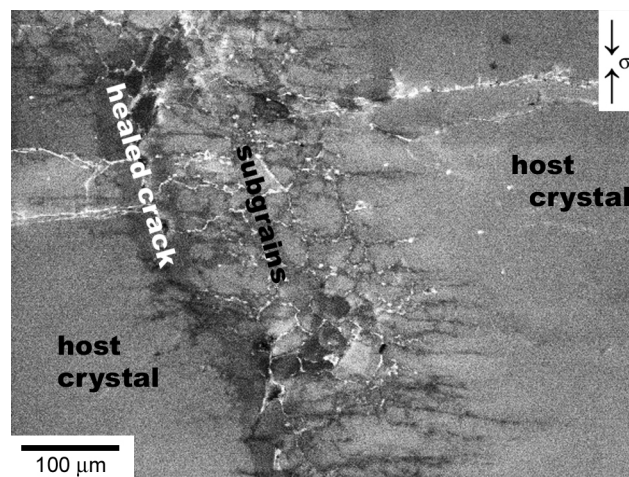


**Figure 5.9:** CL-image of a longitudinal fracture with subgrain network in sample (GRZ21) deformed parallel to  $\langle o+\rangle$ . The area in the picture is similar to the longitudinal domain with subgrains in Fig. 5.5a. The host sample has a medium CL-signal, the healed crack and the subgrain boundaries have a darker CL-signal. Some edges of fresh cracks are bright due to charging artefacts. Acceleration voltage 15 kV.

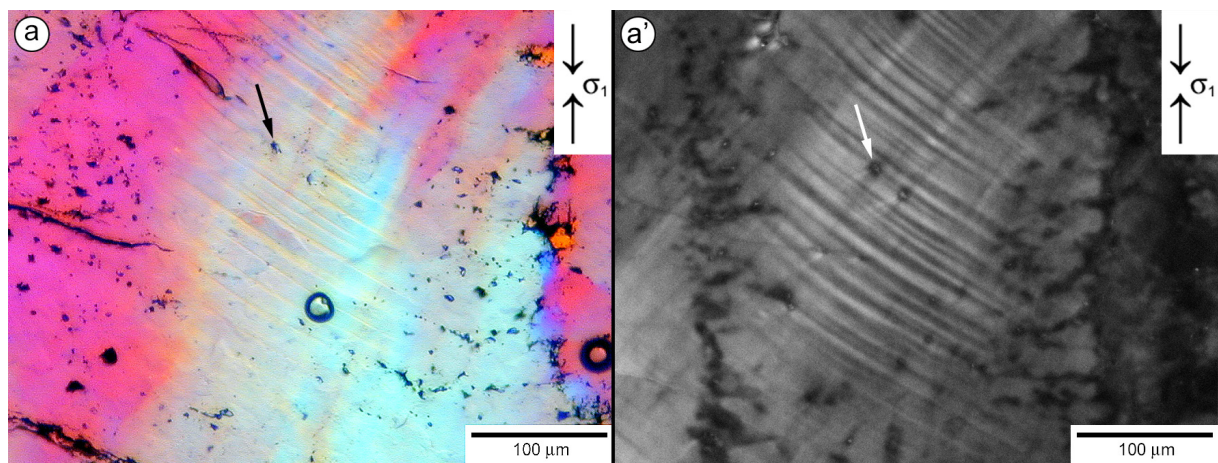


**Figure 5.10:** Optical micrograph (a) of deformation lamellae, undulatory extinction and healed fractures and corresponding CL-image (a') in sample (GRZ30) deformed parallel to  $\langle o+\rangle$  with  $\text{Mn}_2\text{O}_3$ -powder added to the water. Deformation lamellae and undulatory extinction emit a bright CL-signal, the host sample emits a medium CL-signal and the healed fractures emit a darker CL-signal. The arrows indicate the same marker in the two images. Acceleration voltage of CL-image 20kV.

## 5.7 LATTICE ROTATION

Deformation lamellae are low strain features. They are most abundant at low finite strains and vanish with increasing finite strain. They are absent in samples deformed to finite strains larger than 30%. Elongated bands of undulatory extinction are observed in all the deformed samples, irrespective of the amount of strain. They are indicative for the bulk deformation behaviour of the sample. It was illustrated above that the orientation changes in the domains with undulatory extinction are the result of crystal lattice rotations. To measure these crystal lattice rotations, data points were selected from orientation maps along profiles that are perpendicular to the elongated domains of undulatory extinction.

Data from profiles in four different samples were plotted in pole figures (Fig. 5.12). The data points in the pole figures are dispersed away from the starting orientation along well defined trajectories, displacing the  $c$ -axes either towards or away from  $\sigma_1$ . These dispersion patterns correspond to rotations of the crystal lattice about a common axis. Best fits of these rotations (Fig. 5.12) and the corresponding rotation axes (Figs. 5.11 and 5.12b) were calculated. In all samples, the crystal lattice rotates around an axis that is nearly perpendicular to  $\sigma_1$  (Fig. 5.11). The crystallographic orientation of this rotation axis is different for each sample (Fig. 5.11). In sample GRZ23, the rotation axis coincides with  $\langle c \rangle$  and in GRZ25, the rotation axis coincides with  $\{m\}$ . The rotation axes of sample GRZ20 and sample GRZ28 do not correspond to a specified low-index crystallographic orientation. The data points of these samples are also more scattered around the inferred rotation path, i.e. the axis is not as well defined as in a unique rotation as in GRZ23 and GRZ25.

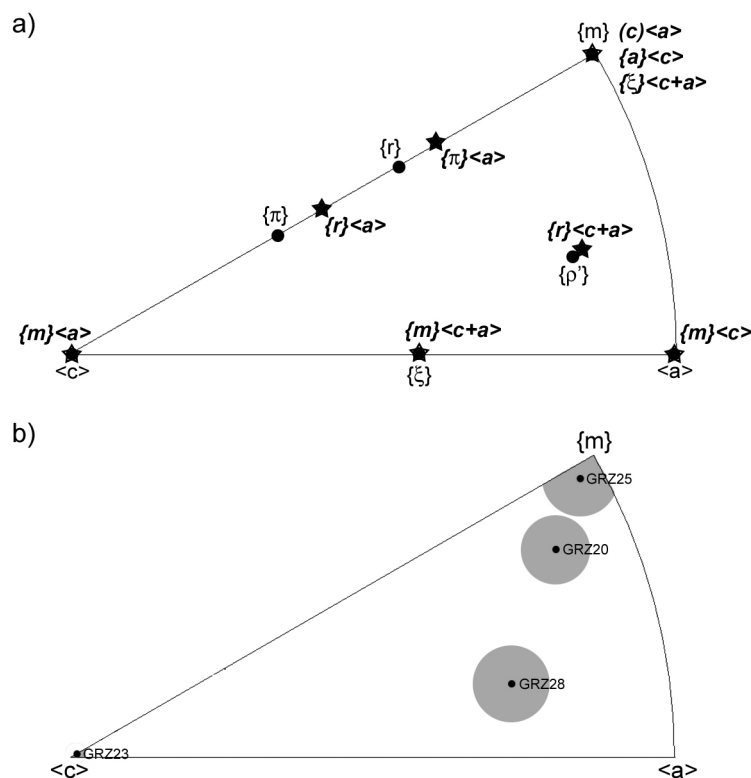
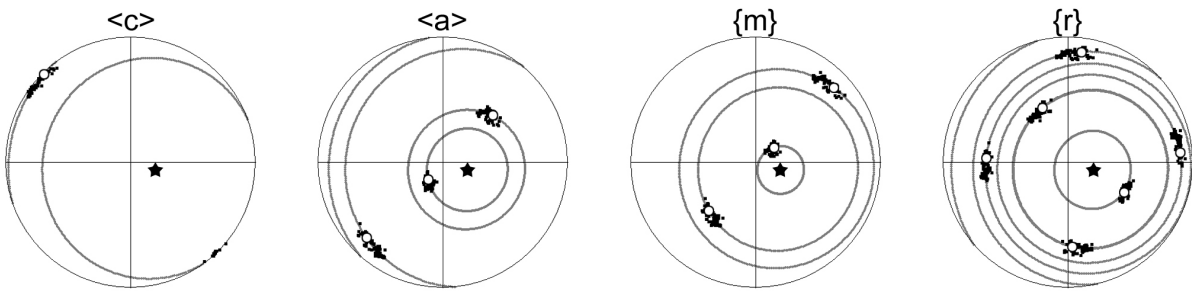


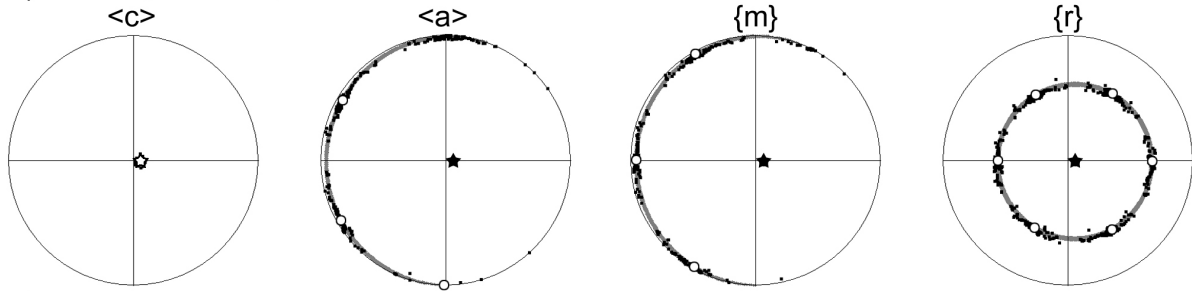
**Figure 5.11:** a) Crystal directions and crystal planes (black circles, normal characters) and the theoretical rotation axes, in terms of edge dislocations, for common and less common slip systems in quartz (black stars, italic bold characters), modified after Neumann (2000) assuming hexagonal crystal symmetry. b) Rotation axes of the data in Figure 5.12. Grey circular areas indicate the error on the rotation axes.



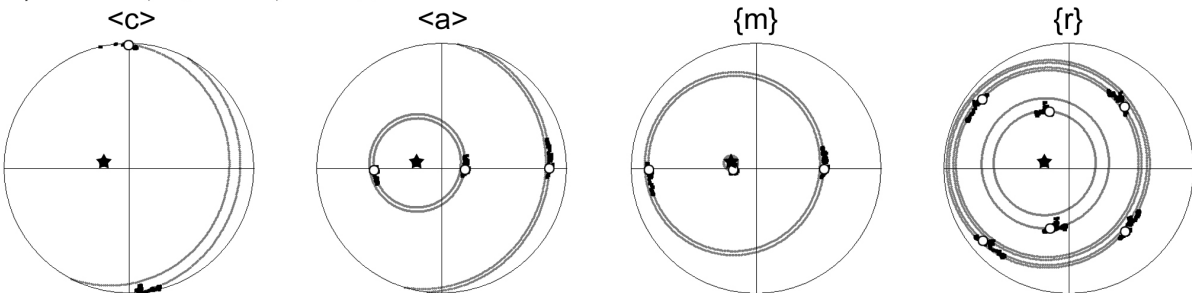
a) GRZ20,  $\sigma_1 // \langle o+ \rangle$ ,  $\epsilon=30\%$



b) GRZ23,  $\sigma_1 // \langle a \rangle$ ,  $\epsilon=44\%$



c) GRZ25,  $\sigma_1 // \langle c \rangle$ ,  $\epsilon=26\%$



d) GRZ28,  $\sigma_1 // \langle r \rangle$ ,  $\epsilon=3\%$

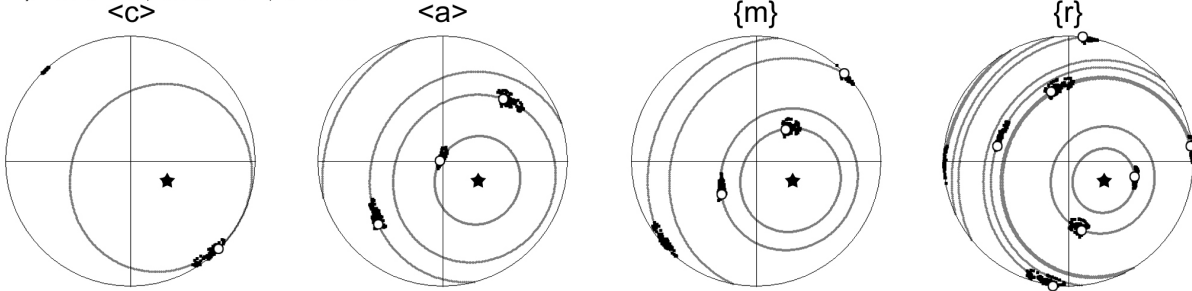


**Figure 5.12:** Pole figures (equal area, upper hemisphere) of crystal lattice rotations in domains with undulatory extinction. The data have been selected along profiles that crosscut the elongated bands of undulatory extinction at a right angle. Grey circles are best fits of the rotation of the data; black stars are the inferred rotation axes; open circles represent the starting orientation of the sample.

## 5.8 DISCUSSION

### 5.8.1 Deformation lamellae

The experimentally reproduced deformation lamellae in single-crystal quartz show great similarity to natural deformation lamellae formed in tectonically deformed quartz (e.g., McLaren and Hobbs 1972). The TEM observations reveal that the optically visible, experimental deformation lamellae represent elongated subgrains, which is in agreement with the microstructural characteristics of deformation lamellae in naturally deformed quartz

(McLaren and Hobbs 1972; White 1973; Blenkinsop and Drury 1988). The formation of the subgrains is due to the recovery of dislocations into gently curved subparallel subgrain walls, resulting in a banded substructure that causes an alternating change in optical birefringence. Overall, the presence of subgrain walls and numerous curved free dislocations indicates that both glide-controlled and climb-controlled processes have been active during the deformation of samples. This coexistence of creep and recovery and the formation of deformation lamellae point to deformation in the so-called exponential creep regime, where the deformation behaviour does not follow any more a power law of creep (McLaren 1991; Drury 1993).

To understand the development of the defect microstructure and, in particular, the formation of deformation lamellae in more detail, it is useful to discuss our observations in the context of previous extensive deformation experiments on quartz (see summaries of McLaren 1991; Doukhan 1995). These experiments have shown that dry quartz is practically undeformable and fails by fracturing, while small amounts of dissolved water lead to a drastic softening of quartz. Thereby, the actual concentration and dispersion of water in the quartz structure plays an important role in the evolution of the deformation microstructure (Doukhan 1995). Quartz supersaturated in water ( $> 180$  ppm) precipitates numerous water bubbles, which subsequently grow with time and are the sources for homogeneous, pervasive emission and climb of dislocations. If quartz is however undersaturated in water, precipitation does not occur. Dislocation nucleation is heterogeneous along slip bands and climb of dislocations is strongly suppressed.

Deformation lamellae have only been found in our quartz crystals that were deformed to low strains (Table 5.3), suggesting that they form in an early stage of deformation when dislocations are heterogeneously emitted in slip bands and the quartz crystals are still undersaturated in water. The presence of homogeneously distributed free dislocations within subgrains and their configuration in form of junctions point however to a change in the deformation mechanism. As the deformation experiments proceeded more and more of the available water was probably incorporated into the quartz crystals and water precipitated as bubbles, from which dislocations were then homogeneously and pervasively emitted. In samples deformed to large strains, the recovery was very efficient and defect microstructures are therefore strongly evolved such that initially formed deformation lamellae can completely vanish.

This model of formation of deformation lamellae by initial dislocation glide in bands and dynamical recovery allows to also understand the subbasal orientations and broad angular variation of lamella orientations. Deformation lamellae are most abundant in quartz crystals deformed with the  $c$  axis at  $45^\circ$  to the compression axis (GRZ16, GRZ28) because in this orientation it is easiest to activate the energetically favourable  $1/3\langle 11\bar{2}0 \rangle$  dislocations in the (0001) plane. While dislocation glide drives these dislocations along the (0001) plane, the synkinematical or subsequent climb of dislocations results in a movement out of the (0001) slip plane and an arrangement of dislocations into subgrain walls that are rotated away from the basal plane. The degree of rotation is thereby controlled by the relative speeds of glide and climb. This explanation for the subbasal orientation of lamellae is supported by the observation that subgrain walls usually consist of well organised straight dislocations. Networks of dislocations are not observed because only a single set of  $a$  dislocations has been emitted in the basal plane. A similar model for the formation of deformation lamellae has been presented by Drury (1993), explaining the formation of subgrain walls containing a network of dislocations in two slip planes.

### 5.8.2 Undulatory extinction

Sweeping undulatory extinction is optically observed in the samples that are deformed with  $\sigma_1$  parallel to  $\langle c \rangle$  and at  $45^\circ$  to  $\langle c \rangle$ . It is associated with gradual reorientation of the crystal lattice. Similar reorientations of the crystal lattice are also measured in the samples that are deformed with  $\sigma_1$  parallel to  $\langle a \rangle$  (Fig. 5.12b), which are optically invisible because of a nearly constant  $c$ -axis which is in extinction. Reorientation of the crystal lattice occurs by gradual rotation. The amount of rotation increases in angle with increasing strain. The bulk deformation of the samples deformed with *pure* water is carried by these crystal lattice rotations. Undulatory extinction is observed at all strains whereas deformation lamellae only occur at low to intermediate strains. Undulatory extinction causes bending of the deformation lamellae. This implies that undulatory extinction develops further in the deformation history than deformation lamellae.

Sweeping (or continuous) undulatory extinction is caused by bending of the crystal lattice in areas with a high dislocation density (e.g. Poirier 1985, Passchier and Trouw 1995). It is especially observed within single grains of experimentally deformed quartz polycrystals (e.g. den Brok 1991, Hirth and Tullis 1992) and within naturally deformed vein quartz (Mancktelow 1987, Stipp et al. 2002). Continuous undulatory extinction is rare in nature. Even when the extinction appeared to be optically continuous, TEM-studies have shown that in most cases the extinction changes in a discontinuous way, because the old grain is subdivided in a number of subgrains (White 1971, McLaren and Hobbs 1972).

At low strains TEM analysis indicates that elongated subgrain *walls* are exclusively related to deformation lamellae and that the areas with undulatory extinction are characterised by a large number of *free* dislocations. Undulatory extinction is thus really continuous and is thus assumed to have a crystal-plastic origin. The development of undulatory extinction most probably starts immediately after loading the sample. With increasing strain subgrain *boundaries* can be observed in the samples. These are related to subgrains and healed fractures. Subgrain *boundaries* can be easily distinguished from subgrain *walls* (Fig. 5.7, white arrows) because they are curved and clearly define subgrains (Fig. 5.7 middle, between the subgrain walls) whereas subgrain *walls* just crosscut the host domains without forming subgrains.

In the domains with undulatory extinction, the crystal lattice always rotates around rotation axes perpendicular to  $\sigma_1$ , regardless of the starting orientation of the sample. Some of the rotation axes coincide with the rotation axes of known slip systems: prism $\langle a \rangle$  for samples with starting orientation  $\sigma_1 // \langle a \rangle$ , and basal $\langle a \rangle$  for samples with starting orientation  $\sigma_1 // \langle c \rangle$ . The basal $\langle a \rangle$  slip system, however, is not expected to be activated in samples deformed with  $\sigma_1 // \langle c \rangle$  (Schmid factor 0.000, Table 5.4). Rotation axis  $\{m\}$  and dominant Burgers vector  $1/3\langle 11\bar{2}0 \rangle$  of the dislocations, though, are clear indications for this slip system (Table 5.5). Samples that are deformed with  $\sigma_1 // \langle o+\rangle$  are most easy to deform (peak stress 60-170 MPa), because they are ideally oriented for slip on the basal plane (Table 5.4). The critical resolved shear stress (CRSS) on the basal plane can be inferred from these experiments;  $\sim 30$ -80 MPa. The peak stress of sample GRZ25 ( $\sigma_1 // \langle c \rangle$ ) is 405 MPa. If the basal plane makes a  $\sim 4$ - $11^\circ$  angle with  $\sigma_1$ , this peak stress is high enough to result in a resolved shear stress able to activate the basal $\langle a \rangle$  slip system. To bring the basal plane in this position, a rigid body rotation of parts of the sample must have taken place, maybe along intracrystalline shear zones (see Fig. 5.2b). Indisputable proof for rhomb $\langle a+c \rangle$  slip systems does not exist, rhomb slip planes combined with  $\langle a+c \rangle$  Burgers vectors have never been observed in the TEM. The existence of rhomb $\langle a+c \rangle$  glide is only theoretically proven by geometrical and energy arguments (Baëta and Ashbee 1969 a and b). The rotation axes of the samples with starting orientation  $\sigma_1 // \langle o+\rangle$  and  $\sigma_1 \sim \perp \{r\}$  are inconsistent with known slip systems and the data

points of these samples are also more scattered around the inferred rotation path than the data of the other two starting orientations. In these samples two (basal<a> and prism <c> for  $\sigma_1 // \langle o+\rangle$ ) or even three (prism<c>, rhomb<a> and basal<a> for  $\sigma_1 \perp \{r\}$ ) common slip systems have a high Schmid factor ( $>0.4$ , Table 5.4). The reason why there is no direct coincidence of the rotation axis with a known slip system could be because of multiple slip system activation. The relative CRSS of basal and prism slip systems at the temperature of the experiments (800°C) is expected to be more or less the same (Blacic 1975).

Slip system	Schmid factor for starting sample orientation with:			
	$\sigma_1 // \langle c \rangle$	$\sigma_1 // \langle o+\rangle$	$\sigma_1 // \langle a \rangle$	$\sigma_1 \perp \{r\}$
Basal {c}<a>	0.000	<b>0.500</b>	0.000	<b>0.433</b>
	0.000	0.250	0.000	<b>0.433</b>
	0.000	0.250	0.000	0.000
Prism {m}<a>	0.000	0.217	<b>0.433</b>	0.217
	0.000	0.217	<b>0.433</b>	0.217
	0.000	0.000	0.000	0.000
Prism {m}<c>	0.000	<b>0.433</b>	0.000	<b>0.500</b>
	0.000	<b>0.433</b>	0.000	0.250
	0.000	0.000	0.000	0.250
Rhomb {r}<a>	0.000	0.325	0.340	<b>0.438</b>
	0.000	0.309	0.340	0.098
	0.000	0.015	0.000	0.000
Rhomb {r}<a+c>	0.458	0.333	0.458	0.374
	0.458	0.262	0.458	0.149
	0.458	0.125	0.229	0.111
	0.458	0.044	0.229	0.111
	0.458	0.044	0.000	0.084
	0.458	0.033	0.000	0.080

**Table 5.4:** This table lists the Schmid factors of the most important known slip systems in quartz for the four different starting orientations of the samples. Schmid factors of common slip systems which are higher than 0.4 are bold.

Starting orientation [ $\sigma_1$ ]	Burgers vector	Slip systems from rotation axes studies of domains with undulatory extinction					
		Best fit with theoretical rotation axis?	Basal<a>	Prism<a>	Prism<c>	Rhomb<a>	Rhomb<a+c>
// <o+>	<a>	no	x	-	x	-	-
// <a>	unknown	yes	-	x	-	-	-
// <c>	<a>	yes	x	-	-	-	-
$\sim \perp \{r\}$	<a>	no	x	-	x	x	-

**Table 5.5:** Comparison of slip system data inferred from the rotation axes studies and Burgers vectors inferred from TEM analyses. The rotation axes of samples deformed parallel to <o+> and about perpendicular to {r} do not fit with theoretical rotation axes and are therefore interpreted to be formed by multiple activation of different slip systems with Schmid factor  $>0.4$  for the corresponding starting orientations (Table 5.3).

### 5.8.3 Subgrains

Subgrains are defined by distinct boundaries separating differently oriented domains up to misorientation angles of  $10^\circ$ . Subgrains (that are not related to deformation lamellae) have a high density of fluid inclusions on their grain boundaries. They crosscut the domains with undulatory extinction and subgrain interiors sometimes contain undulatory extinction. These kinds of subgrains occur exclusively in the vicinity of longitudinal fractures which developed in the samples before deformation, during the pressurising and heating phase.

The presence of subgrains is commonly attributed to dislocation creep (e.g. Twiss and Moores 1992). Their presence can, however, also be explained by cataclastic deformation (e.g. Sander 1930, Nyman et al. 1992). Subgrains are in that case slightly rotated and healed fracture fragments. These kinds of subgrains have been described in experimentally deformed quartzites (den Brok 1992) and in naturally deformed quartz fibres (van Daalen et al. 1999). Their in-situ development is described in experimentally deformed soluble brittle salt ( $\text{NaClO}_3$ ) (den Brok et al. 1998).

Most of the subgrains that were investigated in this study are related to healed fractures as well. The presence of abundant fluid inclusions on the subgrain boundaries strengthens the interpretation that they developed by microfracturing as well. The boundaries of the subgrains have a similarly dark CL-signal as the healed longitudinal fractures indicating that subgrain boundaries are actually also healed fractures. Microcracking perhaps started because crystal-plastic deformation could not take up all the imposed deformation in the samples.

### 5.8.4 Water

The irreproducible mechanical behaviour is associated with the role of water. Water enters the quartz crystals by cracking and crack-healing. During deformation water is present in fluid inclusions. Dislocations in quartz may be nucleated at these fluid inclusions (Fitz Gerald et al. 1991). The strength of the quartz depends on the distribution of the water through the sample (Kronenberg 1994). Consequently, it will be easier to deform a sample if fluid inclusions are abundant, small and finely dispersed after crack healing, than if fluid inclusions are rare, large and the water is broadly dispersed. Cracking is an irregular process and does not necessarily yield to reproducible behaviour (Schmocker et al. 2003). Therefore equilibrium distributions of fluid inclusions are difficult to achieve experimentally and the strength of deformation will be slightly different in each experiment, even if the starting orientation is the same.

## 5.9 CONCLUSIONS

The aim of this chapter was to document processes that are responsible for lattice reorientations in samples deformed with *pure* water. Three main microstructures that influenced the orientation of the crystal lattice successively occurred in the samples: deformation lamellae, continuous undulatory extinction and subgrains. They developed by different deformation processes.

- 1) Deformation lamellae were bounded by subgrain walls that induce alternating misorientations in the sample. They formed in an early stage of deformation when dislocations were heterogeneously emitted in slip bands and the quartz crystals were still undersaturated in water. During proceeding deformation more water was incorporated in the quartz and water precipitated in bubbles from which dislocations were emitted. Subbasal orientations and broad angular variations developed by subsequent recovery. In samples deformed to large strains the recovery was very efficient so that initially formed deformation lamellae could completely vanish.

2) Gradual orientation changes of the crystal lattice gave rise to undulatory extinction and were caused by glide controlled lattice rotations. The lattice rotated around rotation axes that were perpendicular to  $\sigma_1$  and related to the activation of (multiple) dislocation slip systems. Basal and prism slip systems were equally activated in the samples; Rhomb<a+c> was not activated in the samples.

3) Subgrains that were observed in the vicinity of through going longitudinal fractures were interpreted as slightly rotated and healed fracture fragments. Microcracking perhaps started because crystal plastic deformation could not account for all the imposed deformation in the sample.

4) Within the investigated samples neither crystal-plastic deformation, nor microcracking did lead to the development of a significant amount of new recrystallised grains.

## CHAPTER 6

### DEVELOPMENT OF CRYSTALLOGRAPHIC PREFERRED ORIENTATIONS BY NUCLEATION AND GROWTH OF NEW GRAINS IN EXPERIMENTALLY DEFORMED QUARTZ SINGLE CRYSTALS<sup>1</sup>

#### ABSTRACT

Deformation experiments have been carried out to investigate the effect of dynamic recrystallisation on crystallographic preferred orientation (CPO) development. Cylindrical samples of natural single crystals of quartz were axially deformed in a Griggs solid medium deformation apparatus in different crystallographic directions: (i) parallel to  $\langle c \rangle$ , (ii) at  $45^\circ$  to  $\langle c \rangle$  and  $45^\circ$  to  $\langle a \rangle$  and (iii) parallel to  $\langle a \rangle$ . The experiments were performed at a temperature of  $800^\circ\text{C}$ , a confining pressure of 1.2 GPa, a strain rate of  $\sim 10^{-6} \text{ s}^{-1}$ , with 1 vol% of added water to bulk finite strains of  $\sim 15\text{-}30\%$ . Two different microstructural domains were distinguished in the deformed samples; (i) domains with undulatory extinction and deformation lamellae, and (ii) domains with new recrystallised grains. Within the domains of undulatory extinction, crystal-plastic deformation caused gradual rotations of the crystal lattice up to  $\sim 30^\circ$  away from the host orientation. The rotation axes are always about perpendicular to the compression axis regardless of the starting orientation. Some of them are related to low-index crystallographic directions. New recrystallised grains show a strong CPO with  $c$ -axis maxima at  $\sim 45^\circ$  to  $\sigma_1$ . This is the case in *all* experiments, irrespective of initial crystallographic orientation. The results show that  $c$ -axes are not continuously rotated towards the maxima. The new grains thus developed through a mechanism different from subgrain rotation recrystallisation. New grains have a subeuhedral shape and numerous microcavities, voids, fluid channels and fluid inclusions at their grain boundaries. This designates that the new grains were created by precipitation in voids and microfractures. The CPO must have developed due to preferred growth of the freshly precipitated grains with orientations suitable for deformation at the imposed experimental conditions.

#### KEYWORDS

Quartz; experimental deformation; CPO development; dynamic recrystallisation; undulatory extinction; nucleation

#### 6.1 INTRODUCTION

Crystallographic preferred orientations (CPOs) are very often observed in deformed rocks and especially in deformed quartzitic rocks. They can be used as a tool in structural geology, for example, to infer (i) whether deformation was coaxial or non-coaxial, (ii) the sense of shear, (iii) the amount of strain, (iv) the temperature during deformation and (v) the dominant deformation mechanisms (Law 1990). Generally, the presence of a CPO is interpreted as evidence for deformation by dislocation glide and creep (e.g. Wenk 1985). Bons and den Brok (2001), however, argued that solution and precipitation processes may also play a role in CPO development.

---

<sup>1</sup> Manuscript submitted to Tectonophysics: Development of crystallographic preferred orientations by nucleation and growth of new grains in experimentally deformed quartz single crystals. By Martine G.C. Vernooij, Bas den Brok and Karsten Kunze.

The strongest quartz CPOs are commonly measured in rocks that are dynamically recrystallised (e.g. Schmid and Casey 1986). Yet, the effect of dynamic recrystallisation on CPO development is not well understood. Dynamic recrystallisation could either (i) *erase* pre-existing CPOs, (ii) *mimic* pre-existing CPOs, (iii) *modify* pre-existing CPOs or (iv) *lead to* the development of a CPO on its own. To investigate this effect, we deformed four single crystals of natural quartz in the presence of water, in a Griggs solid medium deformation apparatus at conditions where dynamic recrystallisation is known to occur (Hobbs 1968, Tullis et al. 1973, Den Brok 1992). Single crystals are an excellent starting material for studies on CPO development, because they allow us to study both the effects of the compression direction ( $\sigma_1$ ) and of the starting orientation of the sample. Two different domains of microstructures were observed in our deformed samples. Low strain domains with undulatory extinction and deformation lamellae in the host crystal and high strain domains with aggregates of recrystallised grains at the sample ends. The complete CPOs of both domains were measured using electron backscatter diffraction (EBSD).

## 6.2 METHODS

### 6.2.1 Sample description

Deformation experiments were carried out on samples cored from a single crystal of natural quartz. This crystal was completely transparent and optically free from lattice defects, such as fluid inclusions. The intracrystalline water content of the crystal was very low (0.002 wt%, measured by FTIR and calculated using the calibration of Paterson 1982). Cylindrical samples were cored, (i) parallel to  $\langle c \rangle$ , (ii) at  $45^\circ$  to  $\langle c \rangle$  and  $45^\circ$  to  $\langle a \rangle$  (parallel to  $\langle o+\rangle$ ) and (iii) parallel to  $\langle a \rangle$ . The samples were  $11.5 \pm 0.5$  mm long and 5.8 mm in diameter. They were weld-sealed into 400  $\mu\text{m}$  thick gold jackets (following the welding procedure of den Brok 1992) together with 1 vol% of distilled water and 20 mg  $\text{Mn}_2\text{O}_3$  powder, which was in direct contact with the sample during the experiments. The  $\text{Mn}_2\text{O}_3$  powder consisted of angular grains with variable size (maximum diameter  $\sim 2\mu\text{m}$ ) and was added intentionally in order to trigger the development of new grains as observed in the experiments of Ord and Hobbs (1986) and Fitz Gerald et al. (1991).

### 6.2.2 Deformation tests

Experiments were carried out in a Tullis-modified Griggs apparatus (Tullis and Tullis 1986). The sample assembly is shown in Figure 6.1. The experimental data are presented in Table 6.1. At the beginning of each experiment, samples were brought to a confining pressure of 1.2 GPa and a temperature of  $800^\circ\text{C}$  following the water isochore of  $1 \text{ g cm}^{-3}$  as closely as possible in  $\sim 7$  hours. Then they rested for an equilibration period of 16-19 hours. Experiment GRZ29 (precondition run) was ended immediately after the equilibration period and the sample was thus only hydrostatically compressed and not strained. The other samples (GRZ30, GRZ33, GRZ34 and GRU37) were subsequently loaded (no “cold-hit”) and deformed at a constant uniaxial displacement rate corresponding to an initial strain rate of  $\sim 10^{-6} \text{ s}^{-1}$ , to bulk finite strains of  $\sim 15\text{-}30\%$ . After deformation, pressure and temperature were lowered to room conditions in  $\sim 1$  hour, again closely following the  $1 \text{ g cm}^{-3}$  water isochore.

The measured axial displacement was corrected for apparatus distortion ( $20 \mu\text{m kN}^{-1}$  at  $800^\circ\text{C}$  and 1.2 GPa). The axial load was not corrected for friction increase during the experiment. Differential stresses were calculated using the initial cross-section of the samples. Finite strain was calculated with respect to the ex-situ measured sample length at room temperature and pressure.



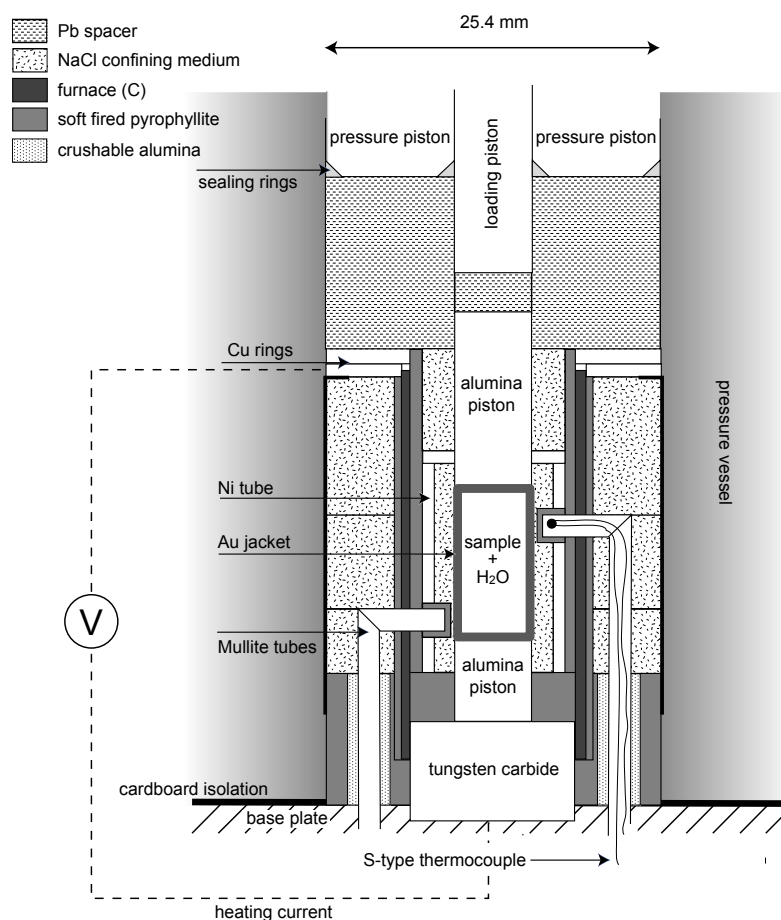


**Figure 6.1:** Sample assembly for deformation in the Griggs apparatus.

Sample number	Starting orientation	Strain rate	$\epsilon$ ex-situ	$\epsilon$ from LVDT	$P_c$	$UTC$	$LTC$	$t_1$	$t_2$	$t_3$	$t_4$	Peak stress
	$[\sigma_1 // ]$	$[s^{-1}]$	$[\%]$	$[\%]$	$[MPa]$	$[^{\circ}C]$	$[^{\circ}C]$	$[h]$	$[h:m]$	$[h:m]$	$[h:m]$	$[MPa]$
GRZ29	$\langle o \rangle$	-	-	-	1150	790	800	63	09:54	15:36	00:42	-
GRZ30	$\langle o \rangle$	$1.0 \cdot 10^{-6}$	29	32	1220	794	806	22	07:12	16:00	00:42	150
GRZ33	$\langle c \rangle$	$1.0 \cdot 10^{-6}$	26	27	1210	804	796	16	07:18	17:36	00:48	210
GRZ34	$\langle a \rangle$	$1.1 \cdot 10^{-6}$	24	26	1210	800	800	16	07:12	19:24	00:42	450
GRU37	$\langle o \rangle$	$1.1 \cdot 10^{-6}$	14	-	1200	820	795	-	23:50*	75:00	02:10	-

**Table 6.1:** Summary of the experimental data. Experiment GRZ29 is a precondition run (only hydrostatically loaded). Sample GRU37 was deformed in the HPT laboratory in Utrecht under similar experimental conditions in the same apparatus (den Brok 1992). The load-displacement data of this sample are not known.  $\epsilon$ , finite strain;  $P_c$ , confining pressure;  $UTC$ , upper thermocouple;  $LTC$ , lower thermocouple;  $t_1$ , time cold pressing at 100 MPa  $t_2$ , elapsed time to reach  $PT$  conditions, \* in GRU37  $t_1$  and  $t_2$  are taken together;  $t_3$ , time at  $PT$  conditions before deformation;  $t_4$ , elapsed time after deformation to reach room  $PT$  conditions.

### 6.2.3 Sample preparation for microstructural analysis

During deformation, the originally cylindrical samples obtained a slightly elliptical cross section. To prepare the sections for microscopic analysis, the samples were cut parallel to the compression direction ( $\sigma_1$ ) and parallel to the long axis of these ellipses. In this way, the  $c$ -axis of the bulk crystal was about parallel to the thin section in samples GRZ30 and GRZ33 and perpendicular to the thin section in sample GRZ34. One half of the samples was then impregnated with Epofix so that thin sections could be made without losing too much material during polishing. The thin sections were polished using 0.05  $\mu\text{m}$  alumina suspension. The non-impregnated half of the samples was used to prepare 200  $\mu\text{m}$  thick sections for EBSD analysis. These thick sections were mechanically polished down to 0.05  $\mu\text{m}$  particle size and lapped for 8 hours in an alkaline colloidal silica suspension (particle size 25 nm). To avoid charging problems in the scanning electron microscope (SEM), lapped thick sections were coated with a  $\sim 4$  nm carbon layer and covered with silver paint around the lapped sample surface.

After EBSD analysis, a thin section was prepared of the lapped surface of sample GRZ30 to select areas for transmission electron microscope (TEM) examination. Copper grids were attached to the selected areas that were subsequently thinned by ion milling in a GATAN DUOMILL until electron transparency was reached ( $<0.1$ - $0.2$   $\mu\text{m}$ ). Specimens were finally carbon coated to avoid charge problems. The TEM investigations were performed with a Philips field emission gun CM20 TEM, operating at 200 kV. We employed conventional bright-field and dark-field imaging techniques to observe and characterize the defect microstructures in quartz.

A 200  $\mu\text{m}$  thick slice was cut from the non-impregnated half of sample GRZ30 and broken intentionally to investigate the grain boundary microstructures on broken surfaces by secondary electron imaging in the SEM (comparable to den Brok 1992 and Mancktelow et al. 1998).

### 6.2.4 Electron backscatter diffraction

Full crystallographic orientation data were obtained from automatically indexed electron backscatter diffraction (EBSD) patterns (Adams et al. 1993, Prior et al. 1999). EBSD patterns were acquired using an EDAX\_TSL DigiviewFW camera system attached to a Camscan CS44LB SEM. The EBSD patterns were obtained using 15 kV acceleration voltage, 35 mm working distance,  $\sim 3$  nA beam current and  $70^\circ$  sample tilt. The step sizes of the automated EBSD analysis were 10  $\mu\text{m}$  for CPO measurements and 1  $\mu\text{m}$  for additional high resolution orientation mapping at a typical scan speed of 9 patterns per second. The patterns were collected and indexed with the commercial TSL software OIM DC 3.5<sup>TM</sup> and analysed with OIM Analysis 3.0<sup>TM</sup> and OIM Analysis 3.5<sup>TM</sup>. The analyses show a large number of data with a high indexing reliability; recorded data with a low confidence index ( $<0.1$ ) were removed prior to analysis. The misorientation angle between adjacent points was calculated by selecting the minimum angle that enables the lattice of one point to be rotated into the other (Wheeler et al. 2001). Rotation axes were specified for data from areas where only gradual orientation changes of the host lattice were observed and no new grains (so called host areas). Data were selected along lines that were approximately perpendicular to bands with undulatory extinction (deformation bands). We developed a program to calculate the rotation axes based on the determination of second order moments of the orientation distributions. The corresponding errors to the rotation axes were calculated from the maximum misorientation angle along the lines according to equation A10 of Kruse et al. (2002), assuming an EBSD-data precision of 1 degree.

The deformation experiments were performed close to the transition temperature from  $\alpha$ - to  $\beta$ -quartz, which is  $850^\circ\text{C}$  at 1200 MPa (Bagdassarov and Delépine 2004). It is not clear if the

indexed Dauphiné twins were induced during cooling (the starting material has no Dauphiné twins) or induced by deformation. Further ambiguity from misindexing in potential Dauphiné twin orientations was therefore avoided by always plotting the quartz data for our samples with hexagonal crystal symmetry.

## 6.3 RESULTS

### 6.3.1 Mechanical data

The mechanical results obtained from deformation tests GRZ30, GRZ33 and GRZ34 are presented in a differential stress versus axial strain curve (Fig. 6.2). All experiments showed a load increase until a peak stress was reached beyond which a drastic weakening took place. The strain at which the peak stress was reached varied between 3 and 6%. The actual strain at this stage is known to be less, but hardly possible to quantify. The weakening effect in sample GRZ33 ( $\sigma_1 // \langle c \rangle$ ) was much more pronounced than in the experiments GRZ30 ( $\sigma_1 // \langle o+\rangle$ ) and GRZ34 ( $\sigma_1 // \langle a \rangle$ ). In experiments GRZ30 and GRZ33, the differential stress increased again after the period of weakening. The flow stress values in the samples were related to the starting orientations of the samples. Sample GRZ33 ( $\sigma_1 // \langle c \rangle$ ) had the highest peak stress of about 450 MPa, while sample GRZ30 ( $\sigma_1 // \langle o+\rangle$ ) had the lowest peak stress at about 150 MPa.

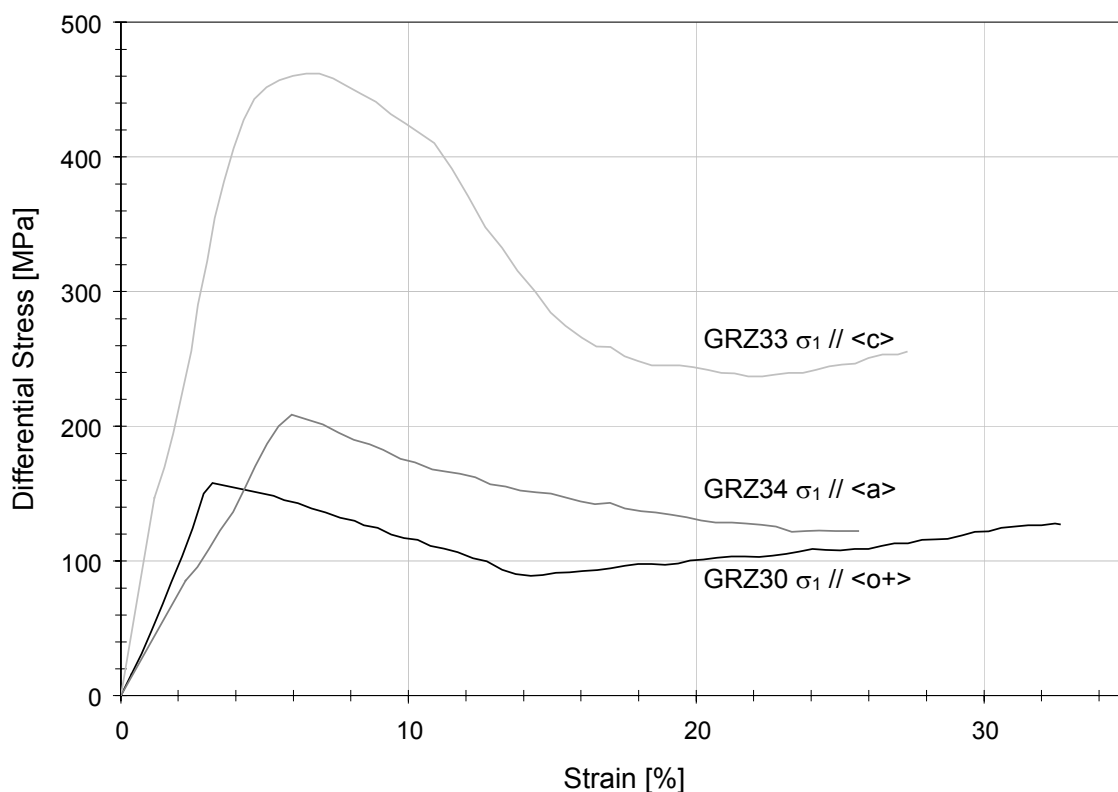
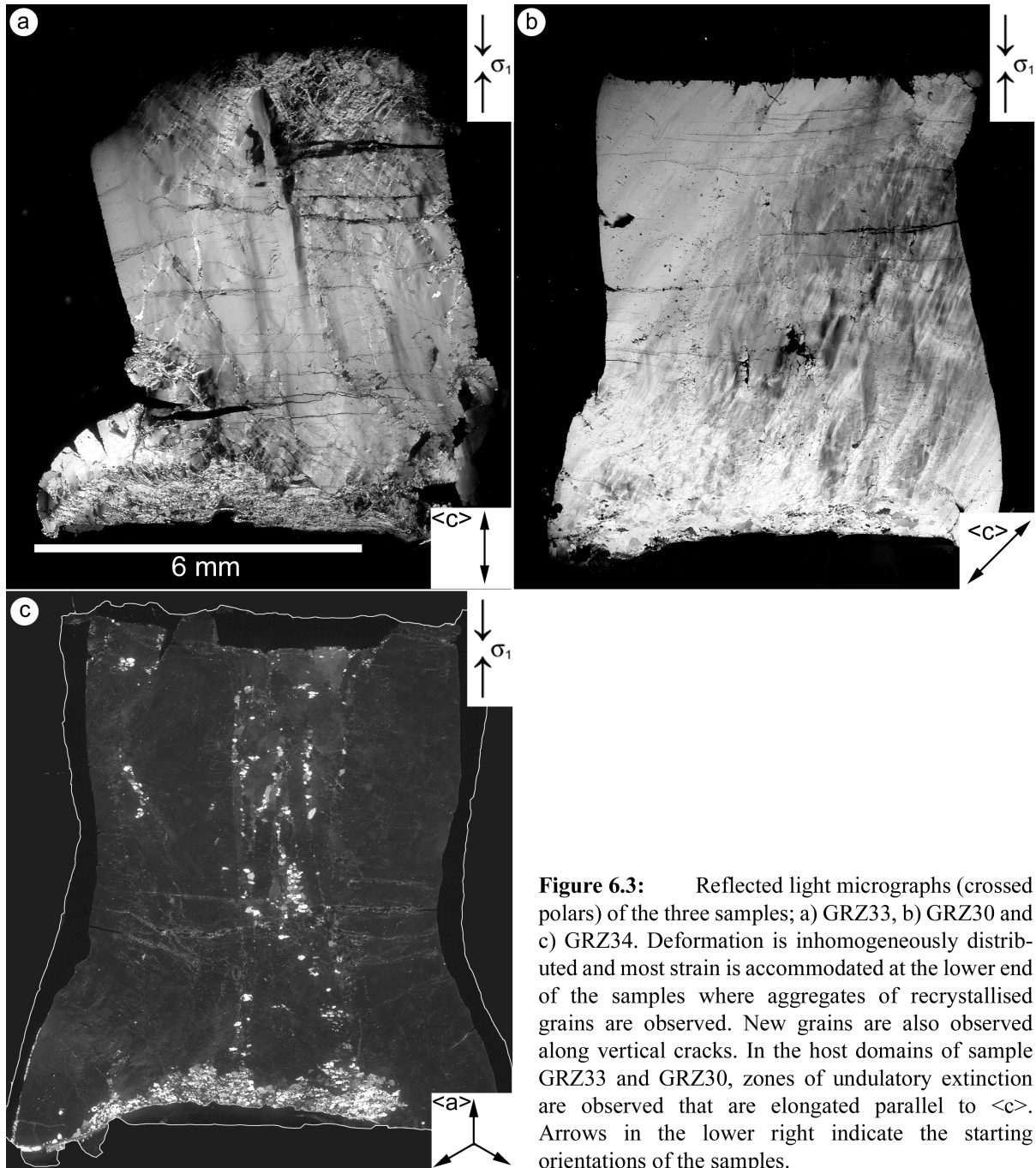


Figure 6.2: Stress-strain curves for the experiments GRZ30, GRZ33 and GRZ34.

### 6.3.2 Deformation microstructures

The precondition run (GRZ29) produced substantial microstructural modifications under nominally hydrostatic conditions. These modifications would certainly have influenced any subsequent deformation experiment. Longitudinal and oblique cracks generated offsets at the edges of the sample. Most of these cracks were healed and decorated with abundant fluid inclusions of irregular shapes.

In the deformed samples, domains were distinguished with (1) recrystallised grains and (2) with undulatory extinction and deformation lamellae. Most of the strain is accommodated in the lower end of the samples, where aggregates of recrystallised grains are observed in a narrow zone (Fig. 6.3). These aggregates are in direct contact with the  $\text{Mn}_2\text{O}_3$ -powder. Isolated patches of recrystallised grains are observed within longitudinal through-going cracks (Fig. 6.3c). Bands of undulatory extinction and deformation lamellae are observed in the host domains of the samples, where no new grains have formed (Fig. 6.3a and b).



**Figure 6.3:** Reflected light micrographs (crossed polars) of the three samples; a) GRZ33, b) GRZ30 and c) GRZ34. Deformation is inhomogeneously distributed and most strain is accommodated at the lower end of the samples where aggregates of recrystallised grains are observed. New grains are also observed along vertical cracks. In the host domains of sample GRZ33 and GRZ30, zones of undulatory extinction are observed that are elongated parallel to  $\langle c \rangle$ . Arrows in the lower right indicate the starting orientations of the samples.

### 6.3.2.1 Domains with undulatory extinction and deformation lamellae

Elongated zones with gradual undulatory extinction (Fig. 6.4) are observed in sample GRZ30 and GRZ33. These zones are aligned and elongated sub parallel to  $\langle c \rangle$ . They arise from gradual misorientations in the crystal and are bounded by longitudinal cracks. Undulatory extinction is not visible in sample GRZ34 because  $\langle c \rangle$  remains fairly constant in this sample and is in extinction perpendicular to the sample cut (Fig. 6.3c). In sample GZ30 and GRZ33 numerous deformation lamellae are associated with the undulatory zones. They are slightly curved elements that mostly have a (sub-)basal orientation and a spacing of  $3.4 \pm 0.3 \mu\text{m}$ . The deformation lamellae induce alternating small ( $2\text{-}3^\circ$ ) misorientations in the crystal along elongated sub grain walls (Christie and Ardell 1976, Drury 1993, Langenhorst and Deutsch 1996, Vernooij and Langenhorst 2005).

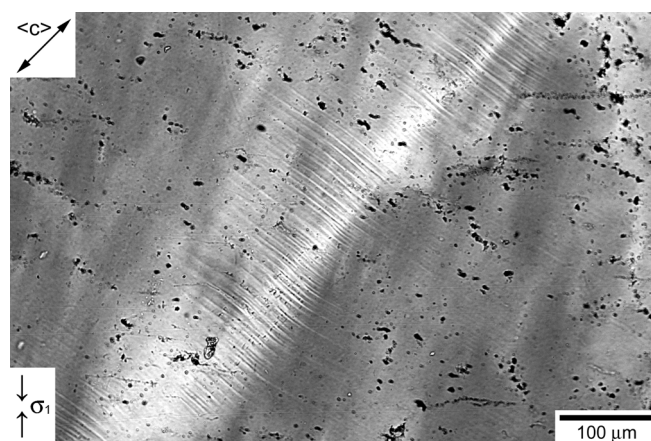


**Figure 6.4:** Sub-basal deformation lamellae and zones of gradual undulatory extinction that are elongated parallel to  $\langle c \rangle$ . GRZ30,  $\sigma_1 // \langle c \rangle$ , starting orientation of  $\langle c \rangle$  indicated (optical micrograph, crossed polars).

### 6.3.2.2 Domains with new grains

New grains are observed in three different ways; (1) isolated, (2) in elongated arrays and (3) in aggregates at the sample boundaries. The optical appearance of the new grains is similar in all samples, irrespective of the starting orientation.

The isolated new grains that are observed in the sample interiors (Fig. 6.5), particularly, provide important information about the onset of recrystallisation. They always occur along (healed) cracks or in areas with fracture fragments, in regions where abundant and large fluid inclusions are found. Small fluid inclusions are situated on boundaries of new grains. New grains display a large range in two-dimensional grain size ( $\sim 2\text{-}50 \mu\text{m}$ ). They are usually smaller than the surrounding fracture fragments. What is interpreted here as fracture fragments are crystal volumes that are separated by sharp boundaries with small angle misorientations. These boundaries are decorated by vast amounts of fluid inclusions (Fig. 6.5a). They are always related to longitudinal cracks (Fig. 6.6) and have irregular, angular shapes, whereas new grains are sub-euhedral with straight grain boundaries and round edges. The recrystallised grains are optically uniform. Their crystallographic orientations are always at high angle to the host domains. The orientation change between the host domains and the new grains is abrupt. Fracture fragments only have a slightly different orientation than the host domains. New grains have occasionally formed elongated vertical arrays within the longitudinal cracks (Fig. 6.3c and 6.6) (see also den Brok 1992).

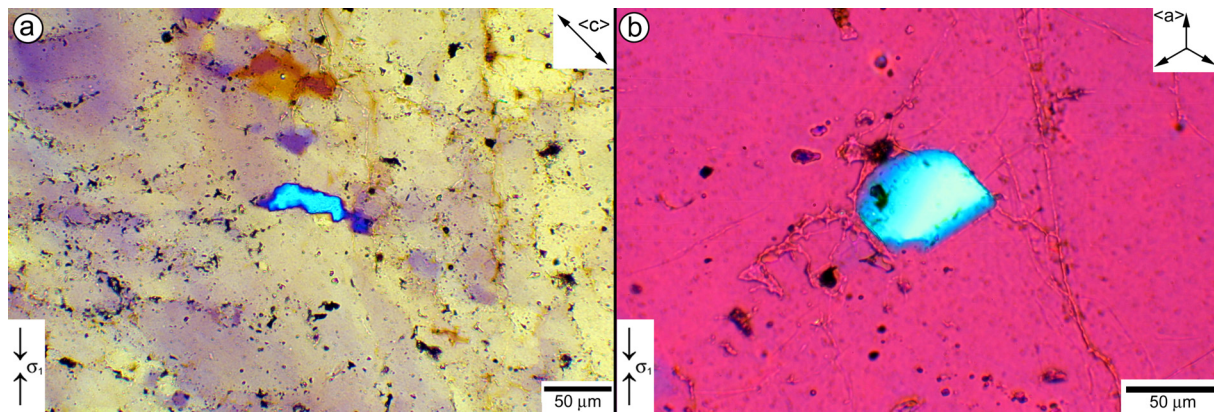


**Figure 6.5:** Isolated new grains within the interiors of the deformed samples. They show homogeneous extinction, have a subeuhedral shape and their orientation deviates significantly from their surroundings. Optical micrographs with crossed polars and gypsum plate, a) GRZ30 ( $\sigma_1 // \langle c \rangle$ , starting orientation of  $\langle c \rangle$  indicated), b) GRZ34 ( $\sigma_1 // \langle a \rangle$ , starting orientation of  $\langle a \rangle$  indicated).

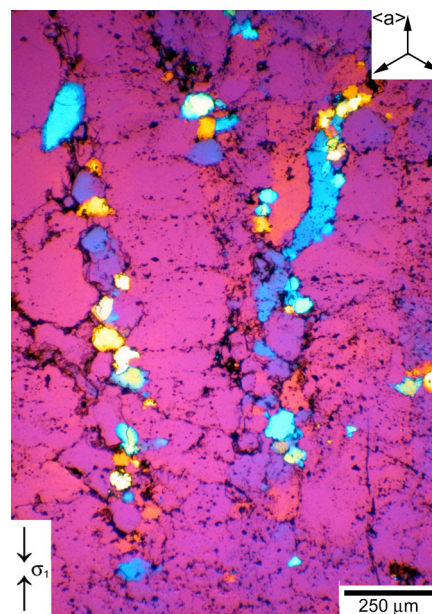


**Figure 6.6:** Arrays of new grains, located within healed cracks that are parallel to  $\sigma_1$ . Optical micrograph with crossed polars and gypsum plate (Experiment GRZ34,  $\sigma_1 // \langle a \rangle$ , starting orientation of  $\langle a \rangle$  indicated).

New grains at the lower end of the samples form  $\sim 500\mu\text{m}$  wide aggregates covering almost the complete end of the sample (Fig. 6.3). Such aggregates develop only if  $\text{Mn}_2\text{O}_3$ -powder is in direct contact with the sample. The grains in the aggregates (Fig. 6.7) have sub-euhedral shapes, straight grain boundaries, grain sizes of  $\sim 2\text{-}50\ \mu\text{m}$  and are optically uniform. In sample GRZ33, recrystallised grains are observed with serrated grain boundaries (Fig. 6.7b). Most recrystallised grains within the aggregates have angular bends that point towards  $\sigma_1$ . The transition between the new grain aggregates and the host domains is discrete (Fig. 6.7a). The SE images (Fig. 6.8) display the three-dimensional grain (boundary) shapes. New grains are equidimensional with rounded edges. They have numerous voids and cavities at their contact surfaces. The grain boundaries are densely covered with fluid inclusions. Porous spaces are also observed at the grain boundaries in the TEM (Fig. 6.9). TEM analysis indicates that although the recrystallised grains are optically uniform, their interiors are occupied by a high density of free dislocations ( $10^{10}\ \text{cm}^{-2}$ ) with Burgers vector mostly parallel



to  $1/3\langle 11\bar{2}0 \rangle$ . Only the tiniest recrystallised grains ( $\sim 1 \mu\text{m}$ ) are dislocation free and seem to grow at the cost of the larger grains with high dislocation densities (Fig. 6.9a).

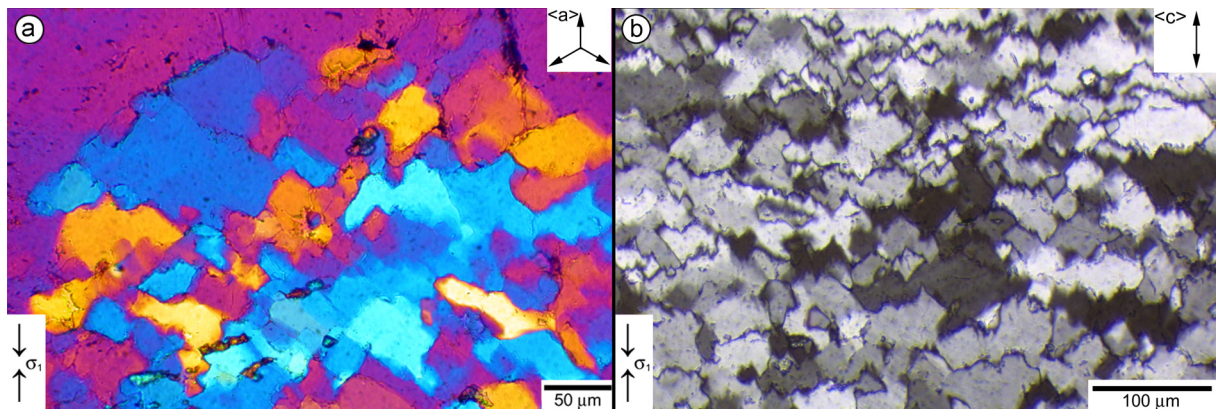


**Figure 6.7:** Aggregates of new grains with homogeneous extinction and angular bends that point towards  $\sigma_1$ . Their grain boundaries are straight, aligned, and occupied by tiny fluid inclusions. Remnants of the  $\text{Mn}_2\text{O}_3$ -powder are observed through the aggregates on grain boundaries. Figure a) illustrates that the orientation change between the new grains and the host is discrete (in the uppermost part of the picture) in sample GRZ34 ( $\sigma_1 // \langle a \rangle$ , starting orientation of  $\langle a \rangle$  indicated). Figure b) illustrates serrated grain boundaries in sample GRZ33 ( $\sigma_1 // \langle c \rangle$ , starting orientation of  $\langle c \rangle$  indicated). Optical micrographs with crossed polars (a and b) and gypsum plate (a).

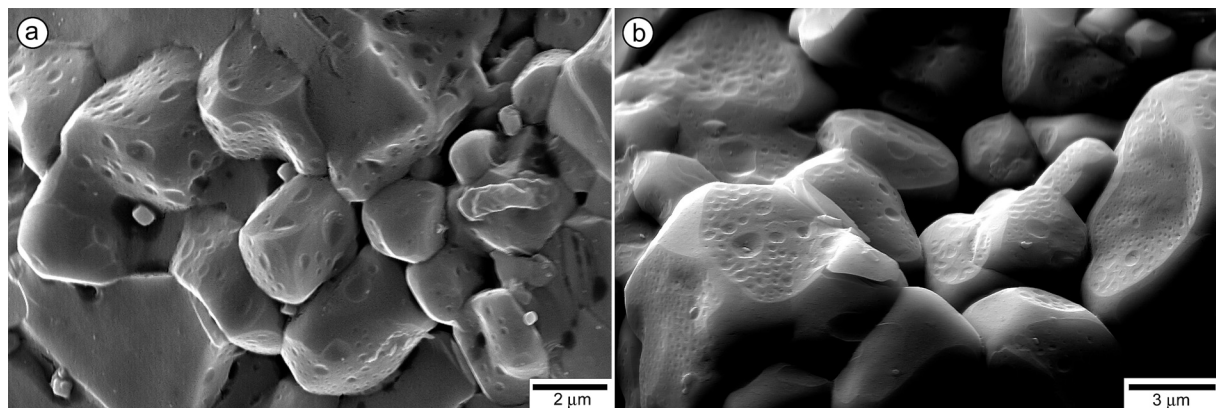


**Figure 6.8:** Grain boundary microstructure of new grains. Fluid inclusions leave depressions on the grain boundaries. Rounded grain edges, voids and cavities between the grains indicate the presence of water at or near the grain boundaries. SEM secondary electron images (acceleration voltage 20 kV) of sample GRZ30 ( $\sigma_1 // \langle o+\rangle$ ).

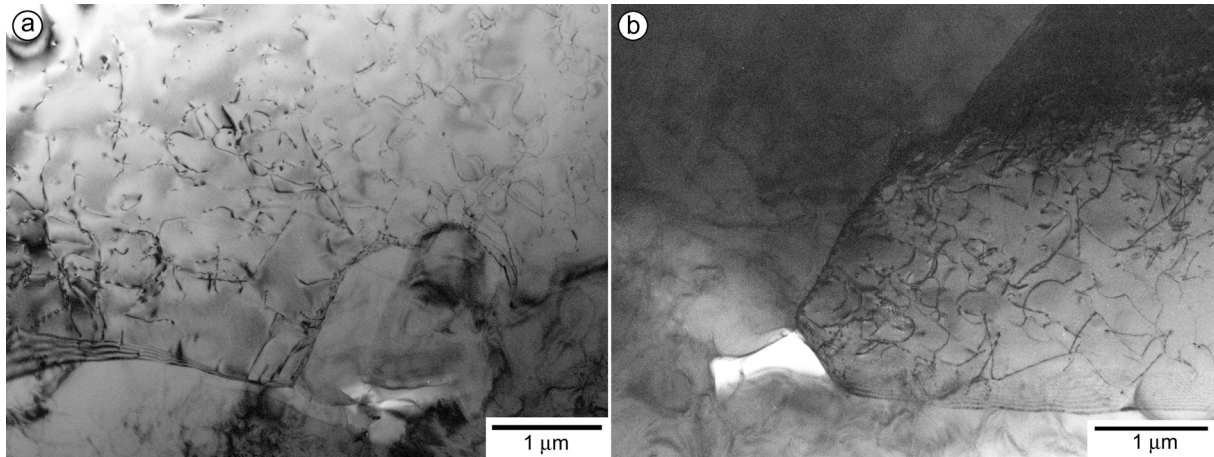


**Figure 6.9:** Intracrystalline microstructure of recrystallised grains and grain boundaries in sample (GRZ30) deformed parallel to  $\langle o \rangle$ . Large recrystallised grains exhibit a high density of free dislocations ( $10^{10} \text{ cm}^{-2}$ ) and dislocation sources. a) Dislocation free tiny ( $1 \mu\text{m}$  diameter) grain migrates into larger grain which is full of dislocations. b) Pore at grain boundary. TEM bright field images.

### 6.3.3 Crystallographic orientation analysis

#### 6.3.3.1 Lattice rotation in low strain host domains

To map crystal lattice reorientations in the host domains, data points were selected from orientation maps along profiles that crosscut the elongated bands of undulatory extinction at a right angle. To check the reliability of this analysis, data were selected along two different profiles for each sample. The individual orientations were plotted in pole figures (Fig. 6.10). The data points spread away from the starting orientation in two directions towards and away from  $\sigma_1$ . These spreads correspond to rotations of the crystal lattice. The rotations could be exactly traced in sample GRZ33 and sample GRZ34. The data of sample GRZ30 are more dispersed, because the sampled part in the host domain was more damaged and contained many fracture fragments (Fig. 6.5a). Still, the rotation of the data in this sample could be well traced. The maximum amount of rotation in the samples is  $\sim 30^\circ$  with respect to the starting orientation. The rotation paths are different for each starting orientation. In GRZ33,  $\langle c \rangle$  rotates away from both  $\sigma_1$  and the starting orientation (Fig. 6.10a), in GRZ30,  $\langle c \rangle$  rotates in two directions towards and away from  $\sigma_1$  (Fig. 6.10b) and in GRZ34, the  $a$ -axes rotate in a clockwise and anticlockwise direction away from  $\sigma_1$ , while the  $c$ -axis hardly changes orientation. In all samples, the crystal lattice rotates around an axis close to the centre of the pole figures, i.e. perpendicular to  $\sigma_1$ . The crystallographic orientation of this rotation axis is different for each sample (Fig. 6.11). In sample GRZ33, the rotation axis is close to  $\langle a \rangle$  for both datasets. The rotation axes of sample GRZ30 and sample GRZ34 do not correspond to a specified crystallographic orientation within the error estimates. In sample GRZ34, the rotation axes of the two datasets are the same; close to  $\langle c \rangle$ . The rotation axes of the two datasets of sample GRZ30 are different, but both fairly close to directions in the basal plane.



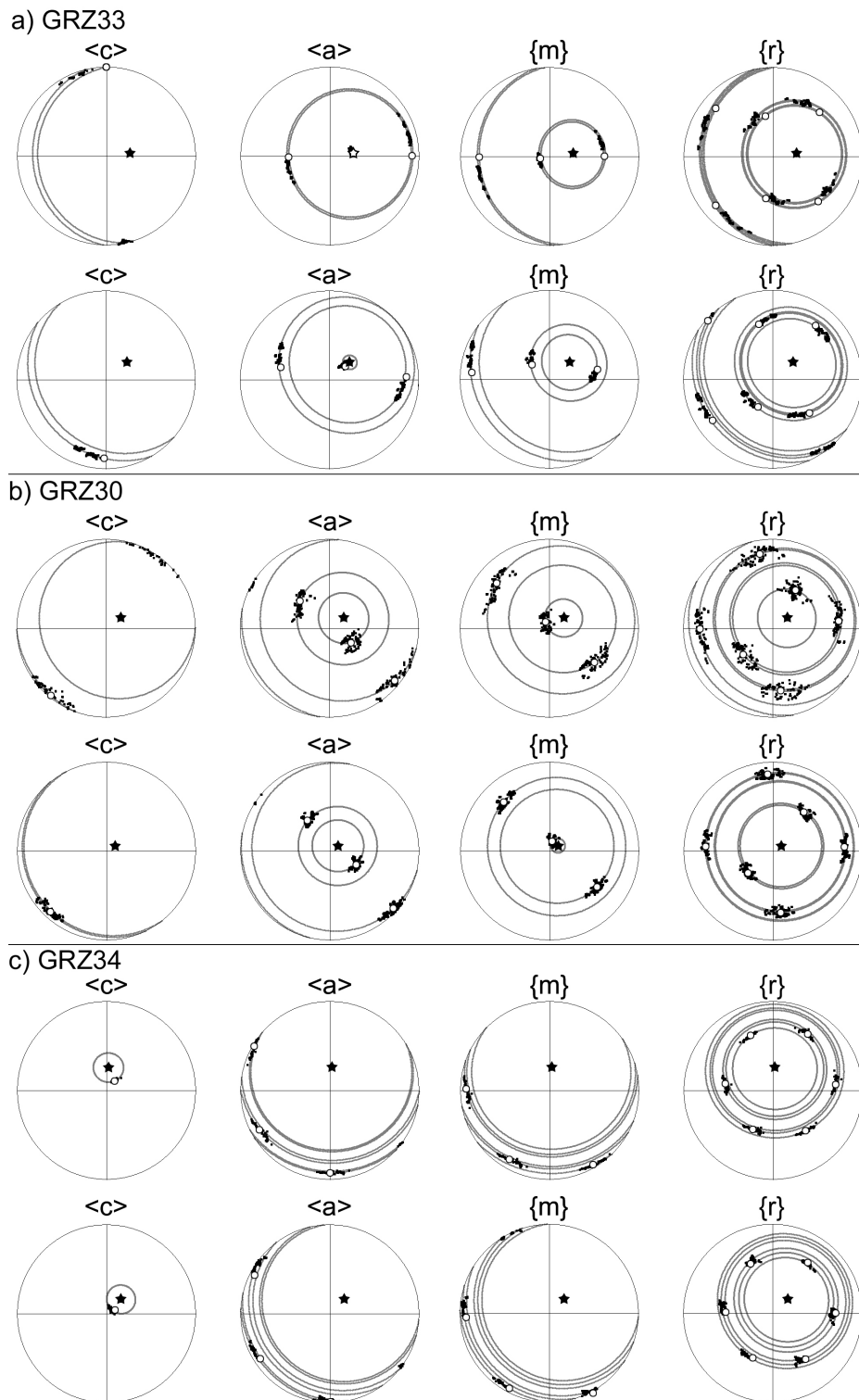


**Figure 6.10:** Lattice rotations in the host domains with undulatory extinction and deformation lamellae. Equal area, upper hemisphere projections of several crystal directions and poles (plotted for hexagonal quartz). Orientations are extracted from EBSD orientation maps (stepsize  $10\ \mu\text{m}$ ) along linear segments with a width of 1 measurement point. Two different representative line segments per sample were selected from a larger number of tested profiles. The segments were chosen perpendicular to the elongated bands with undulatory extinction. The data are plotted as black squares. Open circles indicate the best fit starting orientation with respect to the data-set assigned by  $\langle c \rangle // \sigma_1$  (GRZ33),  $\langle c \rangle$  and  $\langle a \rangle$  are at  $45^\circ$  to  $\sigma_1$  (GRZ30) and  $\langle a \rangle // \sigma_1$  (GRZ34). Black stars are best-fit rotation axes of the data. Grey lines correspond to the calculated rotation path.

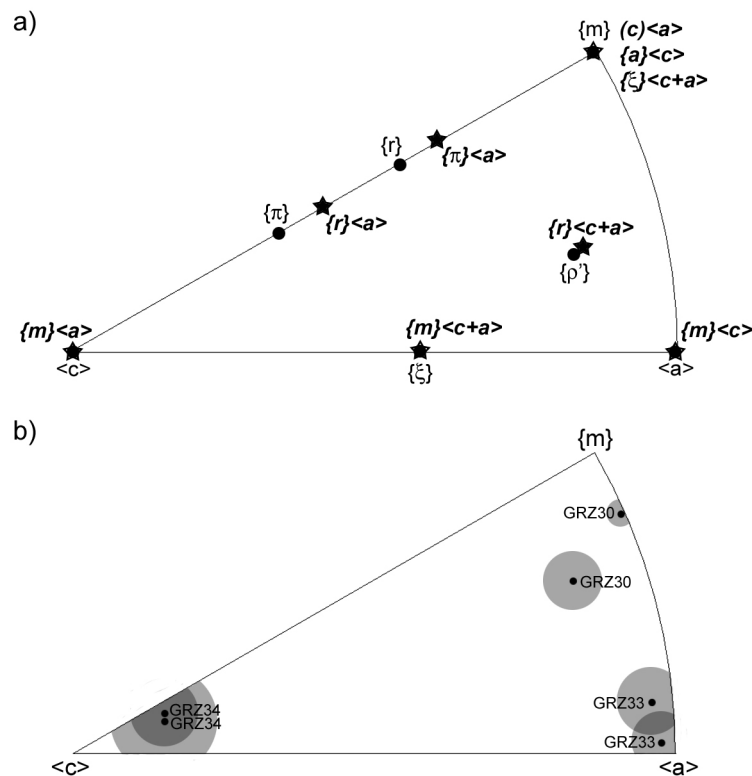
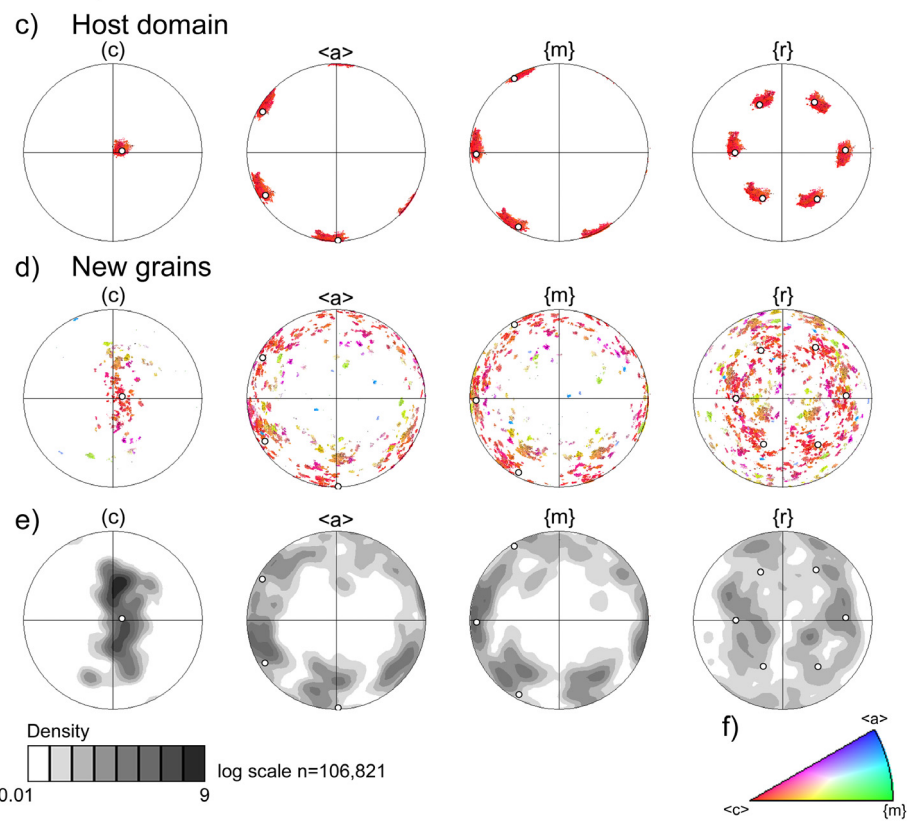
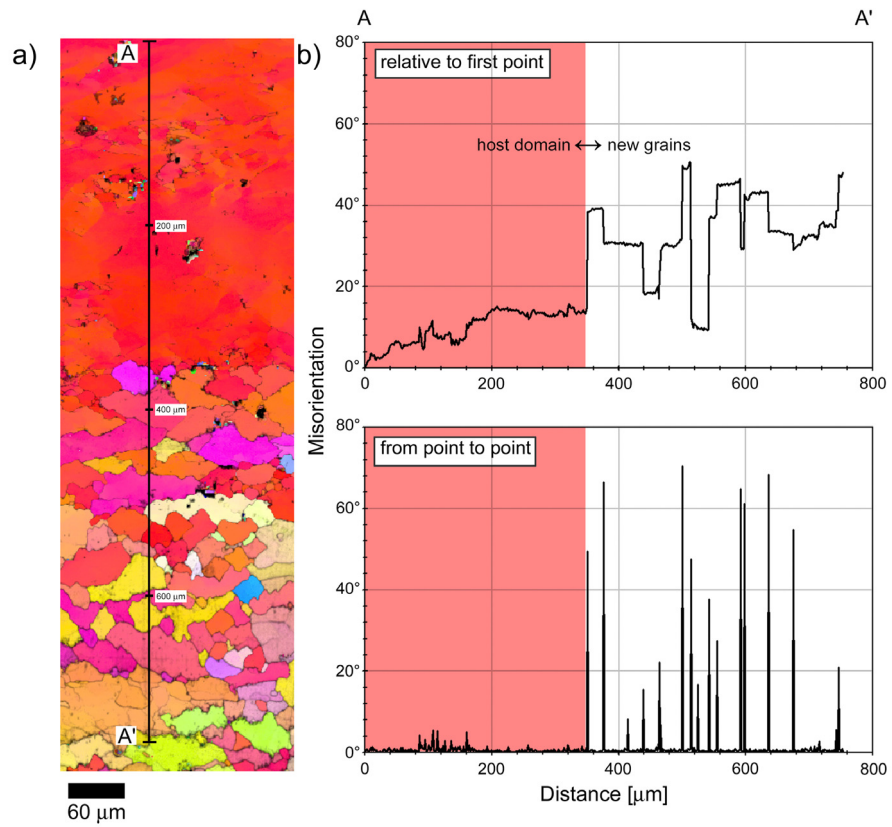


**Figure 6.11:** a) Theoretical rotation axes (black stars and bold italic characters) and crystal orientations of hexagonal quartz (black dots and normal characters) drawn after Neumann (2000) assuming that misorientations are exclusively formed due to edge dislocations on single slip systems. b) Misorientation axes of the calculated rotations of sample GRZ30, GRZ33 and GRZ34 displayed with respect to the crystal reference frame (equal area, upper hemisphere). Grey circular areas indicate the error on the calculated rotation axes given by the maximum misorientation along the rotation path (Eq. A10, Kruse et al. 2002).

### 6.3.3.2 Transition from lattice rotation to new grain development

The orientation map of sample GRZ34 (Fig. 6.12a) is an example of the transition area from the host domain (top of the map) to the domain with new grains (bottom of the map). Gradual colour changes from red to orange in the host domain illustrate gradual orientation changes of the crystal lattice. Abrupt colour changes from red to orange illustrate small angle boundaries. The variety of colours of the new grains, different from the red and orange colours of the host domain, indicates their different crystallographic orientations. New grains are slightly elongated perpendicular to  $\sigma_1$  and have straight grain boundaries that often make a  $35^\circ$ - $60^\circ$  angle with  $\sigma_1$ .

**Figure 6.12 (next page):** The transition from the host domain to an area with new grains in sample GRZ34 ( $\sigma_1 // \langle a \rangle$ ). a) Detailed orientation map (raw data) obtained from an EBSD area scan with a step size of  $1 \mu\text{m}$ . Each pixel is colour coded corresponding to the inverse pole figure colour key for hexagonal symmetry (f) of the direction normal to the section ( $90^\circ$  to  $\sigma_1$ ). The pattern quality map (grey levels) is plotted in the background. A few incorrectly indexed orientations are found next to the black pixels on the map which correspond to indexing artefacts due to surface obstacles (holes, cracks, boundaries). A misorientation profile is drawn along line A-A'. b) The misorientation angle is displayed with respect to the first point and also from neighbouring point to point. c-e) Pole figures (equal area upper hemisphere). Points in the pole figures have colours that correspond to the orientation map (a); open circles indicate the best fit starting orientation of the sample with respect to the data-set allocated by the fact that  $\langle a \rangle$  was parallel to  $\sigma_1$  at the beginning of the experiment. c) Pole figures of the host domain (upper half of the orientation map). d and e) Pole figures of the area with new grains (lower half of the orientation map). e) Contoured pole figures are processed using an expansion of  $L = 22$ , with  $5^\circ$  within the harmonic calculus.



The misorientation profile (Fig. 6.12b) also illustrates that the orientation changes of the crystal lattice in the host domain are gradual (point to point misorientation  $<2^\circ$ ). The misorientation angles between the new grains are large (up to  $70^\circ$  point to point misorientation). The interiors of the new grains only show minor deformation (internal point to point misorientation  $<1^\circ$ ). The crystallographic orientation change between the host domain and the new grains at the border of the recrystallised area is instantaneous and large (point to point misorientation of  $50^\circ$ ).

The pole figures of the host domain indicate that the crystal lattice in the mapped host domain gradually rotates in a clockwise sense around the  $c$ -axis with a maximum amount of rotation of  $20^\circ$  away from the host orientation (Fig. 6.12c). The pole figures of the domain with new grains display a different pattern (Fig 6.12d and e). The  $c$ -axes occupy parts of a single girdle between their original orientation and  $\sigma_1$  with a spread of  $\sim 90^\circ$ . The  $a$ -axes are concentrated near the periphery. The orientations of the individual new grains spread by rotation around their particular  $c$ -axes. There is no common rotation axis for the domains with new grains as observed in the host domains.

### 6.3.3.3 CPOs in the new grain aggregates

The CPOs of the domains with new grains (Fig. 6.13) express high degrees of preferred orientations. In sample GRZ33 (Fig. 6.13a) the CPO of the new grains consists of a strong  $c$ -axis maximum at the periphery of the pole figure,  $\sim 35^\circ$  to  $\sigma_1$ , and a weaker small circle girdle also at  $\sim 35^\circ$  to  $\sigma_1$ . The  $a$ -axes maxima occupy a girdle that is slightly tilted with respect to the horizontal plane in the sample. The new grains in sample GRZ30 (Fig 6.13b) form a strong  $c$ -axis maximum at  $\sim 45^\circ$  to  $\sigma_1$ , parallel to the host orientation of the sample and a weaker  $c$ -axis maximum perpendicular to the host orientation, also at  $\sim 45^\circ$  to  $\sigma_1$ . The same  $c$ -axis pattern was obtained in sample GRU37 (Fig. 6.14) which was deformed in the same orientation, but only to a finite strain of  $\sim 14\%$ . Therefore, the CPO-pattern in these samples must have been stable at relatively low strains. The  $a$ -axes in sample GRZ30 form maxima near the starting orientation along a tilted girdle at  $\sim 45^\circ$  to  $\sigma_1$ . The  $c$ -axes of the new grains in sample GRZ34 (Fig. 6.13c) vary along a single vertical girdle with strong maxima at  $\sim 90^\circ$  (parallel to the starting orientation), at  $65^\circ$  and at  $45^\circ$  to  $\sigma_1$ . Weaker  $c$ -axis maxima are observed at the periphery of the pole figure (at  $\sim 45^\circ$  to  $\sigma_1$  and nearly perpendicular to the starting orientation). The  $a$ -axes are concentrated near the periphery of the pole figure.

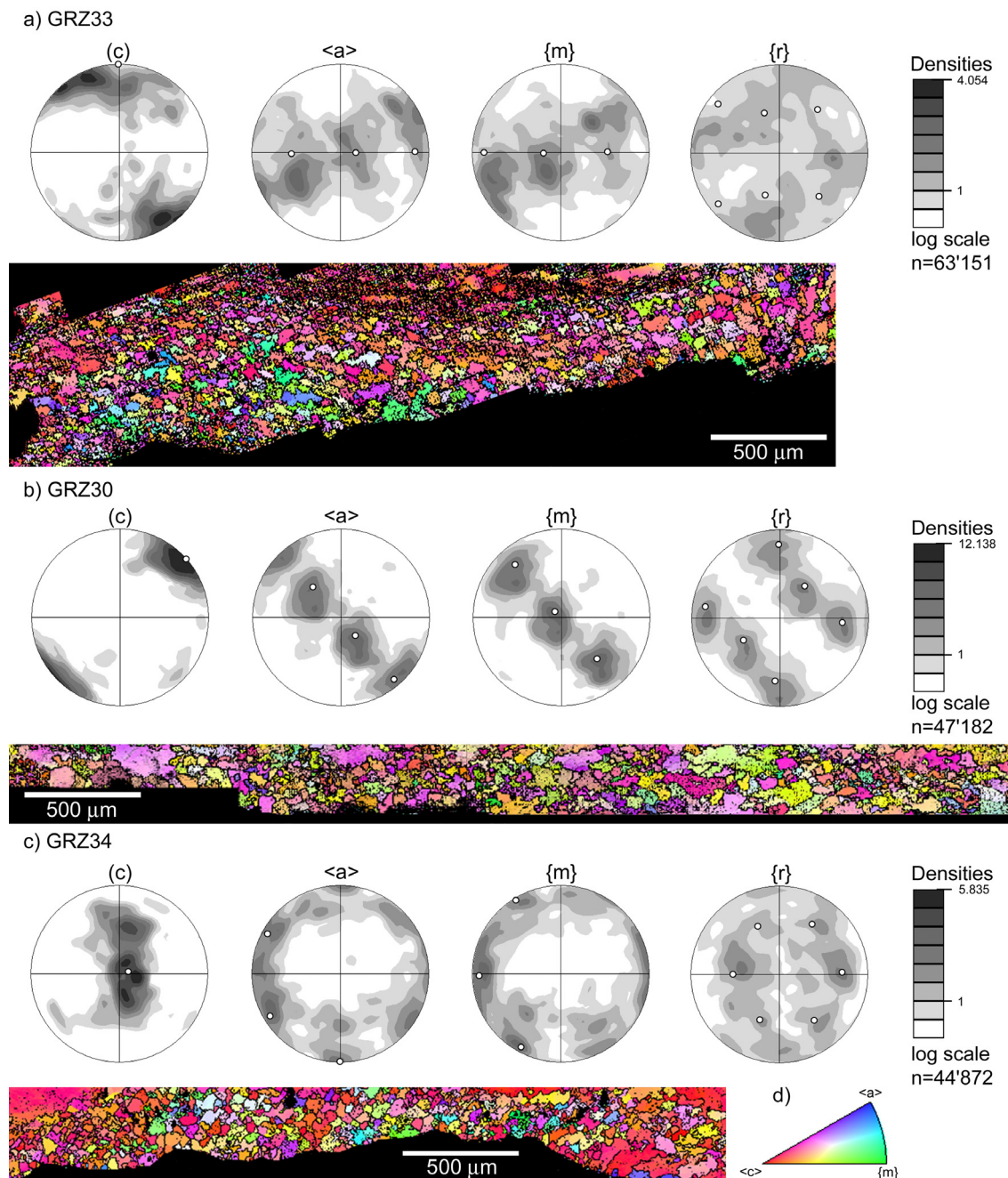


**Figure 6.13:** Pole figures (equal area, upper hemisphere) with CPOs of the domains with new grains determined by EBSD measurements and corresponding EBSD orientation maps. Open circles indicate the best fit starting orientation of the samples with respect to the data-sets allocated by the fact that  $\langle c \rangle$  was parallel to  $\sigma_1$  (a),  $\langle c \rangle$  and  $\langle a \rangle$  were at  $45^\circ$  to  $\sigma_1$  (b) and  $\langle a \rangle$  was parallel to  $\sigma_1$  (c) at the beginning of the experiment. The number of data points ( $n$ ) corresponds to the number of EBSD measurements, constant step size of  $10 \mu\text{m}$ . Contoured pole figures (c, a, m and r) are processed using a Gaussian convolution with a half width of  $5^\circ$  and an expansion of  $L = 22$  within the harmonic calculus. a) GRZ33 ( $\sigma_1 \parallel \langle c \rangle$ ), b) GRZ30 ( $\sigma_1 \parallel \langle c \rangle$ ) and c) GRZ34 ( $\sigma_1 \parallel \langle a \rangle$ ). The EBSD orientation maps and pole figures are constructed from data with confidence index  $>0.1$ . Nearest neighbour misorientations  $>10^\circ$  are marked by black line segments. d) Colour key. Each pixel is colour coded corresponding to the inverse pole figure colour key of the  $\sigma_1$ -direction (a and b) and of the normal to the section ( $90^\circ$  to  $\sigma_1$ ) (c).

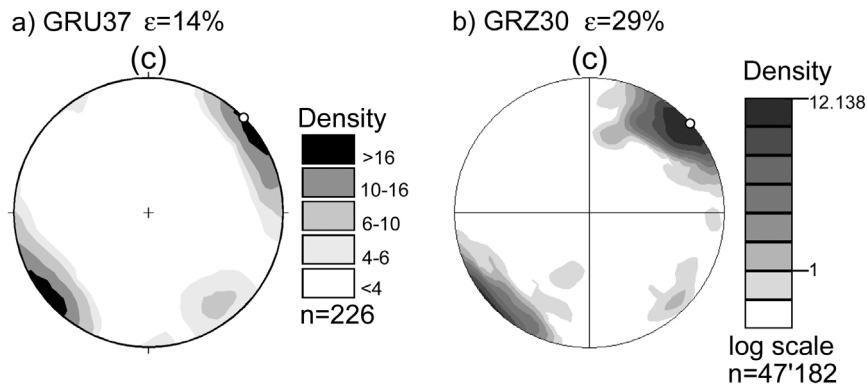


**Figure 6.14:** Similar  $c$ -axis preferred orientations for different total finite strain in samples deformed parallel to  $\langle o \rangle$  measured by a) universal stage (experiment GRU37,  $\epsilon=14\%$ ) and by b) EBSD measurements (experiment GRZ30,  $\epsilon=29\%$ ). The contours in plot a) correspond to  $\langle 4, 4-6, 6-10, 10-16$  and  $>16$  times the standard deviation. Plot b is identical to that in Fig. 6.13b.

## 6.4 DISCUSSION

### 6.4.1 Deformation mechanisms

It is documented above that quartz single crystals that were deformed at  $800^\circ\text{C}$ , at 1.2 GPa and at a strain rate of  $\sim 10^{-6} \text{ s}^{-1}$  in the presence of 1 vol% of water and 20 mg  $\text{Mn}_2\text{O}_3$ -powder show two deformation microstructures: undulatory extinction and recrystallised grains. Continuous undulatory extinction and deformation lamellae in the host domains of the sample are microstructural evidence for crystal-plastic deformation (Passchier and Trouw 1998). The documented rotation of the crystal lattice around well defined rotation axes in these domains strengthens this interpretation. These rotations can be explained by glide controlled lattice rotation. The recrystallised grains must have developed by an additional process. They yield strong  $c$ -axis maxima, but the  $c$ -axes are not continuously rotated towards these maxima (Fig. 6.12c and d). The CPO of the domains with new grains is unrelated to the gradual lattice rotations within the undulatory domains. New grains are at high angles (much greater than  $15^\circ$ ) to adjacent host domains. The new grains thus developed by a mechanism different from subgrain rotation recrystallisation. Microcavities, fluid channels and fluid inclusions, that are observed in the domains with new grains and on the boundaries of the new grains indicate a strong relationship to the presence of the water (den Brok and Spiers 1991). New grains and arrays of new grains within healed cracks may have developed by precipitation from solution (den Brok and Spiers 1991, den Brok 1992, Hippertt and Egydio-Silva 1996) and subsequent growth by fluid assisted grain boundary migration (Drury and Urai 1990, Mancktelow and Pennacchioni 2004), as delineated by the serrated grain boundaries. TEM analyses indicated that small dislocation free new grains have grown at the cost of larger grains with high dislocation densities. The high dislocation densities in the large grains indicate that the recrystallised grains deform further by glide controlled lattice rotation (although they have an optically uniform internal orientation). This could also be deduced from the elongated shape of these grains perpendicular to  $\sigma_1$  and the  $c$ -axis maxima at  $45^\circ$  to  $\sigma_1$ . This orientation is ideal for glide on the basal plane. A stable CPO must already have formed at very low strain, because  $c$ -axes patterns of samples deformed parallel to  $\langle o \rangle$ , GRU37 ( $\epsilon=14\%$ ) and GRZ30 ( $\epsilon=29\%$ ) are similar, despite the difference in strain. Consequently, once recrystallised grains have rotated their  $c$ -axis too far away from the  $45^\circ$  to  $\sigma_1$  orientation they must have been eliminated by growth of freshly precipitated, more favourable oriented grains with lower dislocation densities.

The  $\text{Mn}_2\text{O}_3$ -powder may have triggered dissolution due to local stress concentrations and precipitation of new grains by making the solution impure and acting as precipitation nuclei. No buffering effect of the powder is expected (Post et al. 1996).

### 6.4.2 Crystal lattice rotations in the host domains

Gradual rotations of the crystal lattice are observed within the domains of undulatory extinction. In these domains deformation is crystal-plastic and the lattice is reoriented by glide controlled lattice rotation. The rotation axes in the studied samples are always about perpendicular to  $\sigma_1$ , regardless of the starting orientation. Still, the orientation of these rotation axes depends on the starting orientation of the sample. The potential slip systems are listed in Table 6.2, which also gives their Schmid factors in the three starting orientations.

The two rotation axes that were defined in sample GRZ33 (starting orientation  $\sigma_1 // \langle c \rangle$ ) are very close to  $\langle a \rangle$ . The  $a$ -axis can be the rotation axis for prism  $\langle c \rangle$  slip. This slip system, however, could theoretically not be activated in this sample (Table 6.2). Therefore the sample must have undergone a rigid rotation of a few degrees before crystal plastic deformation started (as observed in Figure 6.3a). Another explanation might be that several rhomb  $\langle a \pm c \rangle$  slip systems are equally well oriented and could therefore be simultaneously activated instead of a single one. This would allow for rotation axes aligned with  $\langle a \rangle$  or with other orientations in the basal plane. However, indisputable proof for rhomb  $\langle a \pm c \rangle$  slip systems does not exist in the literature. Rhomb slip planes combined with  $\langle a \pm c \rangle$  Burgers vectors have never been observed in the TEM. The existence of rhomb  $\langle a \pm c \rangle$  glide is only theoretically based on geometrical and energy arguments (Baëta and Ashbee 1969 a and b). Therefore the first interpretation is favoured.

Slip system	Schmid factor for starting sample orientation with:		
	$\sigma_1 // \langle c \rangle$ GRZ33	$\sigma_1 // \langle a \rangle$ GRZ30 GRU37	$\sigma_1 // \langle a \rangle$ GRZ34
Basal $\langle a \rangle$	0.000	<b>0.500</b>	0.000
	0.000	0.250	0.000
	0.000	0.250	0.000
Prism $\langle a \rangle$	0.000	0.217	<b>0.433</b>
	0.000	0.217	<b>0.433</b>
	0.000	0.000	0.000
Prism $\langle c \rangle$	0.000	<b>0.433</b>	0.000
	0.000	<b>0.433</b>	0.000
	0.000	0.000	0.000
Rhomb $\langle a \rangle$	0.000	0.325	0.340
	0.000	0.309	0.340
	0.000	0.015	0.000
Rhomb(r) $\langle a \pm c \rangle$	0.458	0.333	0.458
	0.458	0.262	0.458
	0.458	0.125	0.229
	0.458	0.044	0.229
	0.458	0.044	0.000
	0.458	0.033	0.000

**Table 6.2:** Schmid factors of the most important slip systems known for quartz (e.g. Lister et al. 1978) for the three different starting orientations of the samples deformed in this study. Schmid factors of common slip systems which are higher than 0.4 are bold.

The two rotation axes that were defined in sample GRZ30 (starting orientation  $\sigma_1 // \langle 0+ \rangle$ ) were not directly related to a specific crystal orientation. This is either because the data from which the rotation axes are deduced are randomised by slightly rotated fracture fragments, and could therefore not be precisely traced, or because several different slip systems were activated during deformation. Two slip systems in sample GRZ30 have a considerably high Schmid factor, basal $\langle a \rangle$  and prism  $\langle c \rangle$  (Table 2) and are equally favoured at the temperature of deformation (Blacic 1975). Their combination can result in any rotation axis within the basal plane. The two measured rotation axes are probably not similar because the relative contributions of both slip systems were different for the two datasets. Both rotation axes are, however, fairly close to  $\{m\}$ , indicating basal $\langle a \rangle$  as being the dominant glide system.

Sample GRZ34 (starting orientation  $\sigma_1 // \langle a \rangle$ ) shows two broadly similar rotation axes. These axes do not coincide with a common crystal direction, but are reasonably close to  $\langle c \rangle$ . The  $c$ -axis is the rotation axis of prism $\langle a \rangle$  slip, which is a common slip system with a high Schmid factor in this sample (Table 6.2).

#### 6.4.3 CPO development in the new grain aggregates

The microstructures of the domains with recrystallised grains provide evidence for solution-precipitation creep. But whereas the new precipitated grains of Hippertt and Egidio-Silva (1996) showed similar orientations as the original host grain and new precipitated grains of den Brok (1992) grew in a random orientation, the new grains that were measured in this study formed well defined CPOs. Why do they exhibit such a strong CPO? Bons and den Brok (2000) presented a model in which the coupled action of preferential growth or dissolution of grains with certain crystallographic orientations and rigid body rotation of grains lead to CPO development. This could, however, not have been the case in the studied samples, because the serrated grain boundaries of the recrystallised grains in sample GRZ33 could not have allowed grain boundary sliding and are additionally a strong indication for grain boundary migration (Wheeler et al. 2004). It is usually suggested that during grain boundary migration, new grains grow that have a suitable orientation for glide (Schmid and Casey 1986). At low temperatures and under uniaxial compression, this should result in  $c$ -axis small circle girdles at  $45^\circ$  to  $\sigma_1$ , since the basal plane is the easiest glide plane. At high temperatures, this should result in  $c$ -axis girdles at  $90^\circ$  to  $\sigma_1$ , since the prism $\langle a \rangle$  slip system is favoured for deformation (Blacic 1975). TEM analyses of the recrystallised grains indeed indicated that they were crystal plastically deformed. In addition, the  $c$ -axis maxima observed in the recrystallised domains of the samples have favourable orientations for glide at low temperatures: (i) a small circle girdle at  $\sim 45^\circ$  to  $\sigma_1$  in sample GRZ33, (ii) point maxima at  $45^\circ$  to  $\sigma_1$  in sample GRZ30, (iii) a single vertical girdle with strong maxima at  $90^\circ$  to  $\sigma_1$  and  $45^\circ$  to  $\sigma_1$  in sample GRZ34 (Fig. 6.13). The weaker  $c$ -axis maxima that are observed at  $90^\circ$  to the host orientations of sample GRZ30 and GRZ33 might have developed by growth twinning (Frondel 1962, McLaren 1986). Especially Japanese growth twins could be responsible for these specific high angle grain boundaries of the grains that build these weak maxima (Fig. 6.15b and c, Kruhl and Peternell 2002, Sunagawa et al. 2004).

Precipitation of recrystallised grains from solution is thus successful in accommodating orientations that are favoured for intracrystalline deformation within the samples. This process must have been responsible for weakening the crystal (GRZ33) or keeping the crystal weak (GRZ30 and GRZ34). It counteracts the crystal lattice rotations within the host domains of samples GRZ30 and GRZ34, where the crystal is rotated out of the weak host orientations.



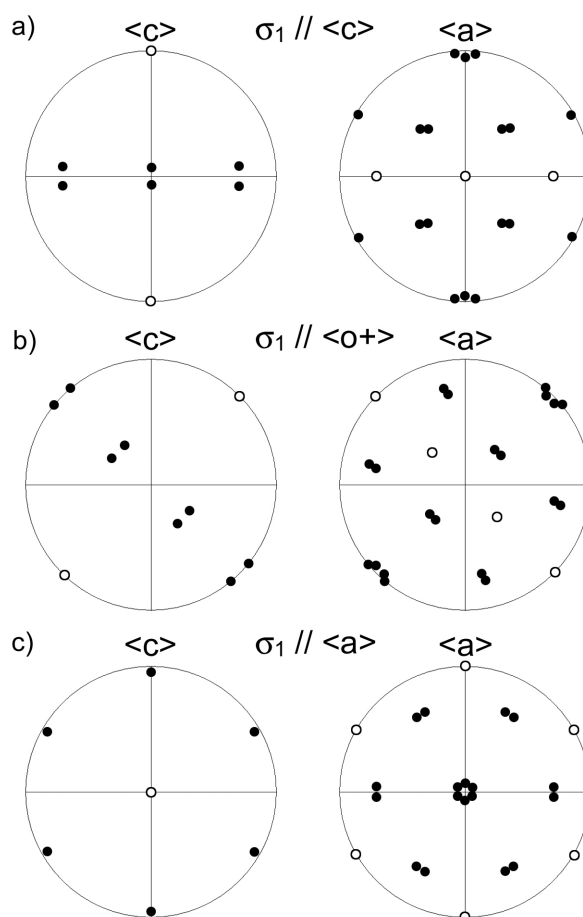


**Figure 6.15:** Japanese twin orientations (upper hemisphere, equal area pole figures) calculated after McLaren (1986) for the three starting orientations of the samples; a)  $\sigma_1 // \langle c \rangle$ , b)  $\sigma_1 // \langle o+ \rangle$  and c)  $\sigma_1 // \langle a \rangle$ . Open circles indicate the starting orientation of the samples; black circles indicate the corresponding Japanese twin orientations.

#### 6.4.4 Comparison with previous data

Hobbs (1968) performed deformation experiments on natural quartz single crystals, also in a Griggs deformation apparatus at a temperature of 900°C, a pressure of 1 GPa, to 50% strain. The water was supplied by a dehydration reaction of the talc confining medium at 900°C. Optically strain-free recrystallised grains that developed in clusters through the samples built  $c$ -axes maxima at 50° to  $\sigma_1$ . Hobbs (1968) found that these maxima formed because new grains grew in a preferred orientation. He inferred that the orientation depended on the orientation of the stress field as well as on the crystallographic orientation of the original crystal. He inferred that these new grains developed from subgrains which differed greatly in orientation from the neighbouring subgrains and therefore started to grow into the adjacent matrix. The difference with our model is that: (i) we interpret subgrains as fracture fragments because their development could be related to longitudinal fractures and because of abundant fluid inclusions on their grain boundaries, (ii) these fracture fragments only rotated by small amounts away from their host orientation, (iii) completely new grains nucleate and grow in far away orientations. In our model, as in the model of Hobbs (1968), recrystallised grains are further selected by preferred growth in orientations suitable for deformation.

Shelley (1971) already pointed out that new grains could perhaps also develop from entirely *new* nuclei. He described straight cross girdle fabrics (Type II) with an opening angle of  $\sim 40^\circ$  to  $\sigma_1$  in flattened quartz phenocryst (that were originally single crystals) from naturally

deformed quartz porphyry. New grains in the flattened phenocrysts were very similar in appearance to those produced in the laboratory experiments of Hobbs (1968) and to those observed in this study. He also showed that the crossed girdles did not significantly change with strain as in the experimentally deformed samples described in this paper. If the *c*-axis patterns of the sample studied are combined (Fig. 6.16) a comparable crossed girdle is observed. This would imply that such a girdle could indeed develop by preferred nucleation and growth. We must, however, take into account that the effect of the three starting orientations acting on each other is unknown and that the crossed girdle pattern can only develop if deformation is not rotational symmetric. During rotational symmetric deformation, a small circle girdle with opening angle  $45^\circ$  is expected to develop.

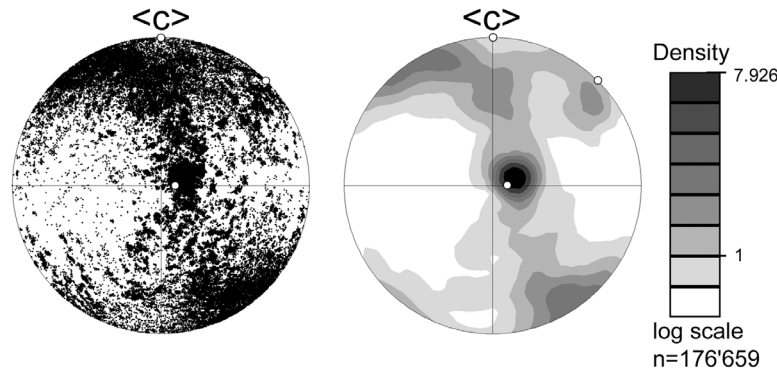


**Figure 6.16:** Upper hemisphere, equal area (contoured) pole figures of the new grain data of sample GRZ30, GRZ33 and GRZ34 plotted together. Open circles indicate the starting orientations of the samples.

## 6.5 CONCLUSIONS

This study yields the following conclusions:

- 1) Single crystals of quartz with different starting orientations were experimentally deformed at  $800^\circ\text{C}$ ,  $1.2\text{ GPa}$  and  $\sim 10^{-6}\text{ s}^{-1}$  to bulk finite strains of 15-30%. They displayed two different types of deformation microstructures: (i) undulatory extinction and deformation lamellae, and (ii) recrystallised grains. Undulatory extinction and deformation lamellae are indicative for intracrystalline plasticity. Isolated new grains, arrays of new grains and aggregates of new grains at the sample ends have developed by precipitation from solution and subsequent fluid assisted growth.
- 2) The crystal lattice rotated around well defined rotation axes by glide controlled lattice rotation within the domains with undulatory extinction. The rotation axes were always approximately perpendicular to  $\sigma_1$  and perpendicular to the sample cut, regardless of the starting orientation. Some of them were related to low-index crystal orientations. The maximum amount of rotation is  $\sim 30^\circ$  away from the host orientation.
- 3) Strong CPOs were observed in the recrystallised aggregates. The CPOs always consisted of *c*-axis maxima at  $45^\circ$  to  $\sigma_1$ , regardless of the starting orientation and regardless of the amount of strain. Crystal orientations within the host domains did not continuously rotate into the domains with new grains. Recrystallised grains, once precipitated from solution, must have grown in orientations that are favoured for intracrystalline plastic deformation at the imposed experimental conditions. Less strong *c*-axis maxima observed perpendicular to the starting orientation and also at  $45^\circ$  to  $\sigma_1$  could be explained by Japanese growth twinning. Dynamic recrystallisation in the samples was a continuous process involving nuclei development by precipitation from solution, fluid assisted growth of nuclei with orientations favoured for deformation and glide controlled lattice rotations.

---

**CHAPTER 7:  
'BRITTLE' SHEAR ZONES  
IN EXPERIMENTALLY DEFORMED QUARTZ SINGLE CRYSTALS<sup>1</sup>****ABSTRACT**

Intracrystalline shear zones developed in a quartz single crystal that was experimentally deformed to 26% finite strain in the macroscopically ductile deformation field. The crystal was uniaxially compressed parallel to  $\langle c \rangle$ , in the presence of 1 vol% of added water, at a temperature of 800°C, a confining pressure of 1200 MPa and a strain rate of  $10^{-6} \text{ s}^{-1}$ . We investigated how the shear zones initiated and how their structure evolved with ongoing deformation. Detailed crystallographic orientation analyses were carried out with the help of the electron backscatter diffraction (EBSD) technique and transmission electron microscopy. The shear zones appeared to develop along planar microcracks oriented parallel to crystallographic rhomb planes. Further microcracking resulted in cataclastic shear zone development. New grains developed by rotation of fracture fragments. The rotation of the fragments in the shear direction was probably facilitated by the high water pressure and the relatively high porosity in the shear zone. Full-grown shear zones finally exhibit a  $\langle c \rangle$  maximum at  $\sim 90^\circ$  to the shear zone boundary. Our results suggest that cataclastic deformation processes may lead to shear zone development. A CPO developed within the shear zones because new grains with  $\langle c \rangle$  oriented perpendicular to the shear zone boundary grew at the cost of other new grains.

**KEYWORDS**

Quartz; Experimental deformation; Shear zones; Microcracking; Electron backscatter diffraction (EBSD); Transmission electron microscopy

**7.1. INTRODUCTION**

Deformation in the Earth's crust is generally inhomogeneous and often localised in shear zones (Ramsay, 1980). Shear zones are very common in quartz-rich rocks deformed in the middle and lower crust. Their geometry, microstructures and crystallographic preferred orientations (CPOs) often possess clear asymmetries with respect to the macroscopic foliation and lineation. Therefore they preserve information about the deformation history and the relative sense of movement.

Still little is known about how shear zones initiate and evolve once they have formed. It has been argued that shear zones can nucleate on grain scale brittle fractures (Segall and Simpson, 1986; Ralser, 1990; van Daalen et al., 1999). It is not yet clear when in the deformation history such fractures are introduced: during a preceding phase of extension (van Daalen et al., 1999), during a preceding phase of compression (Segall and Simpson, 1986; Ralser, 1990), or simultaneously by progressive deformation and shear zone development. The subsequent deformation accommodated by the shear zones has mostly been assumed to be crystal-plastic, because the (small) new grains within the shear zones exhibit a microstructure commonly interpreted to have formed by dynamic recrystallisation. Models that aimed at understanding dynamic recrystallisation are mainly based on two processes: 1) subgrain

---

<sup>1</sup> Manuscript submitted to Journal of Structural Geology: 'Brittle' shear zones in experimentally deformed quartz single crystals. By Martine G.C. Vernooij, K. Kunze and Bas den Brok.

rotation, and 2) grain boundary migration (Urai et al., 1986). However, local analyses of new ‘recrystallised’ grains in naturally deformed dolomite and calcite shear zones have shown that the misorientation relationships between parent and recrystallised grains cannot be explained by simple models of subgrain rotation and grain boundary migration recrystallisation alone (Leiss and Barber, 1999; Bestmann and Prior, 2003). Thus, other processes were discussed to be invoked: (1) rigid body rotation, (2) nucleation and (3) diffusion accommodated grain boundary sliding. These processes may exert an important control on the formation of new grains.

This study focuses on how microscopic shear zones nucleate in quartz deformed in the presence of water and on the role of dynamic recrystallisation during the progressive deformation in these zones. We studied conjugate intracrystalline shear zones that developed during experimental deformation at high pressure (1.2 GPa) and temperature (800°C) in a natural quartz single crystal with the compression direction ( $\sigma_1$ ) parallel to  $\langle c \rangle$ . Various shear zones reflecting different stages in the shear zone evolution are observed in one single sample that was deformed at an approximately constant strain rate of  $10^{-6} \text{ s}^{-1}$ . The shear zones were analysed using detailed orientation and misorientation analysis based on electron backscatter diffraction (EBSD) data that are presented in orientation maps, misorientation profiles and pole figures. The EBSD observations were verified by transmission electron microscope (TEM) images.

## 7.2. METHODS

### 7.2.1 Sample description

In the course of this thesis, a series of quartz single crystal samples were deformed in different starting orientations ( $\sigma_1 // \langle c \rangle$ ,  $\sigma_1 // \langle o+ \rangle$ ,  $\sigma_1 // \langle a \rangle$  and  $\sigma_1 \sim \perp \{r\}$ ) with and without added water. Intracrystalline shear zones developed only in the sample that was deformed parallel to  $\langle c \rangle$ , and only in the presence of water. This sample (GRZ25) is further described in this paper. The sample was cored from a natural quartz single crystal from Arizona, using a diamond coring tool with water as a lubricant. The crystal was transparent, clear of fluid inclusions and without optically visible defects. The internal water content of the crystal was  $\sim 0.002 \text{ wt}\%$  (determined by Fourier transform infrared (FTIR) spectroscopy and calculated using the calibration of Paterson (1982)). The ends of the sample (measuring 5.85 mm in diameter and 12.1 mm in length) were ground flat and parallel. The sample was weld-sealed in a gold capsule together with 1 vol% of pure water following the procedure described in den Brok (1992).

### 7.2.2 Deformation test

The deformation experiment was performed in a Tullis-modified solid medium Griggs deformation apparatus. The sample assembly was brought to a confining pressure of 1.2 GPa and a temperature of 800°C within 7.5 hours following the water isochore of  $1 \text{ g cm}^{-3}$  as closely as possible. Then it was loaded (no “cold hit”) and deformed in uniaxial compression at a constant axial displacement rate corresponding to an initial strain rate of  $1.1 \cdot 10^{-6} \text{ s}^{-1}$ . After deformation of the sample, pressure and temperature were lowered in 1 hour, again closely following the  $1 \text{ g cm}^{-3}$  water isochore. The measured axial displacement was corrected for apparatus distortion ( $20 \mu\text{m kN}^{-1}$  at 800°C and 1.2 GPa). The axial load was not corrected for friction increase during the experiment. Differential stress was calculated using the initial cross-section of the sample. A finite strain of 26% was determined based on the final sample length measured ex-situ at room temperature and pressure.

### 7.2.3 Sample preparation for analysis

During deformation, the cylindrical sample developed a slightly elliptical cross-section. To prepare the sections for microscopical analysis, the sample was cut parallel to the long axis of the ellipse and parallel to the compression direction. One half of the sample was impregnated with Epofix so that a thin section could be polished without losing much material. The thin section was polished to a very fine polishing grade (using 0.05  $\mu\text{m}$  alumina suspension). The other half of the sample was used to prepare a 200  $\mu\text{m}$  thick section for EBSD analysis and to prepare another thin section for TEM analysis. The thick section was mechanically polished like both thin sections and subsequently lapped for 8 hours using an alkaline colloidal silica suspension (particle size 25 nm). To avoid charging, the EBSD thick section was coated with a  $\sim 4$  nm carbon layer and covered around the lapped sample surface with silver paint. The areas that were selected for TEM analysis on the non-impregnated thin section were thinned by ion-milling until electron transparency was reached ( $\sim 0.1$ - $0.2$   $\mu\text{m}$  thickness). The TEM sample was also carbon coated to avoid charging problems. The TEM analyses were performed with a Philips CM20 FEG TEM, operating at 200 kV, at the University of Bayreuth, Germany.

### 7.2.4 EBSD data acquisition and analysis

Full crystallographic orientation data were obtained from automatically indexed electron backscatter diffraction (EBSD) patterns (Adams et al., 1993; Prior et al., 1999). EBSD patterns were acquired using an EDAX\_TSL DigiviewFW camera system attached to an SEM Camscan CS44LB. The EBSD patterns were obtained using 15 kV acceleration voltage, 35 mm working distance,  $\sim 3$  nA beam current and  $70^\circ$  sample tilt. EBSD scans were run on square grids with a stepsize of 0.5  $\mu\text{m}$  at a typical scan speed of 9 patterns per second. The patterns were collected and indexed with the commercial TSL software OIM DC 3.5<sup>TM</sup> and analysed with OIM Analysis 3.0<sup>TM</sup> and 3.5<sup>TM</sup>.

Recorded data contain the crystal orientation (given by three Euler angles), the xy-coordinates of the spot on the sample and an indexing reliability parameter (confidence index between 0 and 1). The analyses show a large number of data with a high reliability (confidence index  $> 0.1$ ). The obtained data are presented in (1) orientation maps, (2) a pattern quality map, (3) misorientation profiles and (4) pole figures.

In orientation maps, the colour of each pixel corresponds to the crystal direction parallel to the compression axis ( $\sigma_1$ ) in the corresponding colour key. In pattern quality maps, grey shades relate to band sharpness of the EBSD-pattern. Since these pattern quality maps reproduce surface damage, fractures and (sub)grain boundaries they form an additional image of the microstructure and are useful to verify the reliability of the orientation maps. The deformation experiment was performed close to the transition temperature from  $\alpha$ - to  $\beta$ -quartz, which is  $850^\circ\text{C}$  at 1200 MPa (Bagdassarov and Delépine, 2004). Therefore it is not clear whether the indexed Dauphiné twins, which are repeatedly indexed, are induced during deformation or during cooling (the starting material was free of Dauphiné twins). Potentially ambiguous results from misindexing in Dauphiné twin orientations are avoided here by treating the quartz data in our analysis as being hexagonal. The raw orientation maps for hexagonal quartz still contain a number of erroneous data, especially along grain boundaries, on subgrain boundaries, on surface scratches, holes or other surface artefacts where the pattern quality was low. The OIM software provides a simple algorithm to clean these erroneous data by replacing them by the most common neighbouring orientation. Because the step-size is much smaller than the grain size, most erroneous data can be identified as single pixels that are different from all surrounding points.

Misorientation profiles were drawn along lines in the cleaned orientation maps. The misorientation angle between adjacent points along these lines was calculated by selecting the

minimum angle that enables the lattice of one point to be rotated into that of the other (Wheeler et al., 2001). The data along the lines were selected, plotted in pole figures and used to specify rotation paths and rotation axes. We developed a simple program to calculate the best-fit rotation axes based on the determination of second order moments of the orientation distributions.

### 7.3. RESULTS

#### 7.3.1 Mechanical data

The stress-strain curve (Fig. 7.1) shows an initial stage of linear work hardening until a peak stress of  $\sim 410$  MPa was reached at  $\sim 2\%$  bulk strain. After that there is a stage of weakening until  $\sim 10\%$  bulk strain, followed by a stage of non-linear work hardening until a constant flow stress was reached ( $\sim 470$  MPa) beyond  $\sim 22\%$  bulk strain.

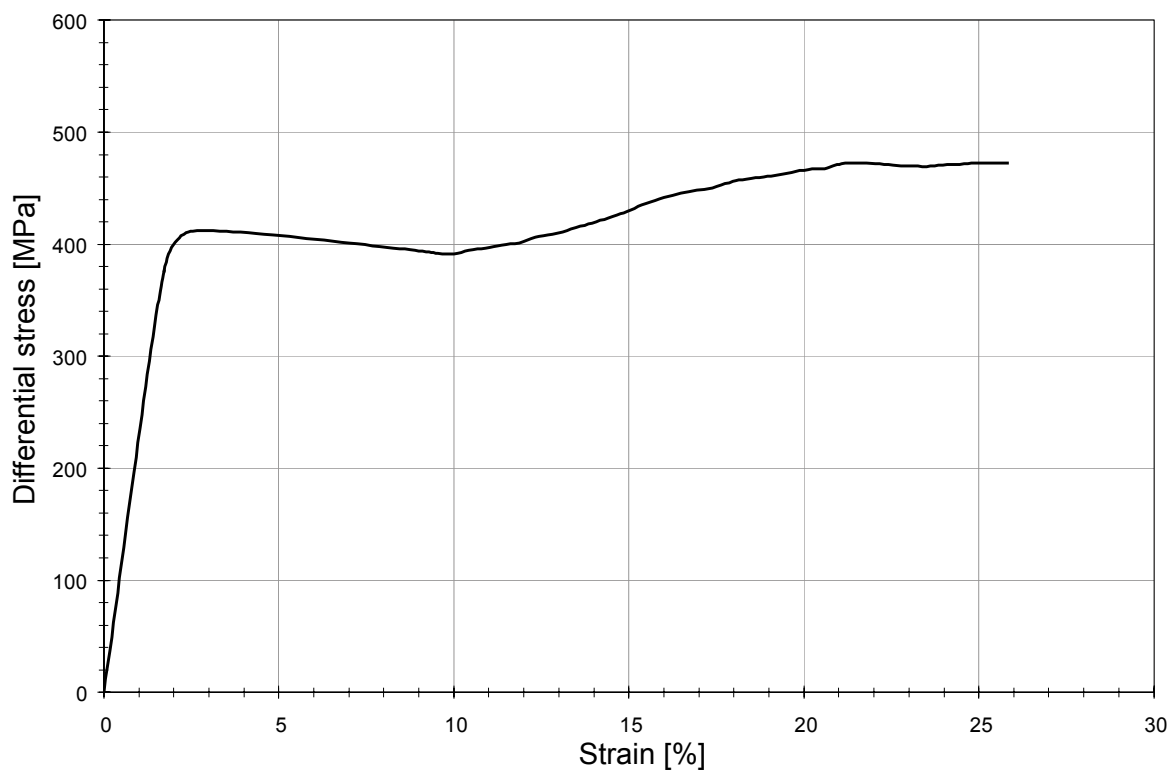


**Figure 7.1:** Differential stress versus strain curve for the deformation experiment. The sample (GRZ25) was deformed with  $\sigma_1 // \langle c \rangle$ , at  $800^\circ\text{C}$ , a confining pressure of 1.2 GPa and an approximately constant strain rate of  $1.1 \cdot 10^{-6} \text{ s}^{-1}$ .

#### 7.3.2 Microstructures

The sample strain is particularly concentrated at the lower end of the sample (Fig. 7.2) in a wedge shaped sector containing a dense network of conjugate intracrystalline shear zones. These shear zones are typically up to  $10 \mu\text{m}$  wide and cross-cut the sample in diagonal directions (Fig. 7.3a). In general, shear zones dipping to the right record a dextral offset and have a blue colour (Fig. 7.3b) under crossed polarisers with the gypsum plate; shear zones dipping to the left have sinistral displacement and a yellow colour (Fig. 7.3c). Grains in the middle of the shear zones are too tiny to be optically distinguishable. Grains near the shear zone boundaries are optically strain-free (no undulatory extinction) and have a sub-euhedral

shape (Fig. 7.3b and c). These grains are slightly elongated with their long axis perpendicular to the shortening direction, at 40-45° to the shear zone boundary. The shear zones are traced by trails of very tiny fluid inclusions (Fig. 7.3a and c). They encompass blocks of the host crystal with low strain deformation microstructures, i.e. continuous undulatory extinction and deformation lamellae. One area with conjugate sets of shear zones that reflect different stages of shear zone evolution was chosen for EBSD analysis (Fig. 7.3d).

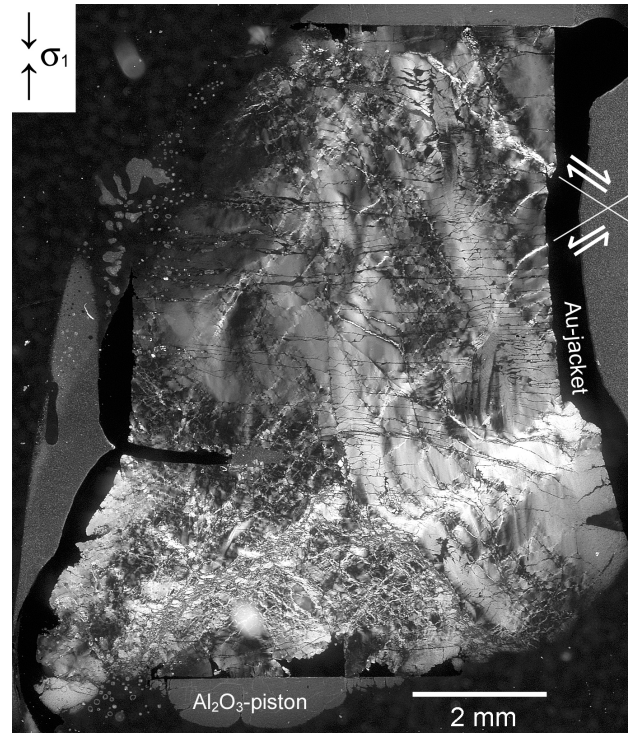


**Figure 7.2:** Optical light micrograph of heterogeneously deformed sample (GRZ25) in cross polarised light. Most strain is accommodated at the lower end of the sample along a wedge shaped network of conjugate sets of shear zones. The few shear zones at the sample edge reveal the sense of shear (white arrows). In the less deformed part of the sample, zones of undulatory extinction developed approximately parallel to  $\langle c \rangle$ .

TEM images reveal that the interiors of the shear zones consist of  $\sim 2 \mu\text{m}$  diameter new grains (Fig. 7.4a). These grains have a variety of crystallographic orientations, straight grain boundaries and round edges. The grain boundaries are decorated with  $\sim 0.1 \mu\text{m}$  voids. Numerous larger voids ( $\sim 1 \mu\text{m}$ ) occupy triple junctions between the new grains (Figs. 7.4a and b) indicating a high (presumably fluid-filled) porosity within the shear zones. Within the new grains, there is a high dislocation density, especially at the grain contacts (Fig. 7.4b). The dislocations are curved, tangled and sometimes occupy straight subgrain walls.

Curved and tangled dislocations are also observed within the host domains of the sample. The dislocation density within the host is high ( $10^{10} \text{ cm}^{-2}$ ). TEM images were taken with diffraction vectors  $g=10\bar{1}1$ ,  $g=10\bar{1}0$  and  $g=0003$  in order to determine the Burgers vectors by applying the  $g \cdot b = 0$  criterion. Most dislocations are out of contrast with  $g=10\bar{1}0$  and  $g=0003$  but are well visible with  $g=10\bar{1}1$  (Fig. 7.4c). Therefore the Burgers vector of the free dislocations is mostly  $b=1/3\langle 11\bar{2}0 \rangle$ . Within the host domains, several straight walls that are decorated with very tiny voids ( $\sim 0.1 \mu\text{m}$ ) occur (Fig. 7.4c). They are oriented parallel to the shear zones and separate areas of slightly different dislocation density.



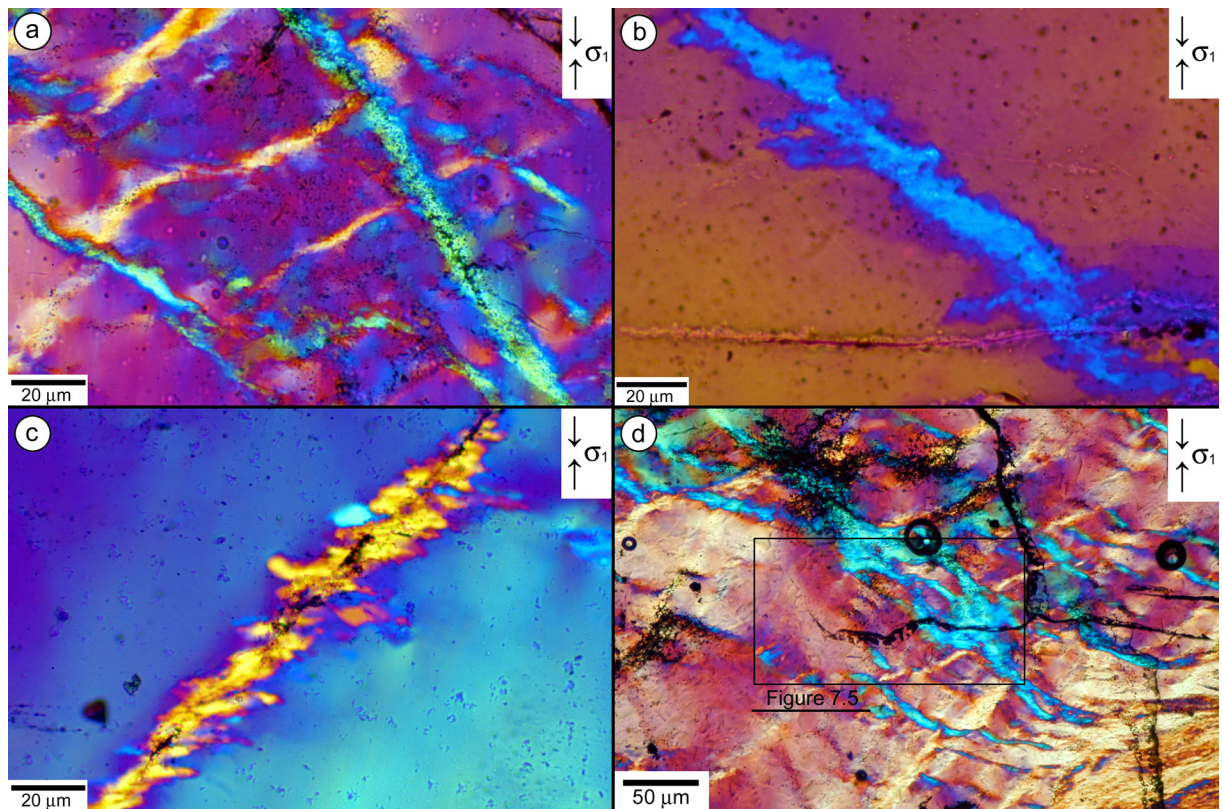


**Figure 7.3:** Light micrographs (crossed polarisers; gypsum plate) of experimentally produced intracrystalline shear zones in sample (GRZ25) deformed parallel to  $\langle c \rangle$  at  $800^\circ\text{C}$ , confining pressure of 1.2 GPa and approximately constant strain rate of  $1.1 \cdot 10^{-6} \text{ s}^{-1}$ . The tiny new grains in the shear zones have a distinctly different crystallographic orientation than the surrounding host material. Shear zones are traced by fluid inclusions. Grains at the shear zone boundaries are elongated perpendicular to  $\sigma_1$ . (a) Conjugate sets of shear zones from the high strain end of the sample. (b) Shear zones dipping to the right are dextral and have a blue interference colour. (c) Shear zones dipping to the left are sinistral and have a yellow interference colour. (d) Part of the sample with shear zones that reflect different stages of shear zone development. Box indicates the location of the EBSD scan of Fig. 7.5.



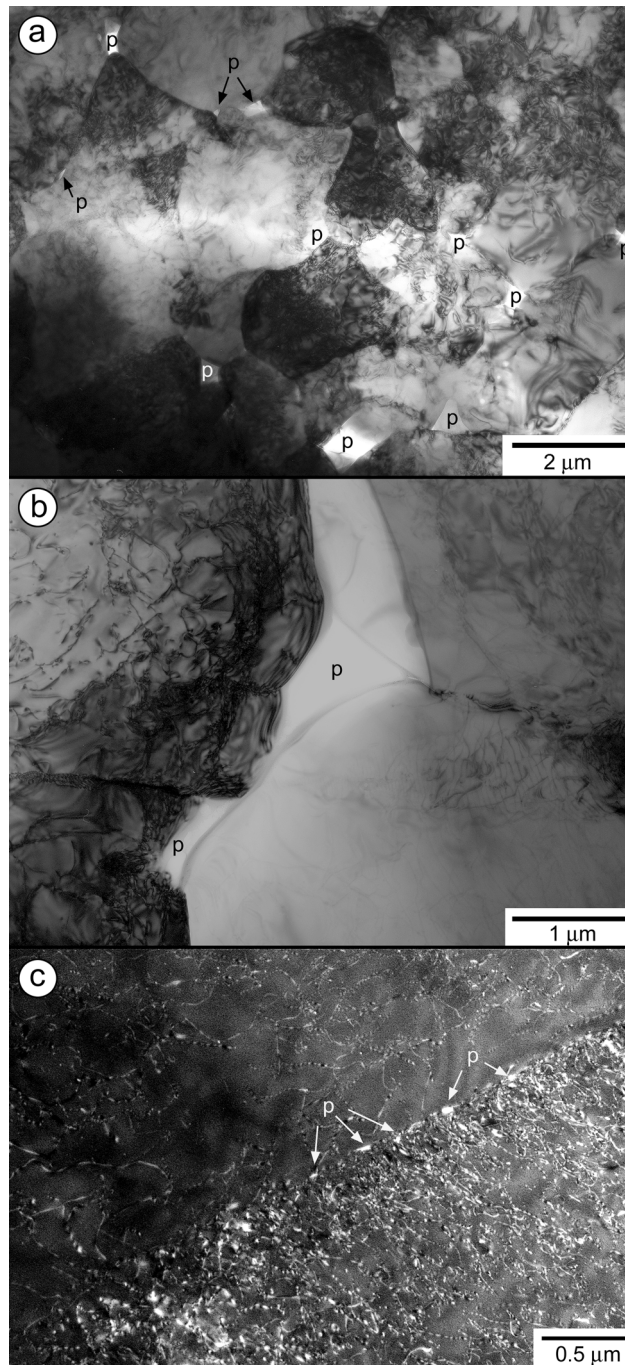


**Figure 7.4:** (a) Bright field TEM micrograph of new grains and voids (marked with “p”) within the interiors of the shear zones in sample GRZ25. The new grains have straight, as well as curved grain boundaries; relatively large numbers of pores are present. (b) Bright field TEM micrograph of triple junction between three new grains. A relatively high density of tangled dislocations and subgrain walls occurs close to the grain boundaries. (c) Dark field TEM micrograph ( $g=10\bar{1}1$ ) of straight wall within the host domain. Tangled and curved dislocations are distributed through the host domains. Walls that are decorated with tiny voids cross-cut the host domains. These walls are approximately parallel to the shear zones.

### 7.3.3 Crystallographic orientations

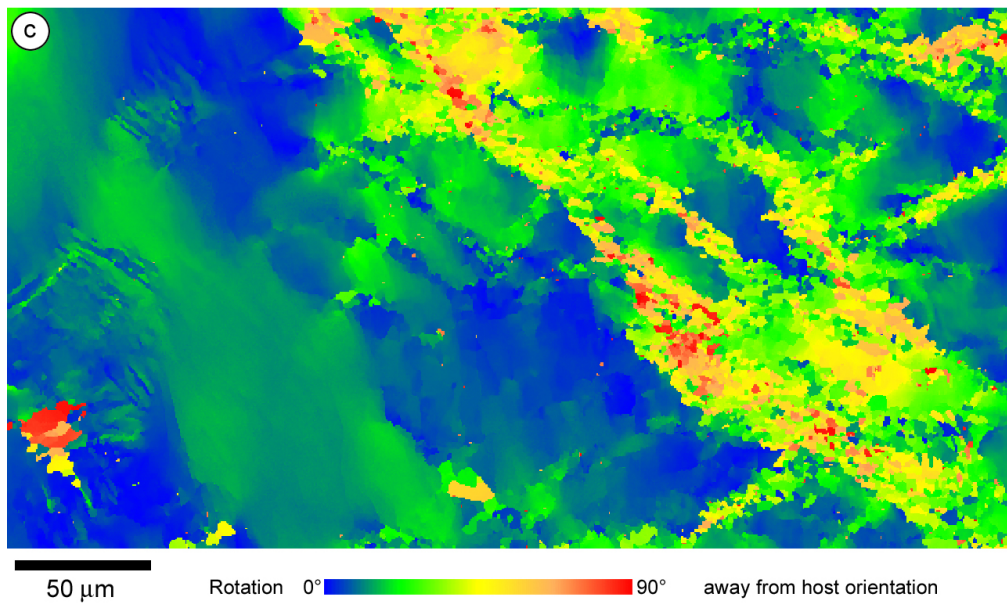
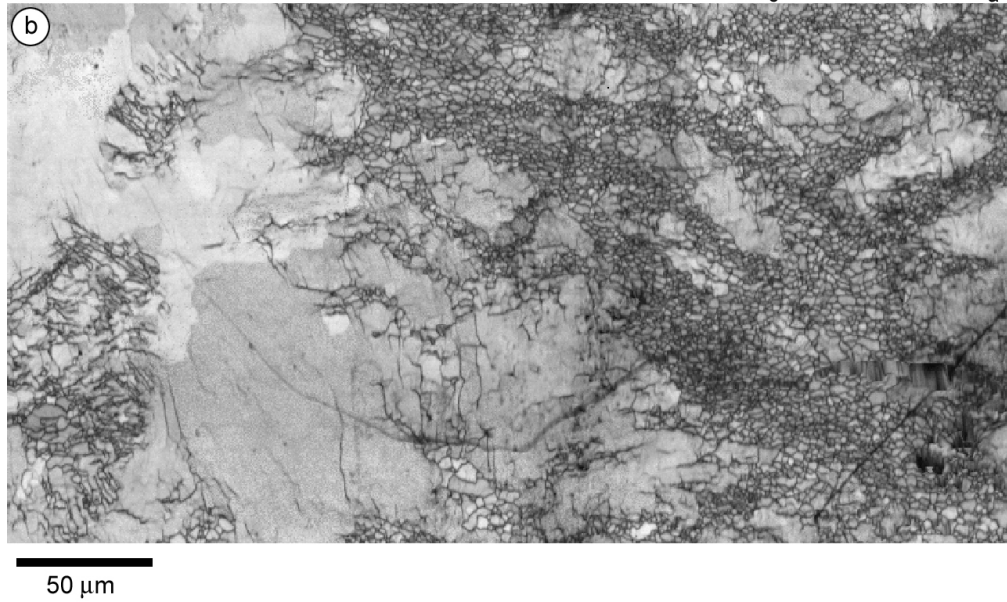
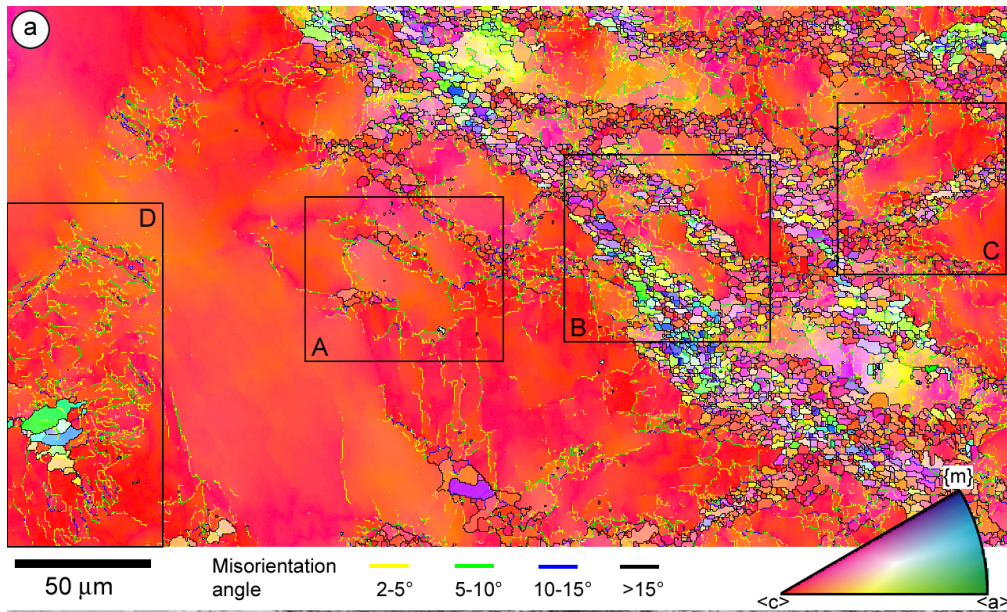
#### 7.3.3.1 Orientation maps

The orientation maps and pattern quality map (Fig. 7.5) reproduce the optical micrograph (Fig. 7.3) accurately. Several different microstructures can be distinguished: (1) gradual orientation changes within the host crystal, (2) aligned small angle boundaries within the host crystal, (3) initial shear zones, consisting of single chains of new (sub)grains along oriented subgrain walls, (4) conjugate sets of transitional and mature shear zones with several rows of new grains and (5) isolated pockets of new grains.

The orientation map (Fig. 7.5a) marks nearest neighbour misorientation angles for different angular intervals, thus indicating and classifying the boundaries. These boundaries are also reproduced in the pattern quality map (Fig. 7.5b) because the data points on subgrain boundaries and grain boundaries have a lower pattern quality than the grain interior. Away from the shear zones, the orientation of the host lattice changes with small spatial gradients, i.e. misorientations below  $2^\circ$  between nearest neighbours. Approaching the shear zones, subgrain boundaries with misorientations of 2 to  $10^\circ$  are observed, which are either aligned more or less parallel or at  $\sim 45^\circ$  to the  $\sigma_1$ -direction. Thus the boundaries may coincide with either prism or rhomb planes of the host crystal, respectively. Within the shear zones, tiny new grains (average size  $3 \mu\text{m}$ ) are observed with high angle grain boundaries, as classified according to White (1977) for misorientation angles  $>10^\circ$ . Close to the shear zone boundaries, the new grains are slightly elongated perpendicular to  $\sigma_1$ . They have a more equidimensional shape in the shear zone interiors. The transition in orientation between the new grains within the shear zones and the host crystal is sudden (misorientation almost exclusively  $>15^\circ$ ). Subgrains in the host crystal are generally larger than the new grains within the shear zones.

Another derived map (Fig. 7.5c) displays the angle of the  $c$ -axes in the deformed sample with respect to the starting orientation of the sample ( $\langle c \rangle // \sigma_1$ ). It illustrates that (1) the angle of rotation increases towards the middle of the shear zone, (2) the angle of rotation is not constant along the shear zones and (3) the largest rotations (up to  $90^\circ$ ) are observed along shear zones that are interconnected or within isolated pockets of new grains.

**Figure 7.5 (next page):** Processed orientation maps. The map is processed by substitution of likely misindexed data. (a) Orientation map colour coded corresponding to the inverse pole figure colour key representing the crystal direction that is parallel to  $\sigma_1$ . To highlight (sub)grain boundaries, nearest neighbour misorientations are colour coded. Shear zones consist of tiny grains with high angle grain boundaries ( $>10^\circ$ ). The host crystal shows gradual rotations and aligned subgrain boundaries. Boxes indicate the locations of the areas that are analysed in detail. (b) Pattern quality map. Grey shades relate to band sharpness of the EBSD-pattern. The pattern quality map reproduces surface damage, fractures and (sub)grain boundaries. (c) Orientation map, colour shaded according to the angle between  $\langle c \rangle$  and the starting orientation of the sample ( $\sigma_1 // \langle c \rangle$ ). The isolated new grains and the new grains in the centres of the shear zones have  $c$ -axes that are up to  $90^\circ$  away from the starting orientation.





### 7.3.3.2 Zone A: Initial shear zones

The orientation map of zone A (Fig. 7.6a) shows two host blocks that are separated by three parallel distorted zones. Each of these zones contains a single array of aligned subgrains and a few new grains that are equal in size but much smaller than the host blocks. The new grains have homogeneous intracrystalline orientations, thus are nominally strain-free. The subgrains display gradual orientation changes internally, similar to gradual rotations within the host blocks. The host crystal orientation shows gradual clockwise and anticlockwise dispersion of up to  $20^\circ$  around an axis perpendicular to  $\sigma_1$  (Fig. 7.7a). The orientations of the few new grains scatter widely around the host orientation. The misorientation profile (Fig. 7.8) illustrates gradual reorientation of the host crystal with point to point misorientations less than  $2^\circ$  and an anticlockwise rotation around a flat lying axis that is near  $\langle a \rangle$  and  $\{m\}$ , but deviates from the common low-index crystal directions. The misorientation axis and the sense of rotation changed where a high angle boundary ( $20^\circ$ ) is crossed (i.e. at the transition from host crystal into a new grain within the shear zone).

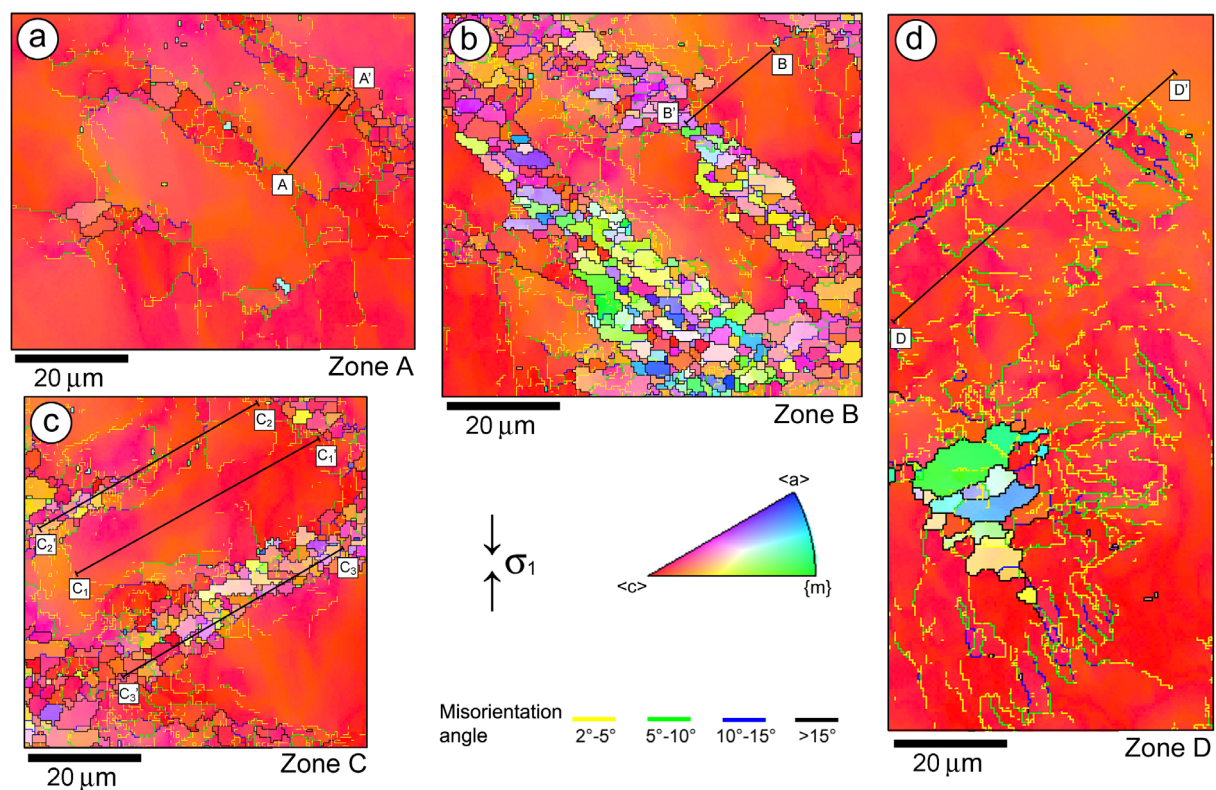


**Figure 7.6:** Processed orientation maps of areas that are analysed in detail. Maps are colour coded corresponding to the inverse pole figure colour key. Grain boundary misorientations are colour coded according to misorientation angle between nearest neighbours. Straight lines indicate the positions of misorientation profiles. (a) Zone A, initial shear zone, (b) Zone B, mature dextral shear zone, (c) Zone C, mature sinistral shear zone and transitional shear zone and (d) Zone D, isolated pocket with new grains.

### 7.3.3.3 Zone B: Dextral mature shear zones

The orientation map of zone B (Fig. 7.6b) shows two mature dextral shear zones that embody several arrays of new grains with fairly constant sizes. The grains in the inner core of the shear zones have equidimensional shapes and the grains near the shear zone periphery are elongated perpendicular to  $\sigma_1$  at  $\sim 45^\circ$  to the shear zone boundary. Especially these elongated grains have  $c$ -axes that are about perpendicular to the shear zone boundary. The host blocks next to the two shear zones are highly deformed and contain several 2 to  $10^\circ$  subgrain boundaries, which separate subgrains with different sizes that are generally larger than the

new grains within the shear zones. New grains are strain-free; subgrains and host crystal show gradual lattice bending. The host lattice spreads roughly  $20^\circ$  away from the starting orientation in all directions (Fig. 7.7b). The new grains show an enormous spread of up to  $90^\circ$  away from the host orientation, with  $c$ -axes almost exclusively displaced in a clockwise sense. The crystallographic orientations of the new grains in the wider shear zone (lower left) are scattered further away from the host orientation than the crystallographic orientations of the new grains in the narrower shear zone (upper right). The misorientation profile (Fig. 7.9) illustrates the counter clockwise rotation of the host lattice around an axis near  $\{m\}$  lying perpendicular to  $\sigma_1$ . Before entering the shear zone, the profile crosses a subgrain boundary which still has the same rotation axis as the host lattice. The crystallographic rotation path of the new grain is inconsistent with that of the host lattice and the subgrain.

#### 7.3.3.4 Zone C: Sinistral mature shear zone and sinistral transitional shear zone

In the orientation map of zone C (Fig. 7.6c), a sinistral mature shear zone (centre right) is displayed with a transitional shear zone (upper left) parallel to it. This transitional shear zone is an initial micro shear zone in the upper right, which develops into a mature zone towards the left. The mature shear zone consists of several arrays of new grains with equidimensional, as well as elongated shapes and high angle grain boundaries as in zone B (Fig. 7.6b). The host lattice shows gradual orientation changes and several subgrain boundaries near the contact with the shear zones. The orientation of the host lattice spreads gradually away from the starting orientation into various directions with a maximum rotation of  $\sim 20^\circ$  (Fig. 7.7c). In the sinistral mature shear zone, the new grains show a large spread up to about  $60^\circ$  away from the host orientation, with  $c$ -axes almost exclusively displaced in an anticlockwise manner. Misorientation profiles show that the reorientation in the host lattice (Fig. 7.10a) is gradual with maximum point to point misorientations less than  $2^\circ$  and a counterclockwise rotation around an axis that is close to  $\{m\}$ . In the profile parallel to the transitional shear zone (Fig. 7.10b), the new grains gradually rotate away from the starting orientation (maximum point to point misorientation of  $15^\circ$ ) instead of the larger jumps in crystallographic orientation that were observed in the misorientation profiles perpendicular to the shear zones (Figs. 7.8 and 7.9). The orientations of the new grains scatter considerably in all directions, but the calculated mean rotation axis of the new grains is close to  $\{m\}$  as well, which is, however, one of the other  $\{m\}$ -poles than the one in the adjacent host lattice. Both the rotation axes of the host crystal and of the new grains in the transitional shear zone are perpendicular to  $\sigma_1$ . The misorientation profile through the mature shear zone (Fig. 7.10c) shows large angle jumps between grains and hardly any orientation spread within the new grains, regardless whether this profile was taken parallel or perpendicular to the shear zone. No common rotation axis of the grains in the mature shear zone could be reliably inferred because of the large spread of the data, which though cluster around an anticlockwise rotated orientation.

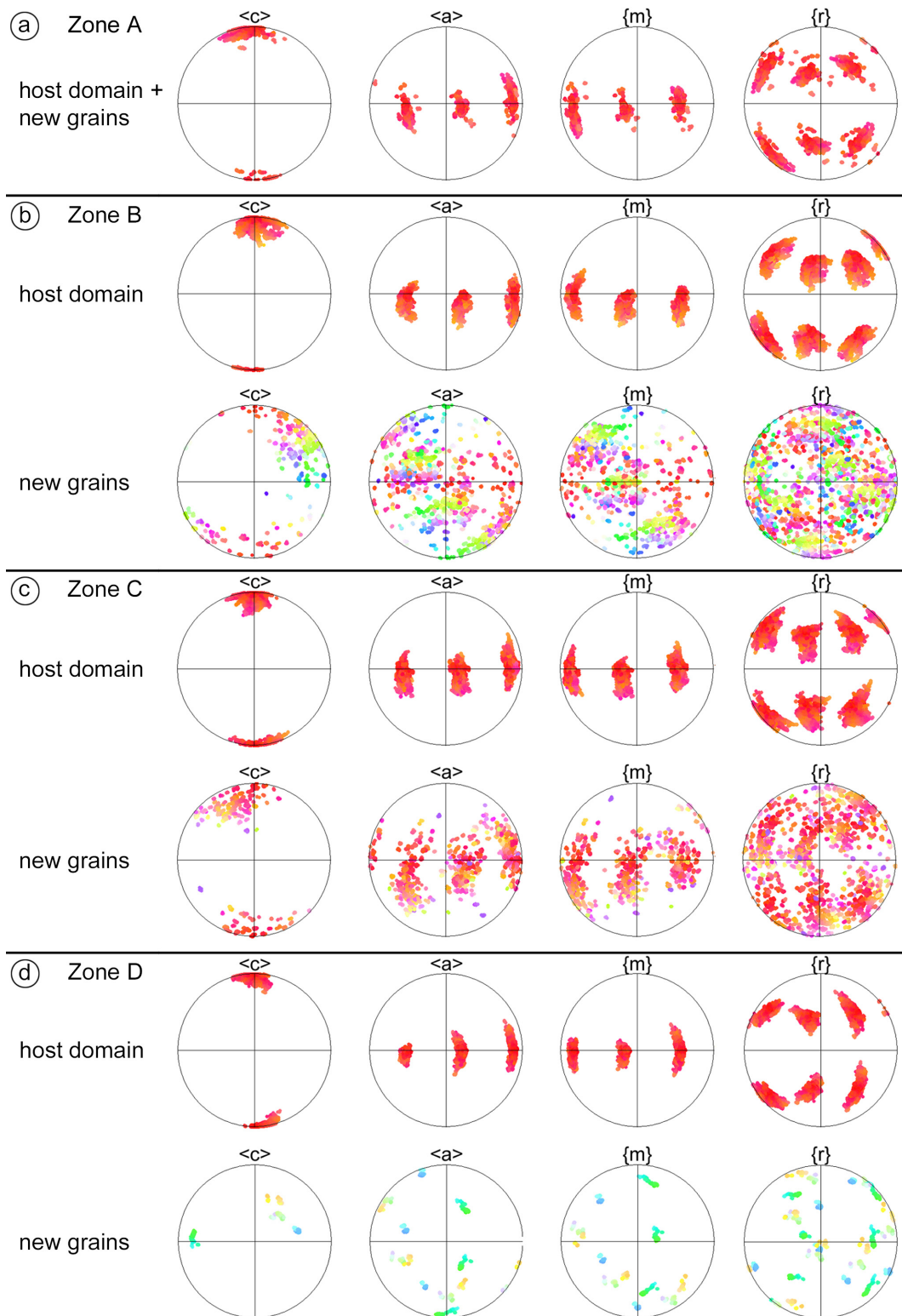


**Figure 7.7:** Pole figures (equal area, upper hemisphere) of the host domains and domains with new grains (defined by grain boundary misorientation  $>10^\circ$  to the host). Figures are coloured with the same colour key as figures 7.4 and 7.5. (a) Zone A, initial shear zone, (b) Zone B, mature dextral shear zone, (c) Zone C, mature sinistral shear zone and transitional shear zone and (d) Zone D, isolated pocket with new grains.

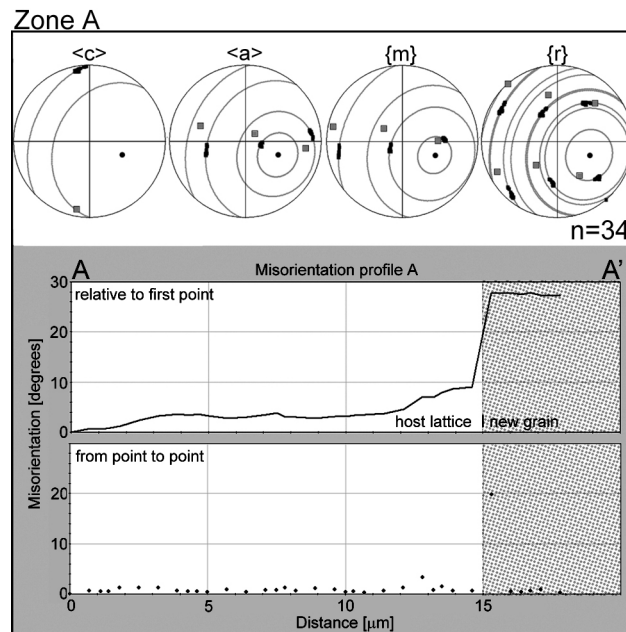


**Figure 7.8:** Profile (A-A'). Its location in zone A (initial shear zone) is given in Figure 7.6a. Top: change of orientation along the line is presented as dispersion patterns in pole figures (equal area, upper hemisphere). Host domain are black squares, new grains are grey squares. Bottom: The continuous change in misorientation angles is displayed with respect to the first point and also from point to point. The domain with the new grain is stippled.

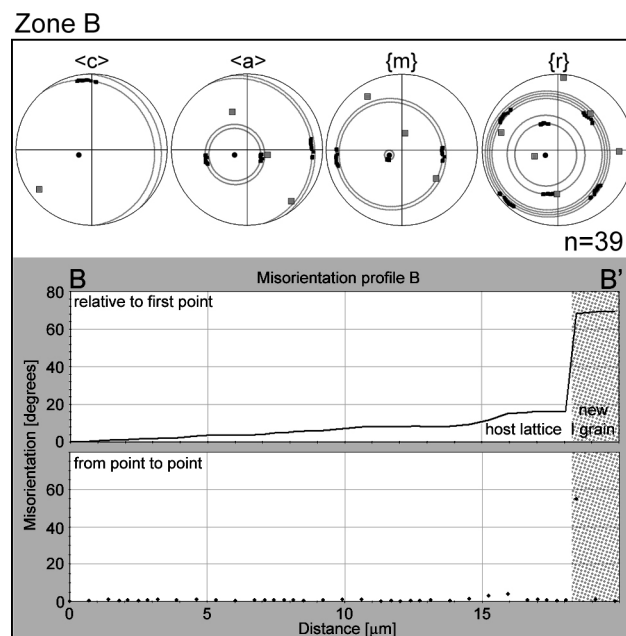


**Figure 7.9:** Profile (B-B'). Its location in zone B (dextral mature shear zones) is given in Figure 7.6b; same presentation as Fig. 7.8.

### 7.3.3.5 Zone D: Isolated pockets of new grains

The orientation map of zone D shows a patch of isolated new grains in a deformed host lattice (Fig. 7.6d). Subgrain boundaries with angles of 5 to 15° are aligned parallel to the rhombohedral planes of the host crystal. The isolated new grains (average size of ~10  $\mu\text{m}$ ) are larger than new grains within the shear zones and are all elongated roughly perpendicular to

$\sigma_1$ . They contain some subgrain boundaries, but no major orientation gradients. The host crystal rotates away from the starting orientation in a clockwise and an anticlockwise sense around a horizontal axis (Fig 7.7d). The new grains scatter largely (up to  $90^\circ$  difference in  $c$ -axes) away from the host orientation and away from each other. The misorientation profile (Fig. 7.11), which crosses several subgrain boundaries with point to point misorientations up to  $9^\circ$ , shows an anticlockwise rotation of the host lattice around an axis close to  $\langle a \rangle$  perpendicular to  $\sigma_1$ . Subgrain boundaries have the same rotation path as the host lattice.

Zone C

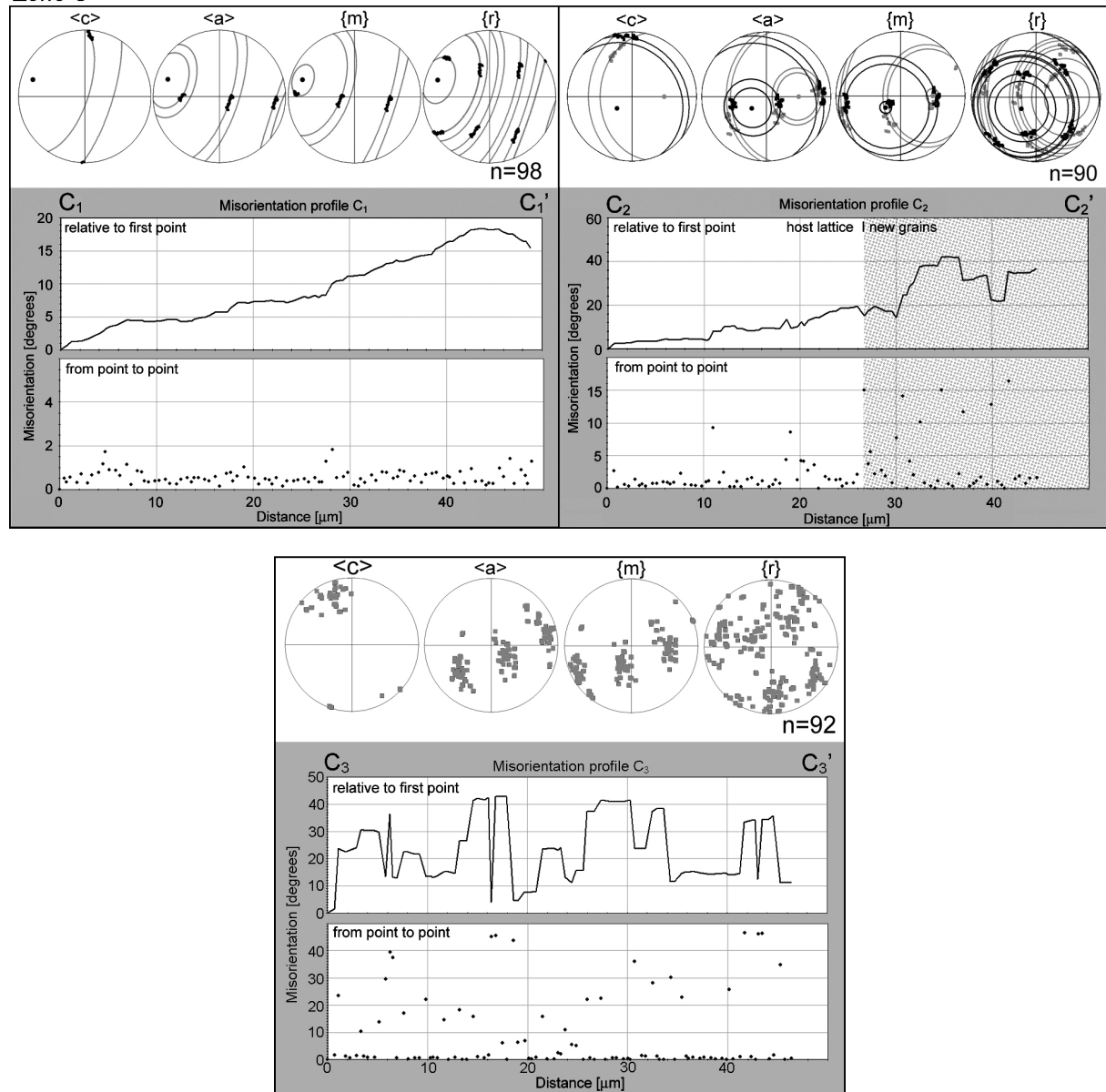


**Figure 7.10:** Profiles ( $C_1$ - $C_1'$ ,  $C_2$ - $C_2'$  and  $C_3$ - $C_3'$ ). The locations in zone C (sinistral mature and transitional shear zones) are given in Figure 7.6c; same presentation as Fig. 7.8.



### 7.3.3.6 Misorientation axes

It is illustrated in the pole figures derived from the data along the profiles (Figs. 7.8-7.11) that axes close to  $\langle a \rangle$  and  $\{m\}$  are possible rotation axes of the deformed host crystal. Given that the rotation axes are determined accurately enough, the inverse pole figure (Fig. 7.12) shows, however, that only one of these rotation axes really coincides with one of the hypothetical rotation axes for single slip on known slip systems in quartz within reasonable limits. Figure 7.13 displays the distribution of the misorientation axes for different intervals of misorientation angle, covering the complete data set containing the host crystal and the new grains. The plots show that especially at low misorientation angles ( $<6^\circ$ ), but even up to  $35^\circ$ ,  $\langle a \rangle$  and  $\{m\}$  are equally favoured as misorientation axes. Misorientation angles up to  $12^\circ$  have a slight preference for  $\langle a \rangle$  as a misorientation axis. Between  $35^\circ$  and  $45^\circ$  there is a more or less homogeneous distribution of misorientation axes after which they start to cluster around  $\langle c \rangle$ , where a  $60^\circ$  rotation represents a symmetry operation of the (hexagonal) quartz crystal.

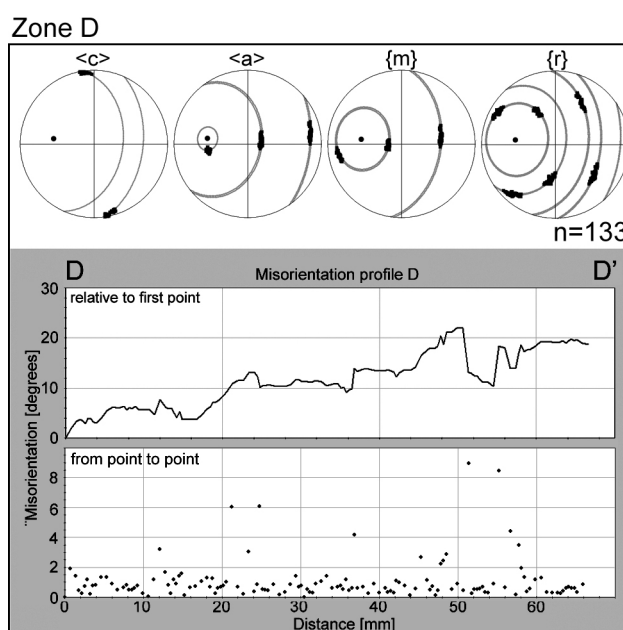


**Figure 7.11:** Profile (D-D'). Its location in zone D (isolated patches of new grains) is given in Figure 7.6d; same presentation as Fig. 7.8.

## 7.4. DISCUSSION

In this paper we aim at understanding how intracrystalline shear zones nucleate and further evolve in quartz during deformation in the presence of water. Strong CPOs and a dynamically recrystallised microstructure are often taken as an indication for a crystal-plastic origin of ductile shear zones (e.g. Urai et al., 1986; Passchier and Trouw, 1998). However, detailed EBSD analyses of naturally deformed rocks have shown that the misorientation relationship observed between parent and recrystallised grains cannot be explained by the mechanisms of subgrain rotation and grain boundary migration recrystallisation alone (Leiss and Barber, 1999; Bestmann and Prior, 2003; Prior et al., 2004; Wheeler et al. 2004). Other processes may exert an important control on the misorientation between host and recrystallised grains. In the following we evaluate our EBSD and TEM data with respect to existing models and discuss conflicting observations.

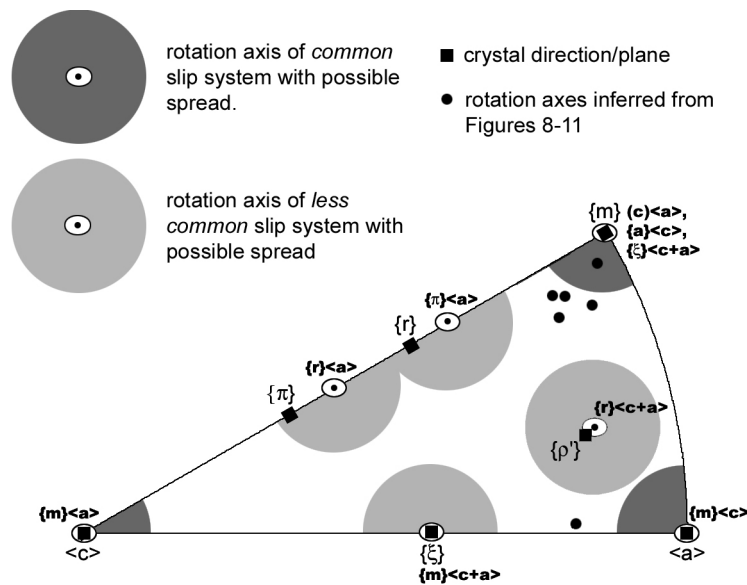


**Figure 7.12:** Misorientation axes of six profiles (Figures 7.8-7.11) displayed with respect to the crystal reference frame (equal area, upper hemisphere). Theoretical rotation axes, slip systems and possible spread are drawn for hexagonal crystal symmetry, modified after Neumann (2000) assuming that misorientations are exclusively formed due to edge dislocations.

#### 7.4.1 Models for shear zone development

In a classical model for shear zone development, including subgrain rotation recrystallisation, a gradual build-up in misorientation along subgrain walls is expected (Poirier and Nicholas, 1975; Urai et al., 1986). Eventually the walls become a high enough angle to lose their internal structure and become grain boundaries. Most new grain boundaries would then be fairly low angle (but  $> 10^\circ$ ) with respect to the host domains (Wheeler et al., 2004) and the new grains should display a rotation path that is similar to that of the host domains.

The rotation paths of the host domains and of the new grains within the shear zones studied in this paper are dissimilar. Grain rotations are not related to grain or boundary crystallography, and the misorientation angles between host domains and new grains are generally large (up to  $90^\circ$ ). Three alternative models were put forward to explain these large angle grain boundaries between new grains and host domains within shear zones: (1) Recrystallised grains, once formed by subgrain rotation, deform partly by diffusion accommodated grain boundary sliding (Bestmann and Prior, 2003). (2) New grains precipitate by growth from solution in intracrystalline microcracks (den Brok and Spiers, 1991; Hippertt and Egydio-Silva, 1996). (3) New grains are slightly rotated and translated fracture fragments that were broken off from the host grain (Nyman et al., 1992; den Brok, 1992; den Brok et al., 1998; van Daalen et al., 1999).

The first model is based on detailed EBSD-data from naturally formed shear zones within a greenschist facies calcite marble (Bestmann and Prior, 2003). The model describes the development of new grains by subgrain rotation and subsequent deformation by grain boundary sliding. It therefore requires that subgrains have similar sizes as the new grains in the shear zones and that new grains progressively lose their misorientation relationship with nearby (sub)grains towards the centre of the shear zones. The misorientation axis of the grains at the shear zone boundaries should still be similar to that of the subgrains and the host domains. The new grains in our studied sample are generally smaller than the subgrains and they have different misorientation axes than the subgrains and the host domains. The CPO that is observed is much different to the orientation of the host domains. Therefore we cannot support an origin of the new grains from previous subgrains in the host.

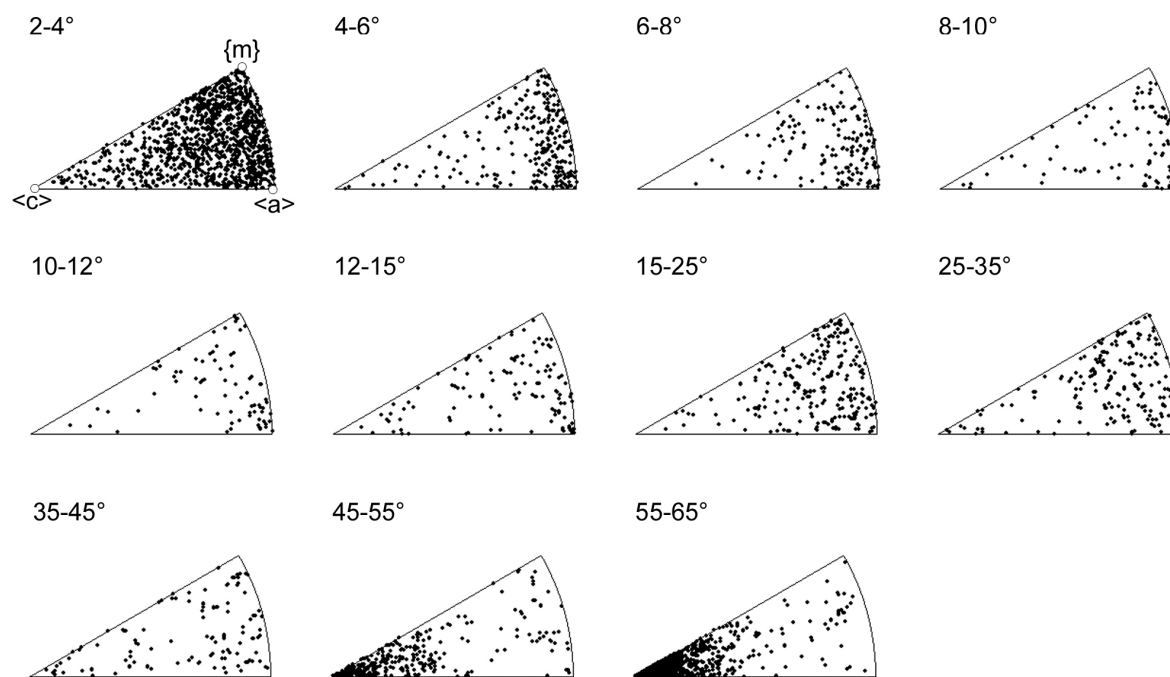


**Figure 7.13:** Distribution of misorientation axes and angles for the whole analysed area (Fig. 7.4). Misorientation axes are displayed with respect to the crystal reference frame (equal area, upper hemisphere projection). Important crystallographic directions and planes are indicated by open circles.

The second model is based on optical observations in experimentally deformed quartzites (den Brok and Spiers, 1991) and in a naturally deformed greenschist facies quartz mylonite (Hippertt and Egydio-Silva, 1996). In this model strain-free new grains nucleate and grow by precipitation from a solution in open microcracks. The new grains nucleate and grow with crystallographic orientations that are not necessarily dependent on the crystallographic orientation of the host grain. The crystallographic data of our studied sample gave clear evidence for progressive large angle rotation of the new grains with the sense of shear away from the host orientation in the shear direction, i.e. for a memory transferred from host grains to new grains.

The third model is based on optical analysis of experimentally deformed quartz (den Brok, 1992), naturally deformed amphibole (Nyman et al., 1992), ‘in-situ’ experimentally deformed salt (den Brok et al., 1998), as well as the combined analysis of computer-integrated polarisation (CIP) microscopy and EBSD-data on naturally formed shear zones within subgreenschist facies quartz fibres (van Daalen et al., 1999). In this model, microcracks form by slow water-assisted stress-corrosion. The fracture fragments subsequently rotate. Van Daalen et al. (1999) showed that fracturing occurred preferentially along the rhomb planes in the deformed quartz fibres. Further movement along these cracks caused the material in between to break apart into fragments that rotate in a direction that is conformable with the applied shear, much like the so called “fracture hypothesis” of CPO-development proposed by Sander (1911). According to this model, new grains are rotated and subsequently healed fracture fragments; subgrain boundaries that are parallel to the rhomb planes are healed microcracks. Several observations in our experimentally deformed sample support the interpretation of microcracking leading to strain localisation and subsequent shear zone formation. These observations are: the presence of fluid inclusions between the new grains within the shear zones, the abundance of water-filled voids at the grain boundaries and at the subgrain walls and the rhombohedral orientation of subgrain boundaries and of entire shear

zones. The relatively high porosity within the shear zones, the angular shape of the new grains and large jumps in crystallographic orientation between the new grains within the shear zones and the host domains suggests that the new grains are rotated fracture fragments. The tangled dislocations at the grain boundaries may have formed in response to crack propagation.

#### **7.4.2 Shear zone development in the studied sample**

Our view on shear zone formation is therefore strongly based on the third model (Fig. 7.14). Because of combined analysis of TEM images and high resolution EBSD data we are able to constrain the mechanisms of shear zone development in greater detail. During the initial phase of linear work hardening, the stress increases to a relatively high value, because the conventional prism and basal slip systems could not easily be activated in this sample. At the highest differential stress, the development of planar microcracks starts; parallel to the rhomb planes and parallel to  $\sigma_1$  (Fig. 7.14a). Some of these cracks heal after little rotational displacement and are now observed as rhombohedral or prismatic ‘subgrain boundaries’. Further microcracking (Fig. 7.6a and 7.14b) may lead to shear zone development. During sliding, fracture fragments may slightly rotate, heal and become ‘subgrains’. These rotations are only related to the geometry and orientation of the shear zone and not to grain or boundary crystallography. During sliding of the fracture fragments, the average misorientation between the subgrains and the host domains increases and misorientation axes are randomised. The fracture fragments become separate grains as they further rotate in a direction conform to the sense of shear (Fig. 7.14c). The rotation of the new grains is probably facilitated by the high water pressure and the relatively high water-filled porosity within the shear zones.

#### **7.4.3 CPO-development in the shear zones**

The elongated shape of new grains (with  $\langle c \rangle$  perpendicular to the shear zone boundary) suggests relatively fast selective growth or grain boundary migration perpendicular to  $\sigma_1$ . Grain boundary migration is strongly enhanced if water is present on the grain boundaries (e.g. Drury and Urai, 1990; Mancktelow and Pennachioni, 2004). It may have caused the development of a strong CPO with  $c$ -axes preferentially aligned perpendicular to the shear zone boundary (Fig. 7.14d). Apparently this orientation is favoured for growth. It is very commonly observed in quartz shear zones (e.g. Burg and Laurent, 1978; Simpson, 1981; Schmid and Casey, 1986) and generally interpreted to develop by preferred growth of grains that are suitably oriented for basal slip.

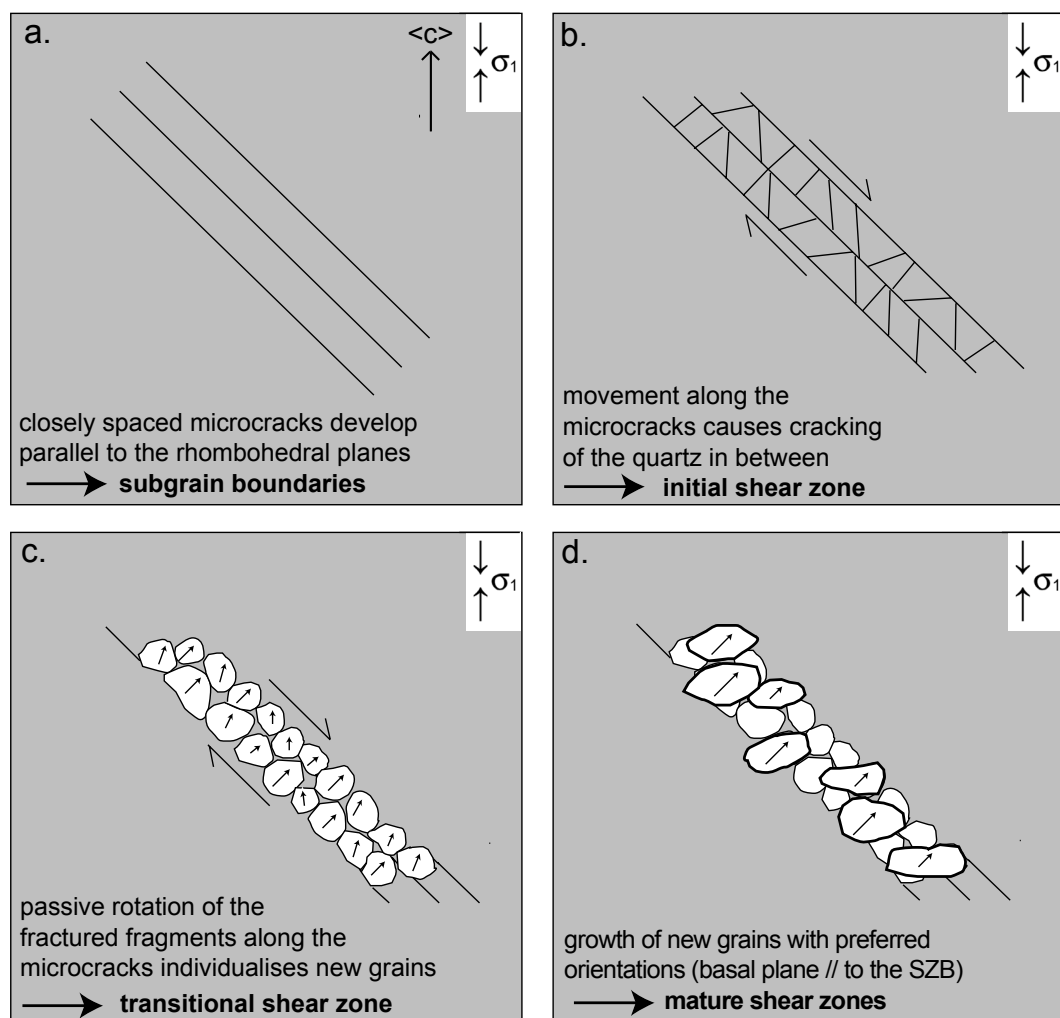


**Figure 7.14:** Schematic model for the evolution of an intracrystalline shear zone in quartz. (a) Microcracks develop parallel to the rhomb planes. In the EBSD orientation maps such microcracks could be identified as aligned subgrain boundaries in cases where rotational offsets were observed. (b) An initial shear zone develops during further microcracking. (c) Fracture fragments become new grains while rotating further in the direction of the shear zone. The rotation may be facilitated by the high water pressure and the relatively high porosity of the shear zone. (d) A strong CPO develops within the shear zone, because new grains with  $\langle c \rangle$  oriented perpendicular to the shear zone boundary (SZB) start to grow at the cost of other new grains.

#### 7.4.4 Isolated pockets of new grains

The above model for shear zone development does not explain the development of the new grains in isolated pockets (Fig. 7.6d). The geometry of the isolated pockets and the crystallographic orientations of the new grains clearly indicate that they did not rotate gradually out of the host orientation. Large grain boundary misorientations (up to  $90^\circ$  difference in  $c$ -axes) occur. We hypothesise that these new grains nucleated with high angle misorientation relative to the host domains (see also Wheeler et al., 2004). Viable nuclei originated on the walls of healing cracks. The elongated shapes of the new grains suggest that their boundaries migrated relatively fast in a direction perpendicular to  $\sigma_1$ . Our data cannot explain how these nuclei originate. However, because of the notable effect of the water on the deformation behaviour of the deformed sample, we suggest that the nuclei develop by precipitation from solution in small voids and microcracks like in the experiments of den Brok and Spiers (1991) and in the natural deformed quartz samples of Hippertt and Egydio-Silva (1996).

## 7.5. SUMMARY AND CONCLUSIONS

This study yields the following conclusions:

- 1) Uniaxial deformation of a quartz single crystal parallel to the  $c$ -axis in the presence of water, at a temperature of 800°C, a confining pressure of ~1.2 GPa and a strain rate of  $\sim 10^{-6} \text{ s}^{-1}$ , led to the development of microscale shear zones that reflect different stages of shear zone development.
- 2) EBSD and TEM analysis complemented each other in providing a detailed picture of the operating deformation mechanisms in intracrystalline shear zones. The (sub)grain boundaries that were identified on EBSD orientation maps and image quality maps were independently verified on the TEM images as being healed microcracks.
- 3) The crystal initially deformed by intracrystalline plasticity which became increasingly heterogeneous. At the highest differential stress, microcracks developed parallel to the rhomb planes, at approximately 45° to the  $\sigma_1$ -direction, and parallel to the prism planes, approximately parallel to the  $\sigma_1$ -direction. These microcracks are traced by fluid inclusions and look similar to subgrain boundaries in the EBSD orientation maps. They must have healed after only little rotational displacement. Further microcracking along the rhomb planes led to shear zone development.
- 4) “New” grains developed during movement along the initial shear zones, by sliding and rigid body rotation of the fracture fragments. Rotation took place in a direction conforming to the shear sense of the shear zone.
- 5) A strong CPO developed because of relatively fast preferred growth of new grains that have  $\langle c \rangle$  perpendicular to the shear zone boundary. Thereby they developed an elongated shape perpendicular to  $\sigma_1$ .
- 6) New grains in isolated pockets probably developed by precipitation and subsequent growth out of solution.

## **CHAPTER 8: GENERAL CONCLUSIONS AND SUGGESTIONS FOR FURTHER RESEARCH**

The objective of this thesis was to assess the effect of dynamic recrystallisation on CPO development by investigating the microstructural record within experimentally deformed quartz single crystals. The purpose of this final chapter is to draw general conclusions on the findings in the previous chapters.

### **8.1 DEFORMATION BEHAVIOUR OF QUARTZ SINGLE CRYSTALS IN THE PRESENT EXPERIMENTS**

The present investigation has focussed on experiments on natural quartz single crystals deformed with 1 vol% of added water in a Griggs solid medium deformation apparatus at  $P_c \approx 1200$  MPa,  $T = 800^\circ\text{C}$  and strain rates of  $10^{-6}$  and  $10^{-7}$   $\text{s}^{-1}$ . The starting orientations of the deformed samples were:  $\sigma_1 // \langle c \rangle$ ,  $\sigma_1 // \langle o+ \rangle$ ,  $\sigma_1 \sim \perp \{r\}$  and  $\sigma_1 // \langle a \rangle$ .

Broadly speaking, the experiments showed that at constant strain rate, the strength of the samples strongly depended on the initial orientation of the sample. At  $\dot{\epsilon} = 10^{-6}$   $\text{s}^{-1}$ , samples that were deformed parallel to  $\langle o+ \rangle$  and parallel to  $\langle a \rangle$  exhibited the lowest peak stresses of ( $120 \pm 20$  MPa and  $140 \pm 36$  MPa). Samples that were deformed approximately perpendicular to  $\{r\}$  exhibited intermediate peak stresses of  $258 \pm 80$  MPa and samples deformed parallel  $\langle c \rangle$  exhibited the highest peak stresses of  $425 \pm 15$  MPa.

The microstructural record of the deformed quartz samples was heterogeneous. Three classes of deformation microstructures were observed.

(i) Sub-basal deformation lamellae, undulatory extinction and arrays of subgrains indicating glide controlled deformation accompanied by distributed brittle failure. The crystal lattice in the domains with undulatory extinction rotated around axes that were approximately perpendicular to  $\sigma_1$ . The orientations of these axes depended on the starting orientation of the sample and were partly related to low-index crystallographic directions that were interpreted as the rotation axes of basal and prism dislocation slip systems. Sub-basal deformation lamellae developed during initial work hardening and appeared under the TEM as elongated subgrain walls. These walls induced alternating small angle misorientations in the sample.

(ii) Few optically strain-free grains, with sub-euhedral shapes recrystallised in axially aligned cracks in samples deformed with 1 vol% of added water. Numerous microcavities, voids, fluid channels and fluid inclusions were present on their grain boundaries. Abundant new grains also developed in aggregates at the ends of samples deformed with 1 vol% of added water and 20 mg  $\text{Mn}_2\text{O}_3$ -powder. The transition in crystallographic orientation from the domains of assumed glide-controlled deformation into the domains with new grains was not continuous and the CPOs of the new grains were unrelated to the small angle crystal rotations within the host. The new grains were interpreted to be precipitated out of solution. They exhibited strong CPOs consisting of  $c$ -axis maxima at  $\sim 45^\circ$  to  $\sigma_1$ , irrespective of the initial orientation of the sample. The recrystallised grains, once precipitated from solution, must have grown in these orientations, because they are favoured for intracrystalline plastic deformation at the imposed experimental conditions. Less strong  $c$ -axis maxima observed perpendicular to the starting orientation and also at  $45^\circ$  to  $\sigma_1$  could be explained by Japanese growth twinning. Dynamic recrystallisation in the samples was a continuous process

involving nuclei development by precipitation from solution, fluid assisted growth of nuclei with orientations favoured for deformation and glide controlled lattice rotations.

(iii) Intracrystalline shear zones developed in samples deformed parallel to  $\langle c \rangle$ , i.e. with an initial starting orientation where prism and basal slip systems could theoretically not be activated. These shear zones were preferentially oriented parallel to the rhomb planes and exhibited strong  $c$ -axis maxima perpendicular to the shear zone boundary. These shear zones appeared to develop along planar microcracks oriented parallel to crystallographic rhomb planes. Further microcracking resulted in cataclastic shear zone development. New grains developed by rotation and translation of fracture fragments. The rotation of the fragments towards the shear direction was probably facilitated by the high water pressure and the relatively high porosity of the shear zone. A strong CPO was accommodated in the samples by preferred growth of the new grains.

## 8.2 COMPARISON WITH CPO DATA AND MICROSTRUCTURES FROM OTHER STUDIES

In the present experiments, strong CPOs were observed in all deformed samples that exhibit abundant recrystallised grains. These recrystallised grains were observed within aggregates at the sample ends (Chapter 6) and within intracrystalline shear zones (Chapter 7). The  $c$ -axis patterns in the new grain aggregates at the sample ends were different in each sample: (1) a small circle girdle at  $\sim 45^\circ$  to  $\sigma_1$  in sample GRZ33, (2) point maxima at  $\sim 45^\circ$  to  $\sigma_1$  in sample GRZ30 and (3) a single vertical girdle with strong maxima at  $90^\circ$  to  $\sigma_1$  and  $45^\circ$  to  $\sigma_1$  in sample GRZ34.

The similarity between all samples was the tendency of the new grains to develop and grow with  $\langle c \rangle$  at  $\sim 45^\circ$  to  $\sigma_1$ , the main compression axis. Comparable  $c$ -axis maxima are common in quartz rocks deformed in nature under greenschist facies conditions (e.g. Bouchez and Pêcher 1981, Schmid and Casey 1986, de Araújo et al. 2003). The  $c$ -axis maximum at  $90^\circ$  to  $\sigma_1$ , as observed in sample GRZ34, is more characteristic for quartz rocks deformed at amphibolite facies conditions (e.g. Schmid et al. 1981, Lister and Dornsiepen 1982, Schmid and Casey 1986, Mainprice et al. 1986, Stipp et al. 2002). The microstructures of the experimentally deformed, dynamically recrystallised quartz (e.g. Fig. 4.10) show great similarities with the microstructures of natural dynamically recrystallised quartz aggregates (Fig. 8.1). The similarities between the CPO in the experimentally deformed samples, as well as the microstructure, and the CPO and microstructure of naturally deformed samples suggest that they may have been formed by the same process.

Dynamic recrystallisation is widely regarded as a process that accompanies dislocation creep. Two different processes are held responsible: subgrain rotation and grain boundary migration. New grains with new orientations develop by progressive rotation of subgrains. During grain boundary migration, grains in unfavourable orientations for glide are partially removed at the expense of more favourably oriented grains (e.g. Schmid and Casey 1986). The difference with our model is that: (i) subgrains were interpreted as being fracture fragments because their development could be related to longitudinal fractures and because of abundant fluid inclusions on their grain boundaries, (ii) these fracture fragments only rotated by small amounts away from their host orientation and (iii) completely new grains nucleated and grew in far away orientations. Similar to the traditional models is that the grains (once precipitated from solution) were further selected by preferred growth in orientations suitable for deformation.



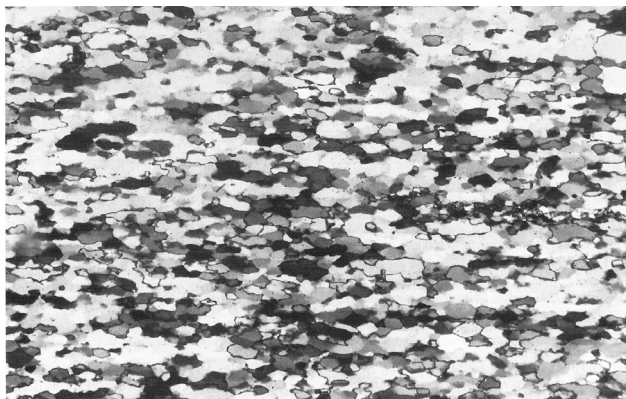


**Figure 8.1:** Optical micrograph of typical fabric of dynamically recrystallised quartz. The grains have a weak shape preferred orientation. Thin section made from a granite mylonite sample, Qin Ling mountains, China. Width of view is 1.8 mm. From Passchier and Trouw 1998.

New grains within intracrystalline shear zones displayed *c*-axis preferred orientations approximately perpendicular to the shear zone boundary. Such *c*-axis maxima are common in natural shear zones as well (e.g. Burg and Laurent 1978, Simpson 1981, Schmid and Casey 1986). These maxima are generally interpreted to develop by subgrain rotation recrystallisation, followed by preferred growth of grains that are suitably oriented for basal slip. Optically, the microstructures of the intracrystalline shear zones in my samples (e.g. Fig. 7.3) were similar to microstructures of natural intracrystalline shear zones (Fig. 8.2 and 8.3). The microstructural and crystallographic characteristics of the experimentally produced shear zones, however, provided evidence for cataclasis. Dynamic recrystallisation took place by rotation of the fracture fragments, leading to the development of new grains, an old idea already proposed by Sander (1911). The CPO developed by preferred growth of the new grains.

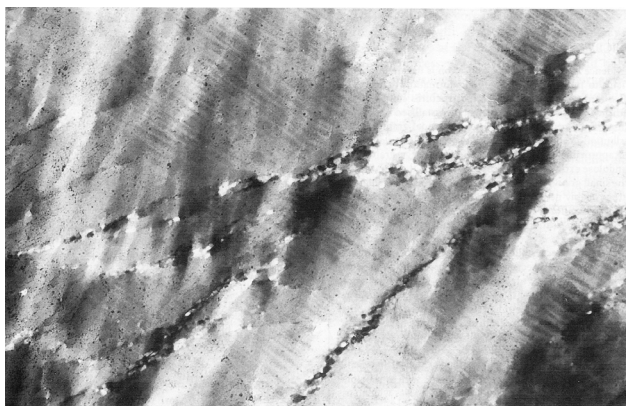


**Figure 8.2:** Optical micrograph of quartz with sub-basal deformation lamellae transected by bands of new grains formed by dynamic recrystallisation. Quartz vein in micaschist, Southern Alps, Italy. Width of view is 1.8 mm. From Passchier and Trouw 1998.

Segall and Simpson (1986) and van Daalen et al. (1999) already indicated that intracrystalline shear zones formed during natural deformation at greenschist facies conditions might have developed along crystallographically controlled microcracks, notably parallel to the rhomb planes. The new grains in their samples exhibited strong *c*-axis maxima and were interpreted to be developed from fracture fragments and not from subgrains, just as in the sample experimentally deformed in this work. These similarities are an additional indication that the deformation behaviour of the studied samples is comparable to natural deformation at

greenschist facies. The relatively high temperature during the experimental deformation might have been compensated by the relatively high strain rate.

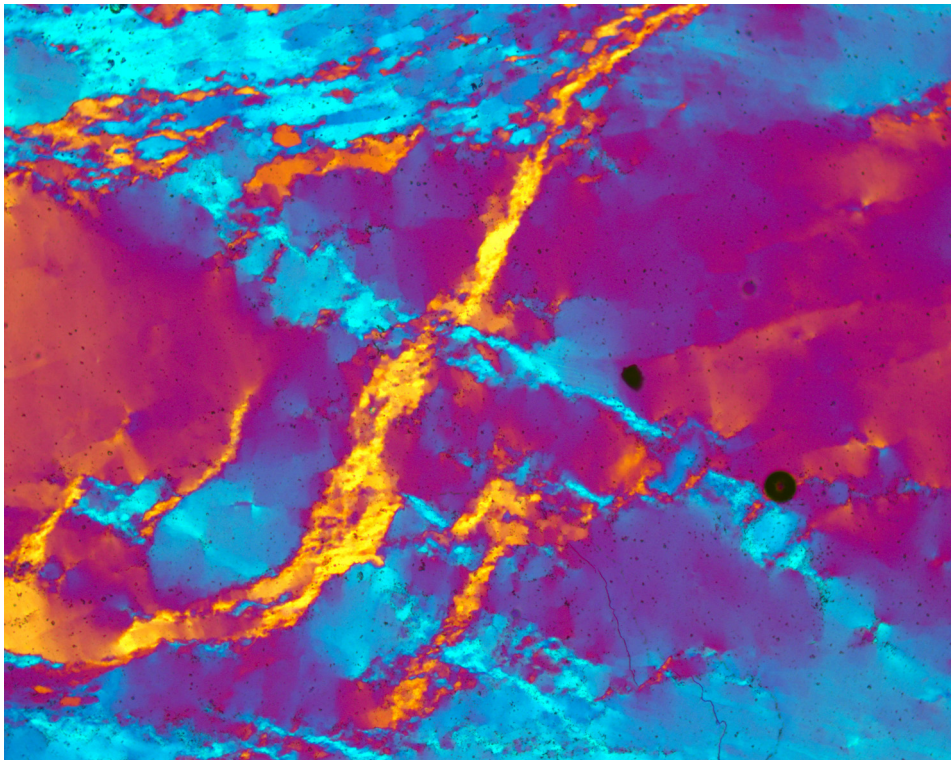


**Figure 8.3:** Naturally deformed quartz with conjugate set of intracrystalline shear zones. Quartz vein within dextral shear zone, Schobergruppe, Barrenlesee, SW Österreich, Tirol. Width of view is 1.37 mm. Micrograph courtesy of Michel Bestmann.

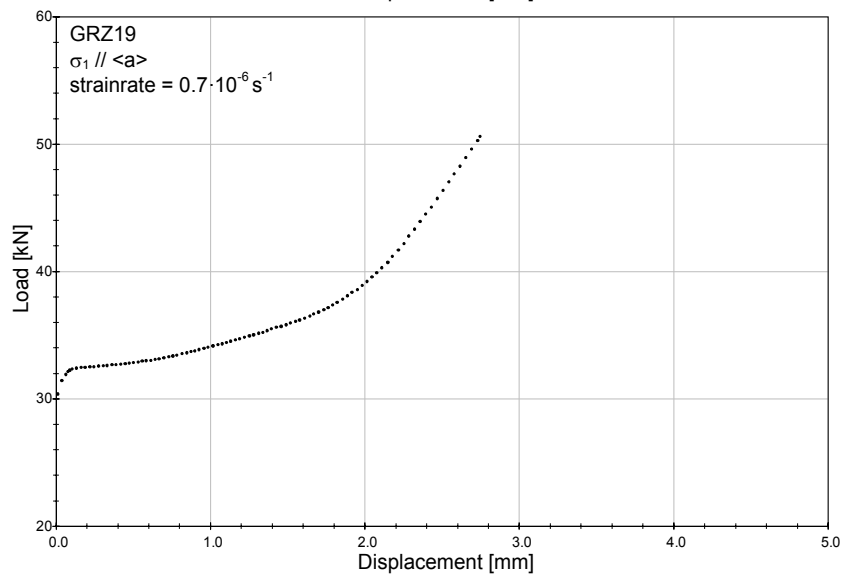
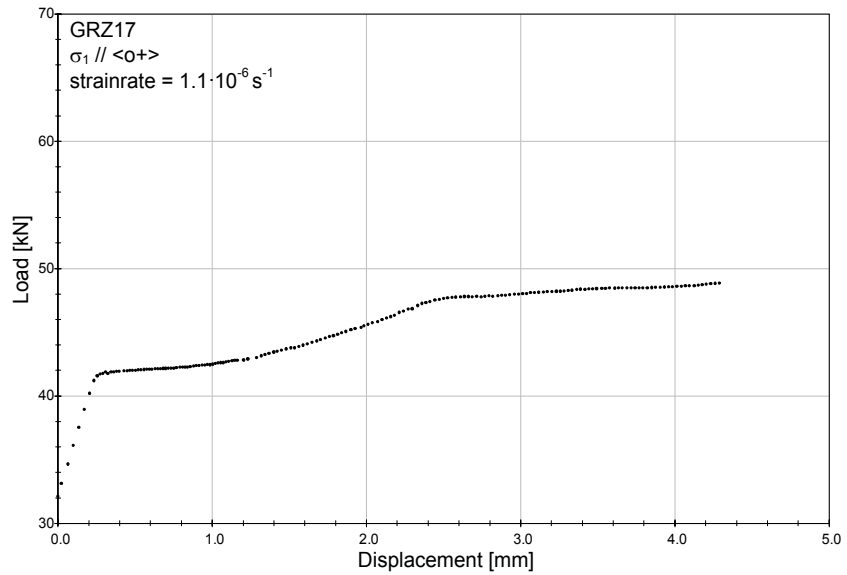
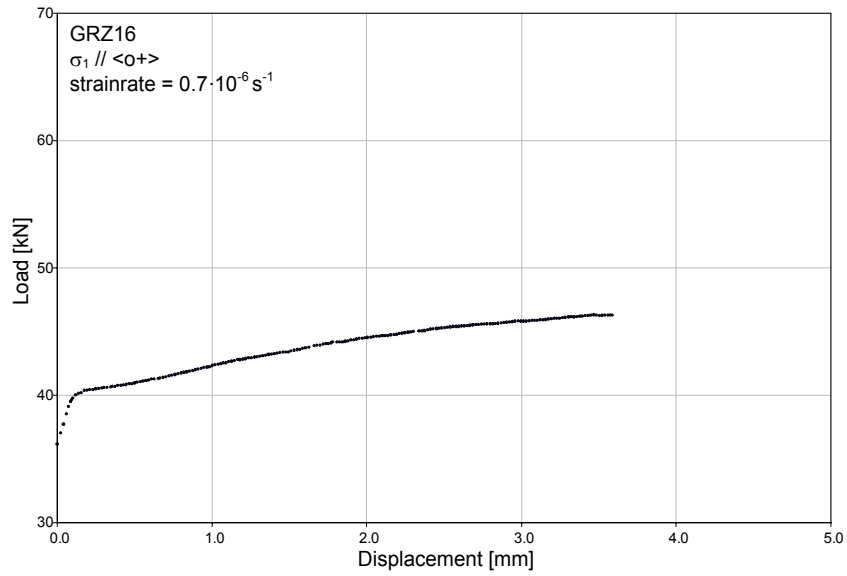
CPOs in dynamically recrystallised rocks are usually attributed to glide controlled deformation. Dynamic recrystallisation is interpreted to take place by glide and climb of dislocations and is mostly assumed to play a passive role in CPO development. In the experiments presented here, the host domains (with no dynamic recrystallisation) showed evidence for glide controlled deformation, resulting in gradual rotations of up to  $30^\circ$  away from the host orientation. Strong CPOs, however, only developed in the dynamically recrystallised domains, where new grains were created by microcracking, precipitation from solution in a preferred orientation, and subsequent preferred growth as also described in earlier literature (e.g. Sander 1911, Kamb 1959, Kamb 1972, den Brok 1991, Nyman et al. 1992, Hippertt and Egydio-Silva 1996). The new grains form strong CPOs because they grow in an orientation that is preferred for intracrystalline deformation at the imposed experimental conditions.

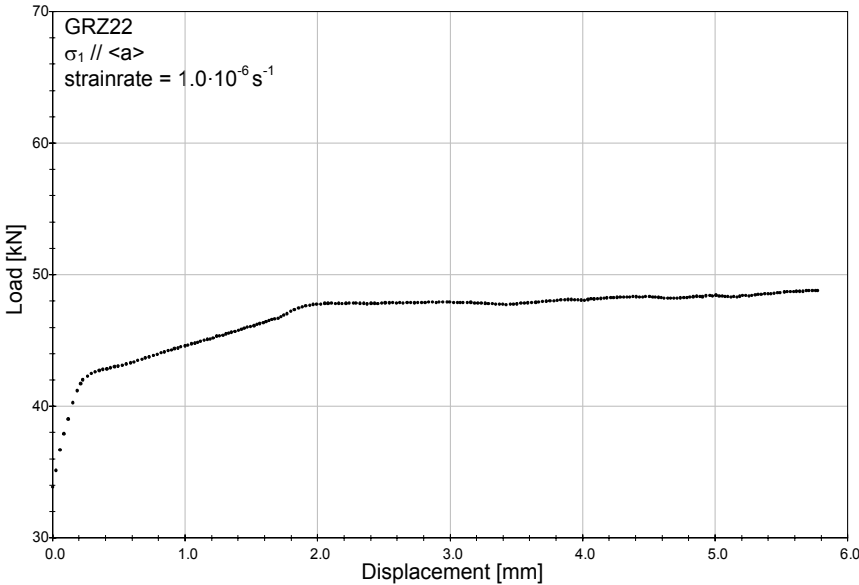
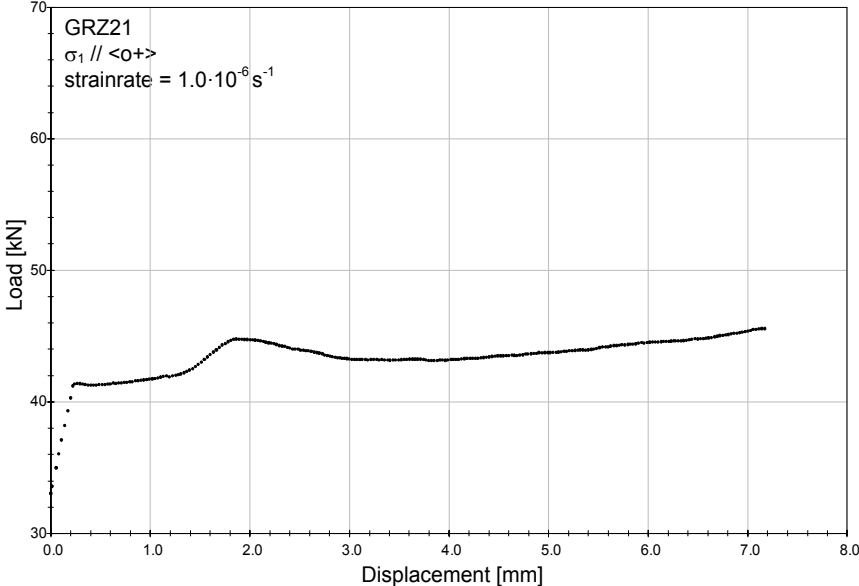
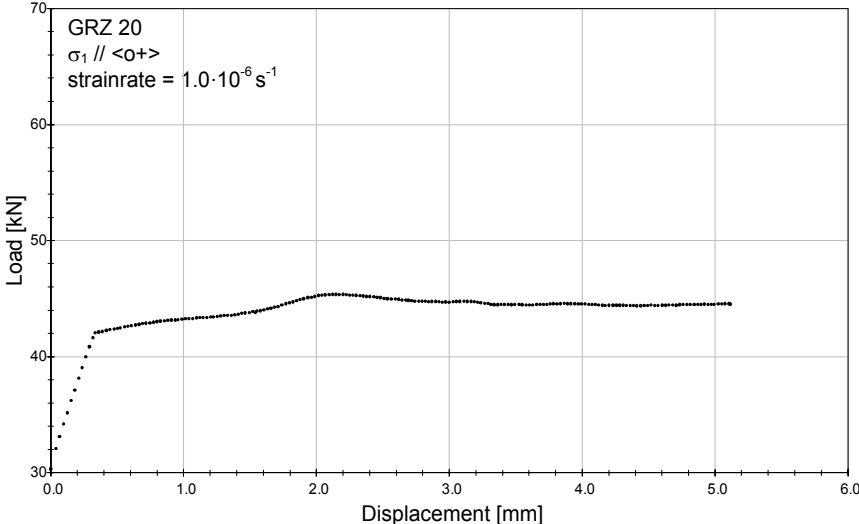
### 8.3 UNANSWERED QUESTIONS

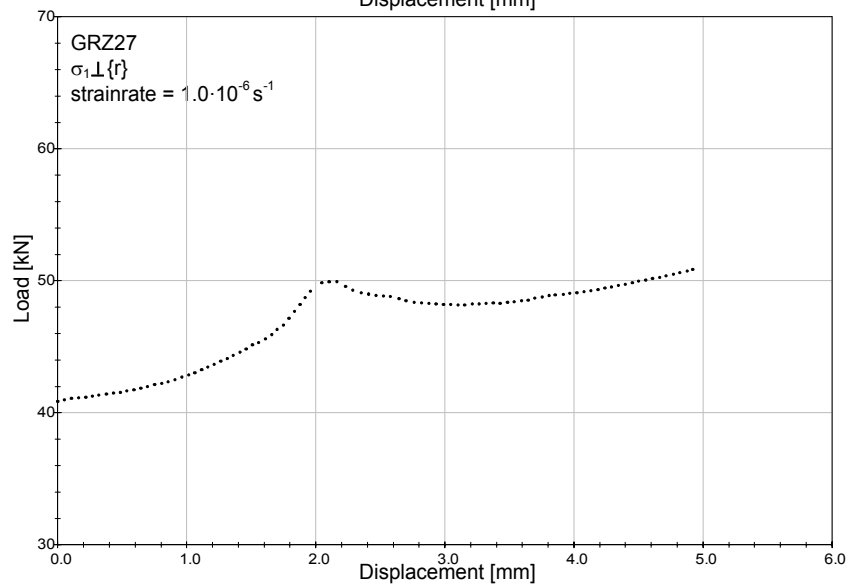
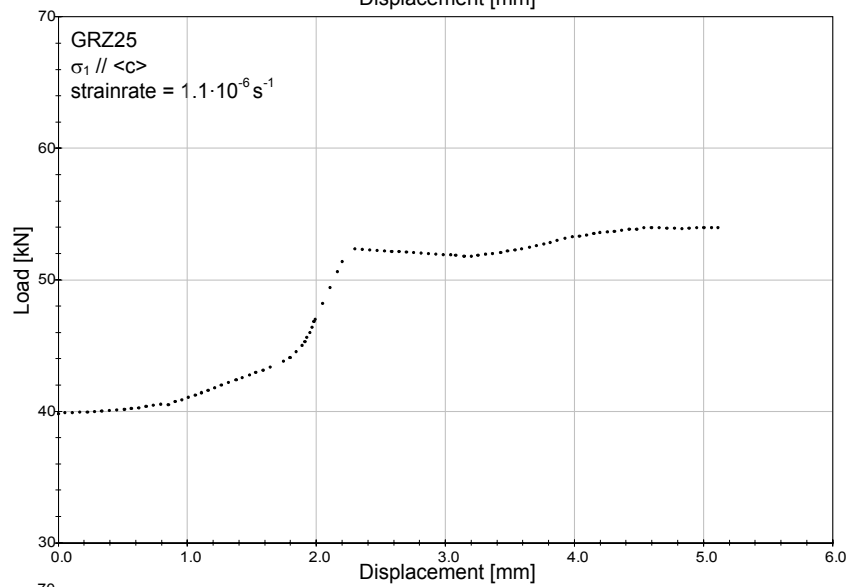
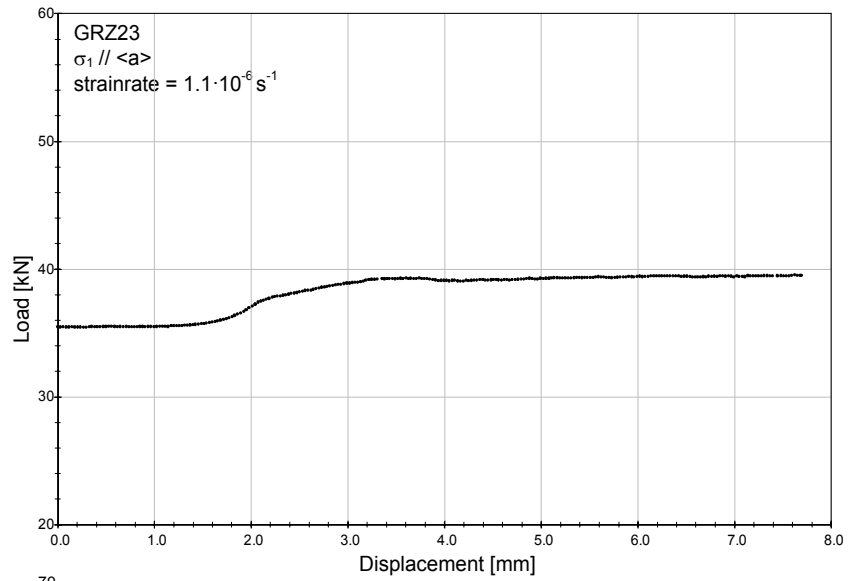
The nature of natural rock deformation is very complex, especially because there are many extrinsic factors that influence the deformation behaviour. The motivation to carry out deformation experiments is to create a relatively simple environment, where these extrinsic factors can be controlled or eliminated. The experiments in this thesis were performed at such simplified conditions: mono-phase instead of poly-phase samples, single crystals instead of polycrystals and with well defined temperatures, confining pressures, strain rates and water content. Several issues still remain unsolved that might be clarified during further research.

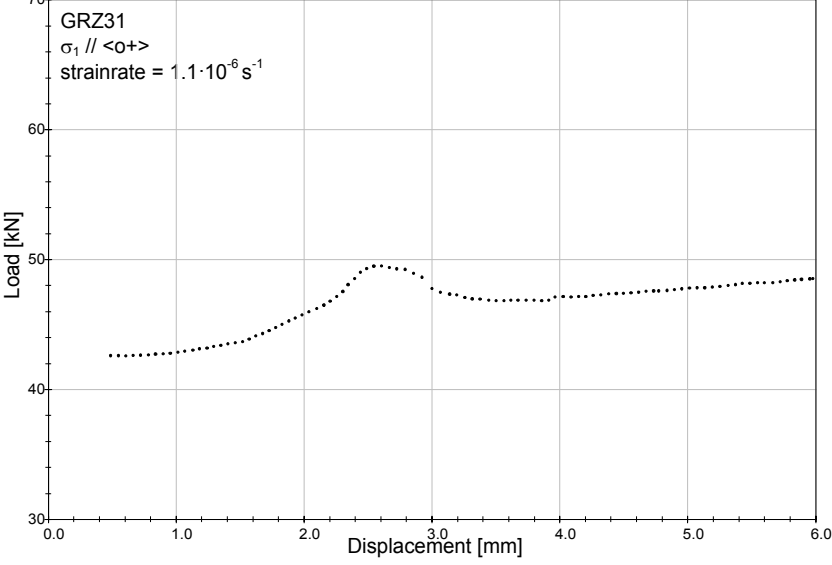
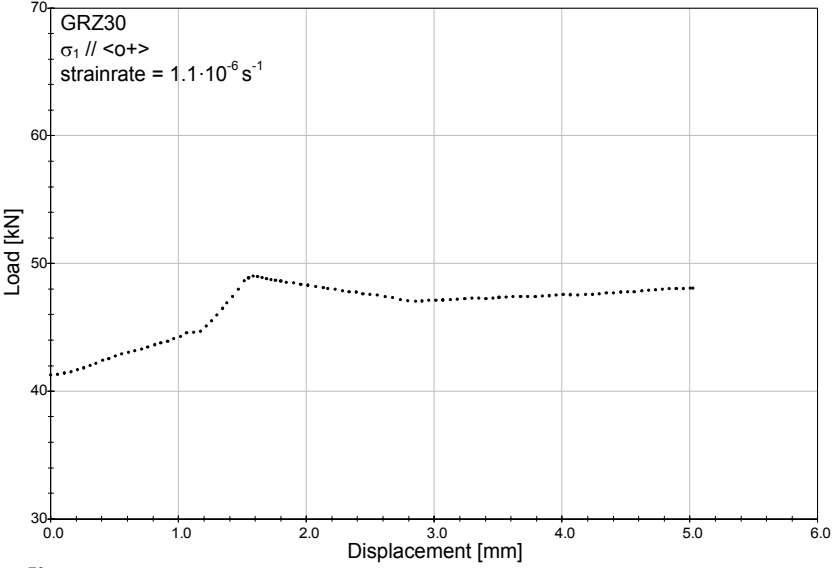
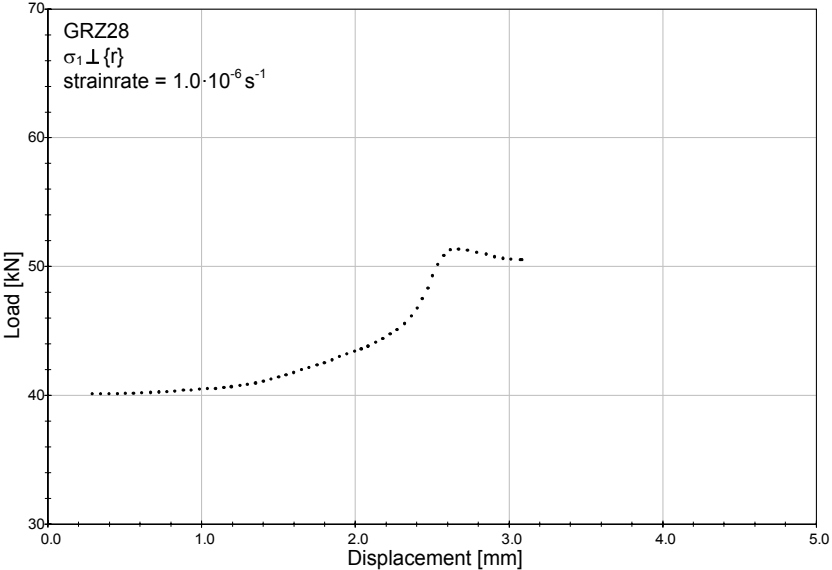
- 1) All samples were deformed at the same temperature (800 °C). New grains developed with  $\langle c \rangle$  at 45° to the compression direction. It was assumed in this work that this orientation was favoured for growth, because it is the best suited orientation for basal  $\langle a \rangle$  glide. The CPOs of naturally dynamically recrystallised rocks show a great dependence on temperature. In a further study, samples should therefore be deformed at lower and at higher temperatures.
- 2) It has been illustrated in chapter 6 that a crossed girdle pattern is obtained by superposing the CPO patterns of the three deformed samples (Fig. 6.15). It has been mentioned that this might be incorrect, because the effects of the three orientations acting on each other is not known. It is possible that in a sample with grains in all three orientations only grains of one orientation (re)crystallise whereas grains in other orientations are progressively removed, or do not participate in the deformation process. To investigate this effect, bi-crystal samples should be deformed and analysed.
- 3) CPOs developed in differently oriented samples had one major characteristic: new grains developed with  $\langle c \rangle$  at 45° to the compression direction. It is recommended for further research to investigate this CPO effect in more detail by creating a larger database by deforming samples with intermediate starting orientations. Eventually, more precise predictions can then be made on the control of the host orientation on the CPO pattern.
- 4) It has been shown in chapters 4 and 6 that  $\text{Mn}_2\text{O}_3$ -powder added to the water triggers the development of new grains. It has been proposed that this effect emerges because the powder makes the water impure and induces stress concentrations at the sample boundaries. The development of new grains may be eased because impurities provide extra nucleation sites for precipitation. To check if this is true, samples should be deformed with other impurities.
- 5) The difference in yield strength between samples deformed with the same starting orientation is very large, for example, the peak stresses between 60 and 170 MPa for the samples deformed parallel to  $\langle o+ \rangle$ . It is not clear if this difference arises just because deformation is heterogeneous. In chapter 3 it is shown that several assumptions were made during data processing of the mechanical data, especially in defining the hit-point and in defining the internal friction of the apparatus. The hit-point can be more precisely determined if the solid-salt sample assembly is modified to a molten-salt assembly. Molten salt allows a clear identification of the 'hit' point and it also reduces the friction on the moving piston, because it does not contribute to the strength of the sample (Gleason and Tullis 1995). The increase in friction can be measured by determining the frictional force on the inner piston before and after the deformation experiment on samples that will not be used for microstructural investigations (Rybacki et al. 1998, Stipp and Tullis 2003).
- 6) In this study, only experimentally formed microstructures have been analysed. To create a link to nature, natural microstructures with the same optical characteristics (i.e. Fig. 8.3) should be analysed by EBSD and TEM.



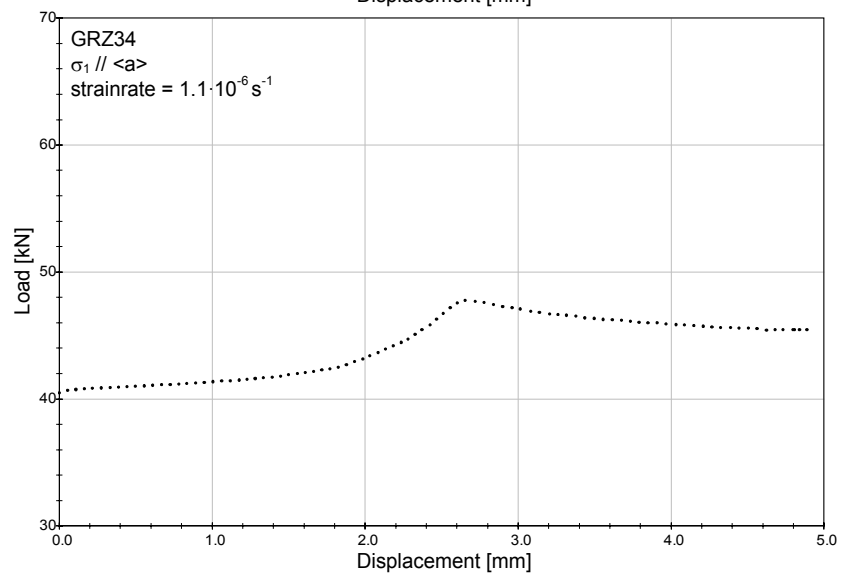
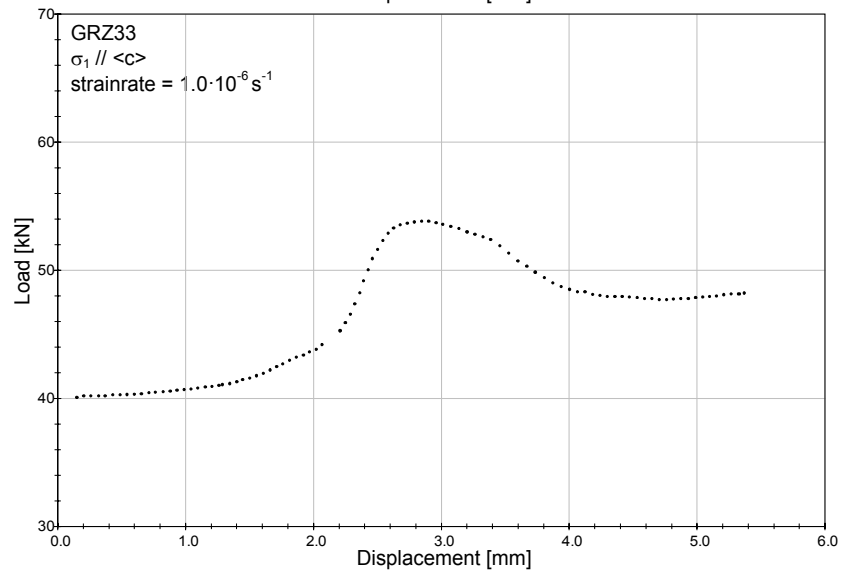
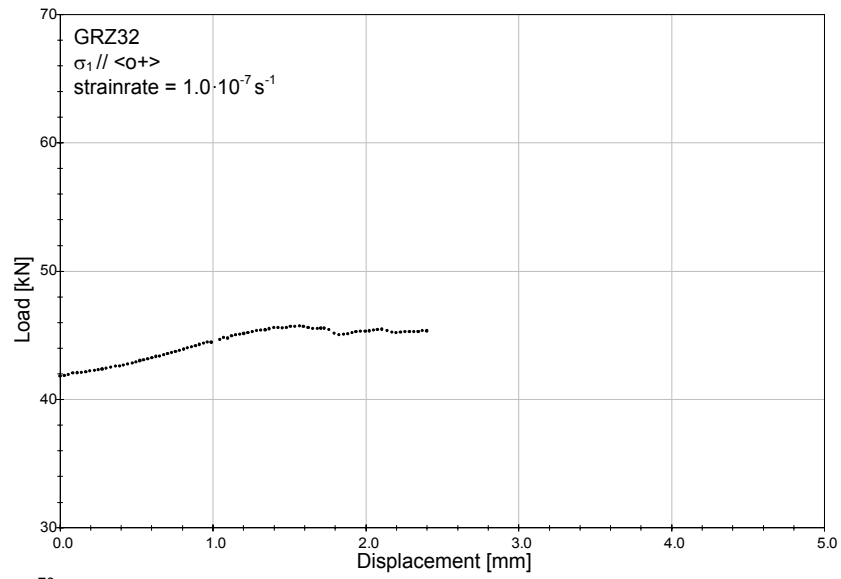
**APPENDIX A:  
RAW LOAD-DISPLACEMENT DATA**













## APPENDIX B

### FLUID INCLUSIONS<sup>1</sup>

Fluid inclusions are tiny quantities of liquid water and gas that are trapped within the quartz crystal at experimental deformation conditions. Because the starting material was inclusion free, the inclusions must have been the result of a cracking, micro cracking and subsequent healing processes that took place during hydrostatic loading and deformation of the wet samples. Fluid inclusions preserve important information about the physical properties (e.g. fluid pressure) of the original parent fluid. Their shape and size strongly depends on the differential stress, finite strain and crystal orientation. In the following sections, the microstructures of the fluid inclusions will be described together with the results of a microthermometry study on fluid pressure of the inclusions.

#### MICROSTRUCTURE

It was shown in chapter 4 that cracking and crack healing were dominant features in the hydrostatically loaded samples. The healed cracks are traced by fluid inclusions. In sample GRZ29, which was kept at  $\sim 1200$  MPa and  $800^\circ\text{C}$  for a period of  $\sim 16$  hours, fluid inclusions are generally very small ( $< 2 \mu\text{m}$ ) and have a constant angular shape with round edges (Fig. B1a). A few larger inclusions ( $\sim 2 \mu\text{m}$ ) developed a more irregular shape with sharp edges.

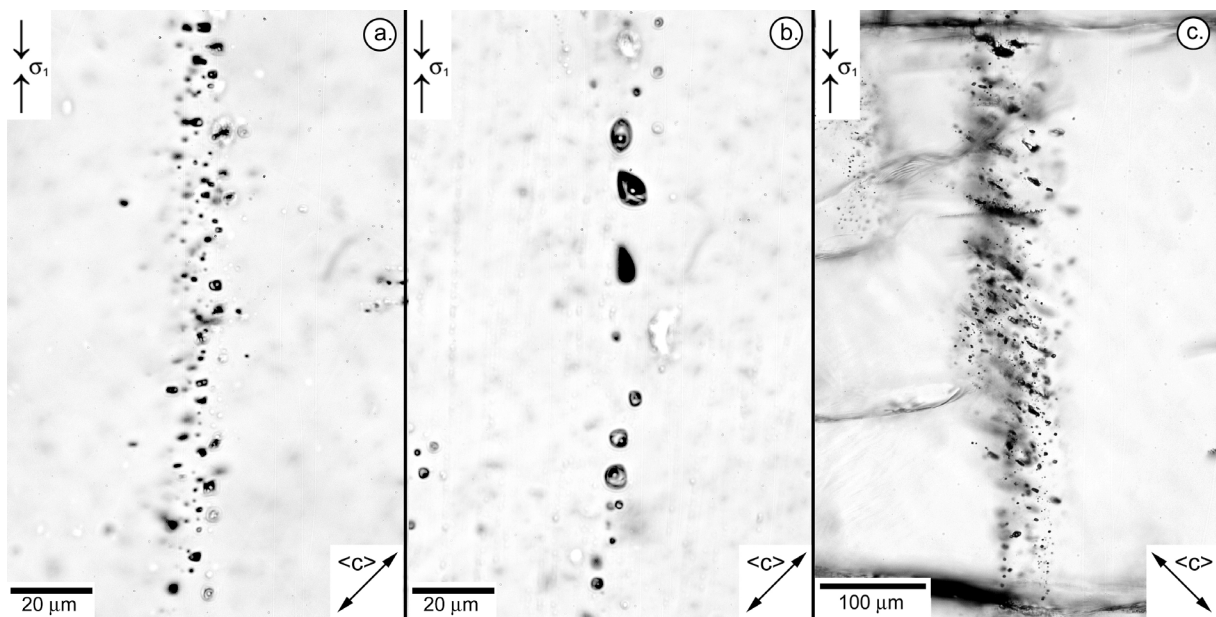


**Figure B1 :** Optical micrographs of healed cracks that are traced by fluid inclusions. a) sample (GRZ29) hydrostatically loaded for  $\sim 16$  hours, b) sample (GRZ26) hydrostatically loaded for  $\sim 221$  hours and c) sample (GRZ17) deformed at  $1.1 \cdot 10^{-6} \text{ s}^{-1}$  to 21% finite strain with  $\sigma_1 // \langle o+ \rangle$ . All samples were heated to  $T \sim 800^\circ\text{C}$  at a confining pressure of  $\sim 1200$  MPa with 1 vol% of added water. C)  $200 \mu\text{m}$  thick section. This figure illustrates the arrangement of the fluid inclusions along the prism planes within a deformed sample.

The fluid inclusions in sample GRZ26, which was kept at  $\sim 1200$  MPa and  $800^\circ\text{C}$  for a period of  $\sim 221$  hours ( $\sim 14$  times longer), have sizes up to  $20 \mu\text{m}$  (Fig. B1b). The fluid inclusions that are larger than  $\sim 2 \mu\text{m}$  have irregular shapes with round edges. This observation is in agreement with TEM observations on nearly equant, spheroidal fluid inclusions in heat-treated synthetic quartz single crystals that appear to coarsen with time at elevated

<sup>1</sup> In cooperation with Ronald Bakker, Montanuniversität Leoben, Austria

temperature (Paterson and Kekulawala 1979, Gerretsen et al. 1989). In the deformed samples, the fluid inclusions tend to align parallel to the prism planes which is very well illustrated in a thick section (Fig. B1c).

In detail, these aligned fluid inclusions have drastically changed shape relative to the undeformed samples. They exhibit a prolate shape (Fig. B2), are elongated approximately parallel to the prism planes and show shape changes which result from post-entrapment modification. The average size of the fluid inclusions decreases with increasing differential stress. Figure B2a displays an example of an inclusion which necked down to form two separate inclusions. The aura of little bubbles around the inclusion is caused by volume compression ('implosion') during deformation. The inclusions in figure B2b exhibit 'sweat haloes' (Audétat and Günther 1999), which indicate that the inclusions once occupied a larger area and then recrystallised back to a more equant shape. The quartz within the 'sweat haloes' has a slightly different orientation than the quartz in the host rocks. We failed to locate the 'sweat haloes' with the TEM in order to investigate their intracrystalline microstructure.

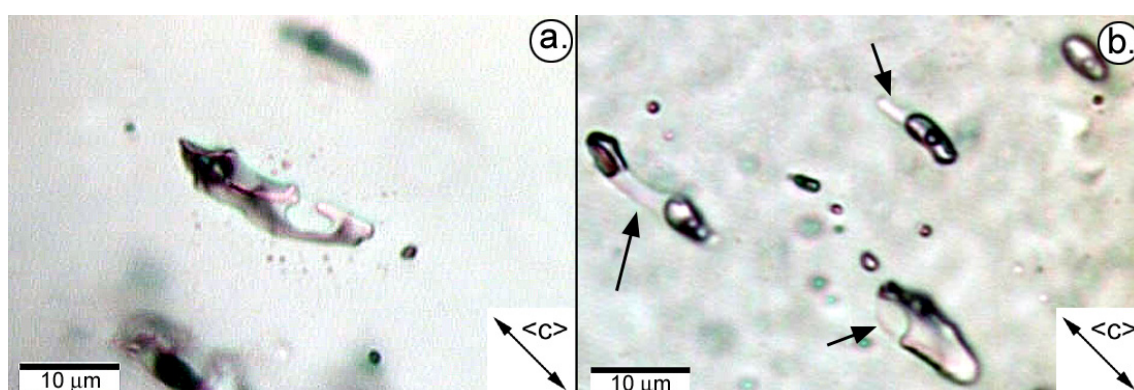


**Figure B2 :** Optical micrographs of fluid inclusions in sample (GRZ16) deformed parallel to  $\langle o \rangle$  with 1 vol% added water at  $T=800^{\circ}\text{C}$ ,  $P_c=1200\text{ MPa}$  and  $\dot{\epsilon}=0.7\cdot 10^{-6}\text{ s}^{-1}$ . a) Fluid inclusion that is surrounded by an aura of little water bubbles and that necked down into two inclusions during deformation. b) Fluid inclusions with 'sweat haloes' (black arrows). Arrows in the lower right indicate the starting orientation of the sample.

TEM reveals that fluid inclusions appear in two different ways: on healed cracks (Figs. B3a and b) and on isolated dislocations (Fig. B3b). Healed cracks form networks of dislocations within the deformed crystal. The fluid inclusions within these networks have a minimum size of  $\sim 0.5\ \mu\text{m}$  and have coronas of dislocations (Fig. B3b). The water bubbles on the free dislocations are very small ( $< 0.2\ \mu\text{m}$ ). Dislocations also form coronas around these small water bubbles (Fig. B3b).

### FLUID PRESSURE

The homogenisation temperatures of three fluid inclusions in a hydrostatically loaded sample (GRZ26) and of nine fluid inclusions in a deformed sample (GRZ16) are measured with a heating-freezing stage, located at the Mineralogy and Petrology group of the Montanuniversität in Leoben, Austria.

From the homogenisation temperature, the fluid density can be calculated (assuming that the fluid was pure water). From the fluid density, the trapping pressures of the fluid were calculated with the computer programs of Bakker (2003), assuming a homogeneous temperature distribution through the sample of  $\sim 800^{\circ}\text{C}$ , using the equation of state for pure  $\text{H}_2\text{O}$  of Haar et al. (1984). The data are presented in Table B1 and plotted in Figure B4.

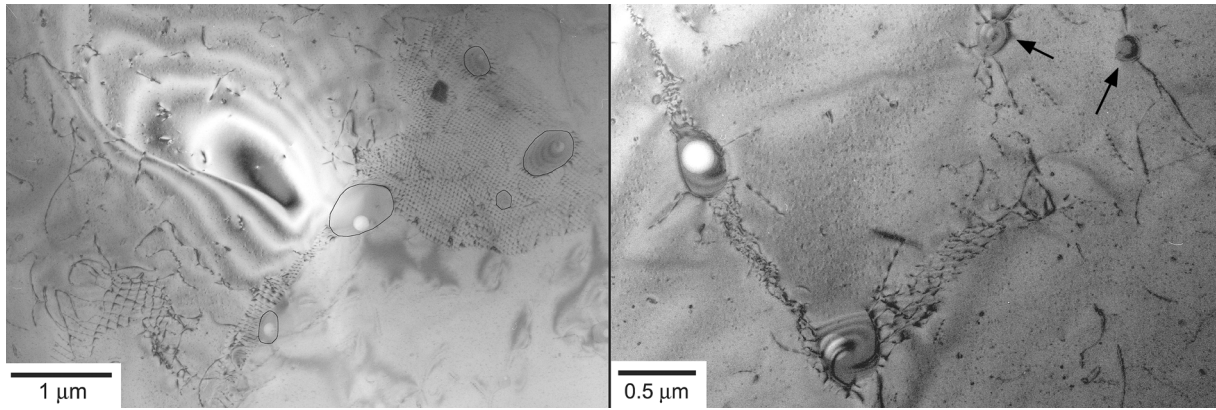


**Figure B3 :** Bright field TEM micrographs of areas with fluid inclusions in sample (GRZ22) deformed parallel to  $\langle a \rangle$  with 1 vol% added water, at  $T=800^\circ\text{C}$ ,  $P_c=1240$  MPa and  $\dot{\epsilon}=1.0 \cdot 10^{-6}\text{s}^{-1}$  to 36% bulk finite strain. a) Dislocations in healed crack form a network. Fluid inclusions (traced with black line) are present within this network. b) Fluid inclusions on healed crack and small free water bubbles (black arrows) surrounded by a corona of dislocations.

Nr	size [ $\mu\text{m}$ ]	$T_{exp}$ [ $^\circ\text{C}$ ]	$T_{hom}$ [ $^\circ\text{C}$ ]	$V_{mol}$ [ $\text{ccmol}^{-1}$ ]	$P_{fluid}$ [MPa]
GRZ26					
1	52	802	192.5	20.63	817
2	11	802	190.0	20.56	825
3	9	802	190.0	20.56	825
GRZ16					
1	20	798	199.7	20.83	789
2	13	798	203.9	20.95	776
3	13	798	195.7	20.72	802
4	-	798	197.5	20.77	796
5	26	798	202.0	20.89	783
6	17	798	190.0	20.56	820
7	25	798	212.5	21.20	750
8	10	798	205.1	20.69	805
9	8	798	211.0	21.16	754

**Table B1:** Homogenisation temperatures ( $T_{hom}$ ) and calculated fluid pressures ( $P_{fluid}$ ) of sample (GRZ26) hydrostatically loaded for 221 hours with 1 vol% added water at  $T_{exp}=802^\circ\text{C}$  and  $P_c=1180$  MPa and sample (GRZ16) deformed parallel to  $\langle o \rangle$  with 1 vol% added water at  $T_{exp}=798^\circ\text{C}$ ,  $P_c=1200$  and  $\dot{\epsilon}=0.7 \cdot 10^{-6}\text{s}^{-1}$  to 11% bulk finite strain.  $V_{mol}$  is the molar volume at  $T_{hom}$ .

The average trapping pressure of the fluids in the hydrostatically loaded sample is  $821 \pm 4$  MPa and the average trapping pressure of the deformed sample is  $786 \pm 8$  MPa. It is not known at which stage the fluids enter the sample during the hydrostatical loading. They may have entered the sample at a very early stage of the initial loading. This would explain the difference between the trapping pressure ( $821 \pm 4$  MPa) and the calculated confining pressure during the hydrostatic loading phase (1180 MPa). Gleason et al. (1993) has measured the

confining pressure in a Griggs rig experiment using the Wollastonite-Garnet structure transition. They found that the confining pressure in a standard experimental assembly with NaCl as confining medium is overestimated by 24%. In that case, the real confining pressure during our experiments could have been ~910 MPa, which is, however, still higher than the trapping pressure of the fluids. During deformation, the fluid inclusions change shape, are compressed, necked down and maybe totally rearranged. The trapping pressure in the deformed samples is lower than the trapping pressure in the hydrostatically loaded samples and shows a larger spread. This decrease in pressure could be explained by the loss of water from fluid inclusions during post entrapment modification (Bakker and Janssen 1994).

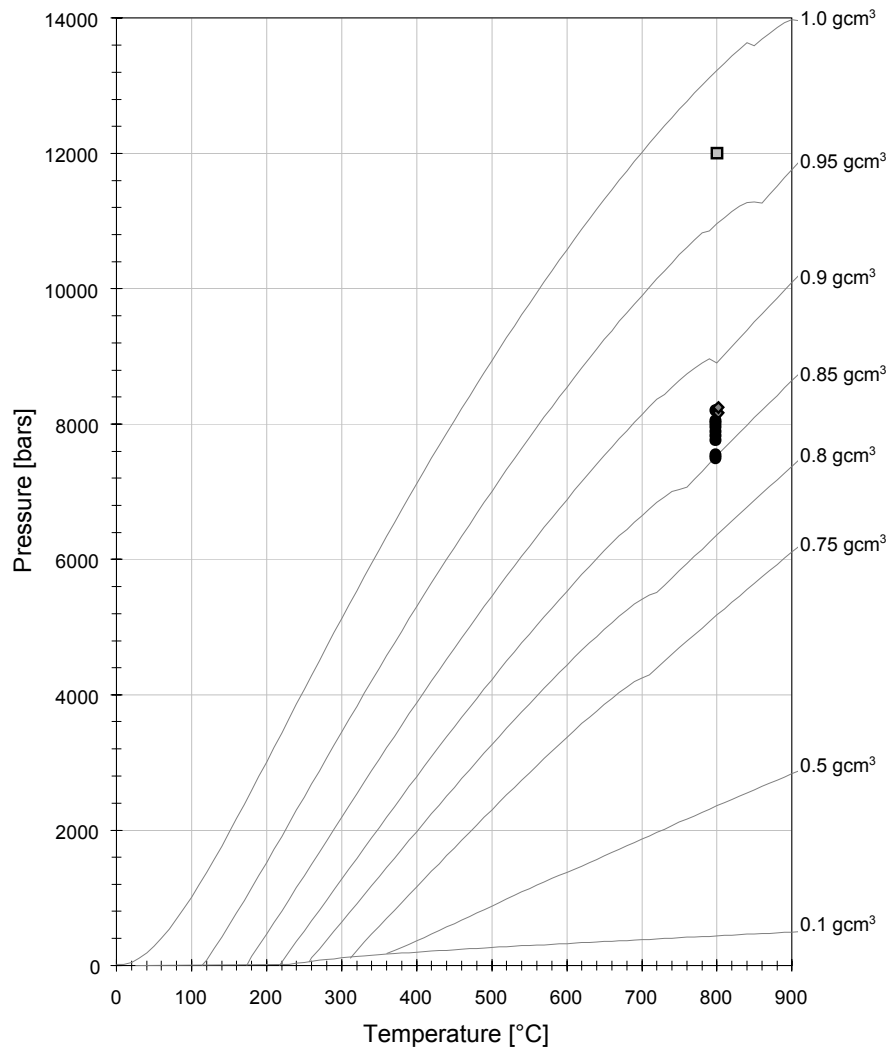


**Figure B4:** Diagram showing the density of the water as a function of pressure and temperature (grey lines). The trapping pressure and temperature of the fluids plotted as grey diamonds (GRZ26) and as black diamonds (GRZ16). Grey quadrant indicates the intended pressure and temperature of the experiments.

**APPENDIX C****EXPERIMENTAL REPRODUCTION OF  
TECTONIC DEFORMATION LAMELLAE IN QUARTZ AND COMPARISON TO  
SHOCK-INDUCED PLANAR DEFORMATION FEATURES**

M.G.C.VERNOOIJ AND F.LANGENHORST

In press in Meteoritics and Planetary Science, Special Stoeffler Issue, September 2005

**ABSTRACT**

Planar features can develop in quartz during comparatively slow tectonic deformation and during very fast dynamic shock metamorphism. Despite their very different structural nature, tectonically induced deformation lamellae have sometimes been mistaken as shock-induced planar deformation features (PDFs). To understand the formation of deformation lamellae and to address the substantial differences between them and PDFs, we have conducted deformation experiments on quartz single crystals in a Griggs-type apparatus, at a temperature of 800°C, a confining pressure of 12 kbar, and a strain rate of  $0.7-1.1 \cdot 10^{-6}$ . The deformed samples were analysed with transmission electron microscopy (TEM) and compared to natural PDFs from the Ries Crater, Germany. TEM revealed that tectonic deformation lamellae are associated with numerous sub-parallel curved subgrain walls, across which the orientation of the crystal changes slightly. The formation of deformation lamellae is due to glide- and climb-controlled deformation in the exponential creep regime. In contrast, the PDFs in shocked quartz from the Ries are perfectly planar, crystallographically controlled features that originally represented amorphous lamellae. Due to post-shock annealing and hydrothermal activity they are recrystallised and decorated with fluid inclusions.





---

**APPENDIX D**  
**CONFERENCE CONTRIBUTIONS**

Vernooij, M. & den Brok, B. Experimental investigation of lattice preferred orientation development in quartz single crystals deformed in the ductile regime with added water. Tectonic Studies Group Meeting, Liverpool, United Kingdom, January 2003.

Vernooij M., den Brok, B. & Kunze K. LPO development in quartz: experiments on natural single crystals. Deformation Mechanisms, Rheology and Tectonics, St. Malo, France, April 2003.

Vernooij M., den Brok B. & Kunze K. CPO development by preferred nucleation and growth in experimentally deformed quartz single crystals. International Geological Congress, Florence, Italy, August 2004.

Vernooij, M., Langenhorst, F. & den Brok, B. Shock metamorphism or tectonic deformation? A TEM investigation of planar features in quartz. Swiss Geoscience Meeting, Lausanne, Switzerland, November 2004.

Vernooij, M., den Brok, B. & Kunze, K. CPO development in experimentally deformed quartz single crystals. Deformation Mechanisms, Rheology and Tectonics, Zürich, Switzerland, Mai 2005.

Vernooij, M., Kunze, K. & den Brok, B. 'Brittle' shear zones in experimentally deformed quartz single crystals. Deformation Mechanisms, Rheology and Tectonics, Zürich, Switzerland, Mai 2005.



## REFERENCES

- Adams, B. L., Wright, S. I. & Kunze, K. 1993. Orientation Imaging - the Emergence of a New Microscopy. *Metallurgical Transactions a-Physical Metallurgy and Materials Science* **24**(4), 819-831.
- Ardell, A. J., Christie, J. M. & McCormic, J. 1974. Dislocation Images in Quartz and Determination of Burgers Vectors. *Philosophical Magazine* **29**(6), 1399-1411.
- Audétat, A. & Günther, D. 1999. Mobility and H<sub>2</sub>O loss from fluid inclusions in natural quartz crystals. *Contributions to Mineralogy and Petrology* **137**(1-2), 1-14.
- Baëta, R. D. & Ashbee, K. H. G. 1969a. Slip Systems in Quartz .2. Interpretation. *American Mineralogist* **54**(11-1), 1574-1582.
- Baëta, R. D. & Ashbee, K. H. G. 1969b. Slip Systems in Quartz .1. Experiments. *American Mineralogist* **54**(11-1), 1551-1573.
- Bagdassarov, N. S. & Delépine, N. 2004. alpha-beta inversion in quartz from low frequency electrical impedance spectroscopy. *Journal of Physics and Chemistry of Solids* **65**(8-9), 1517-1526.
- Bakker, R. J. 2003. Package FLUIDS 1. Computer programs for analysis of fluid inclusion data and for modelling bulk fluid properties. *Chemical Geology* **194**(1-3), 3-23.
- Bakker, R. J. & Jansen, J. B. 1994. A Mechanism for Preferential H<sub>2</sub>O Leakage from Fluid Inclusions in Quartz, Based on TEM Observations. *Contributions to Mineralogy and Petrology* **116**(1-2), 7-20.
- Bestmann, M. & Prior, D. J. 2003. Intragranular dynamic recrystallization in naturally deformed calcite marble: diffusion accommodated grain boundary sliding as a result of subgrain rotation recrystallization. *Journal of Structural Geology* **25**(10), 1597-1613.
- Blacic, J. D. 1975. Plastic-Deformation Mechanisms in Quartz - Effect of Water. *Tectonophysics* **27**(3), 271-294.
- Blacic, J. D. & Christie, J. M. 1984. Plasticity and Hydrolytic Weakening of Quartz Single-Crystals. *Journal of Geophysical Research* **89**(NB6), 4223-4239.
- Blenkinsop, T.G. & Drury, M.R. 1988. Stress estimates and fault history from quartz microstructures. *Journal of Structural Geology* **10**(7), 673-684.
- Bons, P. D. & den Brok, B. 2000. Crystallographic preferred orientation development by dissolution-precipitation creep. *Journal of Structural Geology* **22**(11-12), 1713-1722.
- Bouchez, J. L. & Pecher, A. 1981. The Himalayan Main Central Thrust Pile and Its Quartz-Rich Tectonites in Central Nepal. *Tectonophysics* **78**(1-4), 23-50.
- Burg, J. P. & Laurent, P. 1978. Strain Analysis of a Shear Zone in a Granodiorite. *Tectonophysics* **47**(1-2), 15-42.
- Burg, J. P., Wilson, C. J. & Mitchell, J. C. 1986. Dynamic recrystallization and fabric development during simple shear deformation of ice. *Journal of Structural Geology* **8**, 857-870.
- Christie, J. M. & Raleigh, C. B. 1959. The Origin of Deformation Lamellae in Quartz. *American Journal of Science* **257**(6), 385-407.
- Christie, J. M. & Ardell, A. J. 1974. Substructures of deformation lamellae in quartz. *Geology* **2**, 405-408.
- Christie, J. M. & Ardell, A. J. 1976. Deformation structures in minerals. In: *Electron microscopy in mineralogy* (edited by Wenk, H. R.). Springer, Berlin, 374-404.
- Christie, J. M., Griggs, D. T. & Carter, N. L. 1964. Experimental Evidence of Basal Slip in Quartz. *Journal of Geology* **72**(6), 734-756.
- de Araújo, M. N. C., da Silva, F. C. A., de Sa, E. F. J., Holcombe, R. J. & de Vasconcelos, P. M. 2003. Microstructural evolution of the Serido Belt, NE-Brazil: the effect of two tectonic events on development of c-axis preferred orientation in quartz. *Journal of Structural Geology* **25**(12), 2089-2107.
- Dell'Angelo, L. N. & Tullis, J. 1989. Fabric Development in Experimentally Sheared Quartzites. *Tectonophysics* **169**(1-3), 1-21.
- den Brok, S. W. J. 1992. *An Experimental Investigation into the effect of water on the flow of quartzite*. Geologica Ultraiectina, pp. 178.
- den Brok, S. W. J. & Spiers, C. J. 1991. Experimental evidence for water weakening by microcracking plus solution-precipitation creep. *Journal of the Geological Society, London* **148**, 541-548.
- den Brok, S. W. J., Zahid, M. & Passchier, C. 1998. Cataclastic solution creep of very soluble brittle salt as a rock analogue. *Earth and Planetary Science Letters* **163**, 83-95.
- den Brok, B., Zahid, M. & Passchier, C. W. 1999. Stress induced grain boundary migration in very soluble brittle salt. *Journal of Structural Geology* **21**(2), 147-151.
- Doukhan, J.C. 1995. Lattice-defects and mechanical behavior of quartz SiO<sub>2</sub>. *Journal de Physique III* **5**(11), 1809-1832.
- Drury, M. R. 1993. Deformation lamellae in metals and minerals. In: *Defects and processes in the solid state: Geoscience applications* (edited by Boland, J. N. & Fitz Gerald, J. D.). Elsevier, Amsterdam, 195-212.

- Drury, M. R. & Humphreys, F. J. 1986. The development of microstructure in Al-5% Mg during high temperature deformation. *Acta Metallurgica* **34**(11), 2259-2271.
- Drury, M. R. & Urai, J. L. 1990. Deformation-Related Recrystallization Processes. *Tectonophysics* **172**(3-4), 235-253.
- Durney, D. W. 1972. Solution-Transfer, an Important Geological Deformation Mechanism. *Nature* **235**(5337), 315-317.
- Etchecopar, A. & Vasseur, G. 1987. A 3-D Kinematic Model of Fabric Development in Polycrystalline Aggregates - Comparisons with Experimental and Natural Examples. *Journal of Structural Geology* **9**(5-6), 705-717.
- Fairbairn, H. W. 1949. Synthetic Quartzite. *Geological Society of America Bulletin* **60**(12), 1886-1886.
- Fitz Gerald, J. D., Boland, J. N., McLaren, A. C., Ord, A. & Hobbs, B. E. 1991. Microstructures in water-weakened single crystals of quartz. *Journal of Geophysical Research* **96**, 2139-2155.
- Fronzel, C. 1962. *Dana's system of Mineralogy*. Wiley, New York.
- Gerretsen, J., Paterson, M. S. & McLaren, A. C. 1989. The uptake and solubility of water in quartz at elevated pressure and temperature. *Physics and Chemistry of Minerals* **16**, 334-342.
- Gleason, G. C. & Tullis, J. 1995. A Flow Law for Dislocation Creep of Quartz Aggregates Determined with the Molten-Salt Cell. *Tectonophysics* **247**(1-4), 1-23.
- Gleason, G. C., Tullis, J. & Heidelbach, F. 1993. The Role of Dynamic Recrystallization in the Development of Lattice Preferred Orientations in Experimentally Deformed Quartz Aggregates. *Journal of Structural Geology* **15**(9-10), 1145-1168.
- Gordon, P. & Vandermeer, R. A. 1966. Grain boundary migration. In: *Recrystallisation, grain growth and textures* (edited by Margolin, H.). American Society for Metals, 205-266.
- Green, H. W., Griggs, D. T. & Christie, J. M. 1970. Syntectonic and annealing recrystallization of fine-grained quartz aggregates. In: *Experimental and natural rock deformation* (edited by Paulitsch, P.). Springer Verlag, Berlin, 272-335.
- Griggs, D. T. 1940. Experimental flow of rocks under conditions favoring recrystallization. *The Geological Society of America Bulletin* **51**(7), 1001-1022.
- Griggs, D. 1967. Hydrolytic Weakening of Quartz and Other Silicates. *Geophysical Journal of the Royal Astronomical Society* **14**(1-4), 19-31.
- Guillopé, M. & Poirier, J. P. 1979. Dynamic Recrystallization During Creep of Single-Crystalline Halite - Experimental-Study. *Journal of Geophysical Research* **84**(NB10), 5557-5567.
- Haar, L., Gallagher, J. S. & Kell, G. S. 1984. NBS/NRC steam tables.
- Hippertt, J. & Egydio-Silva, M. 1996. New polygonal grains formed by dissolution-redeposition in quartz mylonite. *Journal of Structural Geology* **18**(11), 1345-1352.
- Hirth, G. & Tullis, J. 1992. Dislocation Creep Regimes in Quartz Aggregates. *Journal of Structural Geology* **14**(2), 145-159.
- Hobbs, B. E. 1968. Recrystallization of Single Crystals of Quartz. *Tectonophysics* **6**(5), 353-401.
- Hobbs, B. E. 1985. The geological significance of microfabric analysis. In: *Preferred orientation in deformed metals and rocks: An introduction to modern texture analysis* (edited by Wenk, H. R.). Academic press, London, 463-484.
- Hobbs, B. E., McLaren, A. C. & Paterson, M. S. 1972. Plasticity of single crystals of synthetic quartz. In: *Flow and fracture of rocks* (edited by Heard, H. C., Borg, I. Y., Carter, N. L. & Raleigh, C. B.) **16**. Geophysical Monograph, 29-53.
- Holm, E. A., Miodownik, M. A. & Rolett, A. D. 2003. On abnormal subgrain growth and the origin of recrystallization nuclei. *Acta Materialia* **51**, 2701-2716.
- Hull, D. & Bacon, D. J. 1984. *Introduction to dislocations*. Pergamon, Oxford.
- Jessell, M. W. 1988. Simulation of Fabric Development in Recrystallizing Aggregates. 2. Example Model Runs. *Journal of Structural Geology* **10**(8), 779-793.
- Jessell, M. W. & Lister, G. S. 1990. A simulation of the temperature dependence of quartz fabrics. In: *Deformation mechanisms, Rheology and Tectonics* (edited by Knipe, R. J. & Rutter, E. H.). Geological Society Special Publication **54**, 353-362.
- Kamb, W. B. 1959. Theory of Preferred Crystal Orientation Developed by Crystallization under Stress. *Journal of Geology* **67**(2), 153-170.
- Kamb, W. B. 1972. Recrystallization of ice. In: *Flow and fracture of rocks: the Griggs volume* (edited by Heard, H. C.). Geophysical monograph **16**, Washington D.C., 211-242.
- Karato, S. I. & Masuda, T. 1989. Anisotropic Grain-Growth in Quartz Aggregates under Stress and Its Implication for Foliation Development. *Geology* **17**(8), 695-698.
- Kikuchi, S. 1928. Diffraction of cathode rays by micas. *Japan. J. Physics* **5**, 83-96.

- Kruhl, J. H. & Peternell, M. 2002. The equilibration of high-angle grain boundaries in dynamically recrystallized quartz: the effect of crystallography and temperature. *Journal of Structural Geology* **24**(6-7), 1125-1137.
- Kruse, R., Stünitz, H. & Kunze, K. 2001. Dynamic recrystallization processes in plagioclase porphyroclasts. *Journal of Structural Geology* **23**(11), 1781-1802.
- Kunze, K. 1991. Zur quantitativen Texturanalyse von Gesteinen: Bestimmung, Interpretation und Simulation von Quarzteilgefügen. Veröffentlichungen ZIPE Potsdam, Ph.D. thesis RWTH Aachen, pp. 136.
- Langenhorst, F. 2002. Shock metamorphism of some minerals: basic introduction and microstructural observations. *Bulletin of the Czech geological survey* **77**(4), 256-282.
- Langenhorst, F. & Deutsch, A. 1998. Minerals in terrestrial impact structures and their characteristic features. In: *Advanced Mineralogy* (edited by Marfunin, A. S.) **3**. Springer Verlag, Berlin, 95-119.
- Lapworth, C. 1885. The highland controversy in British geology: its causes, course and consequences. *Nature* **32**, 558-559.
- Law, R. D. 1990. Crystallographic fabrics: a selective review of their applications to research in structural geology. In: *Deformation Mechanisms, Rheology and Tectonics* (edited by Knipe, R. J. & Rutter, E. H.) **54**. Geological Society Special Publication, 335-352.
- Leiss, B. & Barber, D. J. 1999. Mechanisms of dynamic recrystallization in naturally deformed dolomite inferred from EBSP analyses. *Tectonophysics* **303**(1-4), 51-69.
- Lister, G. S. & Price, G. P. 1978. Fabric Development in a Quartz-Feldspar Mylonite. *Tectonophysics* **49**(1-2), 37-78.
- Lister, G. S. & Paterson, M. S. 1979. Simulation of Fabric Development During Plastic-Deformation and its Application to Quartzite - Fabric Transitions. *Journal of Structural Geology* **1**(2), 99-115.
- Lister, G. S. & Hobbs, B. E. 1980. The Simulation of Fabric Development During Plastic-Deformation and Its Application to Quartzite - the Influence of Deformation History. *Journal of Structural Geology* **2**(3), 355-370.
- Lister, G. S. & Dornsiepen, U. F. 1982. Fabric Transitions in the Saxony Granulite Terrain. *Journal of Structural Geology* **4**(1), 81-92.
- Lister, G. S., Paterson, M. S. & Hobbs, B. E. 1978. Simulation of Fabric Development in Plastic-Deformation and Its Application to Quartzite - Model. *Tectonophysics* **45**(2-3), 107-158.
- Mainprice, D., Bouchez, J. L., Blumenfeld, P. & Tubia, J. M. 1986. Dominant-C Slip in Naturally Deformed Quartz - Implications for Dramatic Plastic Softening at High-Temperature. *Geology* **14**(10), 819-822.
- Mancktelow, N. S. 1987. Quartz Textures from the Simplon Fault Zone, Southwest Switzerland and North Italy. *Tectonophysics* **135**(1-3), 133-153.
- Mancktelow, N. S. & Pennacchioni, G. 2004. The influence of grain boundary fluids on the microstructure of quartz-feldspar mylonites. *Journal of Structural Geology* **26**(1), 47-69.
- Mancktelow, N. S., Grujic, D. & Johnson, E. L. 1998. An SEM study of porosity and grain boundary microstructure in quartz mylonites, Simplon fault zone, central Alps. *Contributions to Mineralogy and Petrology* **131**(1), 71-85.
- Marshall, D. J. 1988. *Cathodoluminescence of geological materials*. Unwin Hyman.
- Masuda, T. & Fujimura, A. 1981. Microstructural Development of Fine-Grained Quartz Aggregates by Syntectonic Recrystallization. *Tectonophysics* **72**(1-2), 105-128.
- Mauler Steinmann, A. 2000. Texture and microstructure of eclogites. Eletron backscatter diffraction applied to samples from nature and experiment, Diss. Naturwissenschaften ETH Zürich, Nr. 13690.
- McLaren, A. C. 1986. Some speculations on the nature of high-angle grain boundaries in quartz rocks. In: *Mineral and rock deformation: Laboratory studies, The Paterson Volume* (edited by Hobbs, B. E. & Heard, H. C.) **36**. Geophysical Monograph, American Geophysical Union, Washington, DC, 233-247.
- McLaren, A.C. 1991. *Transmission electron microscopy of minerals and rocks*. Cambridge topics in mineral physics and chemistry: Cambridge, Cambridge University Press.
- McLaren, A. C. & Hobbs, B. E. 1972. Transmission electron microscope investigation of some naturally deformed quartzites. In: *Flow and fracture of rocks* (edited by Heard, H. C., Borg, I. Y., Carter, N. L. & Raleigh, C. B.) **16**. Geophysical Monograph, 55-66.
- McLaren, A. C., Turner, R. G., Boland, J. N. & Hobbs, B. E. 1970. Dislocation Structure of Deformation Lamellae in Synthetic Quartz - a Study by Electron and Optical Microscopy. *Contributions to Mineralogy and Petrology* **29**(2), 101-115.
- McLaren, A. C., Fitz Gerald, J. D. & Gerretsen, J. 1989. Dislocation Nucleation and Multiplication in Synthetic Quartz - Relevance to Water Weakening. *Physics and Chemistry of Minerals* **16**(5), 465-482.
- Means, W. D. 1983. Microstructure and Micromotion in Recrystallization Flow of Octachloropropane - a 1st Look. *Geologische Rundschau* **72**(2), 511-528.
- Morrison-Smith, D. J., Paterson, M. S. & Hobbs, B. E. 1976. Electron-Microscope Study of Plastic-Deformation in Single-Crystals of Synthetic Quartz. *Tectonophysics* **33**(1-2), 43-79.

- Neumann, B. 2000. Texture development of recrystallised quartz polycrystals unravelled by orientation and misorientation characteristics. *Journal of Structural Geology* **22**(11-12), 1695-1711.
- Nyman, M. W., Law, R. D. & Smelik, E. A. 1992. Cataclastic Deformation Mechanism for the Development of Core-Mantle Structures in Amphibole. *Geology* **20**(5), 455-458.
- Ord, A. & Hobbs, B. E. 1986. Experimental control of the water-weakening effect in quartz. *Geophysical Monograph* **36**, 51-72.
- Passchier, C. W. & Trouw, R. A. J. 1998. *Microtectonics*. Springer, Berlin, pp. 289.
- Paterson, M. S. 1982. The Determination of Hydroxyl by Infrared-Absorption in Quartz, Silicate-Glasses and Similar Materials. *Bulletin De Mineralogie* **105**(1), 20-29.
- Paterson, M. S. & Kekulawala, K. 1979. Role of Water in Quartz Deformation. *Bulletin De Mineralogie* **102**(2-3), 92-98.
- Poirier, J.-P. 1985. *Creep of crystals: High-temperature deformation processes in metals, ceramics and minerals*. Cambridge University press, pp. 260.
- Poirier, J. P. & Nicolas, A. 1975. Deformation-Induced Recrystallization Due to Progressive Misorientation of Subgrains, with Special Reference to Mantle Peridotites. *Journal of Geology* **83**(6), 707-720.
- Poirier, J. P. & Guillopé, M. 1979. Deformation Induced Recrystallization of Minerals. *Bulletin De Mineralogie* **102**(2-3), 67-74.
- Post, A. D., Tullis, J. & Yund, R. A. 1996. Effects of chemical environment on dislocation creep of quartzite. *Journal of Geophysical Research-Solid Earth* **101**(B10), 22143-22155.
- Price, G. P. 1985. Preferred orientations in quartzites. In: *Preferred orientations in deformed metals and rocks: An introduction to modern texture analysis* (edited by Wenk, H. R.). Academic press, London, 385-406.
- Prior, D. J., Boyle, A. P., Brenker, F., Cheadle, M. C., Day, A., Lopez, G., Peruzzo, L., Potts, G. J., Reddy, S., Spiess, R., Timms, N. E., Trimby, P., Wheeler, J. & Zetterstrom, L. 1999. The application of electron backscatter diffraction and orientation contrast imaging in the SEM to textural problems in rocks. *American Mineralogist* **84**(11-12), 1741-1759.
- Prior, D. J., Bestmann, M., Halfpenny, A., Mariani, E., Piazzolo, S., Tullis, J. & Wheeler, J. 2004. Recrystallization and grain growth in rocks and minerals. In: *Recrystallization and Grain Growth, Pts 1 and 2. Materials Science Forum* **467-470**, 545-550.
- Ralsler, S. 1990. Shear zones developed in an experimentally deformed quartz mylonite. *Journal of structural geology* **12**, 1033-1045.
- Ramsay, J. G. 1980. Shear Zone Geometry - a Review. *Journal of Structural Geology* **2**(1-2), 83-99.
- Rybacki, E., Renner, J., Konrad, K., Harbott, W., Rummel, F. & Stockhert, B. 1998. A servohydraulically-controlled deformation apparatus for rock deformation under conditions of ultra-high pressure metamorphism. *Pure and Applied Geophysics* **152**(3), 579-606.
- Sander, B. 1911. Ueber Zusammenhänge zwischen Teilbewegung und Gefüge in Gesteinen. *Tschermak. mineralogische und petrographische Mitteilungen* **30**, 281-314.
- Sander, B. 1930. *Gefügekunde der Gesteine mit besonderer Berücksichtigung der Tektonite*. Julius Springer Verlag, Wien.
- Schmid, S. M. & Casey, M. 1986. Complete fabric analysis of some commonly observed quartz c-axis patterns. In: *Mineral and Rock Deformation: Laboratory Studies. The Paterson Volume* (edited by Hobbs, B. E. & Heard, H. C.). American Geophysical Union **36**, 263-286.
- Schmid, S. M., Casey, M. & Starkey, J. 1981. An Illustration of the Advantages of a Complete Texture Analysis described by the Orientation Distribution Function (ODF) using Quartz Pole Figure Data. *Tectonophysics* **78**(1-4), 101-117.
- Schmocker, M., Bystricky, M., Kunze, K., Burlini, L., Stunitz, H. & Burg, J. P. 2003. Granular flow and Riedel band formation in water-rich quartz aggregates experimentally deformed in torsion. *Journal of Geophysical Research-Solid Earth* **108**(B5), 2242, doi:10.1029/2002JB001958.
- Segall, P. & Simpson, C. 1986. Nucleation of Ductile Shear Zones on Dilatant Fractures. *Geology* **14**(1), 56-59.
- Shelley, D. 1971. Origin of Cross-Girdle Fabrics of Quartz. *Tectonophysics* **11**(1), 61-68.
- Simpson, C. 1981. The Role of Ductile Shear Zones in the Structural Evolution of the Maggia Nappe, Swiss Alps. *Journal of Structural Geology* **3**(2), 193-193.
- Stallard, A. & Shelley, D. 1995. Quartz c-axes parallel to stretching directions in very low grade metamorphic rocks. *Tectonophysics* **249**, 31-40.
- Stipp, M. & Tullis, J. 2003. The recrystallized grain size piezometer for quartz. *Geophysical Research Letters* **30**(21), 2088, doi: 10.1029/2003GL01844.
- Stipp, M., Stünitz, H., Heilbronner, R. & Schmid, S. M. 2002. The eastern Tonale fault zone: a 'natural laboratory' for crystal plastic deformation of quartz over a temperature range from 250 to 700°C. *Journal of Structural Geology* **24**(12), 1861-1884.

- Stöckhert, B. & Duyster, J. 1999. Discontinuous grain growth in recrystallised vein quartz - implications for grain boundary structure, grain boundary mobility, crystallographic preferred orientation, and stress history. *Journal of Structural Geology* **21**(10), 1477-1490.
- Sunagawa, I., Imai, H., Takada, M. & Hoshino, Y. 2004. Morphogenesis of quartz crystals twinned after Japan Law. *European Journal of Mineralogy* **16**(1), 91-97.
- Takeshita, T. & Wenk, H. R. 1988. Plastic Anisotropy and Geometrical Hardening in Quartzites. *Tectonophysics* **149**(3-4), 345-361.
- Takeshita, T. & Hara, I. 1998. C-axis fabrics and microstructures in a recrystallized quartz vein deformed under fluid-rich greenschist conditions. *Journal of Structural Geology* **20**(4), 417-431.
- Takeshita, T., Wenk, H. R. & Lebensohn, R. 1999. Development of preferred orientation and microstructure in sheared quartzite: comparison of natural data and simulated results. *Tectonophysics* **312**(2-4), 133-155.
- Trepmann, C. A. & Stockhert, B. 2003. Quartz microstructures developed during non-steady state plastic flow at rapidly decaying stress and strain rate. *Journal of Structural Geology* **25**(12), 2035-2051.
- Tullis, J. 1977. Preferred Orientation of Quartz Produced by Slip During Plane Strain. *Tectonophysics* **39**(1-3), 87-102.
- Tullis, J. & Tullis, T. E. 1986. Experimental rock deformation techniques. In: *Mineral and Rock deformation: Laboratory studies. The Paterson Volume* (edited by Hobbs, B. E. & Heard, H. C.). Geophysical Monograph Series **36**, 297-324.
- Tullis, J., Christie, J. M. & Griggs, D. T. 1973. Microstructures and Preferred Orientations of Experimentally Deformed Quartzites. *Geological Society of America Bulletin* **84**(1), 297-314.
- Turner, F. J. 1948. Note on the tectonic significance of deformation lamellae in quartz and calcite. *AGU Transactions* **29**, 565-569.
- Turner, F. J. & Weiss, L. E. 1963. *Structural analysis of metamorphic tectonites*. McGraw\_Hill Book Co., New York.
- Twiss, R. J. 1974. Structure and significance of planar deformation features in synthetic quartz. *Geology* **2**(7), 329-332.
- Twiss, R. J. & Moores, E. M. 1992. *Structural geology*. W.H. Freeman and company, New York, pp. 532.
- Urai, J. L., Means, W. D. & Lister, G. S. 1986. Dynamic recrystallization of minerals. In: *Mineral and rock deformation: laboratory studies. The Paterson volume*. (edited by Hobbs, B. E. & Heard, H. C.). Geophysical Monograph **36**, 161-199.
- van Daalen, M., Heilbronner, R. & Kunze, K. 1999. Orientation analysis of localized shear deformation in quartz fibres at the brittle-ductile transition. *Tectonophysics* **303**(1-4), 83-107.
- Vernon, R. H. 1981. Optical Microstructure of Partly Recrystallized Calcite in Some Naturally Deformed Marbles. *Tectonophysics* **78**(1-4), 601-612.
- Vernooij, M.G.C. & Langenhorst, F. 2005. Experimental reproduction of tectonic deformation lamellae in quartz and comparison to shock-induced planar deformation features. *Meteoritics and Planetary Science*. In press.
- Wenk, H. R. 1985. *Preferred orientation in deformed metals and rocks: an introduction to modern texture analysis*. Academic Press Inc, Orlando.
- Wenk, H. R. 1998. Plasticity modeling in minerals and rocks. In: *Texture and anisotropy: preferred orientations in polycrystals and their effect on materials properties* (edited by Kocks, U. F., Tome, C. N. & Wenk, H. R.). Cambridge University press, 560-596.
- Wenk, H. R. & Christie, J. M. 1991. Comments on the Interpretation of Deformation Textures in Rocks. *Journal of Structural Geology* **13**(10), 1091-1110.
- Wheeler, J., Prior, D. J., Jiang, Z., Spiess, R. & Trimby, P. W. 2001. The petrological significance of misorientations between grains. *Contributions to Mineralogy and Petrology* **141**(1), 109-124.
- Wheeler, J., Jiang, Z. T., Prior, D. & Tullis, J. 2004. Dynamic recrystallisation of quartz. In: *Recrystallization and Grain Growth, Pts 1 and 2. Materials Science Forum* **467-470**, 1243-1248.
- White, S. H. 1971. Natural creep deformation of quartzites. *Nature-Physical Science* **234**, 175-177.
- White, S. H. 1973. Deformation Lamellae in Naturally Deformed Quartz. *Nature-Physical Science* **245**(141), 27-28.
- White, S. H. 1976. The effects of strain on the microstructures, fabrics and deformation mechanisms in quartz. *Philosophical Transactions of the Royal Society, London* **A283**, 276-277.
- White, S. 1977. Geological Significance of Recovery and Recrystallization Processes in Quartz. *Tectonophysics* **39**(1-3), 143-170.





## CURRICULUM VITAE

Martine G. C. Vernooij

*Place and date of Birth:* Nieuwegein, November 19, 1977

*Nationality:* Dutch

### *Education:*

1990-1996 VWO, Cals College, Nieuwegein, the Netherlands.

1996-2001 Geology, University of Utrecht, the Netherlands

Diploma thesis: "The relation between dynamic recrystallisation and rheology: observations on tin"

Supervisors: Prof. Dr. C.J. Spiers and Dr. J.H.P. de Bresser

Mapping thesis: "The metamorphic and structural evolution of the Phyllite-Quartzite in the Taygetos Massif in the Peloponnese (Greece)"

Supervisor: Prof. Dr. S. White

2001-2005 Ph.D. student, Geological Institute, Swiss federal institute of technology, Zürich, Switzerland

Dissertation: "Dynamic recrystallisation and CPO development in single crystals of quartz"

Supervisors: Prof. Dr. J.-P. Burg, Dr. S.W.J. den Brok and Dr. K. Kunze

2004 Marie Curie research traineeship, Bavarian Research Institute of Experimental Geochemistry and Geophysics, University of Bayreuth, Germany

Project: "Analysis of defect structures in experimentally deformed quartz samples using TEM"

Supervisor: Prof. Dr. F. Langenhorst.

